UNIVERSITÉ DE GRENOBLE

THÈSE

Pour obtenir le grade de

DOCTEUR DE L'UNIVERSITÉ DE GRENOBLE

Spécialité : **Astrophysique et milieux dilués**

Arrêté ministériel : 7 août 2006

Présentée par

Astrid Lamberts

Thèse dirigée par **Guillaume Dubus**
et codirigée par **Sébastien Fromang**

préparée au sein **l'Institut de Planétologie et d'Astrophysique de Grenoble**
et de **l'Ecole Doctorale de Physique**

Simulations numériques de collisions de vents dans les systèmes binaires

Thèse soutenue publiquement le **14 septembre 2012**,
devant le jury composé de :

M. Gilles Henri
Professeur à l' Université Joseph Fourier, Président
M. Julian Pittard
Reader at the University of Leeds, Rapporteur
M. Frédéric Daigne
Professeur à l'Université Paris 6, Rapporteur
M. Rolf Walder
Professeur à l' ENS-Lyon, Examinateur
M. Guillaume Dubus
Chargé de recherche à l IPAG, Directeur de thèse
M. Sébastien Fromang
Ingénieur de recherche au CEA, Saclay, Co-Directeur de thèse

Contents

List of figures **5**

List of tables **7**

Abstract **9**

Résumé **11**

Chapter 1 - Current understanding of colliding wind binaries **13**

1.1 Introduction 15
1.2 A wealth of observations 18
1.3 Theoretical background : hydrodynamics and radiative acceleration 24
1.4 The contribution of numerical simulations 35
1.5 Introduction en Français 42

Chapter 2 - Simulating colliding wind binaries with RAMSES **47**

2.1 Numerical simulations : why, how and where 49
2.2 Numerical simulations with RAMSES 51
2.3 Numerical setup for colliding wind binaries 60
2.4 Overview of this chapter 63
2.5 Résumé en Français 63

Chapter 3 - Small scale simulations of colliding stellar winds **65**

3.1 Important parameters to determine the shock region 67
3.2 Impact of instabilities 78
3.3 Numerical requirements for a reliable simulation 83
3.4 What did we learn in this chapter? What should be taken into account in improved models? 83
3.5 Resumé en français 85
3.6 Paper: High resolution numerical simulations of unstable colliding stellar winds (MNRAS, 2011) 86

Chapter 4 - Understanding the large scale structure **109**

4.1 Geometry of the shocked arms 112
4.2 The large scale spiral structure 114
4.3 Application to WR 104 123
4.4 What did we learn? What are possible extensions? 127
4.5 Résumé en français 128

4.6 Paper : Impact of orbital motion on the structure and stability of adiabatic shocks in colliding wind binaries (A&A, 2012) 129

Chapter 5 - Towards the simulation of gamma-ray binaries 145

5.1 Extension of RAMSES to relativistic hydrodynamics 147
5.2 Testing, testing and testing... 155
5.3 Analytic predictions for the interaction region in γ-ray binaries 161
5.4 Simulations of γ-ray binaries 163
5.5 What do these first results indicate? What could be improved? 169
5.6 Résumé en Français 171

Chapter 6 - Conclusion and Perspectives 173

6.1 Conclusions 175
6.2 Looking forwards 176
6.3 Conclusions et perspectives en français 177

Appendices

Chapter A - 2D analytic solution of the structure of colliding wind binaries 183

Chapter B - Jacobian matrices for 3D relativistic hydrodynamics 187

References 191

Merci à tous

Wow! La thèse est finie, je me retrouve déjà à faire un premier bilan de ces trois années formidables. Je ne les ai pas vues passer, et c'est grâce au soutien et à la présence de pas mal d'entre vous.

Tout d'abord Guillaume et Sébastien (par ordre alphabétique). J'ai toujours cru que les remerciements enthousiastes envers les directeurs de thèse se faisaient toujours un peu "par tradition, parce qu'il le faut". En tout cas c'est avec un grand sourire que je remercie le duo de choc que vous avez constitué. J'ai tant appris grâce à vous. Il y a la physique bien sûr, mais surtout une méthode et rigueur qui m'ont rendues de plus en plus autonome et qui m'ont amené là où je suis. Et avec le sourire et un éclat de rire de temps en temps. Que du bonheur!

Bien sûr, il y a ma chère équipe de Sherpas aussi. C'est devenu un peu la famille (je préfère ne pas détailler qui est le grand-père, la grand-mère et tout ça). Toujours de bonne humeur, souvent de bon conseil, parfois un peu dingues (pourquoi c'est toujours moi qu'on roule dans la neige?). Vous auriez pu quand même ajouter le logo de l'équipe sur mon mangnifique T-shirt!

Il y a aussi "les gens du labo", avec qui j'ai bu un thé, échangé quelques mots, et qui m'ont rendues ces trois années très agréables. Un merci particulier à l'équipe administrative et Valérie.

Et puis il y a les thésards... Ouh-là-là. C'est sûr que je ne me suis pas ennuyée avec vous. Surtout la fine équipe du deuxième: Rémi l'Insulaire (il faudrait inventer une bidouille LateX pour faire la grosse voix), Vivdoudou, Labretonne, Nico, Ilya tapi au fond du couloir. Je pense que je vais regretter cette ambiance de travail studieuse, calme, parfois un peu stricte cependant. En tout cas, maintenant je vérouille mon pc quand je quitte mon bureau. Et puis evidement tous les autres, les anciens, les petits nouveaux, les agents secrets, même ceux du CERMO et de planéto, ceux qui savent jouer au Frisbee, ceux qui savent pas, ceux qui payent leur apéro (ou pas), ceux qui amènent des gâteaux au tea-time...Je crois que je n'ai oublié personne. Un clin d'oeil à mes co-bureau, Benoît puis Susana. Un merci aussi aux thésards que j'ai pu cottoyer lors de mes passages à Saclay. Une pause café ça fait toujours du bien (surtout entre deux solveurs de Riemann).

Une grosse bise aussi à mes amis, qu'ils habitent à Montréal, Hambourg, Montpellier, Lyon ou Paris... Merci à Lolo, Elo, Jerem, Fab, Ali, Vivianne, Anna-Lea, Rominet, Jen, Mémé, Camilo, Pablo (désolée pour les oublis)... pour les moments passés ensemble, autant de moments à décompresser, penser à autre chose et profiter.

Promis, j'en ai bientôt fini, mais faut quand même que je parle un peu de ma famille! Bedankt moeke, vake, de ondertussen groot geworde zus, meter, Arnoke en al de andere. Bedankt voor al die jaren vol aanmoedegingen, steun, vakanties en lekker eten !

Enfin, le meilleur pour la fin. Christophe, mon amour. Tu m'accompagnes dans chaque étape de mon projet depuis que j'ai commencé ces longues études. Merci d'y avoir cru quand moi je n'y croiyais plus mais surtout de m'avoir apporté la légerté et décontraction nécéssaire à mon équilibre. Une nouvelle page s'ouvre pour nous deux, envolons-nous vers de nouvelles aventures !

Aan diegene die belangrijker zijn dan dit werk

“ Une journée où l’on n’a rien appris est une journée de perdue”
Mike Horn, Explorateur

List of Figures

1.1 Density maps showing the geometry of a colliding wind binary with identical winds (left panel) and when the first wind dominates (right panel). In the latter case the second wind is totally confined. The highest density regions (red) are about a thousand times denser than the lower density regions (purple). 16

1.2 Left panel : *Hubble Space Telescope* observation of an OB star showing a P Cygni profile for N V [Haser et al., 1995]. Right panel : Formation of a P Cygni profile. Image by Daniel Kasen (*http://supernova.lbl.gov/ dnkasen/*). 18

1.3 Spectra of a B star (top), O star (middle) and WR star (bottom) obtained with *XMM-Newton* [Güdel and Nazé, 2009]. 19

1.4 Observed (left panel) and simulated (right panel) intensity distribution at 1.6 GHz from WR 147. Both show isotropic thermal emission from the WR star at the bottom and non-thermal emission at the bow shock close to the early type star at the top of the image. 20

1.5 Very Long Baseline Array (VLBA) radio maps of LSI + 61 303 ° at different orbital phases. The pink star indicates the position of the massive star and the blue squares the positions of the pulsar. The actual size of the orbit ($a \simeq 0.15$ mas) is enlarged to show the different radio observations. The size of the emission region is about 6 mas. 21

1.6 Left: *ROSAT* X-ray light curve from WR+O binary γ^2 Velorum [Willis et al., 1995]. Right: X-ray spectrum from η Carinae. The crosses indicate *Chandra* observations, the solid line is a simulated spectrum [Pittard and Corcoran, 2002] obtained with a hydrodynamical simulation including radiative cooling in an optically thin plasma. 22

1.7 Infrared image of Pinwheel nebula WR 104 [Tuthill et al., 2008]. Image obtained by interferometry with the Keck telescope. 22

1.8 Left panel: Spectral energy distribution of LS 5039 [Hadasch et al., 2012]. Red and blue points show *Fermi*-LAT data, the grey points show H.E.S.S. data. The plot shows values for the inferior (phase = 0.72)and superior conjunction (phase =0.06). The corresponding light curve obtained by H.E.S.S. is given on the right panel. The solid line shows a predicted lightcurve that takes into account anisotropic inverse Compton scattering (dashed line) and attenuation by pair production [Dubus et al., 2008]. 23

1.9 Solutions of the momentum equation of a stellar wind with only gas pressure and gravity. The black dotted solutions have no physical meaning. The brown solution corresponds to a wind that leaves the star with a supersonic velocity, which is unobserved. The blue solution corresponds to a slow *breeze* while the green solution corresponds to Bondi-Hoyle accretion, with matter coming from $r = \infty$ and going towards $r = r_0$. The supersonic wind solution is given by the thick solid red line. 26

1.10 C III line profile (λ 5696) for WR 88 [St-Louis et al., 2011], a star that has no known binary companion. Different spectra show different moments, similar colours indicate similar shapes. The y axis shows time in days. 29
1.11 Left panel: *Chandra* image of the Crab nebula [Hester et al., 2002]. The pulsar is the white dot at the centre of the image, the inner ring is interpreted as the shock between the wind and the nebula. The jets and torus are particles flowing away from the poles of the pulsar. The whole structure is embedded in the supernova remnant that is observed at larger scales. Right panel: H_α observation (Palomar telescope [Chatterjee and Cordes, 2002]) of the so-called Guitar Nebula that results from a high velocity neutron star propagating through the ISM. 30
1.12 Hydrodynamical variables on both sides of the shock in the frame of the laboratory (left panel) and the frame of the shock (right panel). In this particular case, the upstream region is at rest in the frame of the laboratory. 31
1.13 Sketch of the two-wind interaction problem. The stars are the big dots, the interaction region is shown with the thick red line. 33
1.14 Cooling function [Pittard et al., 2005] for solar abundances and carbonated Wolf-Rayet stars. For $T > 10^6\,K$, the chemical composition does not significantly affect the cooling rate. The cooling function takes into account line emission from many elements and free-free emission. 34
1.15 Density (color scale) and velocity (arrows) in a simulated γ-ray binary [Bosch-Ramon et al., 2012]. The pulsar wind is given in blue, the stellar wind in orange. The length scale is set by the binary separation. 38
1.16 Density maps showing the evolution of the Rayleigh-Taylor instability at t=4.47 (left), 8.94 (centre) and 13.42 (right). The heavier fluid ($\rho' = 2$) is shown in red, the lighter one is blue ($\rho = 1$). The instability is seeded by initial random velocity perturbations. The boundary conditions are periodic along the x direction. Image taken from the Athena code [Stone et al., 2008] test suite (Fortran version). . . . 40
1.17 Density maps showing the evolution of the Kelvin-Helmholtz instability at t=1 (left) and t=5 (right). In the upper half of the box, $\rho' = 1, v' = -0.5$, in the lower half $\rho = 2, v = 0.5$. The instability is seeded by initial random velocity perturbations, the boundary conditions are periodic along both directions. Image taken from the Athena code test suite (Fortran version). 41
1.18 Space-time diagram showing the evolution of the radiative overstability. The shocked region is shown in orange, initially the shock is located at $x = 1$, the initial perturbations arise from numerical noise. Image taken from Mignone [2005]. 41
1.19 Density maps showing the evolution of the non linear thin shell instability at t=34 (left), 54 (centre) and 74 (right). Initially, there is a thin, cold dense slab, trapped by two supersonic incoming flows. The instability is triggered by imposing an initial sinusoidal deformation to the slab. As a proof of the non-linear nature, the final result does not depend on the wavelength of the initial perturbations. Image taken from Folini and Walder [2006]. 42
1.20 Density contour of an interaction between a stellar wind (the star is shown in the left bottom angle) and the interstellar medium (right). The initial conditions are set by the analytic solution by Wilkin [1996], both flows are isothermal. The arrows represent the velocity field. The solid line gives the equilibrium solution. 42
1.21 Cartes de densité qui montrent la géométrie d'une binaire à collision de vents avec des vents identiques (à gauche) et quand le vent de l'étoile de gauche domine fortement celui de droite (à droite). Dans ce cas, le vent de l'étoile de droite est totalement confiné. 44

2.1 Left panel : The *Millenium* simulation, with SPH code GADGET [Springel et al., 2001] shows the dark matter density distribution of the Universe at present time. The length scales vary from 10 kpc to several Gpc. Right panel : density map of a local simulation of a vertically stratified accretion disk (shearing box) with finite difference code ZEUS. The arrows represent the magnetic field in the disk mid-plane. The turbulence is triggered by the magnetorotational instability [Balbus and Hawley, 1991]. 49

2.2 Jade supercomputer at CINES. This computer has 23040 processors which rank it at the 43^{rd} place in the worldwide top 500. (*http://www.top500.org/*). 51

2.3 Approximation of $\mathbf{U}$ at different orders. The physical solution is given by the solid red line, the first order approximation by the dashed blue lines, the second order approximation is given by the dotted black line. 53

2.4 The Riemann problem: the left panel shows the initial states $\mathbf{U}_L$, $\mathbf{U}_R$, which decay into three waves (middle panel) separating four different states. The right panel shows the final outcome with the two additional intermediate states $\mathbf{U}^*_L$, $\mathbf{U}^*_R$. The discontinuities are (from left to right) a rarefaction, a contact discontinuity and a shock. 54

2.5 Control volume for the determination of the Godunov flux in the (x, t) plane. S_L and S_R are the fastest waves arising from the solution of the Riemann problem. Left panel : HLL approximation with only one intermediate state (purple zone) right panel : HLLC wave pattern with two distinct intermediate states (red and blue zone). Image inspired by Toro [2009]. 54

2.6 2D simulation of WR104. Left panel : AMR map, the coarse level is $l_{min} = 7$ (yellow), the highest resolution is $l_{max} = 16$ (pale yellow). Right panel : the corresponding density map shows that refinement happens at the shocks. Very high resolution is limited to a small region close to the binary. 58

2.7 2D AMR structure. Octs at level l are related to the father cells at $l - 1$ and children octs at $l + 1$. Image inspired from a lecture by R. Teyssier. 59

2.8 Density, pressure and velocity profiles for a single star along the x axis. There is a good agreement between the simulation (crosses) and the analytic solution (solid line). The centre of the star is located at $x = 0$, the edge of the mask is given by the dotted vertical line. 61

2.9 Example of orbits of two stars using the leapfrog method with $M_1 = 2M_2$, $a = 1$, $e = 0.8$ and $i = 30°$. The center of mass is located at $(0, 0, 0)$. 62

2.10 Global structure of RAMSES : The initialisation takes into account the user defined numerical parameters and the physical setup. The main loop is performed until the simulation is terminated or the computing time is elapsed (or the simulation has failed). At each step, a new timestep is computed, the Godunov fluxes are determined with the Riemann problem and the variables are updated. Outputs occur every X timesteps. The whole algorithm is embedded in the AMR structure. 64

3.1 Density map of the interaction zone for $\eta = 1/32 = 0.03125$. It is a cut perpendicular to the line-of-centres taken from a 3D simulation. A zoom on the binary system is shown at the bottom right corner. The stars are positioned at the intersections of the dotted lines. The first star has coordinates $(0, 0)$, the second one has coordinates $(a, 0)$. Along the line-of-centres, there are three density jumps (for increasing x). The first shock separates the unshocked wind from the first star from the shocked wind. The contact discontinuity separates both shocked winds. It intersects the line-of-centres at the standoff point R_s. The second shock separates the shocked and unshocked parts of the wind from the second star. $R(\theta_2)$ is the distance between the contact discontinuity and the first star, θ_2 is the polar angle. The asymptotic opening angle is given by $\theta_{2\infty}$. 69

3.2 Density (left panel) and velocity (right panel) maps for $\eta = 1, 0.5, 0.25$. The density is given in g cm^{-2} and the velocity in km s^{-1}. The dashed lines give the solution given by Eq. 3.6 and the dashed lines the solution given by Eq. 3.7. . . . 71

3.3 Density (left panel) and velocity (right panel) maps for $\eta = 0.125, 0.0625, 0.03125$. The density is given in g cm^{-2} and the velocity in km s^{-1}. The dashed lines give the solution given by Eq. 3.6 and the dashed-dotted lines the solution given by Eq. 3.7. 72

3.4 Density (left panel) and velocity (right panel) maps for $\eta = 0.0015625, 7.8125 \times 10^{-3}$. The density is given in g cm^{-2} and the velocity in km s^{-1}. The dashed lines give the solution by Eq. 3.6 and the dashed-dotted lines the solution given by Eq. 3.7. 73

3.5 Left panel: zoom on the reconfinement shock for $\eta = 0.015625$. Right panel: Density map showing a reconfinement shock with a Mach disk. The first star is located at $z > 1$, the second star at $z = 0$, the Mach reflexion occurs at $z = -0.32$. Image taken from Bogovalov et al. [2008]. 73

3.6 Left panel : positions of the different density jumps as a function of η in 2D simulations : the first shock (black crosses), the contact discontinuity (blue diamonds) and the second shock (green asterisks). The 2D analytic solution for the contact discontinuity is overplotted (blue solid line). Right panel: Verification of Eq. 3.4, the solid line is the analytic solution, the crosses are the results from the simulations. 74

3.7 Positions of the reconfinement shock (left panel) and asymptotic opening angle (right panel) for increasing η in 2D simulations. The solid line represents the solution by Eq. 3.6 and the dashed-dotted line the solution given by Eq. 3.7. . . . 75

3.8 Density for $\eta = 0.125$ in 2D simulations with different values for decreasing velocity ratios and increasing mass loss rate ratios. The dashed lines give the solution by Eq. 3.6 and the dashed-dotted lines the solution given by Eq. 3.7. The simulation $v_{\infty 1} = v_{\infty 2}$ has the same wind parameters than the simulation in the top row of Fig. 3.3 but extends further away from the binary. The color scale is different to be able to model the lower density far from the binary. 76

3.9 Density maps in 2D simulations with $\eta = 0.25$. From left to right : $\mathcal{M}_1 = \mathcal{M}_2 = 5$, 30, 100; and $\mathcal{M}_1 = 5$, $\mathcal{M}_2 = 30$. The dashed lines give the solution by Eq. 3.6 and the dashed-dotted lines the solution given by Eq. 3.7. The simulation $\mathcal{M}_1 = \mathcal{M}_2 = 30$ is the same as the simulation shown on the bottom row of Fig. 3.3. 77

3.10 Density maps in the orbital plane for 3D adiabatic winds with $\eta = 1, 0.5, 0.125, 0.03125$. The dashed lines represent the solution by Stevens et al. [1992] and the dashed-dotted lines the solution by [Canto et al., 1996]. 100

3.11 Density maps in the orbital plane for 3D isothermal winds with $\eta = 1$, 0.5, 0.125, 0.03125. The dashed lines represent the solution by Stevens et al. [1992] and the dashed-dotted lines the solution by Canto et al. [1996]. The density is given in $\mathrm{g\,cm^{-3}}$. Far from the stars the effects of low resolution are visible. For $\eta = 1$ the shocked zone is composed of only one cell in the x direction and is superposed with the analytic solutions. 101

3.12 Density maps (left column) and r.m.s. of the velocity perturbations (right column) for $\eta = 1$ in the adiabatic case. From top to bottom: ($v_{\infty 1} = 1.1 v_{\infty 2}$, $\rho_1 = 0.91\rho_2$), ($v_{\infty 1} = 2v_{\infty 2}$, $\rho_1 = 0.5\rho_2$), ($v_{\infty 1} = 20 v_{\infty 2}$, $\rho_1 = 0.05\rho_2$). The position of the contact discontinuity given by Eq. 3.7 is overplotted. 102

3.13 Same as Fig. 3.12 but for $\eta = 0.0625$. 103

3.14 Density maps for $\eta = 0.5$ with the adiabatic index $\gamma = 1.1$, 1.05 and 1.01. The dashed lines represent the solution given by Eq. 3.6 and the dotted-dashed lines the solution by Eq. 3.7. 104

3.15 Density maps showing the evolution of a 2D colliding wing binary when $\eta = 1$ and the adiabatic index $\gamma = 1.01$. Time is given in seconds. $t = 0$ corresponds to the restart at high resolution of an initial low resolution simulation (256^2 cells, no mesh refinement). On the left panel there is one level of refinement (maximum resolution equivalent to 512^2 cells), on the right panel there are four levels (maximum resolution equivalent to 4096^2 cells). 105

3.16 Logarithm of the root mean square (r.m.s.)of the velocity on the line-of-centres as a function of time. The curves represent maximal resolutions of 512 (dotted), 1024 (dot-dashed), 2048 (dashed) and 4096 (solid) cells per dimension. The thin straight lines show the fits to the linear phase for each resolution. 106

3.17 Left panel: density map with $\eta = 1$, the adiabatic index $\gamma = 1.01$ and Mach number of the winds $\mathcal{M}_{1,2} = 6$. Time is given in seconds. Right panel: time-averaged map of the r.m.s of the velocity fluctuations. 106

3.18 Density maps (right column) and maps of the r.m.s. (left column) for $\eta = 1$ (top panels) and $\eta = 16$ (bottom panels) with $v_{\infty 1} = v_{\infty 2}$ and $v_{\infty 1} = 2v_{\infty 2}$. The r.m.s. is a time average of the velocity fluctuations (on a logarithmic scale). The black lines give the position of the contact discontinuity determined by Eq. 3.7. 107

4.1 Density map of a colliding wind binary including orbital motion. The stars are shown by the black circles. In this case both shocks from the wind of the second star intersect, totally confining the second wind. 111

4.2 Determination of the skew angle μ for $\{\eta = 0.5, \beta = 0.05\}$ using a density map. The dashed line showes the theoretical position of the contact discontinuity for $\mu = 0$ (no orbital motion). The solid line fits the contact discontinuity in the simulation. The length scale is set by the binary separation a. 113

4.3 Medium scale simulation, from top to bottom :density, velocity, and mixing for a simulation with identical winds $\{\eta = 1, \beta = 1\}$. The density is given in $\mathrm{g\,cm^{-2}}$, the velocity is in $\mathrm{km\,s^{-1}}$, the mixing of the winds is a dimensionless variable. The length scale is the binary separation a. The left column shows a simulation with the exact Riemann solver, the right column shows a simulation using the Lax-Friedrichs solver (opposite direction of motion). 115

4.4 Medium scale simulation: density (left column) and mixing (right column) maps for simulations with $\eta = 1$ and $\{\beta = 2, 20\}$. The length scale is the binary separation a. 116

4.5 Medium scale simulation : density (left column) and mixing (right column) maps for simulations with $\{\eta = 0.0625,\ \beta = 0.05,\ 0.5,\ 2,\ 20\}$ (from top to bottom). The length scale is the binary separation a. For $\beta = 0.05$, the size of the box is reduced to avoid unnecessary computational costs. 117

4.6 Width of the mixed zone in the narrow arm (dashed line) and wide arm (solid line) for increasing levels of refinement. The symbols indicate the measured values. 118

4.7 Large scale simulation : density (top row) and mixing (bottom row) for simulations with $\{\eta = 1, \beta = 1, 2, 20\}$ (from left to right) in the large boxes. The length scale is the binary separation a. The mixing of the winds is a dimensionless variable. 119

4.8 Large scale simulation : same as Fig. 4.7 for $\{\eta = 0.0625, \beta = 0.05,\ 0.1,\ 0.5,\ 1,\ 2,\ 20\}$. When going from left to right and top to bottom, β increases, which corresponds to increasing values of the x axis in Fig. 4.10. 120

4.9 Step of the spiral S/S_1 as a function of β for η =1 (diamonds), 0.5 (diagonal crosses), and 0.0625 (crosses). The symbols are respectively joined by a solid, dashed, and dash-dotted line for easier identification. 121

4.10 Theoretical 2D growth rate of the KHI in colliding wind binaries as a function of the velocity ratio $\beta = v_1/v_2$ of the winds. The solid, dashed and dash-dotted lines correspond to $\eta = 1$, 0.5, 0.0625 respectively. 122

4.11 Density ($\mathrm{g\,cm^{-3}}$), mixing, velocity ($\mathrm{km\,s^{-1}}$), and temperature (K) in the orbital plane of the 3D simulation of WR 104 (left column). Corresponding 2D maps on the same scale (right column). The length scale is the binary separation a. 125

4.12 Density ($\mathrm{g\,cm^{-2}}$), mixing and velocity ($\mathrm{km\,s^{-1}}$) in 2D simulations of WR 104. The length scale is the binary separation. 126

5.1 Shock tube test problem taken from Ryu et al. [2006]. The left panel shows a simulation where the reconstructed variables are the primitive variables. The right panel shows a simulation where we reconstruct Γv instead of the velocity. This test shows the beginning of the simulation as it crashes later. 153

5.2 Shock tube test problem taken from Ryu et al. [2006]. The left panel shows a simulation where there is a switch to first order when the reconstruction leads to $v > c$. The right panel shows a simulation where we reconstruct the Lorentz factor instead. It shows a spurious increase of the Lorentz factor at the shock. The results from the simulations are shown in blue, the analytic solution [Giacomazzo and Rezzolla, 2006] in green. These tests were performed with 2000 grid cells, which is not enough to reach a satisfactory agreement with the analytic solution. They are very stringent because of the important transverse velocity ($\Gamma > 100$), and only very high resolutions give satisfactory results (see §5.2.1). 154

5.3 Density, AMR levels (red line), velocity and pressure in the frame of the laboratory for the shock test 1, with $\Gamma_{max} = 1.4$. First (left panel) and second order without AMR (middle panel) and second order with AMR (right panel). The analytic solution [Giacomazzo and Rezzolla, 2006] is given in blue. In the first panels $l_{min} = l_{max} = 8$. In the last panel $l_{min} = 8$ and $l_{max} = 16$. 156

5.4 Density, AMR levels (red line), velocity and pressure in the frame of the laboratory for the shock test P2 with $\Gamma_{max} = 120$. Left panel : $l_{min} = 5$, $l_{max} = 17$, right panel : $l_{min} = 14$, $l_{max} = 17$. 157

5.5 Simulation domain (in blue) for inclined shock tubes. The interface is shifted by an angle θ with respect to a vertical line. 157

5.6 Inclined shock tests 1 (upper row) and 2 (bottom row). The left panel gives the contour map at the end of the simulation. The right panel gives density, velocity, pressure and Lorentz factor along the shock normal. The blue lines give the 2D results, the dashed black line the 1D results from a simulation with the same resolution and the green line gives the analytic solution. For the second test, I overplot the 1D solution for a simulation with a resolution of 100 grid points. Note that the resolution is much lower than for the 1D tests in §5.2.1. 159
5.7 Simulation of the propagation of a 3D relativistic jet ($\Gamma_{max} = 7.1$). From top to bottom: density at $t = 20, 30, 40$ in a 3D jet starting form the left boundary of the domain. The left panel shows the simulation with RAMSES-RHD, the right panel the simulation from Del Zanna and Bucciantini [2002]. 160
5.8 Density and velocity jump for strong shocks as a function of the pre-shock Lorentz factor (in the frame of the shock). The solid line represents the solution for $\gamma = 4/3$, the dashed line represents the solution for $\gamma = 5/3$. 164
5.9 Density, v_x, v_y and temperature in two similar simulations. One uses the hydrodynamical version of the code (blue solid lines) while the other one uses the relativistic version (black dashed lines). 165
5.10 Position of both shocks and the contact discontinuity for $\eta_{rel} = 1$, $\beta_p = 0.5$ for increasing resolution $l_{max} = 8$ (thin dotted line), 9 (thick dotted line), 10 (thin dashed line), 11 (thick dashed line), 12 (black solid line) and 13 (red solid line). The last two resolutions give the same result, which indicates numerical convergence is reached. At the edges of the box, there is a numerical artefact due to the AMR grid. 166
5.11 Density maps (left panel) and maps of the Lorentz factor (right panel) for simulations with a stellar wind and a pulsar wind with $\eta_{rel} = 0.1$, 1, 10 (from top to bottom) and $\beta_p = 0.5$. The star is located on the left, the pulsar on the right. The density is given in $\mathrm{g\,cm^{-2}}$ and the velocity in $\mathrm{km\,s^{-1}}$. The arrows indicate the direction of the velocity, their size is normalised by the local norm of the velocity vector. The contact discontinuity is smeared out as the simulations use the HLL Riemann solver. 168
5.12 Left panel : position of both shocks and the contact discontinuity in a simulation with $\eta_{rel} = 1$, in simulations with different values for the Lorentz factor of the pulsar wind. We have β_p= 0.01 (thin dotted line), 0.1 (thick dotted lined), 0.5 (thick dashed line) and 0.9 (solid line). Right panel : position of both shocks and the contact discontinuity in a simulation with $\eta_{rel} = 1$, and β_p= 0.5 with the Mach number of the pulsar wind = 10 (dotted line), 20 (thin dashed line), 30 (thick dashed line) and 50 (solid line). 169
5.13 Density (left panel) and mixing (right panel) maps for simulations with $\eta_{rel} = 1$ and $\beta_p = 0.2$ (upper row) and $\beta_p = 0.5$ (lower row). 170

A.1 Diagram of the two-wind interaction problem. The stars are the big dots, the interaction front $\mathrm{R}(\theta_2)$ is shown with the thick red line. 183

List of Tables

3.1 Distance to the second star of both shocks and the contact discontinuity along the line-of-centres. Results from 3D simulations and theoretical values. 76

4.1 Presence (S) or absence (X) of a spiral structure in simulations for various wind momentum (η) and velocity (β) ratio. 119

Abstract

The aim of this thesis is to understand the structure of colliding wind binaries composed of a massive star and a young pulsar, called γ-ray binaries. They are expected to display a similar structure to colliding wind binaries composed of massive stars, with some particularities due to the relativistic nature of the pulsar wind.

The interaction of the supersonic winds from massive stars creates a shocked structure with observational signatures from the radio domain to the X-rays. The structure is affected by various instabilities and by the orbital motion of the stars. To understand their impact, I carried out high resolution simulations of colliding wind binaries with the hydrodynamical code RAMSES. They are computationally demanding, especially when one of the winds strongly dominates the other one.

Small scale simulations highlight the importance of the Non-linear Thin Shell Instability in isothermal collisions while the Kelvin-Helmholtz instability may strongly impact the dynamics of adiabatic collisions. I found that, at larger scales, this instability can destroy the expected large scale spiral structure when there is an important velocity gradient between the winds. WR 104 is a system that displays a spiral structure with important dust emission. The simulation of this system shows a good agreement with the observed structure and indicates cooling processes are necessary to enable dust formation.

To model the pulsar wind in γ-ray binaries, an extension of RAMSES has been developed, that incorporates relativistic hydrodynamics. I used this new relativistic code to perform preliminary simulations of γ-ray binaries. They display a similar structure to colliding wind binaries with small relativistic corrections. We expect to use this code to perform large scale simulations of γ-ray binaries. It will be part of the next public release of RAMSES and is suited for the study of many astrophysical problems such as relativistic jets, pulsar wind nebulae or gamma-ray bursts.

This work is supported by the European Community via contract ERC-StG-200911.

Résumé

L'objectif de cette thèse est de comprendre la structure des binaires γ, binaires à collision de vents composées d'une étoile massive et d'un pulsar jeune. Ces binaires possèdent probablement une structure similaire aux binaires à collision de vents composées de deux étoiles massives, avec des particularités liées à la nature relativiste du vent de pulsar.

L'interaction de deux vents supersoniques d'étoiles massives crée une structure choquée qui présente des signatures observationnelles du domaine radio aux rayons X. Plusieurs instabilités ainsi que le mouvement orbital des étoiles influent sur la structure choquée. Afin de comprendre leur impact, j'ai effectué des simulations à haute résolution de binaires à collision de vents à l'aide du code hydrodynamique RAMSES. Ces simulations sont numériquement coûteuses à réaliser, surtout lorsque un des vents domine fortement l'autre.

A petite échelle, les simulations soulignent l'importance de l'instabilité de couche mince non-linéaire dans les collisions isothermes alors que l'instabilité de Kelvin-Helmholtz peut fortement modifier la structure choquée dans une collision adiabatique. A plus grande échelle, cette instabilité peut parfois détruire la structure spirale à laquelle on s'attend si la différence de vitesse entre les vents est trop importante. WR 104 est une binaire dont on observe la structure spirale grâce à l'émission de poussières. Les simulations de ce système montrent un bon accord avec la structure observée et indiquent que des processus de refroidissement du gaz sont nécessaires à la formation de poussières.

Pour modéliser les vents de pulsar dans les binaires γ, RAMSES a été étendu à l'hydrodynamique relativiste. J'utilise ce nouveau code pour réaliser des simulations préliminaires de binaires γ. Elles montrent effectivement une structure similaire aux binaires stellaires, avec de légères corrections relativistes . Ce code est adapté à l'étude de divers systèmes astrophysiques tels que les jets relativistes, les sursauts gamma ou les nébuleuses de pulsar et fera partie de la prochaine version de RAMSES qui sera rendue publique.

Ce travail a été financé par la Communauté Européenne à travers le contrat ERC-StG-200911

Chapter 1

Current understanding of colliding wind binaries

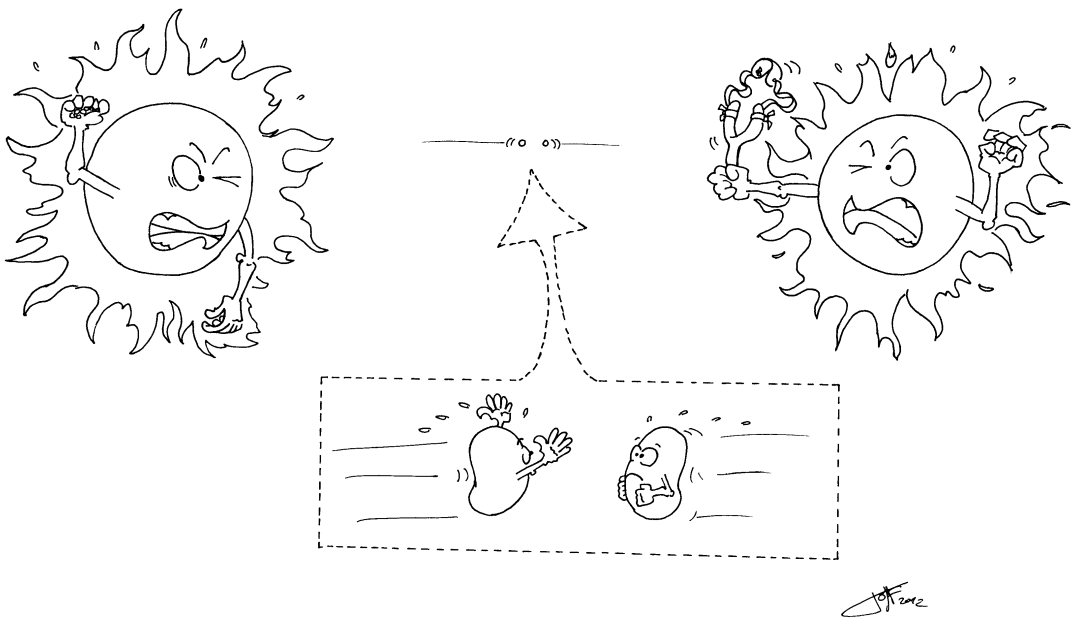

Contents

1.1 Introduction 15
1.2 A wealth of observations 18
1.2.1 Observing stellar winds 18
1.2.2 Clues of binarity 19
1.3 Theoretical background : hydrodynamics and radiative acceleration 24
1.3.1 Individual winds 24
1.3.2 Colliding wind binaries 30
1.4 The contribution of numerical simulations 35
1.4.1 State of the art numerical simulations 36
1.4.2 Hydrodynamical instabilities in colliding wind binaries and colliding supersonic flows 38
1.5 Introduction en Français 42

1.1 Introduction

The air we breathe is essentially composed of oxygen and nitrogen. The Earth we live on is formed of iron, oxygen, silicon, magnesium, sulfur...Our own bodies are mainly made of oxygen, carbon and hydrogen and contain traces of species such as aluminum, phosphorus or potassium. Where do all these elements come from? How did they all come together to form the environment that surrounds us? To answer these questions, one has to look much further away than our own planet. One has to look at massive stars. By massive, astronomers mean that they are at least ten times as massive as our Sun. Although not numerous, massive stars are important actors of the evolution of our Universe. They are the main producers of heavy elements in the Universe and an important source of energy.

In massive stars, like in all stars, nuclear reactions transform hydrogen into helium during the main sequence stage. For massive stars, this phase is very short and they "live" about 10 million years, while the Sun's main sequence will last 10 billion years. When no hydrogen is left, other nuclear reactions successively synthesize heavier and heavier elements : carbon, oxygen, nitrogen..., up to iron. At this point, no new nuclear reaction is possible. The star collapses and liberates an enormous amount of energy (up to 10^{53} erg) during a supernova explosion. The outer layers of the star are violently ejected into the interstellar medium, enriching it with elements produced in the star. The fast moving ejecta also compress the interstellar medium and affect its structure, having an important impact on the formation of new stars. This new generation of stars and their planetary systems will be chemically richer than the former one. This continuous process explains the chemical composition of the Earth.

Massive stars do not inject matter and energy in space only during the supernova explosion, but also during most of their life, in the form of winds. The research presented in this manuscript focuses on winds from massive stars. They are driven by the very high luminosity of massive stars and continuously eject an amount of matter equivalent to $10^{-8} - 10^{-7}$ Solar mass per year during the main sequence stage [Puls et al., 1996]. The matter escapes with a velocity of about $2000\,\mathrm{km\,s^{-1}}$, which is much faster than the sound speed in the winds meaning the winds are supersonic. During later stages of stellar evolution, the mass loss of the star varies. The most impressive stage is the Wolf-Rayet stage, where the mass loss rate can reach up to 10^{-4} Solar mass per year [Puls et al., 2008a]. During this stage, there is no hydrogen left in the star and the wind is mainly composed of helium, nitrogen and carbon. The winds provide elements to the interstellar medium and the total energy injected by stellar winds during the whole lifetime of a massive star is comparable to the amount of kinetic energy released in the supernova explosion [Abbott, 1982b]. After the supernova explosion, the stellar leftover is a compact object that can be a neutron star or a black hole for the most massive stars. Highly magnetised fast rotating neutron stars, called pulsars, emit a very fast wind that provides energy to their surrounding medium similarly to winds from massive stars.

Most of the massive stars are located in binary systems [Kobulnicky and Fryer, 2007]. The range of distances between companion stars is comparable to the range of distances between the Sun and the planets of our Solar System. This is really close! It means that the winds from companion stars will violently interact and form a *colliding wind binary*. This collision creates a shocked structure, as is shown on Fig. 1.1 [Stevens et al., 1992]. Each wind has a freely expanding component and a shocked component. The two shocked winds are separated by a discontinuity. When both winds have the same mass loss rate, terminal velocity and temperature, the structure is symmetric with respect to the midplane of the stars. When one wind strongly dominates the other one, the whole structure is bent towards the star with the weakest wind. As the stars orbit around each other, the whole collision region turns into a spiral at large scale. This interaction region is observed at different length scales, from distances smaller than the binary separation to large scale spirals up to hundred times the binary separation. Numerical simulations have

revealed that several instabilities may arise in the interaction region and affect its dynamics [Pittard, 2009]. The understanding of this complex structure and its stability is at the heart of this thesis.

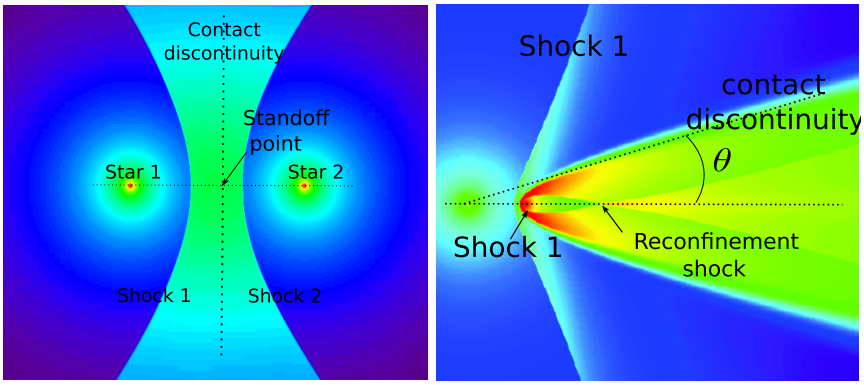

Figure 1.1: Density maps showing the geometry of a colliding wind binary with identical winds (left panel) and when the first wind dominates (right panel). In the latter case the second wind is totally confined. The highest density regions (red) are about a thousand times denser than the lower density regions (purple).

Recent developments in space and ground-based γ-ray observatories such as *Fermi*/LAT and H.E.S.S. have revealed a new class of binaries that emit very energetic light, γ-rays (see *e.g.* Aharonian and HESS collaboration [2006], Abdo and Fermi Collaboration [2009]). A handful of these systems has been discovered. One of them is η Carinae, composed of two very massive stars. All the others are composed of a massive star and a compact object. For one of them, PSR B1259-63 [Johnston et al., 1992], we know that the compact object is a pulsar that has a tenuous but very fast, relativistic wind. Other similar systems, composed of a radio-emitting pulsar and a massive star have been discovered, but their γ-ray emission is too faint to be observed (*Pulsar Catalogue : http://www.atnf.csiro.au/people/pulsar/psrcat/*). In such systems, one can expect to have a shocked structure between the pulsar wind and the stellar wind, similarly to what occurs for a binary composed of two massive stars [Dubus, 2006]. There are radio observations that show a structure looking like a cometary tail, and changing with time [Moldón et al., 2011a]. They are interpreted as the evolution of a shock, similar to the one of Fig. 1.1 as the pulsar orbits around the massive star. Some other systems show similar emission, suggesting a colliding wind scenario is at work but it has not been firmly established yet.

The aim of this thesis is to understand the structure of γ-ray binaries and provide observable diagnostics. The evolution of the system is closely related to the instabilities developing in the shocked region and is too complex to be modelled analytically. Therefore we perform numerical simulations, using the hydrodynamical code RAMSES [Teyssier, 2002]. As stellar wind binaries and γ-ray binaries share a common shocked structure, the study of stellar binaries was a natural direction to follow in this research. Although similarities exist, the exact structure of γ-ray binaries probably differs from the structure of massive colliding wind binaries due to the relativistic nature of the pulsar wind. To understand these important aspects, part of my work has been dedicated to the development of a numerical method to allow the modelling of relativistic flows. The development of this code and its application to γ-ray binaries constitutes the second part of this thesis.

In this first chapter, I will present our current understanding of colliding wind binaries (both stellar binaries and γ-ray binaries), based on observations (§1.2), theoretical calculations (§1.3) and numerical simulations (§1.4). Observations and numerical simulations both indicate the

importance of the orbital motion and instabilities on the structure of the shocked region. These are key aspects that I have studied using the hydrodynamical code RAMSES, which I will describe in Chapter 2. I will present my high resolution simulations at different scales, from very close to the binary (less than ten times the binary separation, Chapter 3) up to several hundred times the binary separation (Chapter 4). In the beginning of Chapter 5, I will detail the rather technical aspects of the extension of RAMSES to relativistic hydrodynamics and the different tests I have performed for its validation. I have used this new relativistic code for simulations of the interaction between a pulsar wind and a stellar wind that I will describe in the rest of the chapter.

Finally I will give a brief summary of this work and propose some future directions of research.

1.2 A wealth of observations

The main aim of observations of stellar winds is to understand the mechanism launching the winds, their structure and their interaction with their environment. Observations in different wavebands allowed to derive their main properties such as the velocity, density profile, chemical composition, or temperature and to progressively sketch out the structure of stellar winds.

1.2.1 Observing stellar winds

1.2.1.1 Line emission

Optical spectroscopy in the 19^{th} century discovered stars with an emission component shifted towards longer wavelengths and an absorption component shifted towards shorter wavelengths [Wolf and Rayet, 1867]. This profile showed similarities with the line profiles of P Cygni, supposed to be a nova star (later analysis showed it is a Luminous Blue Variable). One thus deduced that those types of stars possess a continuous outflow [Beals, 1929]. Chandrasekhar [1934] soon proposed a physical explanation to interpret such profiles that led to the first estimates of the mass loss rates and velocities for stellar winds. Rocket ultraviolet (UV) observations [Morton, 1967] revealed that most P Cygni lines are found for highly ionised species such as C IV, O VI or Si IV. Fig. 1.2 shows a typical so-called P Cygni emission line and a schematic view of its formation process. Such lines result from isotropic emission due to line scattering in a "halo" around the star and absorption between the star and the observer. Their interpretation in terms of mass loss rates requires the knowledge of the abundances in the wind and its ionisation structure [Howarth and Prinja, 1989].

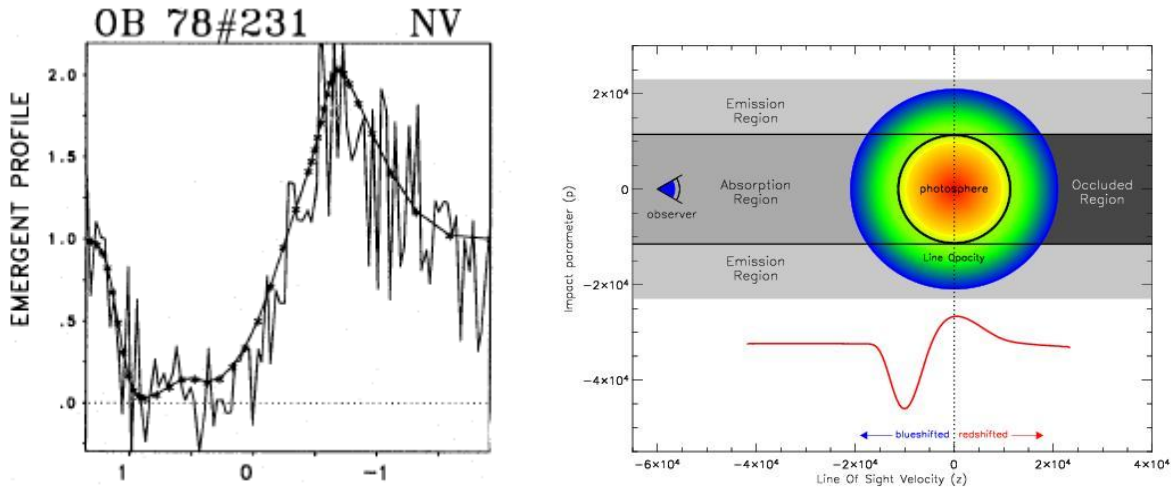

Figure 1.2: Left panel : *Hubble Space Telescope* observation of an OB star showing a P Cygni profile for N V [Haser et al., 1995]. Right panel : Formation of a P Cygni profile. Image by Daniel Kasen (*http://supernova.lbl.gov/ dnkasen/*).

High density winds also show pure emission lines. The most studied one is the optical H_α line but line emission can be found in the UV and even in X-rays. Fig. 1.3 shows high resolution X-ray spectra for different types of massive stars. These lines are mostly formed by recombination and, except for Wolf-Rayet (WR) stars, they form only in the densest parts of the winds, where the terminal velocity has not been reached yet. Their analysis thus strongly relies on the assumed velocity profile of the wind. As the velocity structure relies on the interpretation

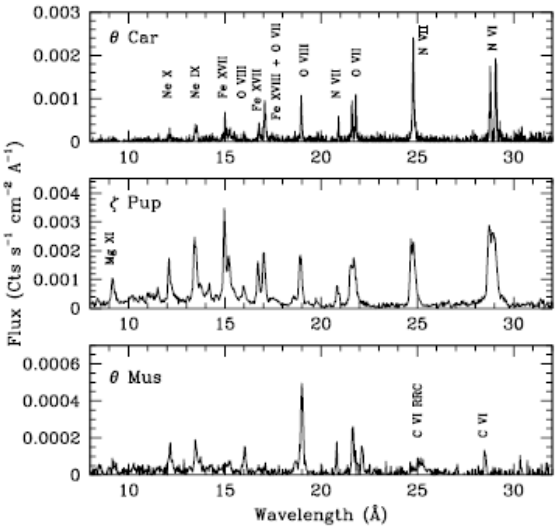

Figure 1.3: Spectra of a B star (top), O star (middle) and WR star (bottom) obtained with *XMM-Newton* [Güdel and Nazé, 2009].

of the line profiles, an iterative analysis based on non local thermodynamical equilibrium models is required to model line emission [Crowther et al., 1995a].

1.2.1.2 Thermal radio emission

P Cygni was the first massive star detected at radiowavelengths [Wendker and Baars, 1973]. The arrival of radio interferometers allowed the first census of radio emission among WR and early type stars [Bieging et al., 1982, 1989]. It indicated most of the WR stars and about a quarter of the observed O and B type stars (early type stars) show radio emission. It results from free-free emission in the winds. The free-free opacity is very high close to the star and proportional to the inverse of the wavelength. Only photons originating far from the star can thus escape the stellar wind, especially at short wavelengths. This results in extended emission that may reach a few hundred times the stellar radius. By measuring the radio excess with respect to the emission expected from the stellar photosphere, one can derive the flux emitted by the wind. It is directly related to the mass loss rate and terminal velocity of the wind [Wright and Barlow, 1975, Panagia and Felli, 1975]. It also enables an estimate of the temperature of the wind. Multifrequency observations indicate the observed flux S varies as ν^{α} where ν is the frequency and α is called the spectral index. The spectral index for free-free emission in homogeneous stellar winds is about 0.6.

Combining spectroscopic and radio observations, one finds that early type stars have a mass loss rate around 10^{-8} $M_{\odot}\,yr^{-1}$ while it may reach several 10^{-5} $M_{\odot}\,yr^{-1}$ for Wolf-Rayet stars [Puls et al., 2008a]. The winds are accelerated to their terminal velocities within a distance of a few stellar radii for early type stars and about ten stellar radii for WR stars. They are highly supersonic with a terminal velocity $v_{\infty} \simeq 2000\,km\,s^{-1}$ for early type stars, this value is slightly lower for WR stars. When massive stars form a binary system, one can thus expect the winds to collide and form a shocked structure that has observational consequences.

1.2.2 Clues of binarity

Historically, some observed systems did not fit within the pattern described in the above paragraphs and further investigations indicated that those systems were actually binary systems. Colliding wind binaries are now observed through the whole electromagnetic spectrum, different wavelengths probing different physical phenomena and different distances from the stars.

1.2.2.1 Non-thermal radio emission

White and Becker [1983] discovered a star with an estimated temperature of about 3×10^5K and a spectral index $\alpha \simeq -0.6$. This was the first indication that a non-thermal emission mechanism was at work in the winds from some massive stars. The fraction of massive stars showing non-thermal radio emission is between 12% [Abbott et al., 1986] and 50% [Benaglia et al., 2001]. A key observation was made by Moran et al. [1989] who obtained a resolved radio map of WR 147. It showed two distinct regions: the thermal emission region from the WR star and a region of non-thermal emission close to a neighbouring early type star.

Non-thermal emission means that particles are accelerated somewhere in the system. This is possible in the diffusive shock acceleration (DSA) mechanism where particles gain energy through the first order Fermi process as they cross and recross a shock several times before escaping downstream [Bell, 1978]. The resulting energy distribution $N(E)$ follows a power-law $N(E) \propto E^{-n}$ where n is the energy index set by

$$n = \frac{\phi + 2}{\phi - 1}, \tag{1.1}$$

where ϕ is the compression ratio of the shock. In adiabatic strong shocks, $\phi = 4$, which gives $n = 2$ while the compression ratio is very high for isothermal shocks, which gives $n = 1$.

Eichler and Usov [1993] explained that particle acceleration could occur at the shocks resulting from the collision between the winds from the WR star and its early type companion. They argued that this non-thermal emission could be observed only in wide binaries, otherwise it would be absorbed in the free winds from the stars. Synchrotron radiation is the dominant emission mechanism although inverse Compton scattering has some influence especially in close binaries [Pittard et al., 2006].

Fig. 1.4 shows there is a good agreement between radio observations and numerical models based on hydrodynamical calculations post-treated with a radiative transfer code [Dougherty et al., 2003]. The emission region extends to a distance of a few times the binary separation. The phase-locked variability of the non-thermal emission in eccentric systems can be explained by the change in geometry of the emitting region [White and Becker, 1995]. Statistical studies [van der Hucht et al., 1992, Dougherty and Williams, 2000] indicate that all WR stars showing non-thermal emission are binary systems. Although there is no undeniable evidence yet, this probably also holds for early type stars [van Loo et al., 2006].

Non-thermal radio emission is also observed in γ-ray binaries [Moldón et al., 2011a, Ribó et al., 2008] and is associated with synchrotron emission at shocks. Emission is measured up to several times the binary separation and shows variability throughout the orbital period. Fig. 1.5 shows resolved radio emission from γ-ray binary LSI + 61 303° at different orbital phases [Dhawan et al., 2006]. The emission region looks like a cometary tail that can be interpreted as a shock cone arising from the collision between the stellar wind and the pulsar wind.

1.2.2.2 X-ray emission

The X-ray luminosity of single massive stars roughly scales as $L_X = 10^{-7} L_{bol}$, where L_{bol} is the total luminosity. This ratio can be up to two orders of magnitude higher in binary systems

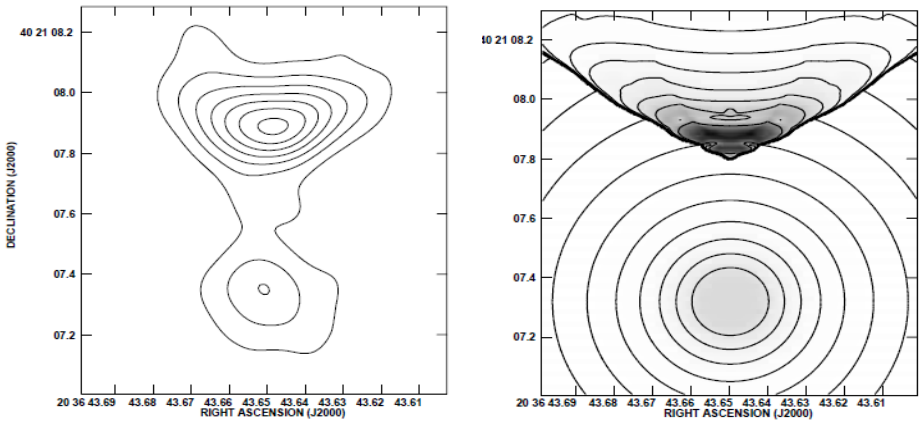

Figure 1.4: Observed (left panel) and simulated (right panel) intensity distribution at 1.6 GHz from WR 147. Both show isotropic thermal emission from the WR star at the bottom and non-thermal emission at the bow shock close to the early type star at the top of the image.

[Chlebowski and Garmany, 1991]. This strong thermal X-ray emission was first predicted by Prilutskii and Usov [1976] and Cherepashchuk [1976] who assumed that at the shocks, the kinetic energy of the winds ($1/2 m_p v_\infty^2$, where m_p is the mass of the proton) is totally converted into thermal energy ($3/2 k_B T$ with T the temperature in the winds and k_B the Boltzmann constant). Close to the line-of-centres, between the shocks, the temperature rises up to 10^8 K for a wind velocity of v_∞ =2000 km s^{-1}. Spectral fits obtained with numerical simulations of colliding wind binaries including radiative cooling reproduce observed spectra with a good agreement. An example can be seen on the right panel of Fig. 1.6. In WR +O binaries, the X-ray emission varies throughout the orbit as absorption increases when the line-of-sight passes through the dense WR wind (Fig. 1.6, left panel).

1.2.2.3 Infrared (IR) emission from dust producing WR winds

Allen et al. [1972] reported the first detection of IR emission associated with a Wolf-Rayet star. The emission is related to the presence of dust in the stellar wind and is found in WC stars, late type WR stars that have a carbon rich atmosphere [Williams et al., 1987]. Such winds are very hostile to dust formation due to their high temperature, low density and absence of hydrogen [Cherchneff and Tielens, 1995]. Higher densities naturally arise in the shocked regions in colliding wind binaries, leading to the hypothesis that dust-producing WR stars have a binary companion [Usov, 1991]. In binary systems, cooling (see §1.3.2.3) probably generates conditions where dust can survive and mixing with the wind from an early type star is likely to facilitate dust formation as it enriches the WR wind with hydrogen. Many dust producing WR stars have now been identified as spectroscopic binaries (Lefèvre et al. [2005], Williams et al. [2009b]...). The most striking evidence for the binary hypothesis comes from the so-called Pinwheel nebulae. These are WC+O-B binaries viewed pole-on showing a spiral structure [Tuthill et al., 2006] that extends up to a few hundred times the binary separation. Their shape is well-matched by an Archimedean spiral with a step related to the orbital period of the system. Fig. 1.7 shows the beautiful example of WR 104 that will be studied in more detail in Chapter 4 in order to have some clues on the conditions of dust formation.

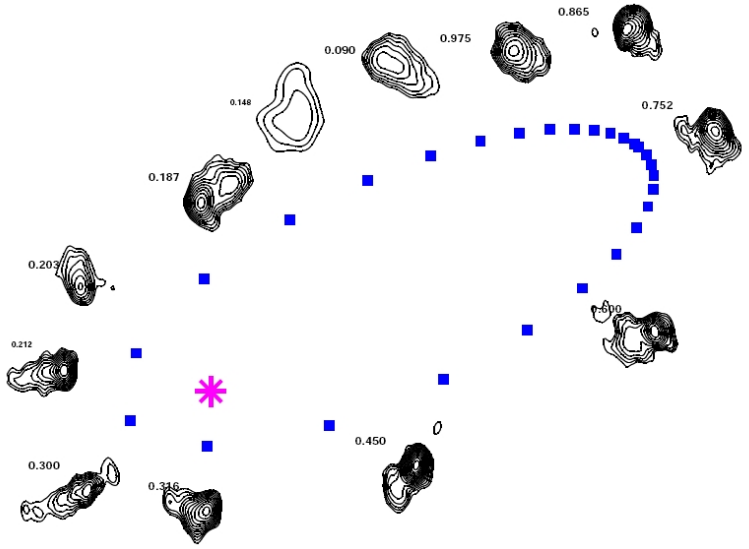

Figure 1.5: Very Long Baseline Array (VLBA) radio maps of LSI + 61 303 ° at different orbital phases. The pink star indicates the position of the massive star and the blue squares the positions of the pulsar. The actual size of the orbit ($a \simeq 0.15$ mas) is enlarged to show the different radio observations. The size of the emission region is about 6 mas.

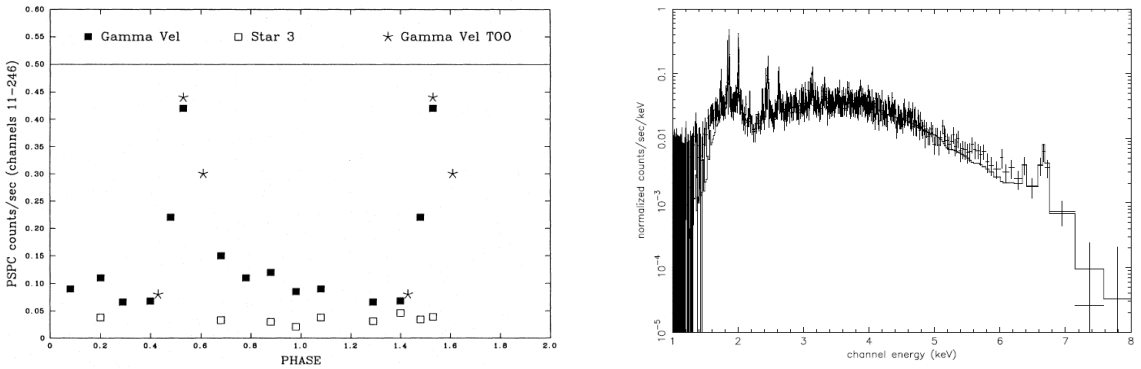

Figure 1.6: Left: *ROSAT* X-ray light curve from WR+O binary γ^2 Velorum [Willis et al., 1995]. Right: X-ray spectrum from η Carinae. The crosses indicate *Chandra* observations, the solid line is a simulated spectrum [Pittard and Corcoran, 2002] obtained with a hydrodynamical simulation including radiative cooling in an optically thin plasma.

1.2.2.4 High energy emission

Non-thermal emission from colliding wind binaries was first detected at radio wavelengths and was explained by synchrotron emission of electrons accelerated at the shocks. The electrons may also interact with photons from the ambient medium through inverse Compton (IC) scattering. Inverse Compton scattering results from the energy transfer from a high energy electron to a low energy photon. As early type stars are an important source of UV photons, this mechanism dominates the high energy emission.

Unfortunately non-thermal soft X-rays have not been detected in stellar colliding wind binaries yet because they are overwhelmed by thermal emission at these wavelengths (see *e.g.* De Becker et al. [2004]). In theory, close binaries would be the best candidates for the detection of non-thermal X-ray emission. In these systems, thermal emission is lower because the winds have

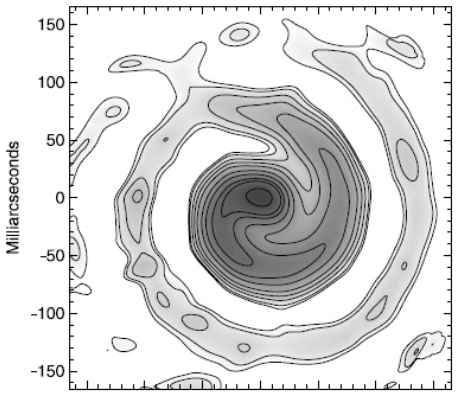

Figure 1.7: Infrared image of Pinwheel nebula WR 104 [Tuthill et al., 2008]. Image obtained by interferometry with the Keck telescope.

not reached their terminal velocity at the collision while the UV flux is higher due to the short distances to the stars [De Becker, 2007].

Up to now, only η Carinae is a confirmed γ-ray emitter composed of two massive stars [Abdo and Fermi collaboration, 2010]. Still, there are tentative associations of γ-ray sources with clusters of massive stars [Chen et al., 1996, Aharonian and HEGRA Collaboration, 2002].

A few binary systems emit most of their radiated power beyond 10 MeV, at high energy (HE, 0.1-100 GeV) and very high energy (VHE, >100 GeV) and are observed with space based telescopes such as *Fermi*/LAT and ground based Cerenkov telescopes such as H.E.S.S. A handful have been detected : PSR-B1259-63 (Aharonian and HESS collaboration [2009], Abdo and Fermi collaboration [2011]), LSI+61 303° (Albert and MAGIC collaboration [2006], [Abdo and Fermi collaboration, 2009]), LSI 5039 (Aharonian and HESS collaboration [2006], Abdo and Fermi Collaboration [2009]) and more recently 1FGL J1018.6-5856 [Corbet et al., 2011] and HESS J0632+057 [Falcone et al., 2011]. All contain a massive star and a compact object. Pulsed radio emission in PSR-B1259-63 [Johnston et al., 1992] indicates the compact object is a fast rotating pulsar, while the nature of the compact object in the other systems is still unclear (see *e.g* [Dubus, 2006] and [Romero et al., 2005]). In LS 5039 and 1FGL J1018.6-5856 the massive star is an O-type star while in the three other systems the massive star is a Be star. These stars display a slow, dense equatorial outflow on top of their isotropic wind.

All these systems show phase-locked variability throughout the electromagnetic spectrum and especially at HE and VHE. As an example, Fig. 1.8 shows the spectrum and VHE lightcurve of LS 5039. The similarities in the variable high energy emission and the extended radio emission between PSR-B1259-63 and the other detected γ-ray binaries suggest the wind collision scenario is at work in all these systems.

1.3 Theoretical background : hydrodynamics and radiative acceleration

This section provides some theoretical background on the formation of stellar winds, and especially winds from massive stars and pulsar winds. I introduce the equations of hydrodynamics and explain how to derive the structure of stellar winds and how it compares with the observations. In colliding wind binaries, observations provide evidence of the presence of shocks. In a second part of this section, I detail the structure of hydrodynamical shocks and explain some analytic results on the structure of colliding wind binaries.

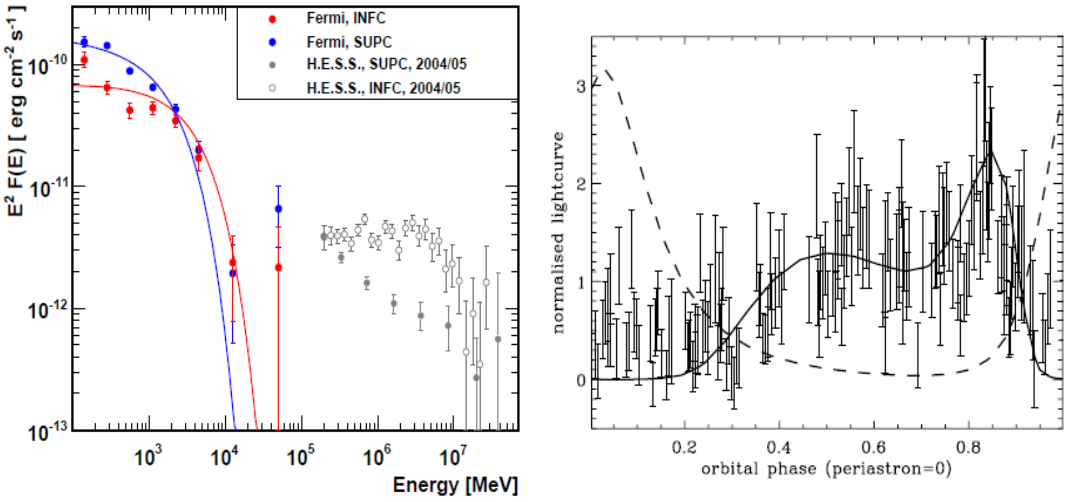

Figure 1.8: Left panel: Spectral energy distribution of LS 5039 [Hadasch et al., 2012]. Red and blue points show *Fermi*-LAT data, the grey points show H.E.S.S. data. The plot shows values for the inferior (phase = 0.72)and superior conjunction (phase =0.06). The corresponding light curve obtained by H.E.S.S. is given on the right panel. The solid line shows a predicted lightcurve that takes into account anisotropic inverse Compton scattering (dashed line) and attenuation by pair production [Dubus et al., 2008].

1.3.1 Individual winds

1.3.1.1 Different types of stars create different winds

There exist several sorts of stellar winds, according to the stellar type and evolutionary stage. Each sort has its typical mass loss rate, velocity and structure. A complete review is given in Lamers and Cassinelli [1999] from which I give a (very) brief overview :

- coronal winds originate from high gas pressure in the coronae of cool stars (later then F5V on the main sequence). The high temperature comes from the dissipation of the mechanical energy from the convective zone or magnetic reconnection. Such winds have very low mass loss rates but are an important topic of study as it was the first interpretation for the solar wind, which study led to the basic equations of stellar winds [Parker, 1958] (see §1.3.1.3).

- Dust driven winds are due to the radiation pressure on dust grains that are coupled to the gas [Gilman, 1972]. These are called continuum driven winds as dust grains absorb radiation in a wide frequency band. This phenomenon is limited to cool stars ($T \leqslant 3000\,K$), with a high luminosity ($L \geqslant 10^4 L_\odot$) such as Mira-type Asymptotic Giant Branch (AGB) stars or red supergiants. The mass loss rate can reach up to $10^{-4} M_\odot\,yr^{-1}$ but the winds have a very low speed, below $50\,km\,s^{-1}$. Stellar pulsations or acoustic wave pressure generate the dense atmosphere that is necessary for efficient coupling between dust and gas.

- Line driven winds are driven by radiation pressure on lines [Milne, 1926] rather than on the continuum. This occurs for stars having a strong UV flux, such as O, B or A type stars, either on the main sequence or some later evolutionary stages such as the Wolf-Rayet stage. The key ingredient is the Doppler effect in an accelerating atmosphere that shifts the lines to longer and longer wavelengths, allowing line scattering through a broad part of the stellar spectrum. The resulting wind may reach a mass loss rate of several $10^{-5} M_\odot^{-1}$ and a highly supersonic velocity above $1000\,km\,s^{-1}$.

- Rapidly rotating magnetized stars generate winds which mass loss rates are determined by the rotation while the escape velocity is determined by the magnetic field [Weber and Davis, 1967]. This occurs for stars with a high rotation speed such as most early type stars. The resulting flow presents an equatorial overdensity.
- Similar outflows are possible even without magnetic fields when stars rotate at a speed close to their critical velocity. This occurs in Be stars, although the exact mechanism to the formation of the decretion disk around the star is not understood yet [Carciofi, 2011].
- Winds can be driven in magnetised stars even when rotation is absent. Oscillations within the stars generate Alfvén waves that dissipate energy and momentum to drive a wind. This mechanism is at work in the Sun, in addition to the coronal wind [Parker, 1965]. It is the main driving mechanism for stars with low radiative fluxes and no hot corona.

This thesis focuses on line driven winds from massive stars, which I will describe in section §1.3.1.4.

1.3.1.2 Equations of hydrodynamics

The Euler equations are given by

$$\begin{aligned} \frac{\partial \rho}{\partial t} + \nabla \cdot (\rho \mathbf{v}) &= 0 \\ \frac{\partial (\rho \mathbf{v})}{\partial t} + \nabla (\rho \mathbf{v}\mathbf{v}) + \nabla P &= 0 \\ \frac{\partial E}{\partial t} + \nabla \cdot [\mathbf{v}(E+P)] &= 0, \end{aligned} \tag{1.2}$$

where ρ is the density, $\mathbf{v}$ the velocity, and P the pressure of the gas. The first equation expresses the conservation of mass, the second one the conservation of momentum, the last one the conservation of the energy given by

$$E = \frac{1}{2}\rho v^2 + \frac{P}{(\gamma - 1)},$$

γ is the adiabatic index, which is equal to $5/3$ in adiabatic flows, and equal to 1 in isothermal flows. This equation implicitly assumes an equation of state for perfect gases

$$P = \rho k_B T / \mu m_H = (\gamma - 1)\rho\epsilon, \tag{1.3}$$

where k_B is the Boltzmann constant, T the temperature μ the mean mass per particle, m_H the mass of the hydrogen atom and ϵ is the internal energy density. Source terms can be added on the right hand side of Eqs. 1.2. Sources of momentum are forces, such as the gravitational force or radiative acceleration. A system can lose/gain energy through cooling/heating and one usually adds a fixed source term $-n^2\Lambda(T)$ where n is the number density of particles and $\Lambda(T)$ the emission rate of the flow (in $\mathrm{erg\,cm^3\,s^{-1}}$) (see §1.3.2.3).

1.3.1.3 Parker wind Parker [1958]

The structure of a stationary wind that is not affected by radiation can be found by solving the Euler equations including the gravitation field of the star. Using a spherical geometry one has

$$\dot{M} = 4\pi r^2 \rho v \tag{1.4}$$

$$v\frac{dv}{dr} = -\frac{1}{\rho}\frac{dP}{dr} - \frac{GM_*}{r^2} \tag{1.5}$$

$$E = \frac{v^2}{r} - \frac{GM_*}{r} + \frac{5\mathcal{R}T}{3\mu}, \tag{1.6}$$

where $\dot{M}$ is the mass loss rate, M_* the mass of the star and $\mathcal{R}$ is the gas constant, the mean mass per particle is assumed to be constant. In isothermal winds, the energy equation is reduced to $T = T(r)$. In a perfect gas one has

$$\frac{1}{\rho}\frac{dP}{dr} = \left(\frac{\mathcal{R}T}{\mu}\right)\frac{1}{\rho}\frac{d\rho}{dr}. \tag{1.7}$$

Mass conservation implies

$$\frac{1}{\rho}\frac{d\rho}{dr} = -\frac{1}{v}\frac{dv}{dr} - \frac{2}{r}. \tag{1.8}$$

Introducing Eq. 1.7 and 1.8 in the moment equation one gets

$$v\frac{dv}{dr} = -c_s^2\left(-\frac{1}{v}\frac{dv}{dr} - \frac{2}{r}\right) - \frac{GM_*}{r^2}, \tag{1.9}$$

where c_s is the sound speed given by

$$c_s^2 = \left(\frac{\partial P}{\partial \rho}\right) = \frac{P}{\rho} \tag{1.10}$$

Dividing by v^2 one gets

$$\frac{1}{v}\frac{dv}{dr} = \frac{\left\{\frac{2c_s^2}{r} - \frac{GM_*}{r^2}\right\}}{v^2 - c_s^2}. \tag{1.11}$$

The lower boundary condition is fixed by the values at r_0, the stellar surface. The topology of the solutions of Eq. 1.9 are given on Fig. 1.9. There is a singularity at the critical point

$$r_{crit} = \frac{GM_*}{2c_s^2}. \tag{1.12}$$

where the velocity gradient is 0 unless $v = c_s$. Similarly the velocity gradient is infinite if $v = c_s$ unless $r = r_{crit}$. Thus the only interesting wind solution goes through the critical point with $v = c_s$, it is a sonic point. This wind solution was first determined by Parker [1958]. It is possible only for one value for the velocity (v_0) and density (ρ_0) at the stellar surface. The important aspect to understand is that this implies that there is only one mass loss rate that allows for a wind solution.

$$\dot{M} = 4\pi r_0^2 \rho_0 v_0. \tag{1.13}$$

The density structure $\rho(r)$ can be found by numerically solving Eq. 1.8.

1.3.1.4 Line driven winds

Massive stars emit the bulk of their radiation in the UV while their atmosphere is rich in elements with absorption lines in the UV. The stellar light can thus be strongly absorbed in the stellar atmosphere. Elements such as C, O Si and N have very strong lines called resonance lines. Their opacity can be 10^6 times higher than opacity for electron scattering [Lamers and Cassinelli, 1999] providing an efficient momentum transfer from the photons to the ions in the atmosphere. Coulomb interactions with the electrons and other ions in the wind then allow the acceleration of the whole atmosphere.

In a static atmosphere, radiation at a given frequency would be totally absorbed at the bottom layers of the atmosphere and would not accelerate the upper layers. In an expanding atmosphere, there is a velocity gradient that induces a Doppler shift. In their rest frame, ions see the photons from the star as redshifted. Photons that have not been absorbed yet can thus be scattered in the upper layers of the atmosphere. Even the outer atmosphere can be efficiently

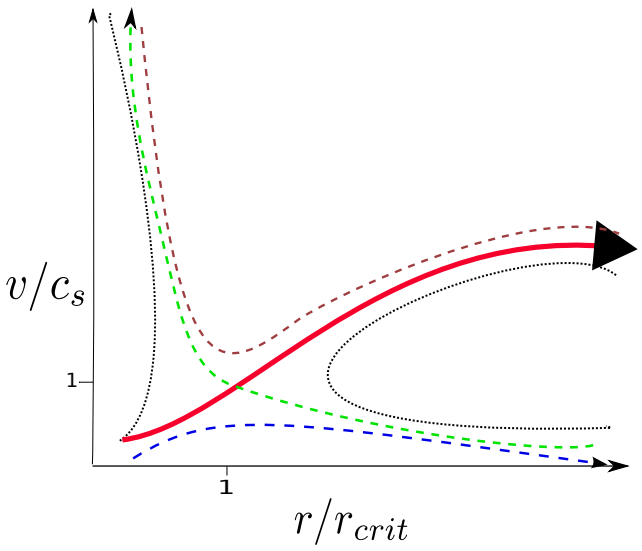

Figure 1.9: Solutions of the momentum equation of a stellar wind with only gas pressure and gravity. The black dotted solutions have no physical meaning. The brown solution corresponds to a wind that leaves the star with a supersonic velocity, which is unobserved. The blue solution corresponds to a slow *breeze* while the green solution corresponds to Bondi-Hoyle accretion, with matter coming from $r = \infty$ and going towards $r = r_0$. The supersonic wind solution is given by the thick solid red line.

accelerated by the continuum from the star and overcome the gravity of the star, resulting in a wind.

The first theoretical model of radiative acceleration on lines was performed by Lucy and Solomon [1970] and extended by Castor, Abbott and Klein [1975] to model the effect of a distribution of lines instead of a few important lines. Their theory is still widely used and is now known as the CAK-theory. The structure of a stationary line driven wind can be found by solving the Euler equations (Eqs 1.2) including radiation forces as source terms to the momentum equation

$$v\frac{dv}{dr} = -\frac{1}{\rho}\frac{dP}{dr} - \frac{GM_*}{r^2} + g^e + g^l, \tag{1.14}$$

where g^l expresses the acceleration due to line scattering and g^e expresses the acceleration due to electron scattering

$$g^e = \frac{\sigma_T L}{4\pi r^2 \mu_e c} \tag{1.15}$$

where L is the luminosity of the star, σ_T the cross section for the Thomson scattering, μ_e the mean mass per free electron and c the speed of light. The idea from Castor et al. [1975] was to express the acceleration due to line scattering as

$$g^l = g^e M(t), \tag{1.16}$$

where M(t) is the *force multiplier*. t is a sort of optical depth given by

$$t = \sigma_T v_{th} \rho \frac{dr}{dv}, \tag{1.17}$$

where v_{th} is the thermal velocity in the wind. As the winds are highly supersonic $v_{th} \ll v$. It is important to notice that the optical depth is directly proportional to the velocity gradient and density of the wind.

The CAK calculations rely on the Sobolev approximation [Sobolev and Gaposchkin, 1960] that assumes the lines profiles are Dirac-functions and implies the interaction region between photons and ions is infinitely narrow. Using the Sobolev approximation and assuming the star is a point source, detailed calculations show that

$$M(t) = kt^{-\alpha}\left(10^{-11}\frac{n_e}{W}\right)^{-\delta}, \tag{1.18}$$

where n_e is the electron density, W a geometrical factor and α, k, δ are called the CAK parameters that are related to number of lines, the ratio of optically thick lines to the total number of lines and the ionisation structure of the wind. k and α have values of about 0.5 for Wolf-Rayet stars [Abbott, 1982a] while the term $10^{-11}n_e/W$ is close to unity and often neglected. In this case momentum conservation can be expressed as

$$v\frac{dv}{dr} = -\frac{GM_*(1-\Gamma_e)}{r^2} + \frac{c_s^2}{v}\frac{dv}{dr} + \frac{2c_s^2}{r} + g^e kt^{-\alpha} \tag{1.19}$$

This equation is more complex than Eq. 1.9 but its solutions have a similar topology. In this case, the only wind solution is first subsonic, becomes supersonic and then passes the critical point r_{crit}, which is different from the sonic point. The resulting velocity profile is given by the so-called β-law

$$v(r) = v_\infty(1 - r_0/r)^\beta, \tag{1.20}$$

where β is of order unity. Line driven winds reach their terminal velocity at a distance of a few stellar radii. The interested reader can refer to the book Lamers and Cassinelli [1999] for a complete description of the solution [1].

Important improvements to the CAK theory were made by Pauldrach et al. [1986] and [Kudritzki et al., 1989] who gave up the point source approximation and took into account multiple line scattering.

1.3.1.5 A more modern view of line driven winds

The above paragraphs describe stellar winds as spherically symmetric, stationary homogeneous flows. The predictions of the CAK-theory in terms of mass loss rates and velocity profiles agree well with most of the observations. However, the above theory fails to explain the X-ray emission from individual stars and the observed variability in the line profiles. Stellar winds present variability on different time and length scales. There is a distinction between cyclic large scale variations induced by changes in the star and stochastic small scale variations intrinsic to the wind itself.

- Large scale variation is related to the effect of rotation, magnetic fields and/or non-radial pulsations in the star. It results for example in time variability of the blue-shifted absorption component in P Cygni profiles. Discrete absorption components (DAC) [Howarth and Prinja, 1989] arise from slowly evolving perturbations in the winds. They may be related to co-rotating interaction regions (CIR) that arise due to longitudinal asymmetries in the initial velocity or density profile. The faster flow catches up with the slower one, which results in spiral co-rotating shocks. The absorption components may be due to the crossing of such shocks [Cranmer and Owocki, 1996] with the line-of-sight.

- Small scale variability manifests itself by transient emission line structures as shown on Fig. 1.10. They are explained by irregular density and velocity profiles in the wind. In other

[1] A shorter description can be found on *http://www.physics.mcgill.ca/čumming/642/notes2006/term_papers/vincent_HB_massive_star_winds.pdf*

words, the wind is clumpy, composed of small zones of different densities and velocities, which interact with each other and are embedded in a lower density medium. Those clumps are probably created by the line-deshadowing instability (LDI, [MacGregor et al., 1979], Owocki and Rybicki [1984]) that arises from perturbations in the wind with a length smaller than the Sobolev length. Their interactions result in shock heated zones that generate X-ray emission.

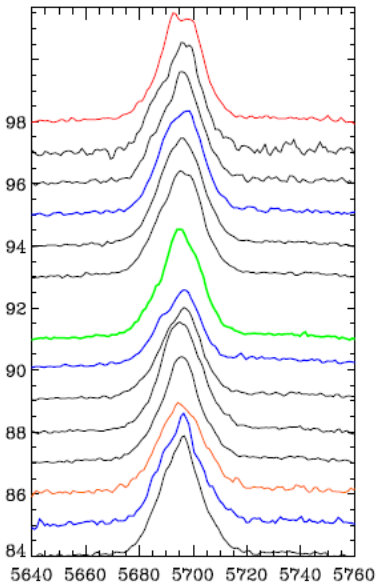

Figure 1.10: C III line profile (λ 5696) for WR 88 [St-Louis et al., 2011], a star that has no known binary companion. Different spectra show different moments, similar colours indicate similar shapes. The y axis shows time in days.

- An indirect proof of small scale clumpiness is the important discrepancy between mass loss rate estimates based on the density ρ, such as scattering of UV photons by resonance lines and diagnostics based on ρ^2, such as recombination line H_α, or free-free radio emission. Measurements based on ρ^2 processes yield mass loss rates that are an order of magnitude higher than for ρ processes. The difference cannot be explained by observational biases. It comes from clumping in the winds: dense clumps naturally lead to more important emission lines ($\propto \rho^2$) while the optical depth of resonance lines remains constant ($\propto \rho$), as it is related to the column density [Fullerton et al., 2006]. Comparing the two types of diagnostics allows to determine a filling factor of clumps within the winds.

1.3.1.6 Pulsar winds

A pulsar is the stellar leftover after a massive star ($8M_\odot \lesssim M_* \lesssim 40M_\odot$) explodes as a supernova. It is a very rapidly rotating neutron star (P$\lesssim$ 1 s for the young pulsars) with a strong magnetic field ($\simeq 10^{12}$ G). This generates a huge electric field that pulls particles from the surface and accelerates them [Rees and Gunn, 1974] up to ultrarelativistic velocities. At the light cylinder, given by the distance R_L where the magnetic field corotates with the pulsar at the speed of light, the magnetic field lines open and the particles escape and form a wind. The exact origin and structure of this wind is not fully understood yet (see *e.g.* Kirk et al. [2009] for a review). The flow is composed mainly of electrons and positrons and carries away part of the rotational energy of the pulsar. The flow is cold, meaning particles have very low thermal energy and do

not radiate [Kennel and Coroniti, 1984]. The proof of existence of pulsar winds comes from their interaction with the surrounding medium. A shocked structure forms where particles are isotropised, re-accelerated through the first order Fermi process and are responsible for high energy emission forming the pulsar wind nebula. The most famous example is the Crab nebula shown on Fig. 1.11. The X-ray emission results from synchrotron emission. The emission is brighter in the upper part of the image due to relativistic Doppler boosting. This phenomenon occurs when a source is moving with a bulk relativistic velocity and results in beamed emission along the direction of motion. If the source is orientated close to the line-of-sight, the resulting intensity is multiplied by $\simeq \Gamma^3$.

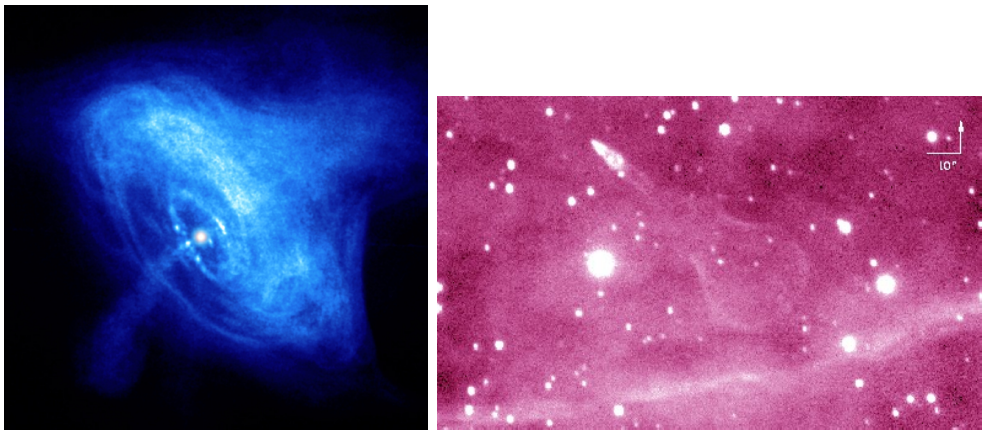

Figure 1.11: Left panel: *Chandra* image of the Crab nebula [Hester et al., 2002]. The pulsar is the white dot at the centre of the image, the inner ring is interpreted as the shock between the wind and the nebula. The jets and torus are particles flowing away from the poles of the pulsar. The whole structure is embedded in the supernova remnant that is observed at larger scales. Right panel: H_α observation (Palomar telescope [Chatterjee and Cordes, 2002]) of the so-called Guitar Nebula that results from a high velocity neutron star propagating through the ISM.

When pulsars are not located within a supernova remnant, the wind may directly interact with the interstellar medium (ISM) as in PSR 2224+65 shown in the right panel of 1.11. In γ-ray binaries such as PSR B1259-63, the pulsar wind interacts with the wind from a massive companion star creating a shocked structure visible at large scales (§1.2.2.4). It also interacts with the very dense photon field from the companion star that results in IC γ-ray emission that may be observable [Cerutti et al., 2008]. Contrary to pulsar winds interacting with diffuse background photons, the photon field is very well constrained in γ-ray binaries. This facilitates the study of the pulsar wind. Moreover, the emission arises close to the pulsar, at 0.1-0.01 AU ($\simeq 10^5 R_L$) while it occurs at much larger scales in pulsar wind nebula (*e.g.* 0.1 pc $\simeq 10^9 R_L$ in the Crab nebula) . γ-ray binaries thus appear as a complementary probe for pulsar winds.

1.3.2 Colliding wind binaries

This section provides theoretical background on the structure of colliding wind binaries, the structure of hydrodynamic shocks and the determination of the position of the contact discontinuity between the winds. The last part explains the main cooling processes at work in colliding wind binaries and how they can impact the structure of the shocked region.

1.3.2.1 Hydrodynamics of shocks

Small amplitude perturbations of a flow propagate adiabatically and are dissipated slowly. When their amplitude increases non-linear effects in the equations of hydrodynamics strongly affect

the flow. *"In particular in an acoustic disturbance a region of compression tends to overrun a rarefaction that precedes it; thus as a acoustic wave propagates, the leading part of the profile progressively steepens, eventually becoming a near discontinuity, which we identify as a shock."* (taken from Mihalas and Mihalas [1984]). Shocks occur when the flow is supersonic, thus no information can propagate from upstream the shock to downstream the shock. They are thus strong disturbances in a flow where the hydrodynamical variables (density, pressure and velocity) might not be continuous. However there are some jump conditions linking the upstream and downstream part of shocks, where I study a 1D hydrodynamical shock propagating along the x

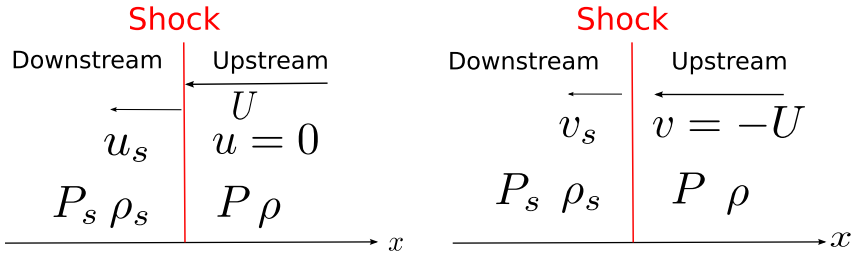

Figure 1.12: Hydrodynamical variables on both sides of the shock in the frame of the laboratory (left panel) and the frame of the shock (right panel). In this particular case, the upstream region is at rest in the frame of the laboratory.

direction with velocity U. One can either use the frame of the laboratory or the frame of the shock, both are shown on Fig. 1.12. ρ is the density, u and v are the velocities in both frames and P is the pressure. Both frames are related by

$$v_x = u_x - U \tag{1.21}$$
$$v_{xs} = u_{xs} - U, \tag{1.22}$$

where the subscript s stands for the shocked medium. From now on I will only consider the rest frame of the shock, where the shock is steady. Across the shock front, the flux of mass, momentum and energy per unit area is constant. The Euler equations (Eqs. 1.2) give

$$\begin{cases} \rho v = \rho_s v_s \\ \rho v^2 + P = \rho_s v_s^2 + P_s \\ \rho v (h + \frac{1}{2} v^2) = \rho_s v_s (h_s + \frac{1}{2} v_s^2) \end{cases} \tag{1.23}$$

where h is the specific enthalpy

$$h = e + \frac{P}{\rho} = \frac{\gamma}{\gamma - 1} P. \tag{1.24}$$

Eqs. 1.23 have two types of solutions [Landau and Lifshitz, 1975]. If there is no mass flux through the interface, $\rho v = \rho_s v_s$ that leads to $v = v_s = 0$ and the equations on the mass and energy flux are satisfied. The equation on the momentum flux then gives $P = P_s$. This is called a contact discontinuity (or tangential discontinuity), the pressure and normal velocity component are continuous while the other hydrodynamical quantities may be discontinuous by any amount. If there is a non-zero mass flux, the density, pressure and normal velocity are discontinuous and related by the above equations. This is a shock. We introduce the Mach number of the shock

$$\mathcal{M} = \frac{v}{c_s} = \frac{v}{\sqrt{\gamma P / \rho}}. \tag{1.25}$$

After some algebra equations 1.23 give

$$\begin{cases} \dfrac{\rho_s}{\rho} = \dfrac{(\gamma+1)\mathcal{M}^2}{2+(\gamma-1)\mathcal{M}^2} \\ \dfrac{P_s}{P} = \dfrac{2\gamma\mathcal{M}^2-(\gamma-1)}{\gamma+1} \\ \dfrac{v_s}{v} = \dfrac{\rho}{\rho_s} = \dfrac{2+(\gamma-1)\mathcal{M}^2}{(\gamma+1)\mathcal{M}^2} \end{cases} \tag{1.26}$$

which are the jump conditions across a shock also called the Rankine-Hugoniot conditions. Stellar winds are highly supersonic and we can simplify the Rankine-Hugoniot conditions in the limit of strong shocks where $\mathcal{M} \to \infty$. In the adiabatic limit ($\gamma = 5/3$) this gives:

$$\begin{cases} \dfrac{\rho_s}{\rho} = 4 \\ \dfrac{P_s}{P} \propto \mathcal{M}^2 \\ \dfrac{v_s}{v} = \dfrac{1}{4} \end{cases} \tag{1.27}$$

and in the isothermal limit ($\gamma = 1$) we have

$$\begin{cases} \dfrac{\rho_s}{\rho} = \mathcal{M}^2 \\ \dfrac{P_s}{P} \propto \mathcal{M}^2 \\ \dfrac{v_s}{v} = \dfrac{1}{\mathcal{M}^2} \end{cases} \tag{1.28}$$

Isothermal shocks thus have much higher compression rates than adiabatic ones. In this section I have assumed no cooling or heating mechanism modifies the energy equation. However, they may have important consequences in colliding wind binaries, as I will show in §1.3.2.3.

1.3.2.2 Analytic solutions for colliding wind binaries

Several analytic solutions have been derived to model the position of the contact discontinuity in colliding wind binaries. Most of them are based on the thin shell hypothesis that assumes there is no thermal pressure in the shocked winds. This means both shocks and the contact discontinuity are merged in one single layer.

First steps were taken modelling the interaction between a stellar wind and the interstellar medium [Dyson, 1975] or a HII region [Baranov et al., 1971]. In both cases, the problem can be reduced to the interaction between a diverging flow and a plane parallel flow.

The first attempt to find the analytic solution of colliding wind binaries was made by Huang and Weigert [1982]. They based their work on two additional important hypotheses: no orbital motion of the binary and no acceleration of the winds. This means that the winds are assumed to have reached their terminal velocity at their interaction. The position of the front is computed using ram pressure balance and conservation of mass and momentum perpendicular to the front [Lebedev and Myasnikov, 1990]. Along the line-of-centres, the ram pressure balance between the winds is simply given by

$$\rho_1 v_1^2 = \rho_2 v_2^2, \tag{1.29}$$

where the subscripts 1 and 2 stand for the different winds. This leads to the position of the standoff point [Stevens et al., 1992]

$$\frac{R_S}{a} = \frac{\sqrt{\eta}}{1+\sqrt{\eta}}, \tag{1.30}$$

with a the binary separation (one assumes a circular orbit) and

$$\eta = \frac{\dot{M}_1 v_{\infty 1}}{\dot{M}_2 v_{\infty 2}}, \tag{1.31}$$

the momentum flux ratio of the winds.

Further away from the binary, numerical integration leads to position of the front according to η. The structure is shaped like a cone, aligned with the line-of-centres, where the stronger wind wraps around the weaker wind. The geometry is sketched in Fig.1.13.

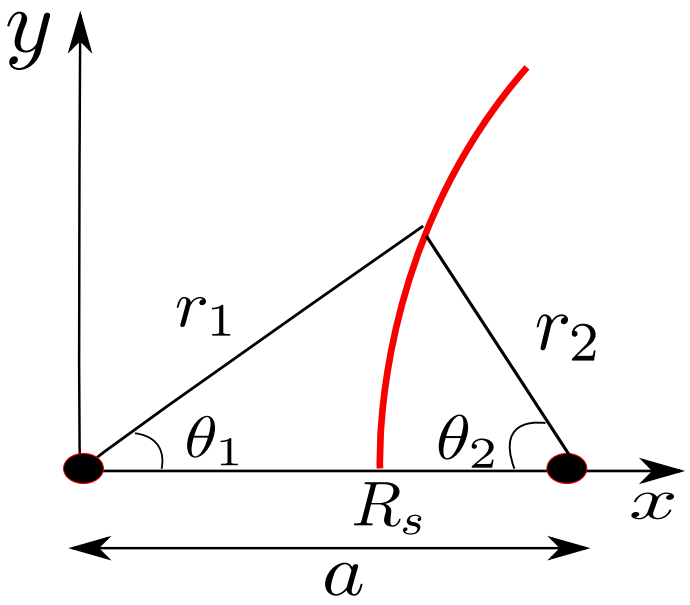

Figure 1.13: Sketch of the two-wind interaction problem. The stars are the big dots, the interaction region is shown with the thick red line.

The solutions are limited to a zone close to the interaction zone but show the presence of an asymptotic opening angle of the cone. Centrifugal effects of matter flowing along the shell have been taken into account [Girard and Willson, 1987], straightening out the front and forming a wider cone like structure. These effects are important far away from the binary. Kallrath [1991] included accelerated winds in the models. A solution is set out in Stevens et al. [1992] and used in Antokhin et al. [2004]

$$\frac{dx}{dy} = \frac{x}{y} - \left(\frac{a}{y}\right)\left(1 + \sqrt{\eta}\left(\frac{r_2}{r_1}\right)^2\right)^{-1}, \tag{1.32}$$

where r_1 and r_2 are the distance between the contact discontinuity and the first and second star, respectively. Numerical resolution of this equation gives the shape of the contact discontinuity and allows the computation of the asymptotic opening angle.

Extending the work by Wilkin [1996] on stellar wind bow shocks, Canto et al. [1996] developed the first algebraic solution of the thin shell two-wind interaction problem. Their computations included centrifugal effects by conserving angular momentum along the contact discontinuity. They obtained a set of four equations that can be solved analytically in order to get the position of the shell. The shape of the shell is given by

$$\theta_1 \cot\theta_1 - 1 = \eta\,(\theta_2 \cot\theta_2 - 1)\,, \tag{1.33}$$

with θ_1 and θ_2 the angle between r_1 and the line of centres and r_2 and the line of centres. This leads to an asymptotic opening angle given by

$$\theta_{2\infty} - \tan\theta_{2\infty} = \frac{\pi}{1-\eta}, \tag{1.34}$$

They confirm that the inclusion of centrifugal effects widens the cone because of matter flowing away from the line-of-centres. Recent work by Gayley [2009] has extended these results to adiabatic winds. He also included the effects of mixing at the contact discontinuity.

Eichler and Usov [1993] provide another estimate of the opening angle

$$\theta_{2\infty} = 2.1\left(1 - \frac{\eta^{2/5}}{4}\right)\eta^{1/3}, \tag{1.35}$$

None of these works take into account the thickness of the shell to enable the computation of the positions of the shocks.

On large scales, orbital motion is expected to turn the shock structure into a spiral, although we will show in Chapter 4 that this is not always true. Orbital motion breaks the symmetry with respect to the binary axis and no analytic solution predicts the detailed structure of the colliding wind region. Material in the spiral is generally thought to behave ballistically, so that the step of the spiral is the wind velocity v times the orbital period $P_{\rm orb}$.

1.3.2.3 Cooling and heating mechanisms in colliding wind binaries

Heating in colliding wind binaries is due to the conversion of kinetic energy into thermal energy at the shocks. The above computations have considered only polytropic equations of state, where two behaviours are possible. In adiabatic winds, thermal support is important in the downstream region and cooling is only possible through expansion of the gas. In radiatively efficient winds, the temperature remains roughly constant across the shocks as the kinetic energy is removed from the system by radiation. This type of winds is usually modelled as an isothermal wind, with a constant temperature. In this manuscript, I will use the term isothermal to designate radiatively efficient winds. Both the adiabatic and isothermal winds represent idealised situations, in real colliding wind binaries additional terms in the energy equation (Eq. 1.2) allow for cooling and heat redistribution.

- Below 10^7K most of the radiative cooling results from line emission. Beyond, it is mostly Bremsstrahlung (free-free emission). At a frequency ν, the emission coefficient (in erg cm^{-3} s^{-1} Hz^{-1}) for free-free emission is given by [Rybicki and Lightman, 1979]

$$\epsilon_\nu^{ff} = 6.810^{-38} Z^2 n_e n_i T^{-1/2} e^{\frac{-h\nu}{k_B T}} g_{ff}, \tag{1.36}$$

  where Z is the ionic charge, n_e and n_i the electronic and ionic number density, respectively. h is the Planck constant and g_{ff} the Gaunt factor (of order unity). One can determine the corresponding energy losses $-n_e n_i \Lambda(T)$ per unit time and unit volume in a certain temperature range. Λ is the cooling coefficient that depends on the chemical abundances, ionisation state and temperature of the plasma. An example of a cooling function is given on Fig. 1.14. $\Lambda(T)$ are tabulated values determined using an optically thin plasma emission code.

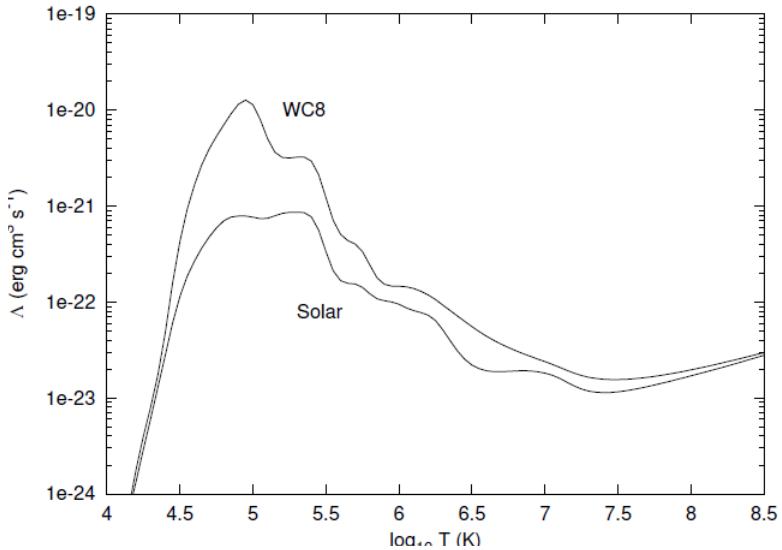

Figure 1.14: Cooling function [Pittard et al., 2005] for solar abundances and carbonated Wolf-Rayet stars. For $T > 10^6\,K$, the chemical composition does not significantly affect the cooling rate. The cooling function takes into account line emission from many elements and free-free emission.

Similarly inverse Compton scattering of thermal electrons on the UV photons of the stars can be important when the shocked region is close to one of the stars. The cooling coefficient can be determined analytically [White and Chen, 1995]

$$\Lambda_{IC}(T) = \frac{4\sigma_T m_H L v_\infty k_B T_s}{m_e c^2 4\dot{M}} = 3.7 \times 10^{-23} \mathrm{erg\ cm^{-3} s^{-1}} \frac{L_6 T_{s,7} v_{\infty,8.5}}{\dot{M}_{-6}}, \tag{1.37}$$

It scales as the inverse of the mass loss and may be particularly important in winds from early type stars.

Generally speaking, cooling is important if the cooling timescale is shorter than the escaping timescale. Stevens et al. [1992] determined the cooling parameter

$$\chi = \frac{t_{cool}}{t_{esc}} = \frac{k_B T_s}{4n\Lambda(T_s)} \frac{c_s}{a} \simeq \frac{v_\infty^4 a_{12}}{\dot{M}_{-7}}, \tag{1.38}$$

where $v_{\infty 8}$ is the velocity expressed in $1000\,\mathrm{km\,s^{-1}}$, a_{12} the binary separation in 10^7 km and $\dot{M}_{-7}$ the mass loss rate of the wind in 10^{-7} Solar mass per year. n is the number density upstream of the shock. This computation assumes a compression rate of 4 at the shocks and an electron temperature given by $3m_e v_\infty^2/16k_B$. A wind can be considered as adiabatic when $\chi \geqslant 1$ while radiative cooling is efficient for $\chi \leqslant 1$. Still, one should be cautious when using Eq. 5.16 as the paremeter χ is given for a certain position in the wind, with a given temperature, chemical composition and density while all these parameters may vary in the colliding wind region. Eq. 5.16 gives only a rough estimate of cooling in the winds and numerical simulations are needed for more realistic modeling. Simulations including cooling show that it decreases the width of the shocked region (see §1.4.2). The shell becomes subject to instabilities that strongly affect the dynamics of the flow.

- A certain amount of the energy released at the shocks goes into particle acceleration. These highly energetic particles radiate away their energy through synchrotron and inverse

Compton losses. Most models assume that less than 1% of the electrons thermal energy density is used for particle acceleration [Dougherty et al., 2003, Falceta-Gonçalves and Abraham, 2012] in colliding wind binaries, but this value can be much higher for ions [Pittard and Dougherty, 2006]. Protons are accelerated at the shocks and collisions between two protons could lead to the production of pions that decay and produce gamma-ray emission [Reimer et al., 2006]. Particle acceleration does not only affect the energetic balance of the shocks but may also affect their structure. Evidence for shock modification due to highly energetic ions has been found in supernova remnants [Völk et al., 2002] but whether this could occur in colliding wind binaries has not been studied yet [Pittard and Dougherty, 2006].

- Thermal electrons can transfer energy from shock heated zones to cooler neighbouring regions [Motamen et al., 1999]. Myasnikov and Zhekov [1998] showed that thermal conduction results in a preheated zone upstream the shock and a slightly lower maximal temperature downstream, which softens the X-ray spectrum. However, in presence of magnetic fields, thermal conduction is strongly reduced in the direction perpendicular to the field [Zhekov and Myasnikov, 2000].

1.4 The contribution of numerical simulations

Analytic solutions are based on simplifying assumptions, they provide the position of the contact discontinuity but do not indicate the exact shocked structure. The exact structure is important when comparing with observations. For example, the positions of the shocks indicate the location for particle acceleration that results in extended non-thermal emission. The density and temperature profiles in the shocked regions determine whether dust formation is possible in certain binaries. Analytic solutions rely on an idealised vision of a stationary smooth flow while the next section will prove colliding wind binaries can be highly unstable.

Numerical simulations are thus necessary to solve the time-dependent evolution of colliding wind binaries. Their objective is twofold : on one hand, they are meant to improve our understanding of the physical processes at work in colliding wind binaries and generally cover a given range of parameters. On the other hand, simulations are designed for comparison with observations and are used to determine spectra, lightcurves and emission maps in order to put constrains on the physical or orbital parameters of specific systems.

1.4.1 State of the art numerical simulations

1.4.1.1 Modelling massive binaries

Luo et al. [1990] presented the first 2D numerical simulations of colliding stellar winds for $\eta = 1$ and $\eta = 0.1$. This gave the first indication of the positions of the shocks. Simulations at larger scales and lower momentum flux ratios revealed the presence of a reconfinement shock behind the star with the weaker wind (Myasnikov and Zhekov [1993], Brighenti and D'Ercole [1995]).

The improvement of numerical methods and the increase in available computing resources quickly allowed to discover that the shocked structure is not smooth but rather unstable. Luo et al. [1990] predicted the presence of the Kelvin-Helmholtz instability (KHI) at the contact discontinuity in their model with unequal wind speeds. Unfortunately they did not have enough numerical resolution to trigger the instability which presence was confirmed by Stevens et al. [1992]. The KHI can arise between identical winds due to the velocity difference created by orbital motion [Lemaster et al., 2007]. However, its impact is unclear as Pittard [2009] and van Marle et al. [2011a] do not see it in their high resolution simulations. Stevens et al. [1992] performed the first simulations including a cooling function $\Lambda(T)$ in the energy equation (Eq.

1.2) to take into account radiative cooling. It leads to an important decrease in temperature in the shocked zone that becomes very narrow and subject to instabilities [Strickland and Blondin, 1995, Blondin and Koerwer, 1998]. Two mechanisms have been proposed: the non-linear thin shell instability (NTSI, Vishniac 1994b) and the transverse acceleration instability (TAI, Dgani et al. 1993, 1996b) ; both may be at work in colliding winds [Blondin and Koerwer, 1998], [Walder and Folini, 1998]. These different instabilities may lead to mixing and variability that has important observational consequences. I will detail their physical mechanisms in §1.4.2 and explain their respective contributions in colliding wind binaries in Chapter 3.

Important advances in modelling more realistic winds have been made by including radiative acceleration of the winds such as in [Pittard, 2009]. The wind from a star can also be influenced by the radiation field of its companion. The CAK theory predicts that the companion can accelerate the wind towards the star it is coming from. This results in decreased wind acceleration, called radiative inhibition [Stevens and Pollock, 1994]. A similar effect may occur close to a star where its radiation field stops the companion wind before the stagnation point causing radiative braking [Gayley et al., 1997]. Although countered by gravity, this effect is able to prevent the collapse of the stronger wind on the star with the weaker wind. Radiative effects also impact the structure of the spiral arms creating an additional pressure for high luminosity stars [Parkin et al., 2011].

Orbital motion turns the colliding wind region in a large scale spiral structure [Walder and Folini, 2003]. High resolution 3D simulations show the effect of the Coriolis force on the shock positions [Lemaster et al., 2007]. Both edges of the spiral develop differently, one expanding and the other one being compressed [van Marle et al., 2011a, Parkin et al., 2011]. Attempts have been made to model large scale colliding wind binary with smoothed particle hydrodynamics (SPH) [Okazaki et al., 2008] although SPH is less performing at capturing shocks than grid based simulations (see Chapter 2).

Thanks to the wealth of available data, the reproduction of X-ray spectra and light-curves has received much attention (*e.g.* Stevens et al. [1992], Pittard and Corcoran [2002]). It allows to constrain the orbital parameters of the system by fitting the lightcurves. It has suggested the presence of radiative inhibition in η Carinae [Parkin et al., 2011] and radiative braking in γ^2 Velorum [Henley et al., 2005]. The effect of clumpiness has been tested for collisions between adiabatic winds by Pittard [2007]. Clumps are mostly destroyed when crossing the shocks, letting the X-ray emission unaffected unless they are very large [Walder and Folini, 2002].

The modelling of radio emission [Dougherty et al., 2003] shows satisfying agreement with observations and has indicated the importance of IC cooling [Pittard et al., 2006]. [Harries et al., 2004a] present a model of WR 104 with radiative transfer to model dust emission. Comparison with infrared images and spectra determine the dust production rate, size of the grains and an upper limit on the inclination of the system.

1.4.1.2 Modelling pulsar winds interacting with their environment

Pulsar winds interacting with their surroundings are expected to display a double shock structure similar to the one observed in colliding wind binaries. Their numerical modelling is computationally demanding as the numerical timestep is limited because of the highly relativistic pulsar wind (CFL condition, see §2.2.1.3) while the dynamical timestep is set by the characteristic velocity in the surrounding medium. More realistic modelling of the interactions between pulsar winds and the interstellar medium, supernova remnant or wind from the companion star was made possible only recently with the increase in available computer power and the improvement of high resolution shock capturing numerical schemes.

Pioneering work was made by Tavani and Brookshaw [1991] who modelled the interaction between an outflow from a millisecond pulsar and a low-mass companion star. Such a system is called a *black widow* : the high energy radiation from the compact object vaporises the companion

star by driving a self-sustained mass loss. Their 2D-SPH simulation modelled the pulsar wind by the presence of a pressure force on the wind from the companion. Still, it indicated the presence of a shocked structure at the centre of the system and a larger scale outflow which shape depends on the orbital parameters and the characteristics of both the pulsar and companion.

The next steps were set by Van der Swaluw and his collaborators [van der Swaluw et al., 2003, van der Swaluw, 2003] who computed the impact of a pulsar wind on the surrounding supernova remnant using a non-relativistic hydrodynamical and magnetohydrodynamical model. Pulsar bow shock nebulae were first investigated by Bucciantini [2002] with a hydrodynamical model that was then improved to include special relativity and magnetic fields [Bucciantini et al., 2005], reaching a maximal Lorentz factor $\Gamma = 10$. [Vigelius et al., 2007] showed that asymmetries in observed nebulae are due to a combination between the anisotropy in the pulsar wind and density gradients in the interstellar medium. The inclusion of the relativistic and magnetised nature of the pulsar wind determines synchrotron emission from the shocked pulsar wind that is in good agreement with observed nebulae (Komissarov and Lyubarsky [2004], Bogovalov and Tsinganos [2005]).

In γ-ray binaries, the pulsar wind interacts with both the wind and photon field of the companion star on much smaller scales than in pulsar wind nebulae. The first relativistic simulation of a γ-ray binary was performed by [Bogovalov et al., 2008] using a numerical method where direct simulation only occurs for the shocked pulsar wind and the rest of the flow is determined by a relaxation method. This quenches the development of instabilities that are likely to arise in the collision region. They studied the impact of the momentum flux ratio on the positions of the different discontinuities. When the winds have equal strengths, they found the pulsar wind re-accelerates, due to adiabatic losses, after the shock to reach a bulk Lorentz factor $\Gamma \simeq 100$ (at roughly 45 times the binary separation), which would lead to an important Doppler boost. Their model has been extended to take into account magnetic fields and anisotropies in the winds [Bogovalov et al., 2012] but it does not significantly modify the colliding wind structure. 3D SPH simulations (in the hydrodynamical limit) including orbital motion study the tidal effects of the pulsar on the equatorial wind from the Be star in PSR B1259-63 [Okazaki et al., 2011] and conclude the density in the disk has to be high in order to match the observed radio lightcurves. [Bosch-Ramon et al., 2012] provide the first relativistic simulation ($\Gamma = 2$) of a γ-ray binary including orbital motion. They assume the stellar wind slightly dominates the pulsar wind. Their 2D simulations show the beginning of a large scale spiral structure and important instabilities at the contact discontinuity, as is shown on Fig. 1.15. These instabilities may destroy the large scale spiral structure [Bosch-Ramon and Barkov, 2011] or introduce important mixing between both winds and prevent non-thermal emission at distances larger than the binary separation [Zdziarski et al., 2010].

Up to now multidimensional simulations at high Lorentz factors remain a numerical challenge. They provide a more and more realistic view of pulsar winds, by taking into account their anisotropic and magnetised nature. Still the differences between a relativistic and non-relativistic model have never been clearly studied, especially for γ-ray binaries.

This section highlights the need to use numerical simulations when modelling large scale structures and adding more complex physical phenomena to allow comparisons with observations. However, including many different physical effects makes it more difficult to measure their respective impacts and care has to be taken when analysing the physical nature of a given feature in colliding wind binaries. Proper modelling requires a high resolution and a well-adapted numerical method. Particular care has to be taken to avoid numerical quenching of instabilities.

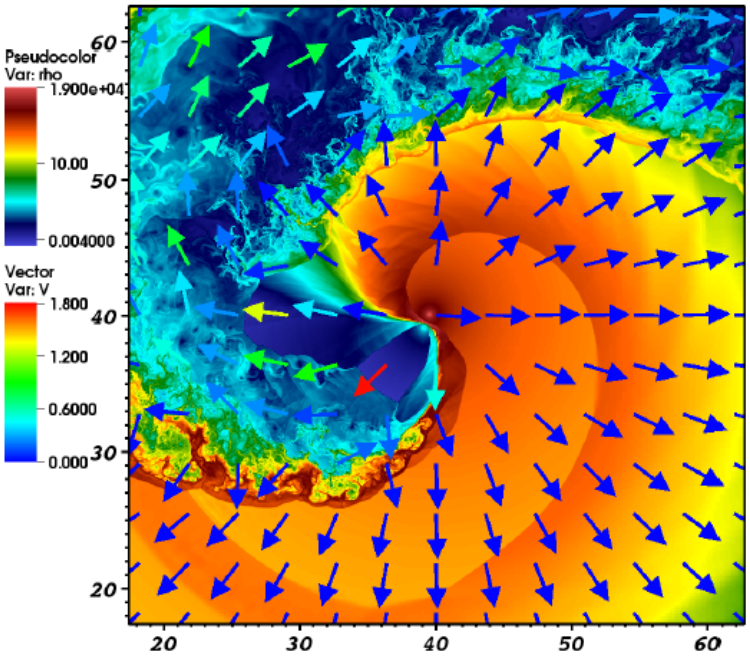

Figure 1.15: Density (color scale) and velocity (arrows) in a simulated γ-ray binary [Bosch-Ramon et al., 2012]. The pulsar wind is given in blue, the stellar wind in orange. The length scale is set by the binary separation.

1.4.2 Hydrodynamical instabilities in colliding wind binaries and colliding supersonic flows

Astrophysical flows are often subject to perturbations from the surrounding medium or internal stress. It is important to know whether the steady equilibrium is stable to these perturbations. If the system is stable the perturbation develops as oscillations or waves that are eventually damped because of dissipation. This situation corresponds to a minimum of energy. If the equilibrium corresponds to a maximum in energy, an infinitesimal perturbation will have a growing amplitude to a finite size and permanently modify the structure of the flow. This corresponds to an instability. One usually assumes it is linear (but this is not always the case), meaning quantities can be expressed as $v = v_0 + v_1\epsilon$ with $\epsilon \ll 1$. The subscript 0 refers to the quantity in the equilibrium state, and 1 to the perturbed state. The Euler equations can then be written with respect to the different powers of ϵ. Terms proportional to ϵ^0 cancel out as they correspond to the equilibrium state. Terms proportional to ϵ correspond to a linear description of the perturbed state. Terms at higher powers are neglected. One then assumes perturbations grow exponentially and quantities can be expanded into planar waves. For example $v_1 = \mathrm{e}^{i(\omega t - \vec{k}.\vec{r})}$, where ω is the oscillation frequency and k the wavenumber. Expressing all quantities like this, one finds the dispersion relation $\omega = \omega(k)$

$$\omega = \omega_{\mathcal{R}} + i\gamma, \tag{1.39}$$

where $\omega_{\mathcal{R}}$ is the real part, which corresponds to the propagation of the wave. The system is stable if the imaginary part γ is > 0 and the amplitude remains bounded. If $\gamma < 0$ the wave grows exponentially and γ can be considered as the growth rate of the instability. This is the linear phase of the instability.

In some cases the dispersion relation may change as several proper modes mix, which leads

to a non-linear state. In other cases the stable system is in a local energetic minimum and is stable to small amplitude perturbations but is unstable for finite perturbations. In this case the instability is non-linear (see the Non-linear Thin Shell Instability below).

When the real part, which corresponds to an harmonic oscillator, is of similar amplitude as the imaginary part, the system shows an oscillating behaviour. This is called an overstability, the Transverse Acceleration instability is one of those (see below).

The following section presents the most common instabilities expected in colliding wind binaries. Some of them may also be very relevant in other astrophysical contexts. Analytic calculations generally model idealised situations, using simplifying assumptions (*e.g.* planar, homogeneous flows...). Astrophysical flows are much more complex and numerical simulations provide a great help to determine the impact of instabilities in more realistic astrophysical contexts. In numerical simulations, instabilities can be triggered because of numerical noise at the grid scale. One can also use unstable initial conditions, by imposing a certain velocity profile for example.

The smallest possible wavelength that can be modelled is set by numerical resolution. Care has to be taken when simulating instabilities dominated by small wavelength perturbations. The result of the simulations also depends on the numerical scheme and especially on the amount of numerical dissipation. Numerical dissipation is non-linear and may affect small wavelengths differently than large wavelengths. The development of instabilities such as the Kelvin-Helmholtz instability are common tests for numerical codes.

- The Rayleigh-Taylor instability. This instability occurs when a heavier fluid of density ρ' is on top of a lighter fluid of density ρ. The dispersion relation is given by

$$\frac{\omega}{k} = \sqrt{\frac{g}{k}\frac{\rho - \rho'}{\rho + \rho'}}. \tag{1.40}$$

  In an astrophysical context acceleration usually plays the role of gravity g. Fig. 1.16 shows three stages of the development of the Rayleigh-Taylor instability. In the first phase fingers of heavy material sink into the lighter fluid, as can be observed in supernova remnants. At later stages the instability has become totally non-linear and has introduced strong mixing between the fluids.

- Kelvin-Helmholtz instability. This instability occurs when two fluids with different velocities v and v' flow along each other. This occurs in many astrophysical contexts. The dispersion relation is given by

$$\frac{\omega}{k} = \frac{\rho v + \rho' v'}{\rho + \rho'}\sqrt{\frac{g}{k}\frac{\rho - \rho'}{\rho + \rho'} - \frac{\rho\rho'(v - v')^2}{(\rho + \rho')^2}}. \tag{1.41}$$

  When there is no gravity nor surface tension the interface between the two fluids is unstable to any velocity discontinuity [Chandrasekhar, 1961]. In the linear phase the growth rate is then $tau \propto \Delta v k$ and the high wavenumbers dominate the structure. The instability manifests itself through the formation of eddies, as can be seen on Fig. 1.17. In the non-linear phase (right panel of the figure) the large scale structures dominate the flow.

- Radiative Instability : This instability is a thermal overstability [Langer et al., 1981, Chevalier and Imamura, 1982] that is related to the temperature dependence of the cooling function $\Lambda(T) = \rho^2 T^\alpha$ (sse § 1.3.2.3). When a shocked zone is very thin, inflowing matter does not have time to cool to the ambient temperature before reaching the edge of the shocked zone. It has too much thermal energy and inflates in order to reach the ambient temperature. The shell is now thicker and matter cools before reaching the edge of the shell. This

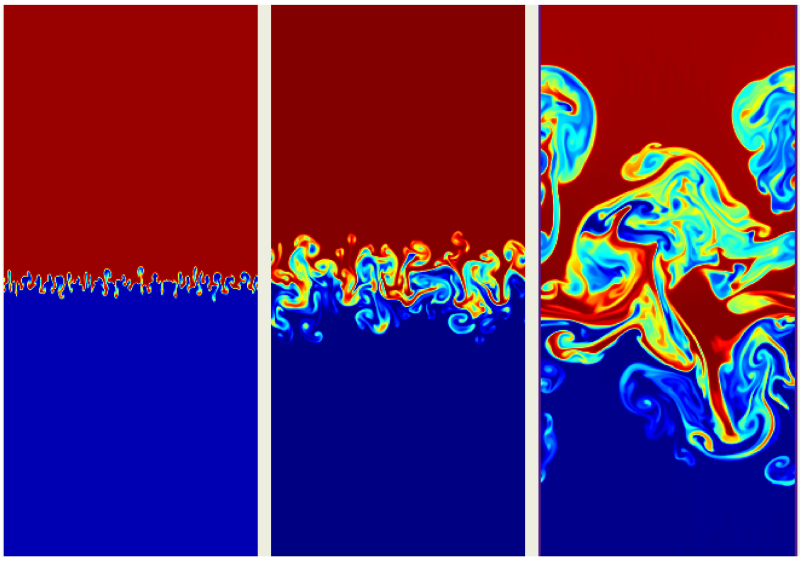

Figure 1.16: Density maps showing the evolution of the Rayleigh-Taylor instability at t=4.47 (left), 8.94 (centre) and 13.42 (right). The heavier fluid ($\rho' = 2$) is shown in red, the lighter one is blue ($\rho = 1$). The instability is seeded by initial random velocity perturbations. The boundary conditions are periodic along the x direction. Image taken from the Athena code [Stone et al., 2008] test suite (Fortran version).

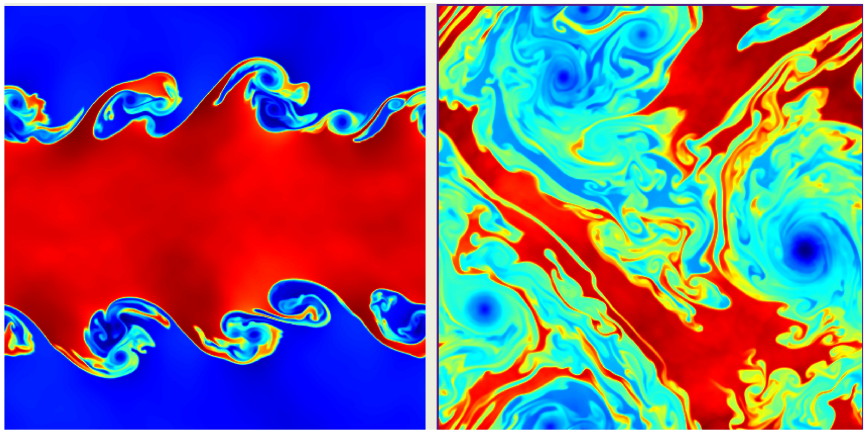

Figure 1.17: Density maps showing the evolution of the Kelvin-Helmholtz instability at t=1 (left) and t=5 (right). In the upper half of the box, $\rho' = 1, v' = -0.5$, in the lower half $\rho = 2, v = 0.5$. The instability is seeded by initial random velocity perturbations, the boundary conditions are periodic along both directions. Image taken from the Athena code test suite (Fortran version).

results in a contraction of the shell. Then, matter will not have enough time to cool and a new cycle begins. The conditions to trigger different modes of the instability depend on the value of α. Several cycles can be seen on Fig. 1.18.

- Non Linear Thin Shell Instability (NTSI) : Shock bounded slabs are unstable to perturbations of order of the thickness of the slab L [Vishniac, 1994b]. The instability is driven by lateral transport of longitudinal momentum that is collected at the curved edges of the slab. When the amplitude of the displacement is large enough, to the first order, the

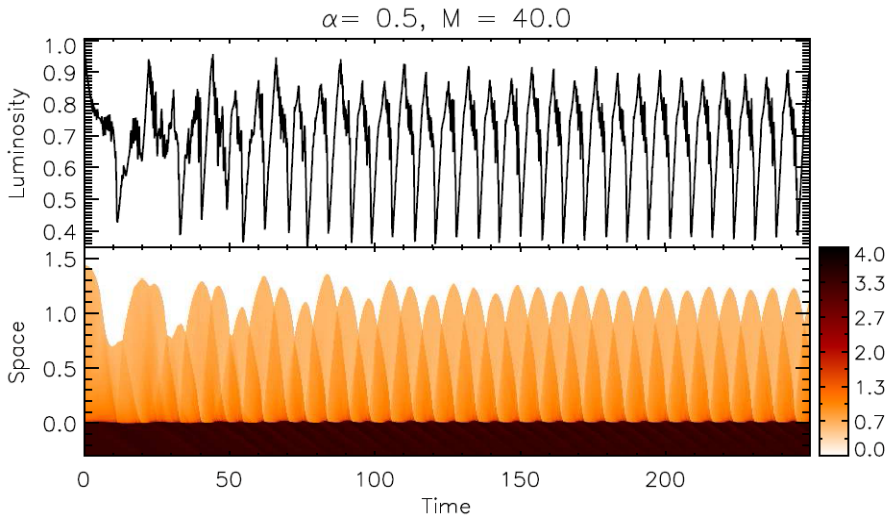

Figure 1.18: Space-time diagram showing the evolution of the radiative overstability. The shocked region is shown in orange, initially the shock is located at $x = 1$, the initial perturbations arise from numerical noise. Image taken from Mignone [2005].

growth rate $1/\tau \propto c_s/L$. Fig. 3.16 shows the development of this instability.

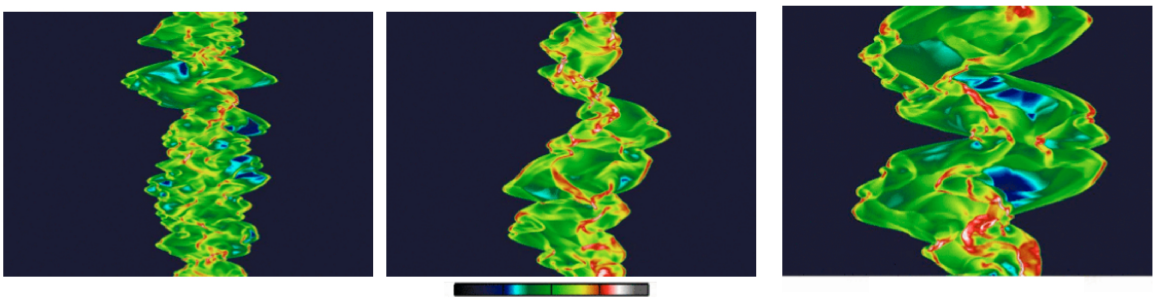

Figure 1.19: Density maps showing the evolution of the non linear thin shell instability at t=34 (left), 54 (centre) and 74 (right). Initially, there is a thin, cold dense slab, trapped by two supersonic incoming flows. The instability is triggered by imposing an initial sinusoidal deformation to the slab. As a proof of the non-linear nature, the final result does not depend on the wavelength of the initial perturbations. Image taken from Folini and Walder [2006].

- Transverse Acceleration Instability (TAI) : This instability occurs between colliding flows separated by a infinitely thin shell of shocked gas if (at least) one of the flows is diverging (Dgani [1993], [Dgani et al., 1996a]). It results from unbalanced ram pressure on both sides of the shell. The ram pressure depends on the distance to the origin of the flow, which are the stars in the case of colliding wind binaries. The instability arises from perturbations in the tangential velocity that result in a torque that in turn increases the bending of the slab. Fig. 1.20 shows the interaction between a stellar wind and the ISM. The instability has been interpreted as the TAI by Blondin and Koerwer [1998]. Its growth rate scales as $k^{-1/2}$, it is an overstability with an oscillation frequency inversely proportional to the wavenumber.

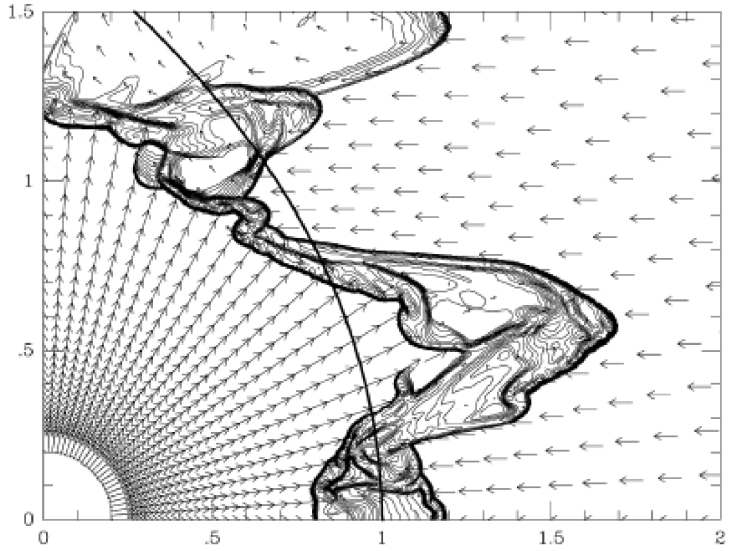

Figure 1.20: Density contour of an interaction between a stellar wind (the star is shown in the left bottom angle) and the interstellar medium (right). The initial conditions are set by the analytic solution by Wilkin [1996], both flows are isothermal. The arrows represent the velocity field. The solid line gives the equilibrium solution.

1.5 Introduction en Français

L'air que nous respirons est essentiellement constitué d'oxygène et d'azote. La planète Terre est composée de fer, d'oxygène, de silicium, de magnésium, de soufre... Le corps humain est surtout fait d'oxygène, de carbone et d'hydrogène et contient des traces d'éléments telles que l'aluminium, le phosphore ou le potassium. D'où viennent tous ces éléments? Comment se sont-ils retrouvés ici, dans notre environnement proche? Pour répondre à ces questions, il faut aller chercher bien plus loin que sur la Terre. Il faut aller chercher dans les étoiles massives. On appelle massive une étoile au moins dix fois plus massive que le Soleil. Bien que peu nombreuses, ces étoiles sont des moteurs essentiels de l'évolution de notre Univers. Ce sont elles qui produisent les éléments lourds et elles constituent une source d'énergie majeure.

Dans les étoiles massives, comme dans toutes les étoiles, des réactions nucléaires transforment l'hydrogène en hélium pendant la séquence principale. Pour les étoiles massives, cette phase est très courte et elles ne "vivent" environ que 10 millions d'années. En comparaison, la séquence principale du Soleil va durer 10 milliards d'années. Quand tout l'hydrogène a été brûlé, d'autres réactions nucléaires démarrent et produisent successivement des éléments de plus en plus lourds : du carbone, de l'oxygène, de l'azote... jusqu'au fer. A ce stade là, la suite de réactions nucléaires ne peut plus continuer. L'étoile s'effondre alors sur elle-même et libère une énorme quantité d'énergie (jusqu'à 10^{53} erg), lors d'une explosion de supernova. Les couches supérieures de l'étoile sont alors violemment éjectées dans le milieu interstellaire et l'enrichissent des éléments produits par celle-ci. Les éjecta sont très rapides et compriment le milieu interstellaire, ce qui peut engendrer la formation de nouvelles étoiles. Celles-ci seront chimiquement plus riches que la génération précédente, et ainsi de suite. Ce processus explique la composition chimique de la Terre.

L'injection de matière et d'énergie dans le milieu interstellaire ne se fait pas seulement lors de l'explosion de supernova, mais a lieu presque tout au long de la vie de l'étoile, sous forme d'un vent stellaire. Les vents des étoiles massives sont au cœur de cette thèse. Ils sont dus à la luminosité très élevée des étoiles massives et durant la séquence principale, ils éjectent de

façon continue l'équivalent de $10^{-8} - 10^{-7}$ fois la masse du Soleil par an [Puls et al., 1996]. La matière s'échappe alors à une vitesse de l'ordre de quelques milliers de kilomètres par seconde. C'est beaucoup plus rapide que la vitesse du son dans le vent, le vent est donc qualifié de supersonique. Pendant les stades plus évolués de l'étoile, la perte de masse varie. La phase la plus impressionnante est la phase de Wolf-Rayet, où le taux de perte de masse peut atteindre 10^{-4} masses solaires par an [Puls et al., 2008a]. A ce stade, il n'y a plus d'hydrogène dans l'étoile et son vent est composé d'hélium, d'azote et de carbone qui viennent enrichir le milieu interstellaire. La quantité d'énergie libérée par l'étoile sous forme de vents est comparable à la quantité d'énergie cinétique libérée lors de l'explosion de supernova [Abbott, 1982b]. Après l'explosion de la supernova, le reste stellaire forme un object compact, qui peut être une étoile à neutrons ou un trou noir dans le cas des étoiles les plus massives. Les étoiles à neutrons en rotation rapide et fortement magnétisées, appelées pulsars, émettent un vent très rapide qui injecte lui aussi de l'énergie dans le milieu environnant.

La plupart des étoiles massives sont situées dans des systèmes binaires [Kobulnicky and Fryer, 2007]. La distance entre deux étoiles compagnons est comparable à celle qui sépare le Soleil des planètes du Système Solaire. C'est très proche! Cela veut dire que deux vents d'étoiles compagnons vont nécessairement interagir et former une *binaire à collision de vents*. La collision crée une structure choquée, comme le montre la figure 1.21 [Stevens et al., 1992]. Chaque vent a une composante qui se propage librement et une composante choquée. Les deux vents choqués sont séparés par une discontinuité. Quand ils sont identiques, la structure est symétrique. Lorsque l'un des vents domine fortement l'autre, l'ensemble de la structure est courbée autour de l'étoile au vent le plus faible. A cause du mouvement orbital des étoiles, la région choquée forme une structure spirale à plus grande échelle. La zone d'interaction est observée à différentes échelles de longueur, allant d'une distance inférieure à la séparation orbitale jusqu'à des spirales qui s'étendent sur plus d'une centaine de fois la séparation orbitale. Les simulations numériques ont montré que diverses instabilités peuvent se développer dans la zone choquée et modifier sa dynamique [Pittard, 2009]. Cette thèse vise à comprendre la structure des binaires à collision de vents, en tenant compte des instabilités et du mouvement orbital des étoiles.

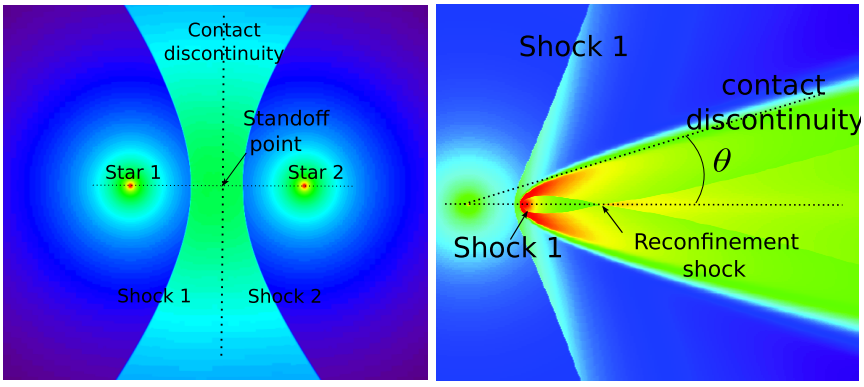

Figure 1.21: Cartes de densité qui montrent la géométrie d'une binaire à collision de vents avec des vents identiques (à gauche) et quand le vent de l'étoile de gauche domine fortement celui de droite (à droite). Dans ce cas, le vent de l'étoile de droite est totalement confiné.

Les progrès récents dans la réalisation d'observatoires γ, qu'ils soient spatiaux comme *Fermi*/LAT ou au sol comme H.E.S.S. ont mis au jour une nouvelle catégorie de binaires. Celles-ci émettent de la lumière très énergétique, des rayons γ, c'est pour cela qu'on les nomme *binaire gamma* (voir par exemple Abdo and Fermi Collaboration [2009], Aharonian and HESS collaboration [2006]). Moins d'une dizaine de ces systèmes ont été découverts. A l'exception de η Carinae, composée de

deux étoiles très massives, ces systèmes sont composés d'une étoile massive et d'un objet compact. Pour l'un d'entre eux, PSR B1259-63, on sait qu'il s'agit d'un pulsar qui possède un vent ténu mais très rapide, relativiste [Johnston et al., 1992]. D'autres systèmes avec une étoile massive et un pulsar qui émet en radio ont été découverts, mais leur émission γ est trop faible pour qu'on puisse l'observer (*Pulsar Catalogue : http://www.atnf.csiro.au/people/pulsar/psrcat/*). Dans ces systèmes,on peut s'attendre à une collision de vents entre le vent de l'étoile massive et le vent du pulsar, avec une structure similaire à celle qui se produit pour deux étoiles massives [Dubus, 2006]. Il existe des observations radio qui montrent une structure étendue ressemblant à une queue cométaire et évoluant avec la phase orbitale [Moldón et al., 2011a]. Ces observations sont interprétées par l'évolution d'une structure choquée, comme celle montrée sur l'image de gauche de la figure 1.21. Il existe d'autres systèmes montrant une émission similaire, ce qui suggère la présence d'une zone de collision de vents, même si cette hypothèse n'a pas encore été totalement prouvée.

L'objectif de cette thèse est de comprendre la structures des binaires γ et de fournir des diagnostics observationnels. L'évolution des ces systèmes est influencée par les instabilités présentes dans la zone choquée et est trop complexe à modéliser analytiquement. C'est pour cette raison que nous faisons des simulations numériques à l'aide du code hydrodynamique RAMSES [Teyssier, 2002]. Les binaires γ possèdent une structure choquée similaire aux collisions entre les vents d'étoiles massives. L'étude des binaires à collisions de vents est donc la première piste suivie dans cette thèse. Bien que des similitudes existent, la structure des binaires γ diffère probablement de celle des binaires stellaires en raison de la nature relativiste du vent de pulsar. Pour quantifier et comprendre ces différences, une part importante de cette thèse a été dédiée au développement d'une méthode numérique qui permet de modéliser des écoulements relativistes. L'écriture de ce code et son utilisation pour des simulations de binaires γ constitue le deuxième volet de cette thèse.

Dans le Chapitre 1, j'explique l'état actuel de connaissances sur les binaires à collision de vents, aussi bien celles composées d'étoiles massives que les binaires γ. Cette introduction est basée sur des observations (§1.2), des calculs théoriques (§1.3) et des simulations numériques (§1.4). Les observations et simulations numériques soulignent l'importance des instabilités et du mouvement orbital sur la structure de la région choquée. Ce sont des aspects clés étudiés au travers de simulations. Les simulation ont été réalisées à l'aide du code hydrodynamique RAMSES que je décrirai au Chapitre 2. Mes simulations à haute résolution modélisent différentes échelles spatiales, elles s'étendent des zones proches de la binaire (plus petite que 10 fois la séparation orbitale) au Chapitre 3 à quelques centaines de fois la séparation orbitale au Chapitre 4. Au début du Chapitre 5, je décrirai en détail les aspects techniques de l'extension de RAMSES à l'hydrodynamique relativiste et je montrerai les différents tests réalisés afin de valider ce nouveau code relativiste. Dans la deuxième partie du chapitre, je montrerai l'utilisation de ce code pour la simulation d'interaction entre un vent d'étoile massive et un vent de pulsar. Pour terminer, je donnerai un bref résumé de ce travail et proposerai des axes de recherche futurs.

Chapter 2

Simulating colliding wind binaries with RAMSES

Contents

2.1	Numerical simulations : why, how and where	49
2.1.1	Lagrangian approach	49
2.1.2	Eulerian approach	49
2.1.3	Supercomputers	50
2.2	Numerical simulations with RAMSES	51
2.2.1	RAMSES : a Godunov method	51
2.2.2	Adaptive Mesh Refinement (AMR)	58
2.3	Numerical setup for colliding wind binaries	60
2.3.1	Implementation of the winds	60
2.3.2	Orbital motion	61
2.3.3	Passive scalars	63
2.3.4	2D and 3D geometry	63
2.4	Overview of this chapter	63
2.5	Résumé en Français	63

After a brief introduction on different types of numerical methods used in astrophysical hydrodynamics (HD), this chapter focuses on the code RAMSES (§2.2) that I have used during my thesis. I will present its global structure and explain my particular setup to model colliding wind binaries. The extension to relativistic hydrodynamics (RHD) will be detailed in Chapter 5.

2.1 Numerical simulations : why, how and where

2.1.1 Lagrangian approach

A Lagrangian method consists in following a fluid particle as it moves through space and time. Imagine one wants to study the flow of a river, the Lagrangian approach would mean to go on a boat and follow the river. The Smoothed Particle Hydrodynamics (SPH) method [Lucy, 1977, Gingold and Monaghan, 1977] is such a method, where the fluid is divided into *particles* that are followed individually. The resolution of the simulation is determined by the number of particles. The physical quantities of the fluid (*e.g.* density) are a sort of average of the properties of the particles within a given distance called the smoothing length (see *e.g.* [Price, 2012] for a review). Particles beyond a certain distance do not influence each other, which reduces computational costs and makes this technique well adapted for large scale cosmological simulations. Fig 2.1.1 (left panel) shows a snapshot of the dark matter distribution in the current Universe, according to the *Millenium* simulation [Springel et al., 2005], one of the most important SPH simulations ever ran, involving more than 10 billion particles. The smoothing length can be adapted to the local density, which results in increased resolution in dense regions that are usually the regions of interest (but not always). The main drawback of this technique is its intrinsic diffusivity [Morris and Monaghan, 1997] that smears out discontinuities and shocks [Commerçon et al., 2008]. Lagrangian methods can also be used in combination with grid-based schemes [Pen, 1998, Springel, 2010]

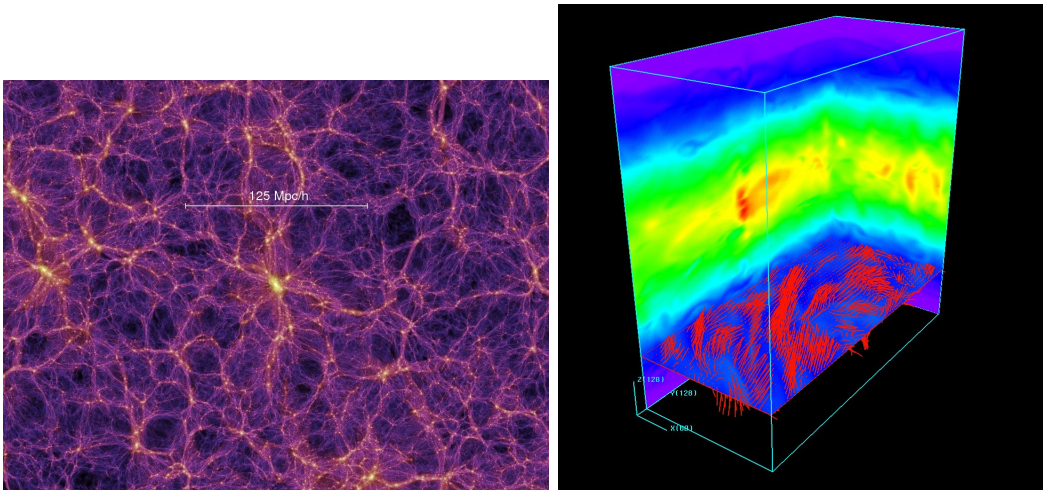

Figure 2.1: Left panel : The *Millenium* simulation, with SPH code GADGET [Springel et al., 2001] shows the dark matter density distribution of the Universe at present time. The length scales vary from 10 kpc to several Gpc. Right panel : density map of a local simulation of a vertically stratified accretion disk (shearing box) with finite difference code ZEUS. The arrows represent the magnetic field in the disk midplane. The turbulence is triggered by the magnetorotational instability [Balbus and Hawley, 1991].

2.1.2 Eulerian approach

Eulerian methods consist in studying a fluid in a specific location in space, as time passes [Leveque, 1998]. In this case, one would study the river while sitting at a given place on its banks. To study the flow, one needs to discretise space and to form a computational grid, which is superposed to the physical space. The number of cells composing the grid determines the resolution of the simulation. The easiest approach is to consider a static and uniform grid. State of the art numerical methods now allow dynamical grids with locally enhanced resolution, this is the Adaptive Mesh Refinement (AMR) technique that I will detail in section 2.2.2. Fig. 2.1.1 (right panel) shows a simulation of part of an accretion disk, obtained with the ZEUS code [Stone and Norman, 1992] that is probably the most widespread grid-based code in astrophysics.

One possibility is to evolve the equations at the grid points, this is the *finite difference* method. At first order, the spatial derivatives can then be replaced by differences between neighbouring cells. This method is straightforward to implement and can be easily extended to higher orders (*e.g* the 6^{th} order Pencil code [Brandenburg and Dobler, 2002]). This method requires to introduce artificial viscosity in order to avoid the development of oscillations at strong gradients.

In the *finite volume* approach, the Euler equations are considered in their conservative form and quantities are considered as averages over the cell volumes. The evolution of the variables is determined by their fluxes between neighbouring cells. RAMSES [Teyssier, 2002] follows this method, which is called a Godunov method. I will describe it in more detail in section §2.2.1. As the equations are solved in their conservative form, such codes conserve mass, momentum and energy in the system. They are able to properly capture discontinuities and shocks (within a few computational cells) that makes them very adapted to the study of supersonic flows.

These three different methods have different fields of application, different advantages and drawbacks. No numerical method is adapted to study any physical phenomenon. It is the role of the scientist to determine the best suited method for his needs. As this thesis deals with the collision between highly supersonic winds, modelling shocks and discontinuities is important. The finite volume method is most adapted. Different length scales are involved, going from the stellar radius to the large scale spiral structure. It is impossible to model all of them using a uniform resolution, that would be computationally too expensive. Therefore I use RAMSES with adaptive mesh refinement in my thesis. During the rest of this chapter, I will focus only on the Godunov method and RAMSES.

2.1.3 Supercomputers

Since the development of numerical simulations in the sixties, there has been an incredible increase in the available computer power. Until 1990, Cray-2 was the fastest computer in the world, with 8 processors, and less than 2 Gigaflop. Flops indicate the number of floating point operations per second and are a good indication of the power of a computer. Modern desktop computers usually reach more than 2 Gigaflop. They are sufficient for the development of numerical methods. However, scientific use of a code requires more computer power, with several processors working together, *in parallel*. Therefore scientists use supercomputers that can be local clusters (with a typical size of a few hundred processors) or national supercomputers (with more than 10 000 processors, dedicated to all fields of science). Local clusters are open to registered users while time on national computers is granted on a yearly basis, after a call for proposals. During my PhD I used the DAPHPC cluster at the Service d'Astrophysique, CEA for simulations using 8 or 16 processors. I have successively been granted 100 000, 300 000 and 400 000 hours on national supercomputers during the three years of my thesis. I have performed my simulations on Jade cluster from the Centre Informatique National de l'Enseignement Supérieur (CINES) that counts 240 Teraflop. Part of it is shown on Fig. 2.1.3. During my thesis

I have used a total computer time (or CPU time) equivalent to one computer running during 100 years. The 3D simulation of WR 104 (§4.3) on its own took 200 000 hours (CPU) time using 512 processors during 2 weeks. On Jade, the simulation time is limited to 24 hours per run. Long simulations have to be restarted several times. At each time, the jobs usually wait for 24 hours before starting. The 3D simulation of WR 104 thus took one month before being completed.

Figure 2.2: Jade supercomputer at CINES. This computer has 23040 processors which rank it at the 43^{rd} place in the worldwide top 500. (*http://www.top500.org/*).

2.2 Numerical simulations with RAMSES

2.2.1 RAMSES : a Godunov method

RAMSES [Teyssier, 2002] is a numerical method for astrophysical hydrodynamics and magnetohydrodynamics [Fromang et al., 2006]. Its main strength is the Adaptive Mesh Refinement (AMR) that allows to locally increase the resolution at a reasonable cost. It was initially designed to study the evolution of cosmological structures with a N-body solver. It includes many physical features such as self-gravity, cooling, radiative transfer, star formation, supernova feedback...It is written in Fortran 90, parallelised with the MPI library and perfectly suited for supercomputers. The HD version resolves the Euler equations (reminder of § 1.3.1.2):

$$\frac{\partial \rho}{\partial t} + \nabla \cdot (\rho \mathbf{v}) = 0 \tag{2.1}$$

$$\frac{\partial (\rho \mathbf{v})}{\partial t} + \nabla (\rho \mathbf{v}\mathbf{v}) + \nabla P = 0 \tag{2.2}$$

$$\frac{\partial E}{\partial t} + \nabla \cdot [\mathbf{v}(E+P)] = 0, \tag{2.3}$$

where ρ is the density, $\mathbf{v}$ the velocity, and P the pressure of the gas. The total energy density E is given by

$$E = \frac{1}{2}\rho v^2 + \frac{P}{(\gamma - 1)},$$

where γ is the adiabatic index. This equation implicitly assumes an equation of state for perfect gases

$$P = \rho k_B T / \mu m_H = (\gamma - 1)\rho\epsilon, \tag{2.4}$$

where k_b is the Boltzmann constant, T the temperature, μ the mean mass per particle, m_H the mass of the hydrogen atom and ϵ is the internal energy density. These equations express the conservation of mass, momentum and energy and can be rewritten in a compact form

$$\frac{\partial \mathbf{U}}{\partial t} + \frac{\partial \mathbf{F}}{\partial x} + \frac{\partial \mathbf{G}}{\partial y} + \frac{\partial \mathbf{H}}{\partial z} = 0, \tag{2.5}$$

where $\mathbf{U}$ is the vector of conserved variables and $\mathbf{F}, \mathbf{G}, \mathbf{H}$ its fluxes along each direction. One has

$$\mathbf{U} = \begin{pmatrix} \rho \\ \rho v_x \\ \rho v_y \\ \rho v_z \\ E \end{pmatrix} \quad \mathbf{F} = \begin{pmatrix} \rho v_x \\ \rho v_x^2 + P \\ \rho v_x v_y \\ \rho v_x v_z \\ v_x(E+P) \end{pmatrix} \quad \mathbf{G} = \begin{pmatrix} \rho v_y \\ \rho v_x v_y \\ \rho v_y^2 + P \\ \rho v_y v_z \\ v_y(E+P) \end{pmatrix} \quad \mathbf{H} = \begin{pmatrix} \rho v_z \\ \rho v_x v_z \\ \rho v_y v_z \\ \rho v_z^2 + P \\ v_z(E+P) \end{pmatrix} \tag{2.6}$$

For the sake of simplicity I will describe the numerical method to solve Eq. 2.6 considering only one dimensional flows. The computational domain is divided into cells of volume Δx, I note x_i their centre, $x_{i-1/2}$ their left boundary and $x_{i+1/2}$ their right boundary. Similarly, time is divided in timesteps of size Δt, going from t^n to t^{n+1}. Eq. 2.5 can be integrated in space and time over the control volume V=$[x_{i-1/2}, x_{i+1/2}] \times [t^n, t^{n+1}]$

$$\int_{x_{i-1/2}}^{x_{i+1/2}} \mathbf{U}(x, t^{n+1})dx - \int_{x_{i-1/2}}^{x_{i+1/2}} \mathbf{U}(x, t^n)dx + \int_{t^n}^{t^{n+1}} \mathbf{F}(x_{i+1/2}, t)dt - \int_{t^n}^{t^{n+1}} \mathbf{F}(x_{i-1/2}, t)dt = 0. \tag{2.7}$$

The Godunov method (Godunov [1959], see Toro [2009] for a complete handbook) is based on the above expression of the Euler equations. It is an exact expression, and could theoretically give $\mathbf{U}(x, t^{n+1})$ to machine precision. The variables are averaged over the whole volume of the cell Δx

$$\mathbf{U}_i^n = \frac{1}{\Delta x} \int_{x_i - 1/2}^{x_i + 1/2} \mathbf{U}(x, t^n)dx, \tag{2.8}$$

and the fluxes, which are defined at cell interfaces, are expressed as

$$\mathbf{F}_{i\pm1/2}^{n+1/2} = \frac{1}{\Delta t} \int_{t^n}^{t^{n+1}} \mathbf{F}(x_{i\pm1/2}, t^{n+1/2})dt. \tag{2.9}$$

Replacing Eq. 2.7 with the above expressions gives

$$\frac{\mathbf{U}_i^{n+1} - \mathbf{U}_i^n}{\Delta t} + \frac{\mathbf{F}_{i+1/2}^{n+1/2} - \mathbf{F}_{i-1/2}^{n+1/2}}{\Delta x} = 0. \tag{2.10}$$

This expression can be used to numerically compute $\mathbf{U}_i^{n+1}$, provided one knows the fluxes between neighbouring cells. They are determined by the resolution of a Riemann problem (next section) at the cell interfaces.

2.2.1.1 The Riemann problem for the intercell fluxes

The fluxes between the cells are determined by solving local Riemann problems at the cell boundaries. The solution of the Riemann problem describes the evolution of two constant states initially separated by an interface. In this case, the interface is the cell boundary and the left and right state correspond to the values of the hydrodynamical variables at the cell boundaries.

One thus needs to know the values of the variables at the cell boundaries. Fig. 2.3 shows different approximations of the physical solution. At first order, one can consider variables are constant in the whole cell. Higher orders assume linear (second order) or parabolic (third order) variation of the variables (see Fig 2.3). A second order scheme is implemented in RAMSES and will be detailed in §2.2.1.2. In the following, I will assume a constant state in the whole cell.

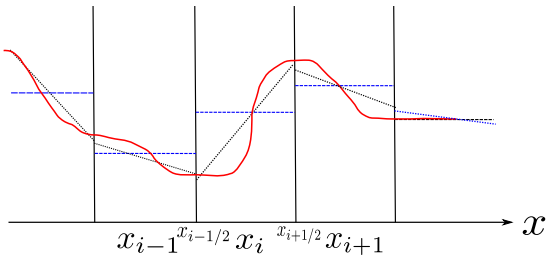

Figure 2.3: Approximation of $\mathbf{U}$ at different orders. The physical solution is given by the solid red line, the first order approximation by the dashed blue lines, the second order approximation is given by the dotted black line.

In this section I describe the general method to solve a Riemann problem for the Euler equations. I assume the interface is at $x = 0.5$ and call the left state $\mathbf{U}_L$ and the right state $\mathbf{U}_R$. We have the initial conditions

$$\mathbf{U}(x,0) = \begin{cases} \mathbf{U}_L & \text{if } x < 0.5 \\ \mathbf{U}_R & \text{if } x > 0.5 \end{cases} \tag{2.11}$$

In the most general case, such a system evolves into four different states $\mathbf{U}_L$, $\mathbf{U}_L^*$, $\mathbf{U}_R^*$, $\mathbf{U}_R$ separated by three waves of speeds S_L, S^*, S_R. An example is given on fig. 2.4. The central wave is a contact discontinuity while the two others can be shock waves or rarefactions. The solution to the Riemann problem is given by $\mathbf{U}(x,t)$. As it is a similarity solution, one usually computes $\mathbf{U}(x/t)$. For convenience reason, one can introduce $\chi = (x-0.5)/t$. The values at the cell boundaries are given by $\mathbf{U}(\chi = 0)$, according to the flow, it corresponds to one of the four different states. For example, in the middle panel of Fig. 2.4, one has $\mathbf{U} = \mathbf{U}_L^*$ at the location of the initial interface.

At the shock, one can use the Rankine-Hugoniot jump conditions to determine the values of the variables in both "star" regions and then determine the Godunov flux at the interface between the cells using

$$\mathbf{F}_{i+1/2} = \mathbf{F}(\mathbf{U}_{i+1/2}(0)), \tag{2.12}$$

where $\mathbf{U}_{i+1/2}(x/t = 0)$ is the exact similarity solution of the Riemann problem.

The solution to the Riemann problem cannot be given in a closed analytic form but one can find solutions numerically to any required degree of accuracy, which results in an exact Riemann solver. However, this involves time consuming algorithms and approximate solutions have been developed. Some of them compute the intermediate states $\mathbf{U}_{L,R}^*$ and then determine the flux across the central wave using Eq. 2.12. Others, such as the HLL and HLLC solvers I will describe next, directly compute the flux across the central wave without computing the intermediate state.

The example of the HLL Riemann solver

The HLL [Harten and Van Leer, 1983] solver is one of the most easy solvers, as it does not take into account the contact discontinuity and considers only one constant intermediate state.

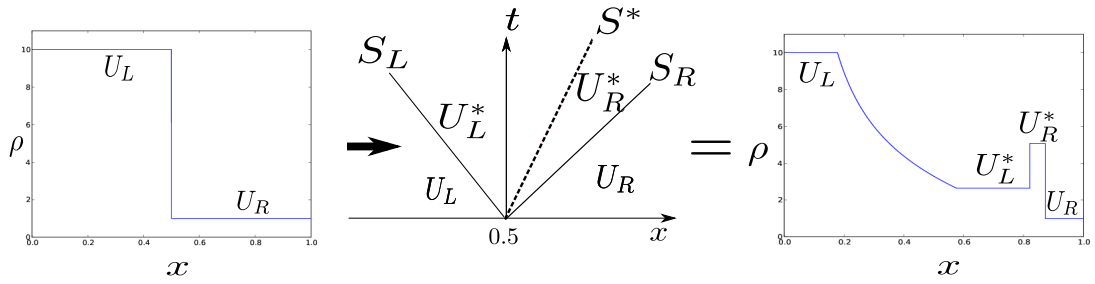

Figure 2.4: The Riemann problem: the left panel shows the initial states $\mathbf{U}_L$, $\mathbf{U}_R$, which decay into three waves (middle panel) separating four different states. The right panel shows the final outcome with the two additional intermediate states $\mathbf{U}_L^*$, $\mathbf{U}_R^*$. The discontinuities are (from left to right) a rarefaction, a contact discontinuity and a shock.

One thus has

$$\mathbf{U}(\chi) = \begin{cases} \mathbf{U}_L & \text{if} \quad \chi \leqslant S_L \\ \mathbf{U}^* & \text{if} \quad S_L \leqslant \chi \leqslant S_R \\ \mathbf{U}_R & \text{if} \quad S_R \leqslant \chi \end{cases} \tag{2.13}$$

The pattern of the solution is given on the left panel of Fig. 2.5. Assuming that one knows the wavespeeds S_L, S_R of the fastest propagating signals in both directions, one can determine the Godunov flux by directly using the integral of the conservation laws (Eq. 2.10) without computing the intermediate states.

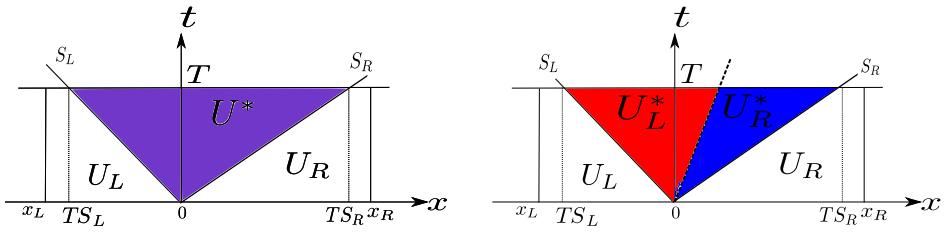

Figure 2.5: Control volume for the determination of the Godunov flux in the (x,t) plane. S_L and S_R are the fastest waves arising from the solution of the Riemann problem. Left panel: HLL approximation with only one intermediate state (purple zone) right panel: HLLC wave pattern with two distinct intermediate states (red and blue zone). Image inspired by Toro [2009].

In order to find the Godunov flux one studies the control volume $[x_L, x_R] \times [0, T]$ with $x_L < TS_L$ and $x_R > TS_R$ (see left panel of Fig. 2.5). Eq. 2.7 then gives

$$\int_{x_L}^{x_R} \mathbf{U}(x,T)dx - \int_{x_L}^{x_R} \mathbf{U}(x,0)dx + \int_0^T \mathbf{F}(x_R,t)dt - \int_0^T \mathbf{F}(x_L,t)dt = 0. \tag{2.14}$$

Assuming $x_L = TS_L$ and $x_R = TS_R$, this gives

$$\mathbf{U}^* = \mathbf{U}_{HLL}(x_R - x_L) - (\mathbf{U}_R x_R - \mathbf{U}_L x_L) - \mathbf{F}_L T + \mathbf{F}_R T = 0. \tag{2.15}$$

Rearranging this gives the integral average of the intermediate state

$$\mathbf{U}_{HLL} = \frac{\mathbf{U}_R S_R - \mathbf{U}_L S_L + \mathbf{F}_L - \mathbf{F}_R}{S_R - S_L}. \tag{2.16}$$

If one now studies a control volume $[x_L, 0] \times [0, T]$, the integral form of the conservation law gives

$$\int_{TS_L}^{0} \mathbf{U}(x,T)dx - \int_{TS_L}^{0} \mathbf{U}(x,0)dx + \int_{0}^{T} \mathbf{F}(0,t)dt - \int_{0}^{T} \mathbf{F}(x_L,t)dt = 0, \tag{2.17}$$

that gives

$$\mathbf{U}_{HLL}x_L - \mathbf{U}_L x_L - \mathbf{F}_L T + \mathbf{F}_{HLL}T = 0. \tag{2.18}$$

Combining this equation with Eq. 2.16 one gets the HLL flux

$$\mathbf{F}_{HLL} = \frac{S_R\mathbf{F}_L - S_L\mathbf{F}_R + S_R S_L(\mathbf{U}_R - \mathbf{U}_L)}{S_R - S_L} \tag{2.19}$$

Where $\mathbf{F}_L$ and $\mathbf{F}_R$ are computed using Eq. 2.6. The corresponding Godunov flux at the interface between cells is then given by

$$\mathbf{F} = \begin{cases} \mathbf{F}_L & \text{if} \quad \chi \leqslant S_L \\ \mathbf{F}^* & \text{if} \quad S_L \leqslant \chi \leqslant S_R \\ \mathbf{F}_R & \text{if} \quad S_R \leqslant \chi \end{cases}$$

Finding the wavespeeds

In the HLL and HLLC solvers, the fastest propagating perturbations have wavespeeds S_L, S_R are approximated by

$$S_L = min(v_L, v_R) - max(c_{sL}, c_{sR}) \tag{2.20}$$
$$S_R = max(v_L, v_R) + max(c_{sL}, c_{sR}), \tag{2.21}$$

where $S_L < 0$ and c_s is the sound speed of the flow.

Restoring the contact wave : the HLLC solver

The HLLC Riemann solver [Toro et al., 1994] is an extension of the HLL solver including proper treatment of the contact discontinuity (that is why it is called hllC). It uses the full wave pattern in the Riemann fan by separating the intermediate state into $\mathbf{U}_L^*$ and $\mathbf{U}_R^*$ separated by a wave whose velocity S^* is initially unknown. The structure is shown on the right panel of Fig. 2.5. One has

$$\mathbf{U}(x,t) = \begin{cases} \mathbf{U}_L & \text{if} \quad S_L \geqslant \chi \\ \mathbf{U}_L^* & \text{if} \quad S_L \leqslant \chi \leqslant S^* \\ \mathbf{U}_R^* & \text{if} \quad S^* \leqslant \chi \leqslant S_R \\ \mathbf{U}_R & \text{if} \quad S_R \leqslant \chi \end{cases} \text{and} \quad \mathbf{F} = \begin{cases} \mathbf{F}_L & \text{if} \quad S_L \geqslant \chi \\ \mathbf{F}_L^* & \text{if} \quad S_L \leqslant \chi \leqslant S^* \\ \mathbf{F}_R^* & \text{if} \quad S^* \leqslant \chi \leqslant S_R \\ \mathbf{F}_R & \text{if} \quad S_R \leqslant \chi \end{cases} \tag{2.22}$$

As one knows $\mathbf{U}_L$ and $\mathbf{U}_R$, one and can determine the fluxes across the three waves using the Rankine-Hugoniot jump conditions

$$\left.\begin{aligned} \mathbf{F}_L^* &= \mathbf{F}_L + S_L(\mathbf{U}_L^* - \mathbf{U}_L) \\ \mathbf{F}_R^* &= \mathbf{F}_L^* + S^*(\mathbf{U}_R^* - \mathbf{U}_L^*) \\ \mathbf{F}_R^* &= \mathbf{F}_R + S_R(\mathbf{U}_R^* - \mathbf{U}_R) \end{aligned}\right\} \Rightarrow S_{L,R}(\mathbf{U}_{L,R}^* - \mathbf{U}_{L,R}) = \mathbf{F}_{L,R}^* - \mathbf{F}_{L,R} \tag{2.23}$$

that gives 10 equations for 21 unknows $\mathbf{U}_L^*, \mathbf{U}_R^*, \mathbf{F}_L^*, \mathbf{F}_R^*$ (5 components each) and S^*. As pressure and the normal velocity are constant across a contact discontinuity there are three additional equations, but still more unknowns than equations. The resolution can only be done assuming the fluxes $\mathbf{F}_{L,R}^*$ follow the structure given by Eq. 2.6

$$\mathbf{F}(\mathbf{U}) = v_x\mathbf{U} + P\mathbf{D} \qquad \text{where} \qquad \mathbf{D} = [0, 1, 0, 0, v_x]^T, \tag{2.24}$$

that yields

$$P_{L,R}^* = P_{L,R} + \rho_{L,R}(S_{L,R} - v_{x,L,R})(S^* - v_{L,R}), \tag{2.25}$$

using $P_L^* = P_R^*$, after some algebraic manipulations one gets

$$S_* = \frac{P_R - P_L + \rho_L v_{x,L}(S_L - v_{x,L}) - \rho_R v_{x,R}(S_L - v_{x,R})}{\rho_L(S_L - v_{x,L}) - \rho_R(S_R - v_{x,R})}, \tag{2.26}$$

that gives the velocity of the contact wave. Using Eq. 2.23 and the definition of pressure in the intermediate region (Eq. 2.25) one finds the intermediate state $\mathbf{U}_L^*$

$$\mathbf{U}_L^* = \frac{1}{T(S^* - S_L)}\int_{TS_L}^{TS^*} \mathbf{U}(x,T)dx = \left(\frac{S_L - v_{x,L}}{S_L - S^*}\right)\begin{pmatrix} \rho_L \\ \rho_L S^* \\ \rho_L v_{y,L} \\ \rho_L v_{z,L} \\ \frac{E_L}{\rho_L} + (S_* - v_{x,L})\left(S^* + \frac{P_L}{\rho_L(S_L - v_{x,L})}\right) \end{pmatrix}$$

a similar equation can be written for $\mathbf{U}_R$.

Eq. 2.23 then gives

$$\mathbf{F}_{L,R}^* = \frac{S^*(S_{L,R}\mathbf{U}_{L,R} - \mathbf{F}_{L,R}) + S_{L,R}(P_{L,R} + \rho_{L,R}(S_{L,R} - v_{x,L,R})(S^* - v_{x,L,R}))\mathbf{D}^*}{S_{L,R} - S^*}. \tag{2.27}$$

According to the position in the Riemann fan (Eq. 2.22) one can then determine the intercell flux.

There exist many other Riemann solvers [Toro, 2009] based on different determinations of the wavespeeds and of the intermediate states and fluxes. The proper choice of the Riemann solver is an important aspect of a simulation as it is used at every timestep, at every cell boundary. During my thesis I used an exact Riemann solver for some 2D simulations (*e.g.* §3.2 or §4.1), but it was computationally too expensive for important 3D simulations. I used the HLLC solver for the 3D simulation of WR 104 (§4.3). In some simulations, where I did not want instabilities to impact the structure of the colliding wind binary (§3.1, but also in relativistic simulations in §5.4.2), I used the HLL Riemann solver that introduces more numerical diffusivity. Although in my case it was chosen on purpose, diffusive Riemann solvers should be used with caution.

The numerical scheme I have described so far is a first order numerical method that gives inaccurate results. In the next section I describe how this can be greatly improved when using a second order method.

2.2.1.2 Second order MUSCL scheme

The first order Godunov method is very diffusive and a better approximation is to assume variables vary linearly within a cell, which gives second order accuracy in space. One possibility is to use a Monotone Upstream-centred Scheme for Conservation Laws (MUSCL) scheme [Van Leer, 1977] that performs the update of the conservative variables in two steps, the *predictor* and *corrector* steps. The predictor step consists in determining the variables at the cell interfaces,

half a timestep ahead of the current step, at $t^{n+1/2}$. The corrector step then consists in solving the associated Riemann problem.

In RAMSES, these steps are performed with the primitive variables

$$\mathbf{q} = \begin{pmatrix} \rho \\ v \\ P \end{pmatrix} \tag{2.28}$$

rather than the usual conservative variables. The primitive variables are also used to compute the sound speed and their physical interpretation is simpler than the conserved variables. For each interface we thus need $\mathbf{q}_L{=}\mathbf{q}^{t+1/2}_{i-1/2,R}$ and $\mathbf{q}_R = \mathbf{q}^{t+1/2}_{i+1/2,L}$, which implies a spatial reconstruction and a prediction in time. Using a Taylor expansion we have

$$\begin{cases} \mathbf{q}^{n+1/2}_{i-1/2,R} = \mathbf{q}^n_i + \Delta\mathbf{q}^t_i + \dfrac{\partial \mathbf{q}_i}{\partial t}\dfrac{\Delta t}{2} \\ \mathbf{q}^{n+1/2}_{i+1/2,L} = \mathbf{q}^n_{i+1} - \Delta\mathbf{q}^t_{i+1} + \dfrac{\partial \mathbf{q}_{i+1}}{\partial t}\dfrac{\Delta t}{2} \end{cases} \tag{2.29}$$

The $\Delta\mathbf{q}_i$ are the slopes of the variables in the cell. Using a centred finite difference approximation one has

$$\frac{\partial \mathbf{q}}{\partial \mathbf{x}} \simeq \frac{\Delta \mathbf{q}}{\Delta x} = \frac{\mathbf{q}_{i+1} - \mathbf{q}_{i-1}}{2\Delta x}, \tag{2.30}$$

that may lead to new local extrema in the flow that create oscillations. To avoid this, one uses a so-called Total Variation Diminishing scheme (TVD, [Toro, 2009]) that checks whether the slopes $\Delta\mathbf{q}$ satisfy the monotonicity condition and switch back to a first order reconstruction when necessary. The so-called source terms are given by

$$\frac{\partial \mathbf{q}_i}{\partial t}\frac{\Delta t}{2} \quad \text{and} \quad \frac{\partial \mathbf{q}_{i+1}}{\partial t}\frac{\Delta t}{2}. \tag{2.31}$$

We thus need to express $\partial\mathbf{q}$ that is determined by

$$\frac{\partial \mathbf{q}}{\partial t} + \mathbf{A}\frac{\partial \mathbf{q}}{\partial x} = 0, \tag{2.32}$$

where $\mathbf{A}(\mathbf{q}) = \frac{\partial \mathbf{F}}{\partial \mathbf{q}}$ is the Jacobian matrix of the system. Eq. 2.32 gives

$$\begin{pmatrix} \frac{\partial \rho}{\partial t} \\ \frac{\partial v_x}{\partial t} \\ \frac{\partial P}{\partial t} \end{pmatrix} = \begin{pmatrix} v_x & \rho & 0 \\ 0 & v_x & 1/\rho \\ 0 & \gamma P & v_x \end{pmatrix} \begin{pmatrix} \frac{\partial \rho}{\partial x} \\ \frac{\partial v_x}{\partial x} \\ \frac{\partial P}{\partial x} \end{pmatrix} \tag{2.33}$$

The source terms thus depend on the gradients of the different variables, this will be a crucial aspect in RHD (§5.1.4). One can then use the Riemann solver to determine the fluxes

$$\mathbf{F}[\mathcal{RP}(\mathbf{q}_L, \mathbf{q}_R)]. \tag{2.34}$$

In multidimensional simulations, the fluxes are determined separately along each direction. After that, the variables are updated using simultaneously the fluxes along all directions. This is called an *unsplit* scheme.

2.2.1.3 Determination of the timestep

The timestep is constrained by the fact that no wave or fluid element is allowed to move over more than one cell in a timestep [Toro, 2009]. This means that fast flows are evolved with smaller

timesteps than slow flows. One can define the Courant number C_{CFL} [Courant et al., 1928] such that:

$$\Delta t = C_{CFL} \frac{\Delta x}{S^n_{max}}, \tag{2.35}$$

where S^n_{max} is the maximum wavespeed of the whole domain at a given timestep n. In classical HD S^n_{max} is given by $max(c_s + abs(v))$. In a MUSCL scheme, C_{CFL} may theoretically reach 1 but it is usually set to 0.8.

2.2.2 Adaptive Mesh Refinement (AMR)

Astrophysical problems often display an important range of length scales and the regions of interest might cover only small parts of the computational domain. The idea of AMR is to increase the resolution only in some parts of the simulation, according to some user defined criteria. In my case, high resolution is required at the shocks and at the contact discontinuity between the winds, as this is the place where the instabilities arise. In the simulations in this thesis, refinement is thus based on density gradients, as is shown on Fig. 2.6. Refinement can also be limited to certain region, on geometrical criteria. In my 3D simulations I prevent refinement far from the orbital plane to reduce computational costs.

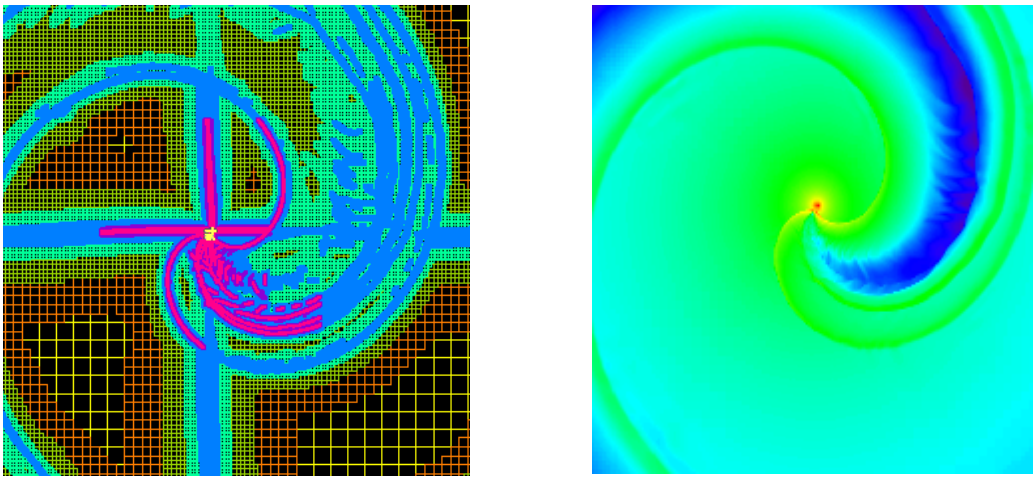

Figure 2.6: 2D simulation of WR104. Left panel : AMR map, the coarse level is $l_{min} = 7$ (yellow), the highest resolution is $l_{max} = 16$ (pale yellow). Right panel : the corresponding density map shows that refinement happens at the shocks. Very high resolution is limited to a small region close to the binary.

The first attempt to create an adaptive mesh was performed by Berger and collaborators (Berger and Oliger [1984], Berger and Colella [1989]) who developed the *patch-based AMR* technique. The zones of increased resolution were rectangular patches on different positions. Alternatively to this *patch based* method, a more adjustive technique was developed by Kravtsov et al. [1997] where parent cells are refined into children cells in a recursive *tree based* structure. RAMSES follows this method, neighbouring cells are gathered together to form octs that relate within a tree structure. As is shown on Fig. 2.7 an oct at level l is related to its father cell and the $2 \times ndim$ ($ndim$ is the number of dimensions) neighbouring cells at level $l-1$ but also to the 2^{ndim} child octs at level $l+1$. A refined cell is called a *split* cell while a cell that is not refined is called a *leaf* cell. The lowest level of uniform resolution is called the *coarse* level. The equivalent resolution of a simulation is given by 2^{lmax}.

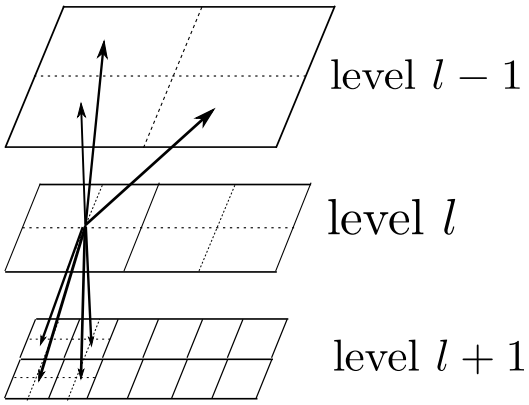

Figure 2.7: 2D AMR structure. Octs at level l are related to the father cells at $l-1$ and children octs at $l+1$. Image inspired from a lecture by R. Teyssier.

Building a new refinement map is computationally expensive so it is done only every n timesteps, where n is a user defined criterion. It is usually set to 10. It should not be too high, otherwise one might not capture interesting features in a quickly evolving flow. To build a new refinement map, the code goes recursively through all the refinement levels, starting from the highest level, and marks cells for refinement. A cell is marked for refinement if it satisfies the user defined criterion or is composed of (at least) one child cell that is refined or marked for refinement. When a cell is marked for refinement, the other cells from the oct also are. Following this method, cells are automatically derefined if they do not follow the user defined criteria.

Hydrodynamic calculations are only performed on leaf cells. The coarse levels are recursively updated by averaging down the variables from higher levels. At the boundaries between level l and $l+1$, a buffer zone is created where variables are interpolated from level l to $l+1$ in order to compute the Godunov fluxes between cells of equivalent levels.

Using the AMR frame thus involves to know

- how to interpolate variables from a level l to $l+1$
- how to average down variables from level l to $l-1$

The averaging step consists of computing the mean value of the variables over the cells forming the child oct to determine their value in the father cell. The interpolation step reconstructs variables from level l to $l+1$. It can be done at first order or at second order, using a TVD scheme for the linear reconstruction (a TVD scheme avoids the creation of spurious oscillations, see §2.2.1.2). Usually both the averaging step and interpolation are done with the conserved variables, ρ, $\rho\mathbf{v}$, E. It can be replaced by a reconstruction of ρ, $\rho\mathbf{v}$, P when the energy of the flow is strongly dominated by kinetic energy. This may lead to inaccurate estimates of the pressure. When using this technique, the numerical scheme is not strictly conservative anymore.

When using AMR, the structure of the algorithm is (much!) more complex than for a uniform grid. This also holds for the structure of the data in the outputs. The resulting reduction in computing time is effective only if the high resolution is limited to small zones. For the 2D simulation in §4.1.2, that has $l_{min} = 6$ and allows 7 levels of refinement, I have used 704 hours CPU time while I have estimated that a simulation on a uniform grid with the same resolution

would last roughly 4000 hours, about six times longer. AMR enables a substantial gain in computer time. Still, the gain is limited by the filling factor of the cells at different levels. In this simulation, the filling factor (with respect to a uniform grid) is of 60% at $l = 8$, 15% at $l = 10$ and about 1% at $l = 13$. More than half of the cells in the simulation are cells at $l = 13$.

The AMR drastically decreases the number of computational cells (with respect to a undiform grid) and the amount of memory necessary for a simulation. Theoretically, one can use $l_{min} = 0$ and any value for l_{max}. However, very low levels of refinement may not capture the flow well enough to trigger refinement and may lead to important errors, as I will show in test simulations of relativistic flows (§5.2.1). On the other hand, very high levels of refinement ($l_{max} \geqslant 17$) induce a very complex structure of data. In RAMSES, each cell is ordered with an integer that does not follow its geometrical position but a more elaborate scheme meant to optimise parallel computing. Very high levels of refinement need an accurate (and thus time-consuming) scheme for domain decomposition. The highest value I have used for refinement is $l_{max} = 19$ for test simulations of the impact of orbital motion (2D). This gives an equivalent resolution of about 500 000 cells in each direction. I have had trouble with the AMR map in the 3D simulation of WR104 (§4.3) when progressively adding levels of refinement when restarting the simulation. It led to failures in the communications between processors when computing the new AMR map. The only way we found to solve it was changing the MPI library that deal with the paralelism.

2.3 Numerical setup for colliding wind binaries

In the following paragraphs, I describe the numerical setup I developed within RAMSES to model colliding wind binaries.

2.3.1 Implementation of the winds

My method to implement the winds is similar to the one developed by Lemaster et al. [2007] and described in the appendix of their paper. Around each star, I create a wind by imposing a given density, pressure and velocity profile in a spherical zone called mask. The masks are reset to their initial values at all timesteps to create steady winds. This involves modifying hydrodynamical variables "by hand" after every hydrodynamical update.

The velocity is purely radial and set to the terminal velocity $v = v_\infty$ of the wind in the whole mask. Setting the velocity to v_∞ supposes the winds have reached their terminal velocity at the interaction zone. This might not be applicable for very close binaries or if the momentum fluxes of the winds are very different because the shocks are then very close to one of the stars. The density profile $\rho(r)$ is determined by mass conservation through the mask. The pressure is determined using $P\rho^{-\gamma} = K$ with K constant in each region. Both the pressure and density are floored close to the centre of the masks. Time is expressed in years and mass loss rates are expressed in $10^{-8} M_\odot$ yr^{-1}. All distances are scaled to the binary separation a, usually taken to be constant and set to 1 AU but the results of a simulation ($\tilde{\rho}$, $\tilde{v}$ $\tilde{P}$) can easily be rescaled to real systems with a different separation using

$$\begin{cases} \rho = \dfrac{\tilde{\rho}}{a^2} \quad \text{(2D)} \quad \dfrac{\tilde{\rho}}{a^3} \quad \text{(3D)} \\ v = \tilde{v} a \\ P = \tilde{P} \quad \text{(2D)} \quad \dfrac{\tilde{P}}{a} \quad \text{(3D)} \end{cases} \tag{2.36}$$

For each simulation, the input parameters are the mass loss rate, terminal velocity and Mach number $\mathcal{M}$ of each wind. The Mach number is set by its value at $r = a$, in the case of a single star, when the wind expands freely. By default, I set $\mathcal{M}(a)$ to 30. As I will show in §3.1.2.3,

the exact value does not influence the outcome, as long as the the Mach number is large enough ($\geqslant 20$). Using this setup implies that, at the collision, which occurs at a distance smaller than the binary separation, the Mach number is smaller than 30. If the collision occurs very close to one of the stars, it is possible that the Mach number in the weaker wind has not reached a high value and that pressure may play a role.

The surrounding medium is filled with a density $\rho_{amb} = 10^{-4}\rho(a)$ and pressure $P_{amb} = 0.1P(a)$. These values are arbitrary values (they actually correspond to the density and temperature of an HII region), chosen to be low enough so that the winds can easily expand and push the initial medium out of the simulation box. We cannot set them to very small values for numerical reasons. Simulations with different ρ_{amb} and P_{amb} show the same final result, to round-off precision. Fig. 2.3.1 shows the density, pressure and velocity profiles for a single star in a 2D simulation with a uniform resolution of $n_x = 256$. The dashed lines represent analytic profiles, the crosses show the results of the simulation. They are in very good agreement, which validates our numerical method. The dotted vertical line shows the edge of the mask.

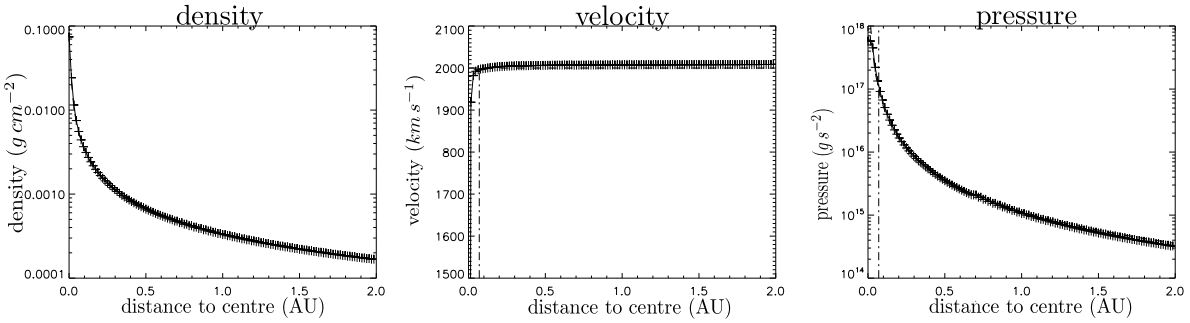

Figure 2.8: Density, pressure and velocity profiles for a single star along the x axis. There is a good agreement between the simulation (crosses) and the analytic solution (solid line). The centre of the star is located at $x = 0$, the edge of the mask is given by the dotted vertical line.

When the wind from one star strongly dominates the other one, the shocks form very close to the star with the weakest wind. In this case, the mask of the star has to be as small as the stellar radius so that the shocks can form properly [Pittard, 1998]. However I determined the masks need to have a minimum length of 8 computational cells per direction to obtain spherical symmetry of the winds. I thus fix the size of the masks to 8 computational cells in each direction for the highest value of refinement. I performed tests with a single star for different sizes of the mask ranging from $0.03a$ to $1.5a$. The tests were performed for $n_x = 128$ and 4 levels of refinement. The resulting density profiles all agree with the analytic solution with less than 1 % offset.

At each boundary of the grid, there are three additional cells, called ghost cells, where one determines the boundary conditions of the simulation. In my simulations of colliding wind, I use zero-gradient conditions, meaning matter can just flow out of the computational domain. This gives, on the left side of the box:

$$\begin{cases} \mathbf{U}(1,j,k) = \mathbf{U}(4,j,k) \\ \mathbf{U}(2,j,k) = \mathbf{U}(4,j,k) \\ \mathbf{U}(3,j,k) = \mathbf{U}(4,j,k) \end{cases} \tag{2.37}$$

On the right side we have

$$\begin{cases} \mathbf{U}(n_x-2,j,k) = \mathbf{U}(n_x-3,j,k) \\ \mathbf{U}(n_x-1,j,k) = \mathbf{U}(n_x-3,j,k) \\ \mathbf{U}(n_x,j,k) = \mathbf{U}(n_x-3,j,k) \end{cases} \tag{2.38}$$

The boundaries along the othere directions are found in a similar way.

2.3.2 Orbital motion

The stars orbit around their common centre of mass, following Newton's law of motion. The winds are isotropic in the frame of the simulation, I do not directly add the orbital velocity to the speed of the winds. However, as in the simumated systems, the speed of the winds is much higher than the orbital velocity, the winds can also be considered as isotropic in the frame corotating with the corresponding star. The easiest and fastest numerical method to determine the positions of the stars is the Euler method where positions are updated between t^n and t^{n+1} using

$$\begin{cases} v_x^{n+1} = & v_x^n + a_x^n \Delta t \\ x^{n+1} = & x^n + v_x^n \Delta t, \end{cases} \tag{2.39}$$

where v_x is the velocity and a_x the acceleration along the x direction. The same equations can be written along y and z. Similar equations hold for both stars. This method is inaccurate and fails to reproduce the proper orbit when systems are highly eccentric. Therefore we prefer to use the leapfrog method that is second order accurate at a reasonable computational cost. In this method, the velocities are computed at midpoints of the timesteps

$$\begin{cases} v_x^{n+1/2} = & v_x^{n-1/2} + a_x^{n-1} \Delta t \\ x^{n+1} = & x^n + v_x^{n+1/2} \Delta t \end{cases} \tag{2.40}$$

The positions of the stars are initialized with respect to the centre of mass $(x_{cen}, y_{cen}, z_{cen})$ using

$$\begin{cases} x_{ini1} = & x_{cen} + \dfrac{M_2}{M_1 + M_2} a(1-e)\cos\theta\cos i \\ y_{ini1} = & y_{cen} + \dfrac{M_2}{M_1 + M_2} a(1-e)\sin\theta\cos i \\ z_{ini1} = & z_{cen} + \dfrac{M_2}{M_1 + M_2} a(1-e)\sin\theta\sin i \end{cases} \tag{2.41}$$

$$\begin{cases} x_{ini2} = & x_{ini1} - a(1-e)\cos i \\ y_{ini2} = & y_{ini1} - a(1-e)\cos i \\ z_{ini2} = & z_{ini1} - a(1-e)\sin i \end{cases} \tag{2.42}$$

where the subscripts 1 and 2 stand for both stars, M is their mass, e is the eccentricity of the orbit, i the inclination of the system. By default, I use $\theta = 0$ at the beginning of the simulation. The initial velocity can be computed using

$$\mathbf{v}_{1,2} = \frac{d\mathbf{r}_{1,2}}{dt} = \frac{d\mathbf{r}_{1,2}}{d\theta}\frac{d\theta}{dt}, \tag{2.43}$$

where $\mathbf{r}_{1,2}$ is the distance from each star to the centre of mass and $d\theta/dt = (a(1-e^2)G(M_1 + M_2))^{1/2}/(r_1 + r_2)^2$. During my thesis, I have only studied circular orbits without inclinations $(i = 0°, e = 0)$, which simplifies the above equations. This general method that has been implemented to model the *gamma*-ray binary PSR B1259-63, where the pulsar has an eccentric orbit around the Be star. This system has an intrinsic 3D geometry as the pulsar orbit is inclined with respect to the Be circumstellar disk. The above implementation gives satisfactory results even for highly eccentric orbits as can be seen on Fig 2.9. To keep track of the positions of the stars when restarting a simulation, I have modified the outputs to store the positions and velocity of both stars. The orbital parameters and physical parameters of the winds are all stored in an input file that can be easily modified.

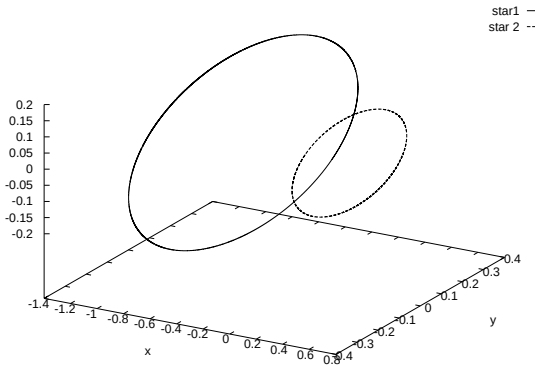

Figure 2.9: Example of orbits of two stars using the leapfrog method with $M_1 = 2M_2$, $a = 1$, $e = 0.8$ and $i = 30°$. The center of mass is located at $(0, 0, 0)$.

2.3.3 Passive scalars

In some simulations we want to clearly distinguish both winds and to be able to measure the amount of mixing between them. This can be done by introducing two passive scalars s_1 and s_2 that indicate the concentration of wind 1 and wind 2, respectively. The passive scalars are initialised in the masks, their evolution is determined by

$$\frac{\partial \rho s_i}{\partial t} + \nabla \cdot (\rho s_i \mathbf{v}) = 0 \qquad i = 1, 2, \tag{2.44}$$

In the free wind of the first star $s_1 = 1$ and $s_2 = 0$, in the second wind it is the other way round. In the shocked zone both scalars have an intermediate value that accounts for the mixing of the winds.

2.3.4 2D and 3D geometry

The 2D setup differs from those usually found in the literature (*e.g.* Stevens et al. 1992, Brighenti and D'Ercole 1995, Pittard et al. 2006). Usually, the simulations represent the cylindrical (r, z) plane, and one views the system edge on. In our simulations, we model the (r, θ) plane instead, and view the system pole on. A drawback of this method is that, the structure of the colliding wind binary is not identical when going from a 2D to 3D simulation with the same wind parameters. Our method implicitly assumes stars are cylindrical instead of spherical. The density thus decreases $\propto r^{-1}$ instead of $\propto r^{-2}$. However, we found that the 3D structure is mostly recovered in 2D by using the scaling $\sqrt{\eta_{3D}} \rightarrow \eta_{2D}$ (see §3.1.3.1). An advantage of this 2D approach is that it is straightforward to include binary motion without resorting to full 3D simulations.

2.4 Overview of this chapter

Fig. 2.10 gives an overview of the global structure of RAMSES. Several parts of this algorithm will be modified to model relativistic flows. This will be detailed in chapter 5.

2.5 Résumé en Français

Dans ce chapitre je présente le code RAMSES ainsi que l'usage que j'en ai fait pour pouvoir simuler les collisions de vents d'étoiles massives. RAMSES [Teyssier, 2002] est un code massivement parallèle utilisé pour la modélisation de fluides astrophysiques, allant de la formation

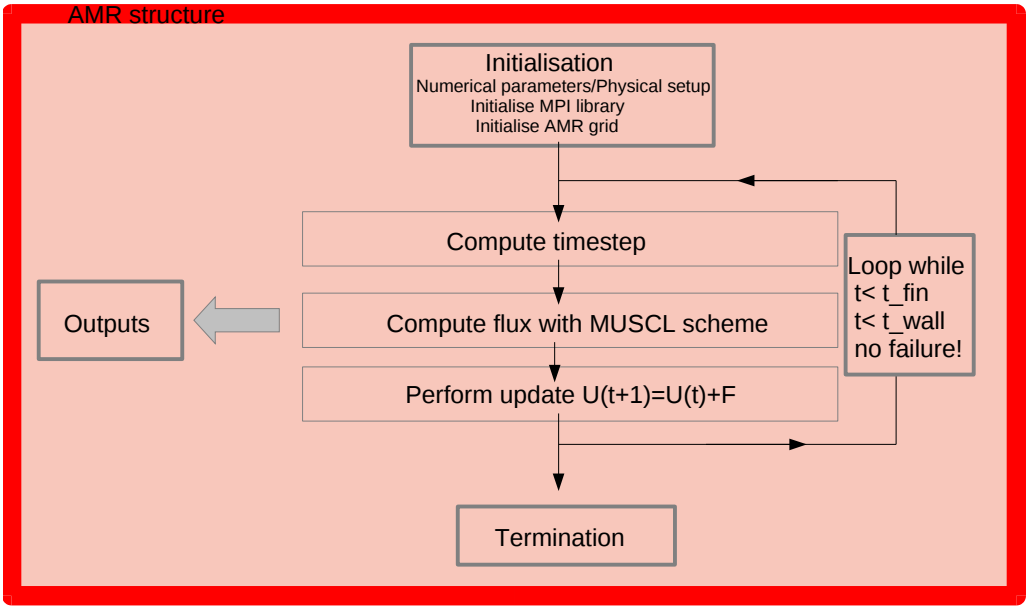

Figure 2.10: Global structure of RAMSES : The initialisation takes into account the user defined numerical parameters and the physical setup. The main loop is performed until the simulation is terminated or the computing time is elapsed (or the simulation has failed). At each step, a new timestep is computed, the Godunov fluxes are determined with the Riemann problem and the variables are updated. Outputs occur every X timesteps. The whole algorithm is embedded in the AMR structure.

stellaire à l'évolution de grandes structures de l'Univers. Son atout majeur est le raffinement adaptatif de maille (AMR), permettant d'augmenter localement la résolution d'une simulation en fonction des propriétés de l'écoulement et permet d'atteindre une résolution élevée pour un coût numérique (relativement) raisonnable. Dans mes simulations le raffinement est nécessaire autour des chocs et se base sur des critères de densité.

Pour modéliser les collisions de vents stellaires, RAMSES résout les équations d'Euler sous forme conservative en utilisant une méthode dite de Godunov. Le vecteur de variables conservées $\mathbf{U}$ est composé de la masse, de l'impulsion et de l'énergie. Dans RAMSES, on considère que les variables varient linéairement à l'intérieur d'une cellule, ce qui donne une précision du second ordre au schéma numérique. L'évolution temporelle des variables est déterminée par les flux de masse, impulsion et énergie entre les différentes cellules. Ces flux sont obtenus en résolvant un problème de Riemann aux interfaces entre les cellules. Cette méthode permet une bonne modélisation des chocs, ce qui la rend bien adaptée à la simulation de collisions de vents supersoniques. Je l'ai étendue à la modélisation des écoulements relativistes afin de pouvoir modéliser les binaires gamma. Cela est expliqué en détail dans le Chapitre 5.

Les vents sont générés dans un 'masque' [Lemaster et al., 2007] où la densité, pression et vitesse sont remis à jour à chaque pas de temps. Les paramètres d'une simulation sont donc le taux de perte de masse, la vitesse et le nombre de Mach des deux vents. Il faut aussi préciser les masses et éléments orbitaux si on veut tenir compte de la rotation des étoiles. Un scalaire passif permet de distinguer les deux vents. Les simulations à deux dimensions que j'ai effectuées montrent l'évolution de la binaire dans le plan orbital (r, θ). Nous simulons le système vu par dessus, ce qui suppose implicitement que le système possède une géométrie cylindrique. Cela donne des résultats différents des simulations dans le plan (r, z) [Stevens et al., 1992], où le système est vu par la tranche, ce qui suppose une géométrie sphérique. La complémentarité des deux méthodes sera présentée dans les Chapitres 3 et 4.

Chapter 3

Small scale simulations of colliding stellar winds

Contents

3.1 Important parameters to determine the shock region 67

3.1.1 Determination of the 2D analytic solutions 68

3.1.2 Comparison with 2D simulations 68

3.1.3 3D results 75

3.2 Impact of instabilities 78

3.2.1 The Kelvin-Helmholtz Instability 79

3.2.2 Isothermal winds : Non-linear Thin Shell Instability and Transverse Acceleration Instability 80

3.2.3 A dominant instability? 82

3.3 Numerical requirements for a reliable simulation 83

3.4 What did we learn in this chapter? What should be taken into account in improved models? 83

3.5 Resumé en français 85

3.6 Paper: High resolution numerical simulations of unstable colliding stellar winds (MNRAS, 2011) 86

In this chapter I present simulations of the close environment of the binary, where the curvature of the shocked structure due to orbital motion can be ignored. In this case 3D analytic solutions of the position of the contact discontinuity exist, assuming isothermal infinitely thin shocked layers where pressure can be neglected (see §1.3.2.2). They are useful for comparisons with high resolution observations [Dougherty et al., 2003]. Two solutions are commonly used [Stevens et al., 1992, Canto et al., 1996] and are based on different assumptions. Their respective domains of validity have never been clearly established. We computed the equivalent solutions in 2D (§3.1.1) and then I compared them to the results of the simulations (§3.1.2). I determined the impact on the structure of the shocked region of the momentum flux ratio,

$$\eta = \frac{\dot{M}_2 v_{\infty 2}}{\dot{M}_1 v_{\infty 1}}, \tag{3.1}$$

thermal pressure, the velocity and mass loss rate and the equation of state. Most simulations were performed in 2D but I ran a few 3D simulations for completeness (§3.1.3).

An important shortcoming of the analytic solutions is the impossibility to model the development of different instabilities that have been found in colliding wind binaries with numerical simulations (§3.2) The impact of the Kelvin-Helmholtz instability (KHI) is not clear yet : some simulations indicate its presence [Stevens et al., 1992, Lemaster et al., 2007] while other do not (Pittard [2009], van Marle et al. [2011a]). When cooling is important, the shocked shell becomes violently unstable. It results in strong mixing and variability, which can have important observational consequences. Two physical mechanisms are probably at work in this case : the Transverse Acceleration Instability (TAI) [Dgani et al., 1993] and Non-Linear Thin Shell Instability (NTSI) [Vishniac, 1994b] but their respective contributions are not well defined [Walder and Folini, 1998] and one usually refers to them as *thin shell instabilities*. One of the goals of this chapter is to determine which instability dominates in colliding wind binaries, in both the adiabatic and isothermal limit. Proper modelling of these instabilities in only possible when stringent numerical conditions are satisfied, especially at high η (§3.3).

The questions we want to answer are

- What are the limits of the analytic solutions?
- Does the KHI impact the structure of colliding wind binaries?
- Which instability dominates when the winds are isothermal?
- How important is the variability due to instabilities?
- What is necessary for a reliable numerical simulation of a colliding wind binary?

The purpose of this chapter is to understand how the analytic solutions compare with simulations and determine the impact of the instabilities, especially when one wind strongly dominates the other one. Therefore I neglect several physical phenomena that would make comparisons with analytic solutions more complex and make it more difficult to assess their respective contributions. Physical mechanisms such as cooling, radiative effects or orbital motion are important to take into account when comparing simulations to observations. I will briefly discuss their impact on the answers to the above questions (§3.4).

3.1 Important parameters to determine the shock region

The overall structure of the colliding wind binary is recalled in Fig. 3.1. The density map shows two shocks separating the free winds from the shocked winds. The shocked winds from both

stars are separated by a contact discontinuity. As the wind from the second star is collimated due to the low momentum flux ratio of the winds, there is a reconfinement shock along the line-of-centres.

3.1.1 Determination of the 2D analytic solutions

As our setup assumes a cylindrical geometry (see §2.3.4), and the structure of the interaction region differs from the 3D analytic solutions found in the literature. In this first section I give the corresponding 2D solutions we computed and some additional analytic results we have found. The Bernouilli relation is preserved across shocks hence

$$\frac{1}{2}v_{\infty 1}^2 = \frac{\gamma}{\gamma-1}\frac{P_{1s}}{\rho_{1s}} + \frac{1}{2}v_{1s}^2 \tag{3.2}$$

across the first shock. The subscript s refers to quantities in the shocked region and we neglect the thermal pressure in the unshocked wind due to its high Mach number. A similar equation holds for the second shock. At the contact discontinuity, $P_{1s} \equiv P_{2s}$ by definition and $v_{1s} = v_{2s} = 0$ on the line-of-centres so that the two Bernouilli equations combine to give $\rho_{1s}v_{\infty 1}^2 = \rho_{2s}v_{\infty 2}^2$, with ρ_s the value of the density on each side of the contact discontinuity. Assuming that the density is constant in each shocked region on the binary axis (the numerical simulations carried out below show this is a very good approximation) then

$$\rho_1 v_{\infty 1}^2 = \rho_2 v_{\infty 2}^2, \tag{3.3}$$

where ρ_1 (ρ_2) is the value of the density at the first (second) shock. The above relation states the balance of ram pressures [Stevens et al., 1992]. Using the definition of η and mass conservation we get

$$r_2 \approx \sqrt{\eta} r_1 \quad \text{(3D)} \qquad r_2 \approx \eta r_1 \quad \text{(2D)}, \tag{3.4}$$

where r_1 is the distance between the first star and the first shock and r_2, the distance between the second star and the second shock. If the shock is thin then $r_1 + r_2 \approx a$ and the distance $R_s \approx r_2$ of the contact discontinuity to the second star is

$$\frac{R_s}{a} \approx \frac{\sqrt{\eta}}{1+\sqrt{\eta}} \quad \text{(3D)} \qquad \frac{R_s}{a} \approx \frac{\eta}{1+\eta} \quad \text{(2D)}. \tag{3.5}$$

Following the computation by Stevens et al. [1992], we find the 2D shape of the contact discontinuity is given by

$$\frac{dx}{dy} = \frac{x}{y} - \left(\frac{a}{y}\right)\left[1 + \sqrt{\eta}\left(\frac{r_2}{r_1}\right)^{3/2}\right]^{-1}. \tag{3.6}$$

Similarly, the results from Canto et al. [1996] can be adapted to our geometry, which gives

$$\frac{\cos\theta_1 - 1}{\sin\theta_1} = \eta\frac{\cos\theta_2 - 1}{\sin\theta_2}. \tag{3.7}$$

(see Fig. 3.1 for the definition of θ_1 and θ_2.) This gives an asymptotic opening angle given by

$$\cos\theta_{2\infty} = \frac{1-\eta}{1+\eta}. \tag{3.8}$$

The complete demonstration can be found in Appendix A.

There is no contact discontinuity when $v_{\infty 1} = v_{\infty 2}$, even when $\eta \neq 1$ as Eq. 3.3 results in $\rho_1 = \rho_2$ at the contact discontinuity.

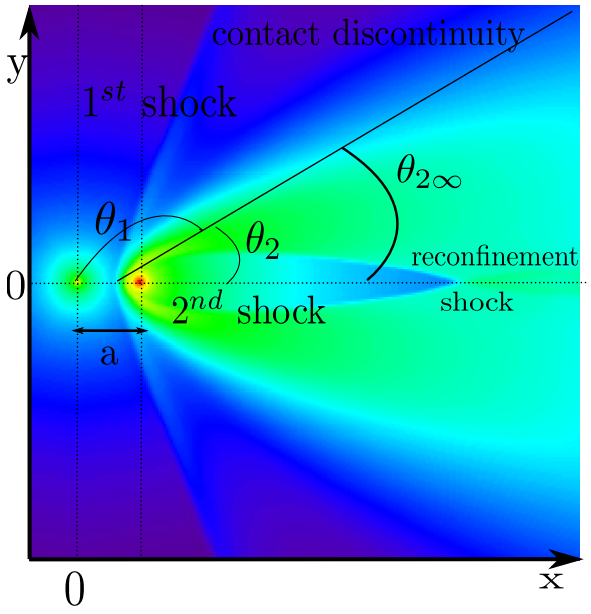

Figure 3.1: Density map of the interaction zone for $\eta = 1/32 = 0.03125$. It is a cut perpendicular to the line-of-centres taken from a 3D simulation. A zoom on the binary system is shown at the bottom right corner. The stars are positioned at the intersections of the dotted lines. The first star has coordinates $(0, 0)$, the second one has coordinates $(a, 0)$. Along the line-of-centres, there are three density jumps (for increasing x). The first shock separates the unshocked wind from the first star from the shocked wind. The contact discontinuity separates both shocked winds. It intersects the line-of-centres at the standoff point R_s. The second shock separates the shocked and unshocked parts of the wind from the second star. $R(\theta_2)$ is the distance between the contact discontinuity and the first star, θ_2 is the polar angle. The asymptotic opening angle is given by $\theta_{2\infty}$.

3.1.2 Comparison with 2D simulations

My first aim is to study the binary structure to understand the underlying hydrodynamics. I perform adiabatic simulations with various setups and compare them to the analytic solutions given in section 1.3.2.2 (for 3D solutions) and 3.1.1 (for 2D solutions) to determine their accuracy and limits. In adiabatic simulations the shocked zone is wide and one distinguishes both shocks and the contact discontinuity. In this whole section, numerical diffusion is chosen just high enough to avoid the development of instabilities that affect the binary structure and prevent comparison with analytic results.

3.1.2.1 Impact of η

In the first set of simulations I study the impact of the momentum flux ratio η performing simulations with $\eta = 1$, 0.5, 0.25, 0.125, 0.06125, 0.03125, 0.015625, 7.8125×10^{-3}. In all these simulations $v_{\infty 1} = 1/\eta v_{\infty 2} = 2000$ km.s$^{-1}/\eta$, $\dot{M}_1 = \dot{M}_2 = 10^{-7} M_\odot$ yr^{-1} and $\mathcal{M}_1 = \mathcal{M}_2 = 30$. The size of the simulations domain is $l_{box} = 8a$, the coarse grid is set by $n_x = 128$ and up to six levels of refinement are allowed.

The density and velocity maps are given in Fig. 3.2 - Fig 3.4. The stars are located at $\{x = 0, y = 0\}$ and $\{x = a, y = 0\}$, at the intersection of the dotted lines shown on the density maps. On the density maps (left columns) one can clearly see both shocks and the contact discontinuity. For $\eta = 1$ there is no contact discontinuity as both winds are identical, the structure is perfectly symmetric. As η decreases the whole structure bends more and more towards the second star. For $\eta < 0.125$ the second wind is totally trapped as there is a reconfinement shock on the binary axis behind the second star. The unshocked winds propagate freely with a $\propto r^{-1}$ density profile (2D). At the shocks there is density jump of a factor 4. At the contact discontinuity the density jump may be much higher, and increases as η decreases. Along the line-of-centres the density is constant in the shocked winds. There is a quick decline further away from the axis.

The corresponding velocity maps are given in the right columns of Fig. 3.2 - 3.4. The arrows give the direction of the field. Initially the winds have a radial outward velocity, as can be seen in the unshocked winds. The velocity is constant in the whole unshocked region as I have set it to the terminal velocity in the masks. As pressure is very low, the winds do not accelerate when they propagate. At the shock the normal velocity decreases by a factor of 4, the tangential velocity is not affected. At the contact discontinuity the normal velocity components cancel out and tangential velocities equalise within a thin layer. Close to the line-of-centres the winds are subsonic after the shocks but they re-accelerate further away and rapidly become supersonic again. The limit between the subsonic and supersonic flow is indicated on the velocity maps by a white line close to the standoff point. As η decreases, it gets closer and closer to the standoff point and is barely visible.

The analytic solutions given by Eq. 3.6 and Eq. 3.7 are overplotted on the density maps with respectively a dashed and dashed-dotted line. At high η the solution from Canto et al. [1996] gives a better agreement. For low values of η the solution from Stevens et al. [1992] gives a better agreement. i found no clear explanation to this difference. For $\eta < 0.03125$, after the reconfinement shock, the second shock and the contact discontinuity intersect causing the contact discontinuity to refract. A zoom on this part of the flow is shown on the left panel of Fig. 3.5. This cannot be modelled analytically and is important as it widens the asymptotic opening angle.

In my simulations, the stars are always situated at a given distance from the edges of the computational box and there are no spurious effects due to the boundary conditions. Simulations with low η, with the stars located at the edge of the domain, *e.g.* $y = 0$ such as in Brighenti and D'Ercole 1995, Bogovalov et al. 2008 show the presence of a so-called Mach disk. The reconfinement shock has a different shape than in my simulation because there is a Mach reflection. A Mach reflection occurs when an oblique shock bounces on a solid wall with an incident angle

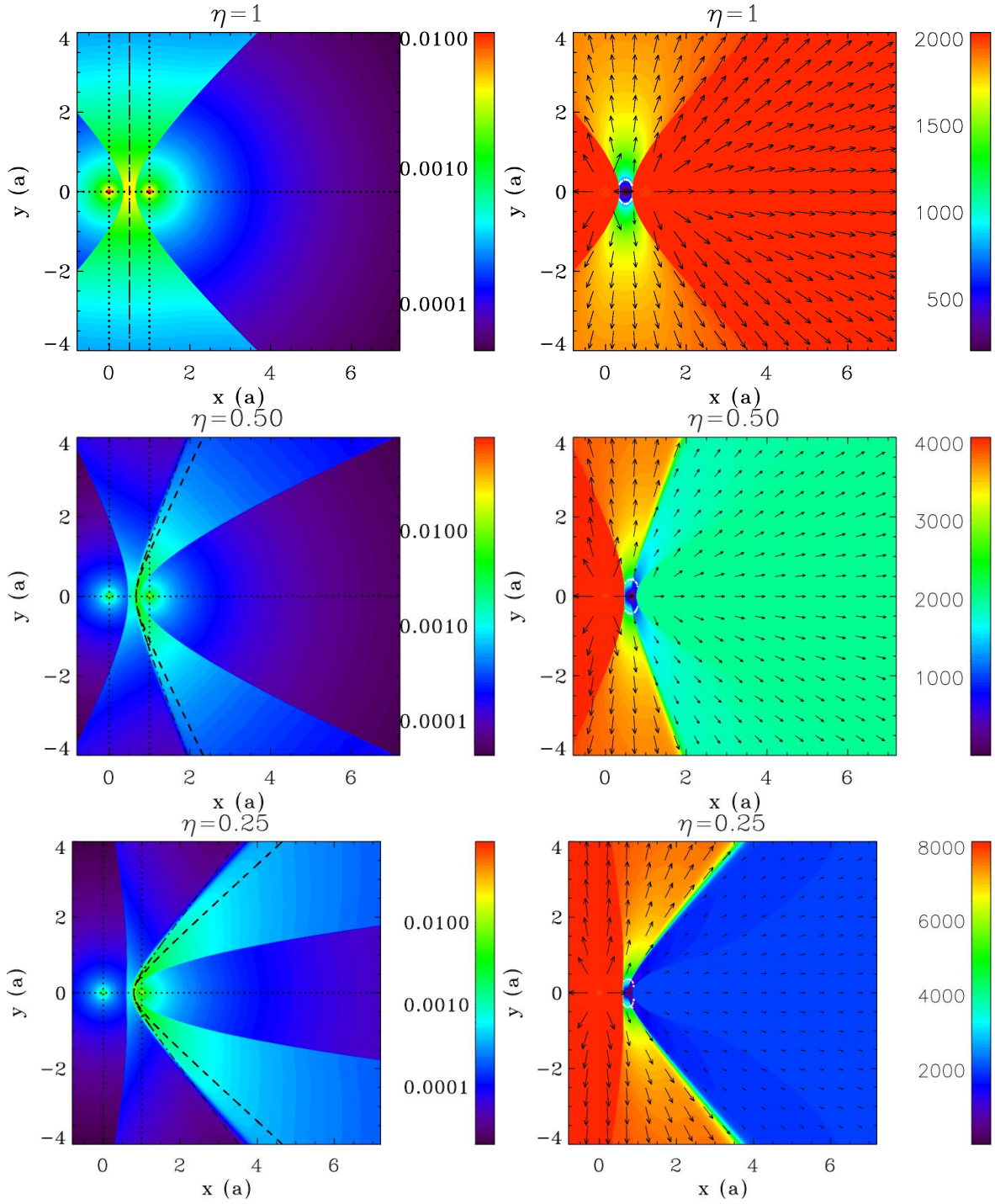

Figure 3.2: Density (left panel) and velocity (right panel) maps for $\eta = 1$, 0.5, 0.25. The density is given in g cm $^{-2}$ and the velocity in km s^{-1}. The dashed lines give the solution given by Eq. 3.6 and the dashed lines the solution given by Eq. 3.7.

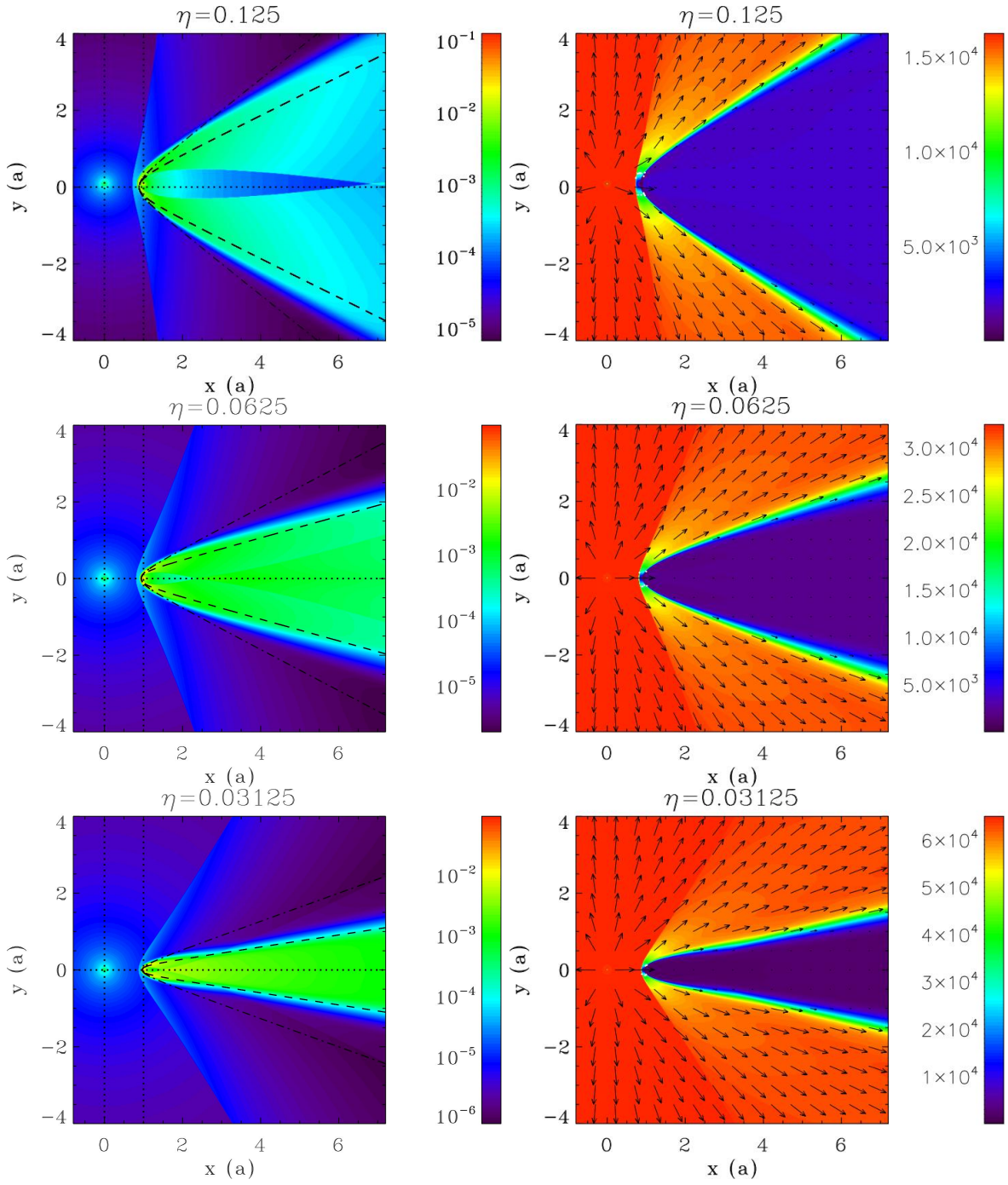

Figure 3.3: Density (left panel) and velocity (right panel) maps for $\eta = 0.125, 0.0625, 0.03125$. The density is given in g cm^{-2} and the velocity in km s^{-1}. The dashed lines give the solution given by Eq. 3.6 and the dashed-dotted lines the solution given by Eq. 3.7.

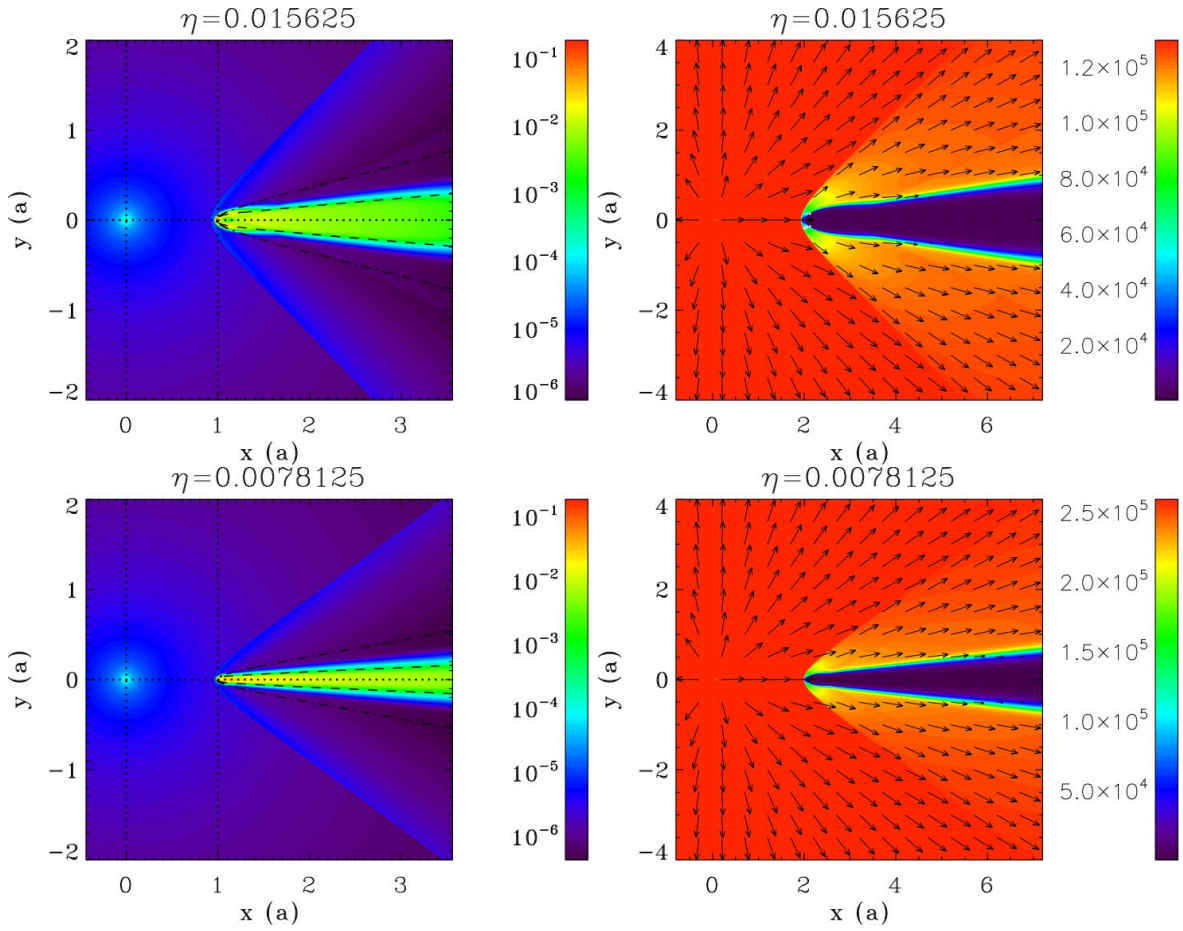

Figure 3.4: Density (left panel) and velocity (right panel) maps for $\eta = 0.0015625$, 7.8125×10^{-3}. The density is given in $\mathrm{g\,cm^{-2}}$ and the velocity in $\mathrm{km\,s^{-1}}$. The dashed lines give the solution by Eq. 3.6 and the dashed-dotted lines the solution given by Eq. 3.7.

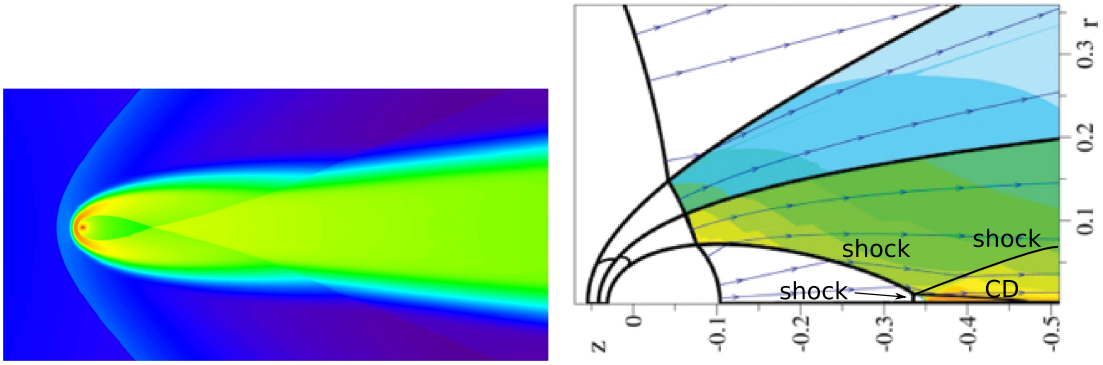

Figure 3.5: Left panel: zoom on the reconfinement shock for $\eta = 0.015625$. Right panel: Density map showing a reconfinement shock with a Mach disk. The first star is located at $z > 1$, the second star at $z = 0$, the Mach reflexion occurs at $z = -0.32$. Image taken from Bogovalov et al. [2008].

θ_i larger than a certain value θ_m. Normally the shock is reflected at the wall and its reflection angle is set by the Rankine-Hugoniot jump conditions according to the incoming flow. For angles larger than θ_m the Rankine-Hugoniot conditions cannot be satisfied anymore and the reflection point unties itself from the wall. This results in a complex structure with 3 shocks and a contact discontinuity [Landau and Lifshitz, 1975]. The right panel of Fig 3.5 shows such a structure, the left panel shows one of my simulations for comparison. I never observed a Mach disk and it is likely to be a numerical artefact resulting from the boundary conditions at the edges of the domain. No reflection should occur as there is no solid wall in reality.

The left panel of Fig. 3.6 shows the position of both shocks and the contact discontinuity on the line-of-centres. I compute the positions of the different density jumps on the binary axis as a function of η. They are determined by the local extrema of the slope of the density on the binary axis. I exclude the masks in my computation. I overplot the analytic solution for the position of the standoff point given in Eq. 3.5 and find there is a very good agreement. The relation given in Eq. 3.4 is verified (right panel) and confirms the hypothesis of a constant density along the binary axis. The thickness of the shell decreases as η decreases. For low η, proper modelling of the shock formation thus requires high resolution.

The left panel of Fig. 3.7 shows the distance from the reconfinement shock to the second star. Additional simulations at larger scales show that for $\eta = 0.25$, there is no reconfinement up to a distance of more than 100 times the binary separation, while a reconfinement is found for $\eta = 0.2$. As η decreases the second wind gets more and more collimated and the shock gets closer and closer to the star. The presence of a reconfinement shock behind the second star for low enough values of η is impossible to model analytically. The right panel of Fig. 3.7 displays the asymptotic opening angle resulting from the simulations and the analytic solution given in Eq. 3.8. There is a good agreement at high η. For lower values, there is more than a factor two difference between the analytic solutions and the simulations, although shock refraction has a widening effect. This is important when deriving η from observations [Varricatt et al., 2004].

3.1.2.2 Impact of mass loss rates and terminal velocities for given η

Up to now I have assumed the relevant parameter determining the structure of colliding wind binaries is their momentum flux ratio, regardless of the mass loss rates and velocities of the winds. However, one can wonder what is the independent impact of the velocity or mass loss

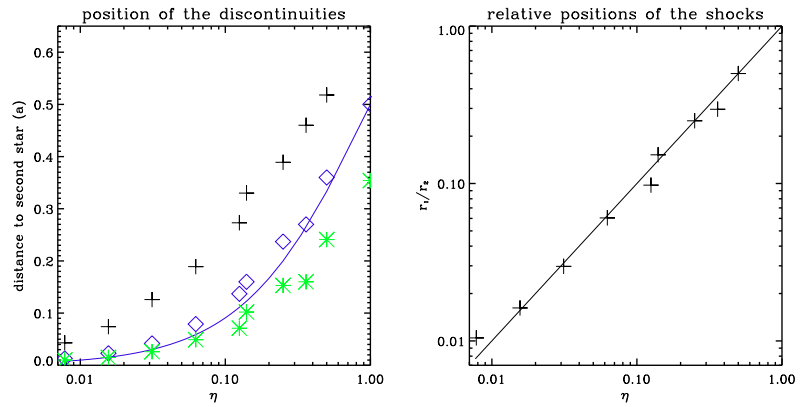

Figure 3.6: Left panel : positions of the different density jumps as a function of η in 2D simulations : the first shock (black crosses), the contact discontinuity (blue diamonds) and the second shock (green asterisks). The 2D analytic solution for the contact discontinuity is overplotted (blue solid line). Right panel: Verification of Eq. 3.4, the solid line is the analytic solution, the crosses are the results from the simulations.

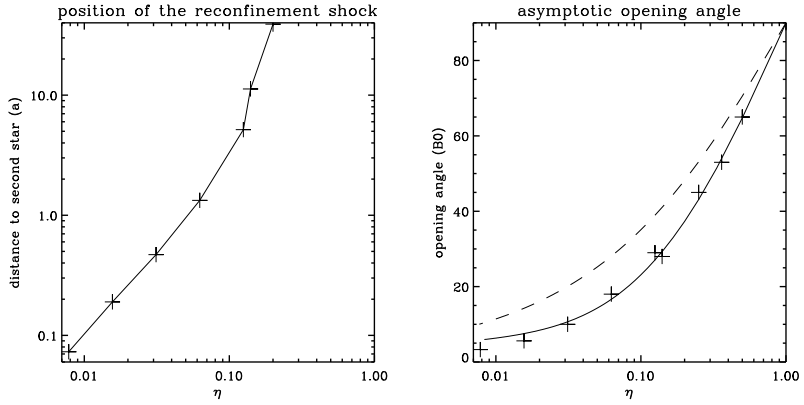

Figure 3.7: Positions of the reconfinement shock (left panel) and asymptotic opening angle (right panel) for increasing η in 2D simulations. The solid line represents the solution by Eq. 3.6 and the dashed-dotted line the solution given by Eq. 3.7.

rate ratios. I performed tests for $\eta = 0.125$ with $\{(v_{\infty 1} = 8v_{\infty 2},\ \dot{M}_1 = \dot{M}_2)$, $(v_{\infty 1} = 16v_{\infty 2},\ \dot{M}_1 = 0.5\dot{M}_1)$, $(v_{\infty 1} = 4v_{\infty 2},\ \dot{M}_1 = 2\dot{M}_2)$, $(v_{\infty 1} = v_{\infty 2},\ \dot{M}_1 = 8\dot{M}_2)$, $(v_{\infty 1} = 0.1v_{\infty 2},\ \dot{M}_1 = 80\dot{M}_2)\}$. Fig. 3.8 gives the corresponding density maps. The case $v_{\infty 1} = 8v_{\infty 2}$ has the same parameters as the simulation shown in the upper row of Fig. 3.3. As predicted at the end of §3.1.1, when $v_{\infty 1} = v_{\infty 2}$ there is no contact discontinuity. The maps show that although the density and velocity fields are different in all these setups, both shocks and the contact discontinuity are located at the same place, even far away from the stars. As expected, the important parameter to determine the positions of the discontinuities is the momentum flux, not the velocity or mass loss rate. These simulations are a good benchmark that indicates our numerical setup is reliable. We will see in §3.2 that, for a given η, the mass loss rate and velocity are important for the development of instabilities.

3.1.2.3 Impact of Mach numbers

The analytic solutions are based on the thin shell hypothesis, which assumes there is no thermal support in the shocked layer. Implicitly this correspond to a gas with an infinite Mach number.

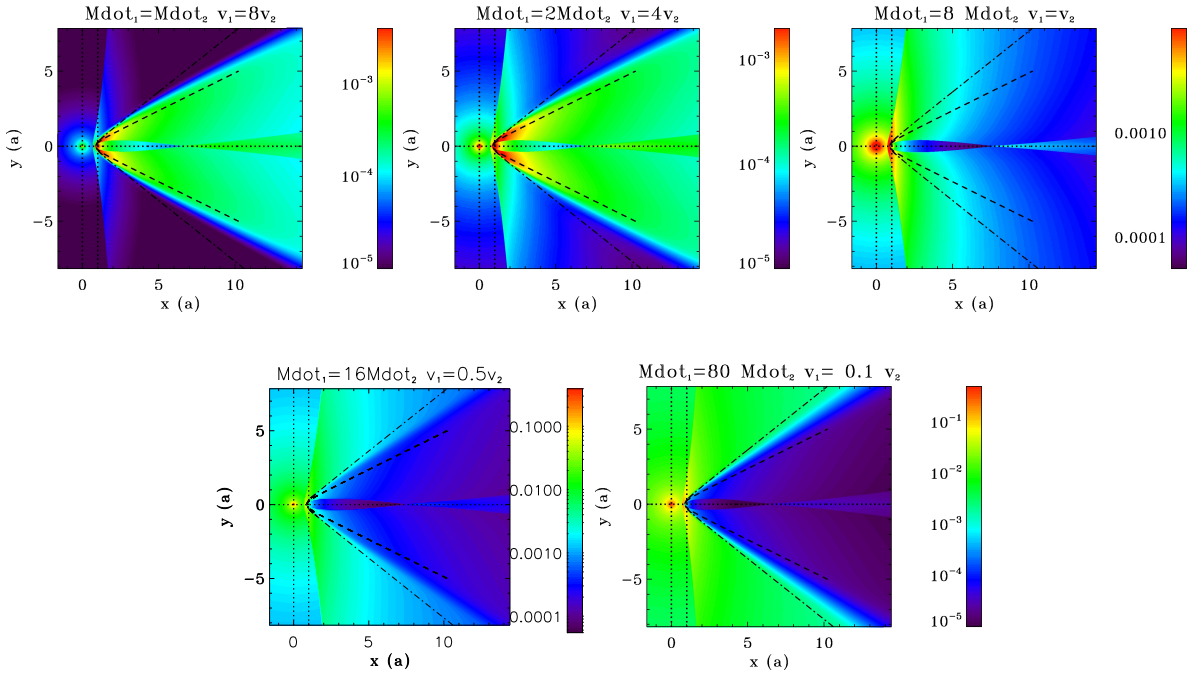

Figure 3.8: Density for $\eta = 0.125$ in 2D simulations with different values for decreasing velocity ratios and increasing mass loss rate ratios. The dashed lines give the solution by Eq. 3.6 and the dashed-dotted lines the solution given by Eq. 3.7. The simulation $v_{\infty 1} = v_{\infty 2}$ has the same wind parameters than the simulation in the top row of Fig. 3.3 but extends further away from the binary. The color scale is different to be able to model the lower density far from the binary.

We have seen that the analytic solutions are in good agreement with adiabatic simulations with $\mathcal{M}_1 = \mathcal{M}_2 = 30$. What happens for different values of the Mach numbers in the winds? Observationally Mach numbers are not well constrained and estimates lay between 20 and 50 [Waldron and Cassinelli, 2007]. The Mach number is thus a free parameter in the simulations, and it is important to know how it affects their results.

I performed 2D simulations for $\eta = 0.25$ in four different cases: $\mathcal{M}_1 = \mathcal{M}_2 = 5$, 30, 100; and $\mathcal{M}_1 = 5$, $\mathcal{M}_2 = 30$. The values of the Mach number is given for a distance equal to the binary separation. In free winds, its value increases with increasing distance from the star. Fig. 3.9 shows the density maps in the different simulations. When both winds have different Mach numbers, the whole shocked structure is more bent towards the wind with the higher Mach number. If both winds have a $\mathcal{M} = 5$ instead of $\mathcal{M} = 30$, the shocked region is wider due to higher pressure (see the jump conditions given in §1.3.2.1). The density in the shocked winds is rather independent of the Mach number. Larger scale simulations show the second wind is confined in this case. The position of the contact discontinuity is the same as for the case of $\mathcal{M}_1 = \mathcal{M}_2 = 30, 100$. There is no difference between the simulations with $\mathcal{M}_1 = \mathcal{M}_2 = 30, 100$. This indicates that the exact value of the Mach number is not important, as long as it is large enough. Modelling very high Mach numbers is numerically delicate, therefore we set them to 30 in our simulations.

3.1.3 3D results

For computational reasons 3D simulations are limited in resolution and spatial extension, especially when one wind strongly dominates the other one. However, observations provide 3D quantities and care has to be taken when comparing them to 2D simulations as the underlying

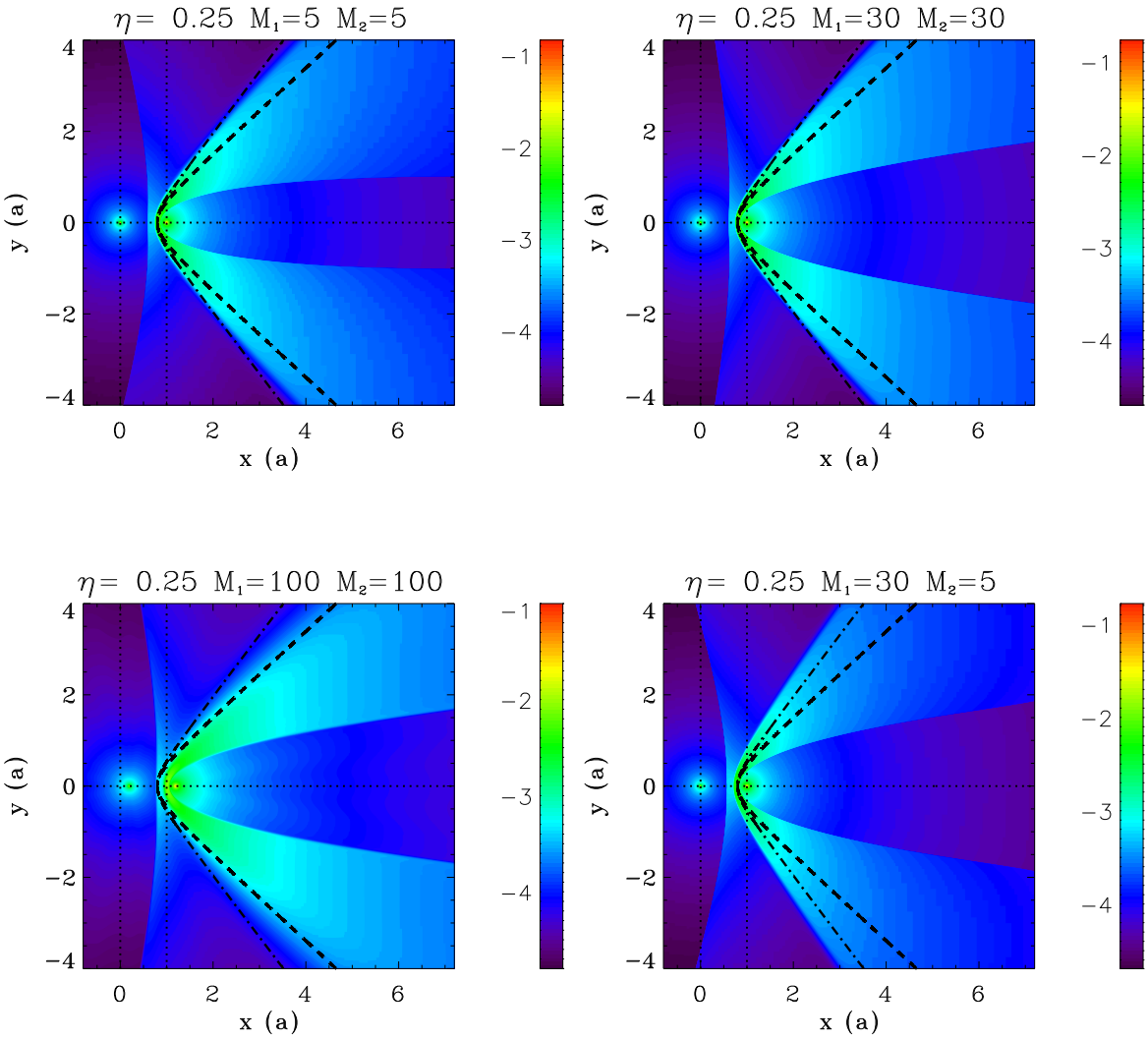

Figure 3.9: Density maps in 2D simulations with $\eta = 0.25$. From left to right : $\mathcal{M}_1 = \mathcal{M}_2 =$ 5, 30, 100; and $\mathcal{M}_1 = 5$, $\mathcal{M}_2 = 30$. The dashed lines give the solution by Eq. 3.6 and the dashed-dotted lines the solution given by Eq. 3.7. The simulation $\mathcal{M}_1 = \mathcal{M}_2 = 30$ is the same as the simulation shown on the bottom row of Fig. 3.3.

geometry is different. The aim of this section is to highlight the similarities and discrepancies between 2D and 3D simulations. I perform 3D simulations with $l_{box} = 8$, the coarse level is set by $n_x = 32$ and I use 5 levels of refinement. The density maps for 3D simulations with $\eta = 1$, 0.5, 0.125 and 0.03125 are given in Fig. 3.10. Again, the analytic solutions are overplotted. As for the 2D case, the shape of the contact discontinuity is better approximated by the solution of Stevens et al. [1992] at low η, while the solution by Canto et al. [1996] gives a better agreement for higher values of η.

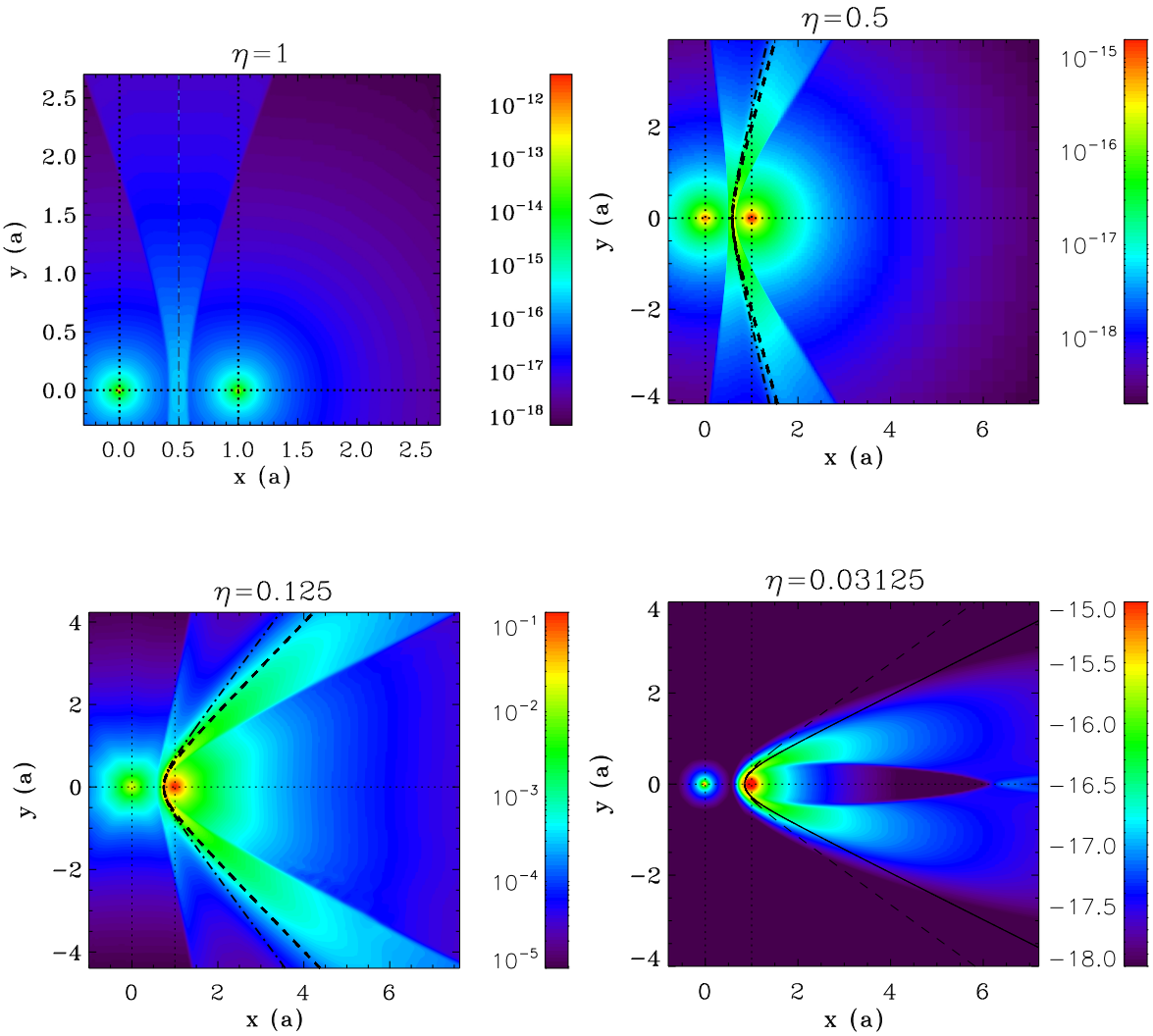

Figure 3.10: Density maps in the orbital plane for 3D adiabatic winds with η = 1, 0.5, 0.125, 0.03125. The dashed lines represent the solution by Stevens et al. [1992] and the dashed-dotted lines the solution by [Canto et al., 1996].

Using the same method as for the 2D analysis, I measure the positions of the discontinuities and compare them with the analytic expectations. The results are given in Tab. 3.1 and show an agreement within 2%. For $\eta = 0.5$ I measure an asymptotic opening angle $\theta_{2\infty} = 71°$ whereas the asymptotic angle from both Stevens et al. [1992] and Canto et al. [1996] give 78°; for $\eta = 1/32 = 0.03125$ I get 23° compared to theoretical estimates of 27° [Stevens et al., 1992] and 35° [Canto et al., 1996].

η	1	.5	.125	.03125
first shock	0.58	0.49	0.34	0.23
contact discontinuity	0.50	0.42	0.28	0.16
contact discontinuity (theory)	0.50	0.42	0.27	0.16
second shock	0.43	0.36	0.23	0.12
second shock (theory)	0.42	0.37	0.22	0.13

Table 3.1: Distance to the second star of both shocks and the contact discontinuity along the line-of-centres. Results from 3D simulations and theoretical values.

3.1.3.1 Switching from 2D to 3D simulations

Globally the structure is less bent towards the weaker star in 3D simulations than in the 2D simulations. Eq. 3.5 suggests the rough mapping $\sqrt{\eta_{3D}} \rightarrow \eta_{2D}$. Indeed the position of the contact discontinuity, for $\eta_{3D} = 8$, is bracketed by the positions for the contact discontinuity for $\eta_{2D} = 2$ and 4. The same occurs for $\eta_{3D} = 32$ and $\eta_{2D} = 4$ and 8. Similarly, the asymptotic opening angle is wider and higher momentum ratios are needed to form a reconfinement shock. In additional simulations, not shown here, I find that for $\eta = 0.016$ the reconfinement shock occurs at $2.2\,a$ while there is no reconfinement shock for 3D simulations with $\eta = 0.08$. This would correspond to $\eta_{2D} \approx 0.29$ in Fig. 3.6. These results are in agreedment with Pittard and Dougherty [2006] who performed 2D axisymmetric simulations showing a reconfinement shock for $\eta = 0.02$ but not for $\eta = 0.036$.

For $\eta \geq 0.03125$, close to the line-of-centres, the shocked region is thinner in the 3D case than in the 2D case. For smaller values of η, the shocked zone is thicker in the 3D case. In all cases the contact discontinuity is further away from the second star in the 3D case than in the 2D case. This means that for low η, less resolution is needed in 3D to allow proper shock formation.

3.1.3.2 Isothermal winds

In the isothermal case all the discontinuities are merged in one thin shell as the shocked region is much thinner because the density jump is proportional to $\mathcal{M}^2$. The shocked shell is unstable and only low resolution simulations with high numerical diffusion can prevent their development. This section only deals with simulations where no instabilities are present.

For numerical reasons simulations cannot be performed with γ strictly equal to 1 [Truelove et al., 1998] and I set γ to 1.01 for isothermal simulations. The density maps for $\eta = 1$, 0.5, 0.125 and 0.0325 are given in Fig. 3.11. In this case pressure support is weaker and the shell is much thinner, as expected. The position of the contact discontinuity along the line-of-centres is within 10% of the contact discontinuity position found in adiabatic simulations. The asymptotic angle is difficult to assess as the transitions between the winds is smoother than in the adiabatic case, still the bracketing values are consistent with those found in the adiabatic case. I find that the weaker wind can be fully confined as in the adiabatic case. However, this occurs further away from the star than in the adiabatic case shown in Fig. 3.6.

3.2 Impact of instabilities

Up to now all simulations have been performed at relatively low resolution and using a diffusive Riemann solver to quench the development of instabilities. Instabilities are ubiquitous in astrophysical flows and several affect colliding wind binaries (see §1.4.2). They modify the structure and dynamics of the colliding region and allow for important mixing between the winds. They are probably responsible for the observed variability in colliding wind binaries. In this section I describe the effect and relative importance of the instabilities at work close to the binary system.

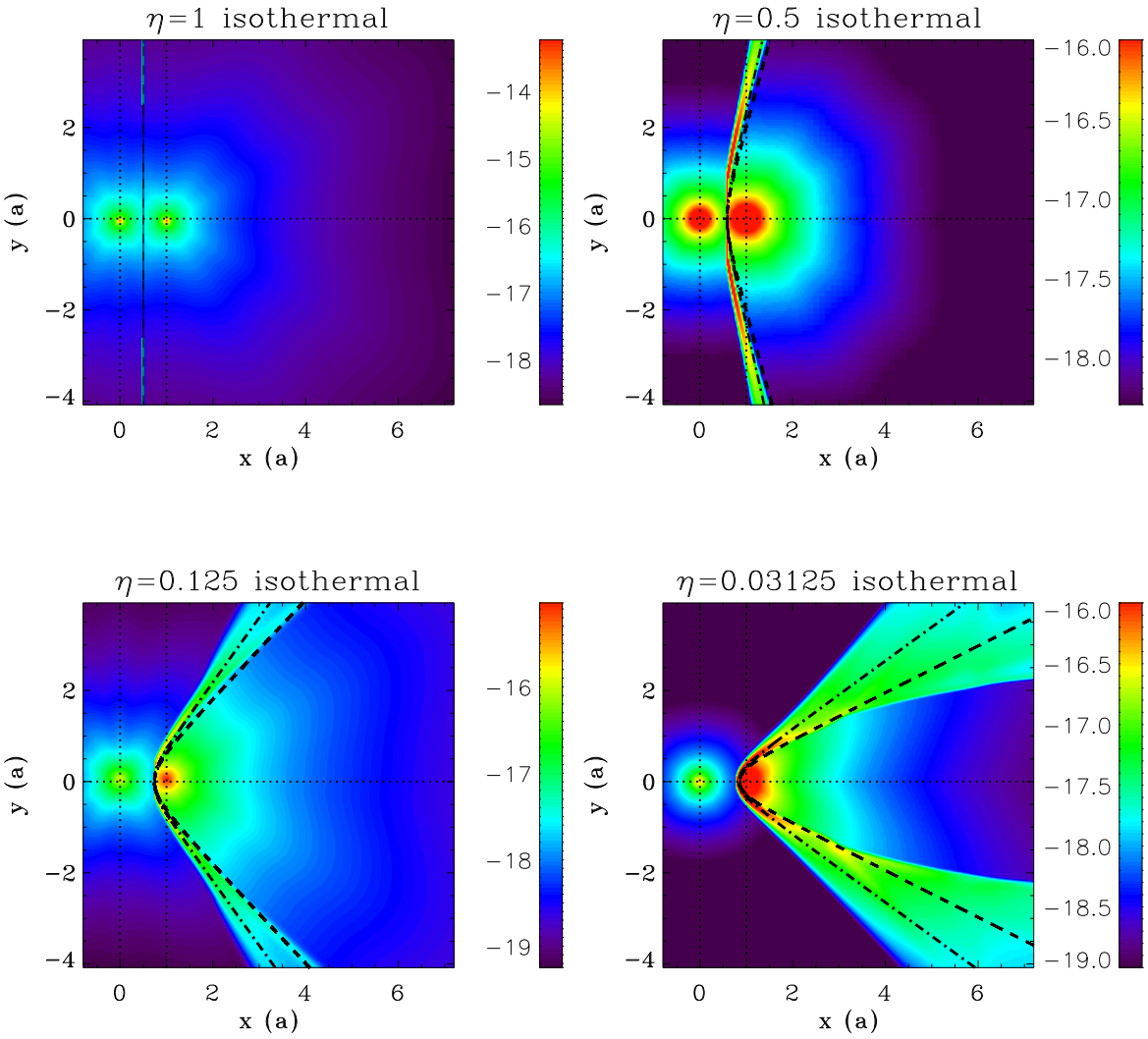

Figure 3.11: Density maps in the orbital plane for 3D isothermal winds with η = 1, 0.5, 0.125, 0.03125. The dashed lines represent the solution by Stevens et al. [1992] and the dashed-dotted lines the solution by Canto et al. [1996]. The density is given in g cm^{-3}. Far from the stars the effects of low resolution are visible. For $\eta = 1$ the shocked zone is composed of only one cell in the x direction and is superposed with the analytic solutions.

In practice, numerical simulations are limited by diffusivity and the minimum resolvable structure, inevitably stunting instabilities at small wavelengths. High resolution is thus important when studying instabilities, especially when small wavelength perturbations dominate the dynamics as it is for the linear stage of the TAI and KHI. In §3.2.1, I study the KHI using $l_{box} = 8$, $n_x = 128$ with 5 levels of refinement while for the isothermal simulations to study the NTSI and TAI (§3.2.2) I use $l_{box} = 3$ with $n_x = 128$ and 5 levels of refinement. In both cases, the equivalent number of cells is 4096^2. Numerical diffusion strongly decreases the development of the instabilities, this is why I used the exact Riemann solver, which creates the lowest amount of diffusion. All the following simulations are in 2D to reduce the computational costs. As I wanted to study the growth rate of the instabilities, it was import to have well-defined, stable initial conditions. At high resolution, instabilities develop as the winds start colliding, before a steady state is reached. To avoid this, I first performed low resolution simulations in order to get a stationary structure. Then I changed the Riemann solver and increased the resolution to study the instabilities.

3.2.1 The Kelvin-Helmholtz Instability

When winds have different terminal speeds, the Kelvin-Helmholtz instability develops at the contact discontinuity. The linear theory predicts that the instability develops for any velocity difference Δv with the growth rate $1/\tau_{KH} \propto \Delta v/\lambda$, where λ is the wavelength of the perturbation. The size of the smallest wavelength that develops is set by the resolution of the simulation. Large wavelength perturbations can be hampered by their advection in the flow. A perturbation cannot develop if its growth time is longer than the advection time (or dynamical time). The dynamical timescale can be estimated by $\tau_{dyn} \sim a/c_s$ where c_s is the post-shock sound speed, that is of the order of the wind velocity v_∞ in a strong adiabatic shock. For two identical winds with terminal velocities of 2000 km s^{-1} and $a = 1\,\mathrm{AU}$, $\tau_{dyn} \simeq 6.8 \times 10^4\,\mathrm{s} = 2.2 \times 10^{-3}\,\mathrm{yr}$. The scale of the perturbations is thus limited to $\lambda/a < \Delta v/v$.

I perform a set of simulations with $\eta = 1$, increasing the velocity $v_{\infty 1}$ of the first wind to investigate the impact of the KHI in the adiabatic case. The mass loss rate $\dot{M}_1$ is simultaneously decreased. The second wind is the same in all simulations. The purpose is to have a qualitative knowledge of the impact of the KHI on the shocks and to quantify the amplitude of the perturbations. No instabilities are present when the two winds are exactly identical, as expected since there is no velocity difference. In Chapter 4 we will see that orbital motion allows the development of the KHI at the interface between identical winds.

I run the simulations up to $t = 600\tau_{dyn}$. This means the flow has reached a steady state where the total root mean square (r.m.s.) of the density or velocity perturbations over the whole simulation domain remains constant. I then compute the time average of the velocity r.m.s. for each cell of the domain and use the median value over the same time period as a reference. I only consider the steady state period. The results for $v_{\infty 1}/v_{\infty 2} = 1.1$, 2 and 20 are shown in Fig. 3.12. The left panel gives the density maps for the different cases while the corresponding right panels show the time average of the r.m.s of the velocity fluctuations. Introducing a 10% difference in the velocity of the winds leads to low amplitude perturbations that are significant only close to the contact discontinuity. A dominant wavelength can be identified. This is probably because the growth is restricted to a small domain by diffusivity at short wavelengths and advection at long wavelengths. The r.m.s. of the velocity and density perturbations saturate at about 10%. When $v_{\infty 1} = 2v_{\infty 2}$ small scale eddies are visible. They are stretched in the direction of the flow. The position of the shocks is barely affected by the instability. The perturbations affect a larger zone on both sides of the contact discontinuity but their amplitude remains around a few tens of percent r.m.s. When $v_{\infty 1} = 20v_{\infty 2}$ (last panel) the instability has become non-linear judging by the 100% r.m.s. of the velocity fluctuations. The location of the contact discontinuity fluctuates

significantly and the positions of the shocks is affected, yet the region with the strongest r.m.s. is not much wider than for the previous cases. The position of the stagnation point is not affected by the KHI as along the line-of-centres the winds have no tangential velocity.

I perform similar simulations with $\eta = 0.0625$ (Fig. 3.13). As for $\eta = 1$ there is no KHI when winds have equal speeds (not shown here). When $v_{\infty 1} = 1.1 v_{\infty 2}$ only weak perturbations are present, limited to a small region close to the contact discontinuity. As for $\eta = 1$, a dominant wavelength can be identified. When $v_{\infty 1} = 2 v_{\infty 2}$ the centre line of the perturbations approximately matches the shape of the unperturbed contact discontinuity. The first shock is not affected by the instability. The velocity perturbations affect all the region of the shocked second wind and part of the shocked wind of the first star. The velocity perturbations are strong when $v_{\infty 1} = 20 v_{\infty 2}$ and are mostly confined to the shocked second wind, probably because the growth is limited by advection in the fast wind from the first star. The position of the backward reconfinement shock fluctuates, and occurs much closer to the second star than in the case with equal wind velocities.

The KHI modifies the interaction region as soon as the wind velocities are slightly different. The simulations suggest that the relative amplitude of the perturbations becomes significant when $v_{\infty 1} \geq 2 v_{\infty 2}$, although we cannot rule out that limited numerical resolution does not impact the growth of the instability for smaller velocity differences. The instability does not erase completely the contact discontinuity. However, the turbulent motions tend to smooth out the initial structures in the region of the wind with the smaller velocity.

3.2.2 Isothermal winds : Non-linear Thin Shell Instability and Transverse Acceleration Instability

By decreasing the adiabatic index γ, one increases the compressibility of the gas and decreases the size of the shocked layer [Mac Low and Norman, 1993]. Fig. 3.14 shows the morphology of the binary for different values of the adiabatic index. One can see the lower the adiabatic index the more unstable the shocked layer. For $\gamma = 1.1$ one can still distinguish the original shape of the colliding wind binary. For the purely isothermal case the structure is strongly distorted and asymmetric.

The instability is usually referred to as 'thin shell instability' although several physical mechanisms may be at work, including the KHI as in the most general case there is a velocity difference between the winds. The non-linear thin shell instability (NTSI, Vishniac 1994b) is found in hydrodynamical simulations when the thin shell is moved away from its rest position by perturbations with an amplitude at least greater than the shell width [Blondin and Marks, 1996]. The instability is due to an imbalance in the momentum flux *within* the shell as the shocked fluid moves towards opposing kinks. The transverse acceleration instability (TAI, Dgani et al. 1993, 1996b) occurs when at least one of the colliding flows is divergent. It assumes an *infinitely thin shell* and results from the perturbations in the tangential velocity that create a torque that bends the shell even more.

The aim of this section is to distinguish both instabilities in colliding wind binaries and to determine which one dominates. As seen in the introduction (§1.4.2) the TAI has a growth rate $\propto \sqrt{\lambda}$ while the NTSI has a growth rate that is independent of the wavelength but depends on the thickness of the shell. By performing simulations with increasing resolution, the behaviour of the NTSI should remain similar while the TAI should grow faster at high resolution. Fig. 3.15 shows the evolution of a colliding wind binary with identical winds and an isothermal equation of state. I set $v_{\infty 1} = v_{\infty 2}$ to avoid any initial contamination by the KHI. The simulation on the right panel is 8 times more resolved than the one on the left panel. At low resolution, perturbations become visible away from the line-of-centres early in the simulation ($t = 9.5 \times 10^4$ s). These perturbations grow slowly while they are advected, thickening the layer. At $t = 1.5 \times 10^5$ s another instability

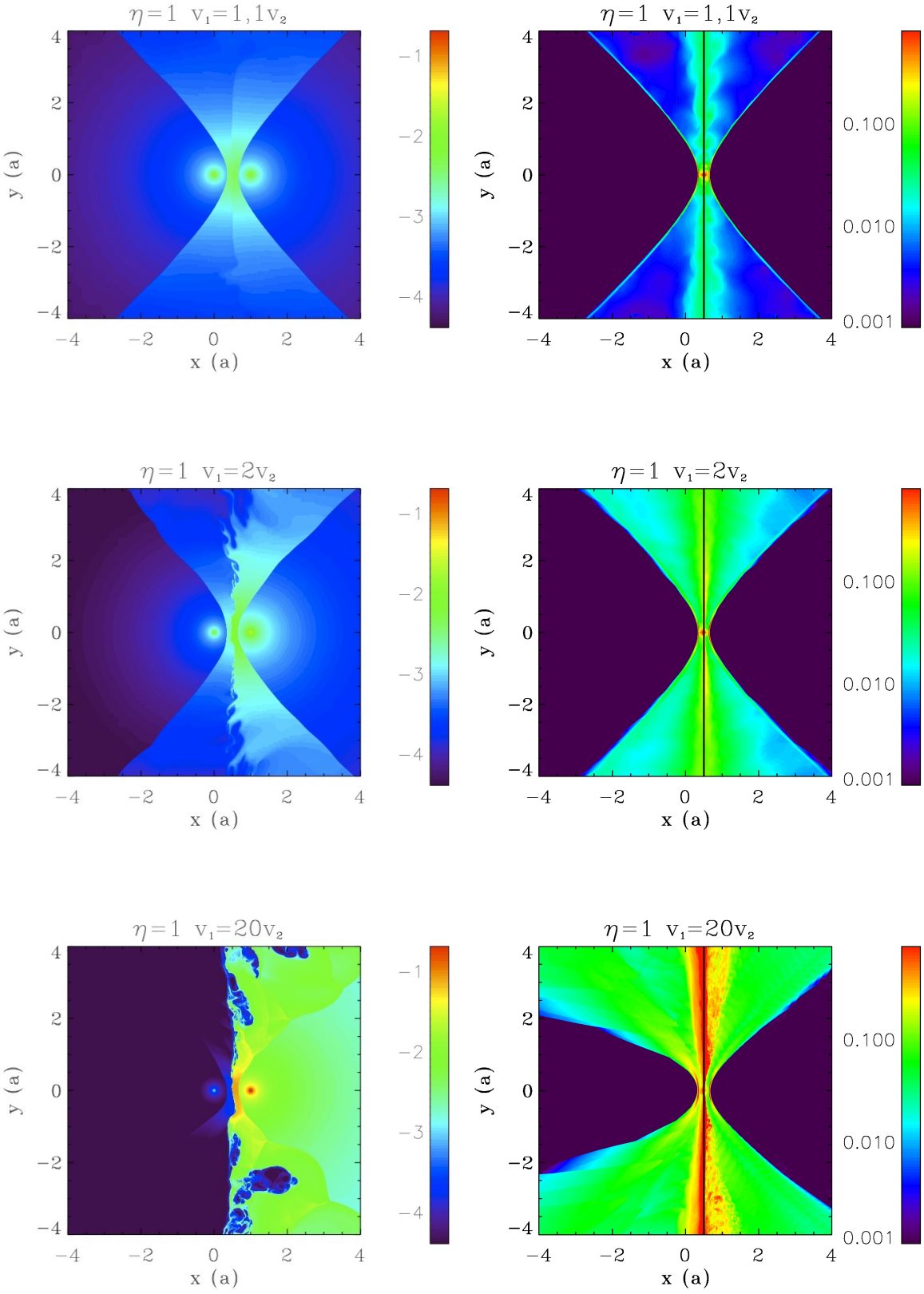

Figure 3.12: Density maps (left column) and r.m.s. of the velocity perturbations (right column) for $\eta = 1$ in the adiabatic case. From top to bottom: ($v_{\infty 1} = 1.1 v_{\infty 2}$, $\rho_1 = 0.91\rho_2$), ($v_{\infty 1} = 2v_{\infty 2}$, $\rho_1 = 0.5\rho_2$), ($v_{\infty 1} = 20v_{\infty 2}$, $\rho_1 = 0.05\rho_2$). The position of the contact discontinuity given by Eq. 3.7 is overplotted.

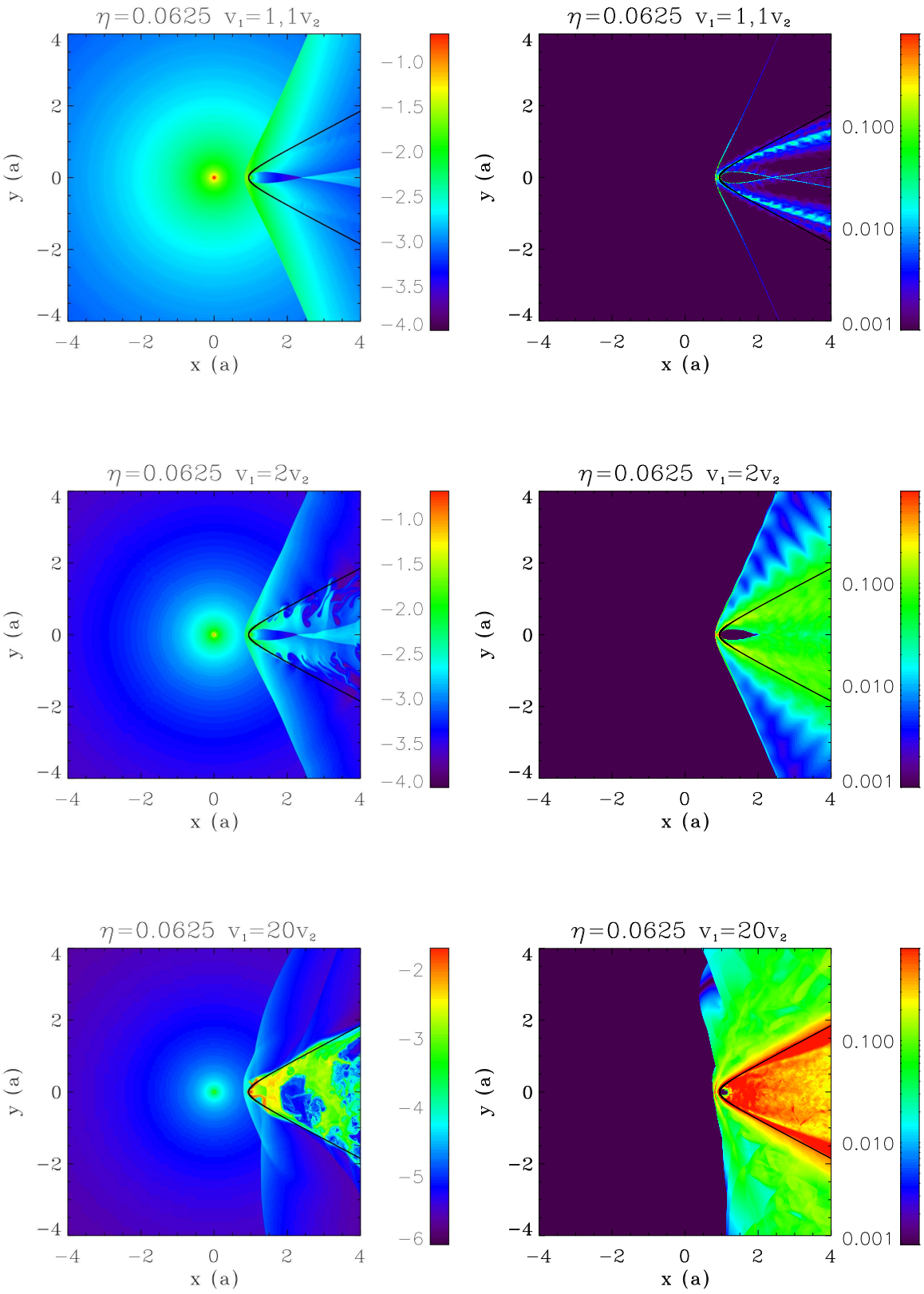

Figure 3.13: Same as Fig. 3.12 but for $\eta = 0.0625$.

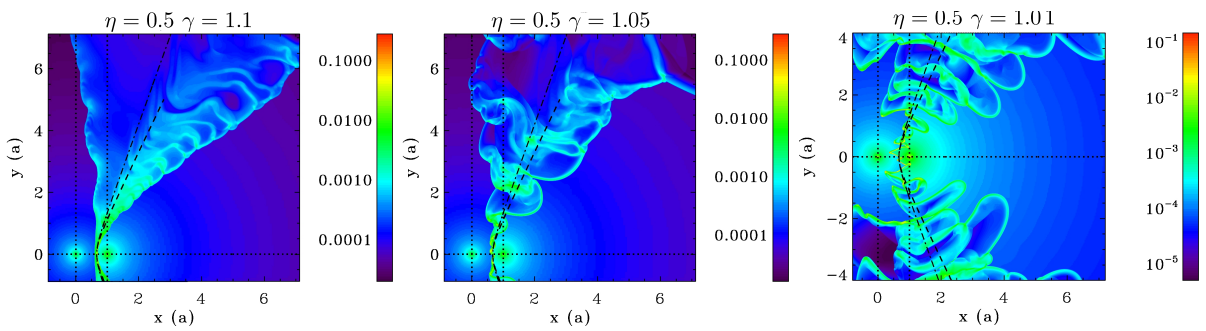

Figure 3.14: Density maps for $\eta = 0.5$ with the adiabatic index $\gamma = 1.1$, 1.05 and 1.01. The dashed lines represent the solution given by Eq. 3.6 and the dotted-dashed lines the solution by Eq. 3.7.

develops close to the binary with a growth rate higher than the advection rate and a distinct morphology. In this case matter piles up in the convex parts of the shell, which move steadily away from the initial shock position without the oscillatory behaviour seen further away from the binary. This probably is the development of a second instability. At the end of the simulation ($t = 3.1 \times 10^5$ s) the colliding wind region is dominated by these large scale perturbations. At higher resolution (right panels), the initial instability appears earlier and is also present closer to the binary axis. At $t = 9.5 \times 10^4$ s there already is a superposition of modes and one cannot define a unique wavelength any more. At $t = 1.8 \times 10^5$ s oscillations are present even on the binary axis and the structure is not symmetric any more. The final density maps shows a thicker shell with small scale structures. The oscillations are smaller than for the low resolution simulation at this time. Later evolution of the simulation shows comparable amplitudes in the oscillations at high and low resolution.

3.2.2.1 Evidence for the Non-linear Thin Shell Instability (NTSI)

The growth rate of the NTSI is estimated in the simulations by measuring the r.m.s. of the velocity perturbations. I focus on the cells on the line-of-centres where we expect the NTSI to dominate [Blondin and Koerwer, 1998]. To complete the set of simulations shown in Fig. 3.15, I perform two simulations with intermediate resolutions (2 and 3 levels of refinement). Fig. 3.16 shows the growth of the perturbations for the simulations with the different resolutions. I normalize the r.m.s to the amplitude at an arbitrary time at the beginning of the simulation and smooth it in order to avoid small wavelength perturbations that occur at higher resolutions. Up to $t \simeq 9.5 \times 10^4$ s the shell readjusts to the higher numerical resolution. Close inspection of the density maps reveals the presence of density fluctuations on the scale of the shock width during this transition. This numerical relaxation is the trigger for the NTSI close to the binary axis (left panels of Fig. 3.15). At highest resolution (upper right panel of Fig. 3.15) the NTSI develops in a region that seems already perturbed by the growth of a first instability (most likely the TAI) that probably contributes to trigger the NTSI. The exponential growth timescales estimated from fitting the r.m.s values are $\tau \approx 3.1 \times 10^4$, 2.9×10^4, 4.5×10^4 and 4.7×10^4 s for increasing resolutions. This is in reasonable agreement with the theoretical estimate $\tau_{th} = L/c_s = 2.0 \times 10^4$ s [Vishniac, 1994b]. We thus identify the instability that develops on the line-of-centres as the NTSI. Fig. 3.16 also shows that the saturation amplitude is somewhat smaller as the resolution is increased.

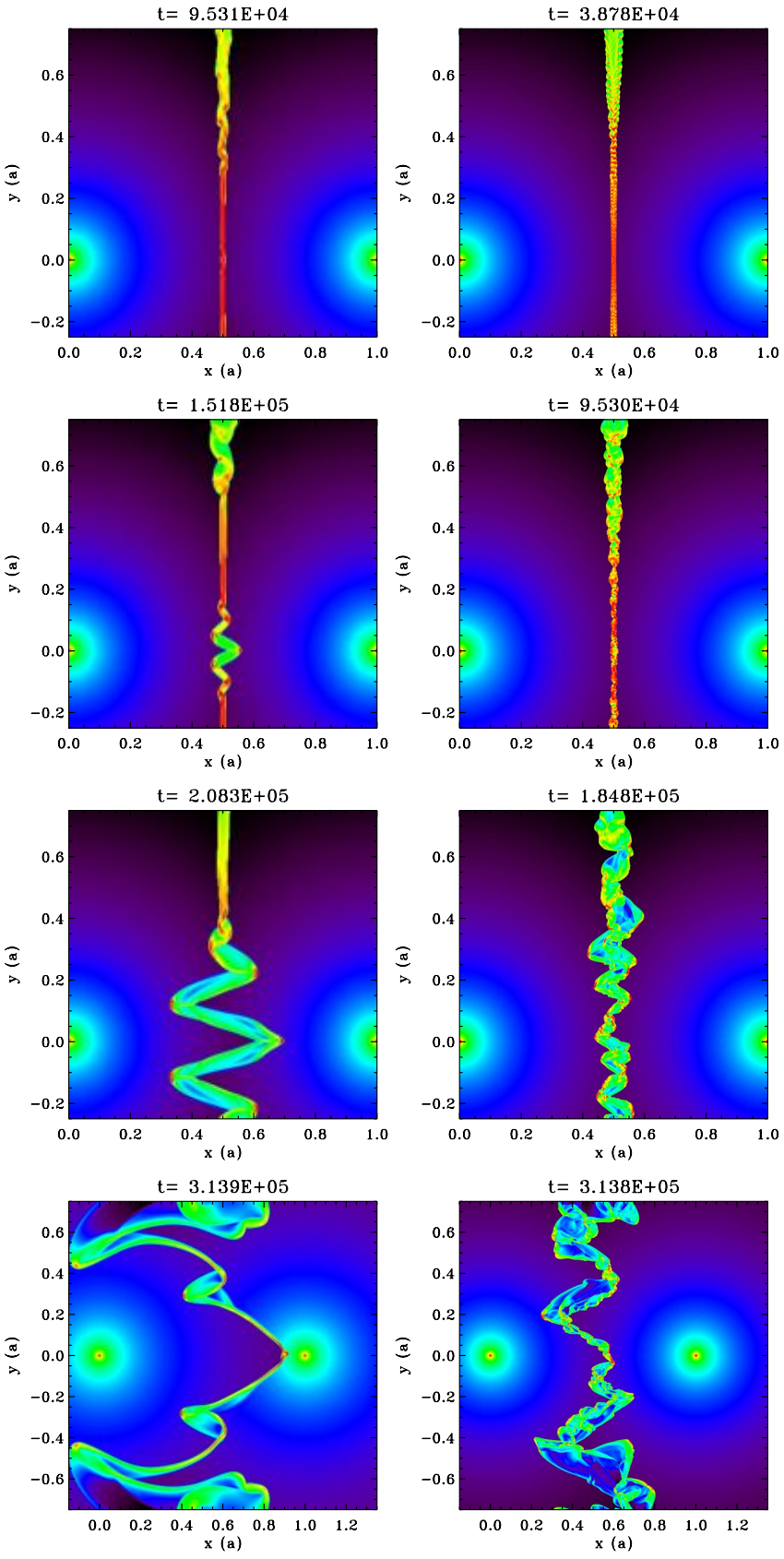

Figure 3.15: Density maps showing the evolution of a 2D colliding wing binary when $\eta = 1$ and the adiabatic index $\gamma = 1.01$. Time is given in seconds. $t = 0$ corresponds to the restart at high resolution of an initial low resolution simulation (256^2 cells, no mesh refinement). On the left panel there is one level of refinement (maximum resolution equivalent to 512^2 cells), on the right panel there are four levels (maximum resolution equivalent to 4096^2 cells).

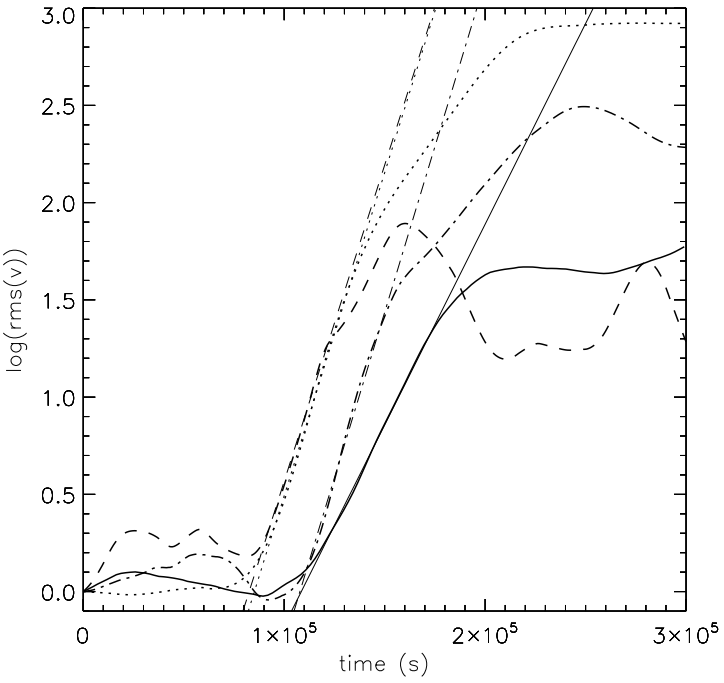

Figure 3.16: Logarithm of the root mean square (r.m.s.)of the velocity on the line-of-centres as a function of time. The curves represent maximal resolutions of 512 (dotted), 1024 (dot-dashed), 2048 (dashed) and 4096 (solid) cells per dimension. The thin straight lines show the fits to the linear phase for each resolution.

3.2.2.2 Clues for the Transverse Acceleration Instability (TAI)

The numerical simulations show that the initial perturbations are preferentially located off the binary axis with an oscillatory behaviour. Fig. 3.15 show that the perturbation has a smaller wavelength for the high resolution simulation. Measurements of the r.m.s of the velocity perturbations indicate a faster growth rate in this case. The rapid development of these perturbations is consistent with a linear instability, which theoretically arises for any perturbation. For a non-linear instability to arise, a stronger distortion of the shell is needed. The instability developing off the binary axis could be the TAI [Dgani et al., 1993, 1996b]. It is an overstability with an oscillation frequency of the velocity perturbations that scales as λ^{-1} and a has a growth timescale proportional to $\sqrt{\lambda}$. I tried to do a similar analysis than for the NTSI, but measuring the velocity perturbation off the binary axis. This does not give clear results. I do not find $\tau \propto \lambda^{1/2}$ although the instability develops faster at high resolution. I tried measuring the density perturbations, I tried focussing on zones of different spatial extention and different temporal resolution but nothing clear came out. Similarly, a Fourier analysis does not give an oscillation frequency scaling with λ^{-1}. A possible explanation, is that, even at very early stages of the simulation, several modes mix and make the identification of one single mode impossible. Although the instability we observe is compatible with the TAI, we do not formally identify it.

Vishniac [1994b] noted that the TAI grows faster than the NTSI off the binary axis when

$$\frac{l}{R_s} > \frac{2\pi}{\mathcal{M}^2}\frac{R_s}{\lambda}, \tag{3.9}$$

where l is the minimum distance along the contact discontinuity ($l = 0$ on the binary axis) beyond which the TAI can develop for a given wavelength. The instability develops preferentially along

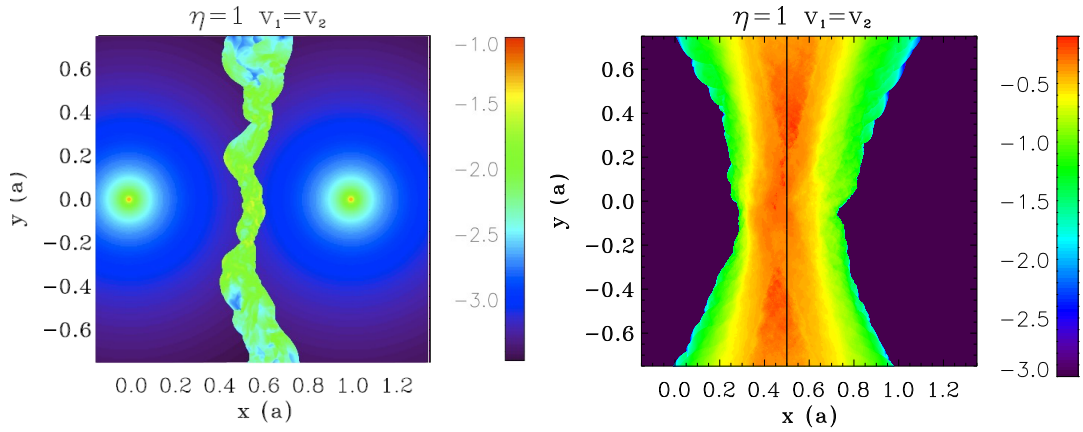

Figure 3.17: Left panel: density map with $\eta = 1$, the adiabatic index $\gamma = 1.01$ and Mach number of the winds $\mathcal{M}_{1,2} = 6$. Time is given in seconds. Right panel: time-averaged map of the r.m.s of the velocity fluctuations.

the wings [Blondin and Koerwer, 1998]. The presence of this instability closer to the binary axis at the highest resolution may explain why the growth rate of the NTSI (see Fig. 3.16) does not perfectly match the theoretical value.

My simulations indicate an initial velocity profile along the contact discontinuity that is inconsistent with the equilibrium solution proposed by Dgani et al. [1993]. I find that the azimuthal velocity of the flow varies along the contact discontinuity while their calculations assume this can be neglected. This was corrected by Myasnikov et al. [1998] who suggested another profile and concluded that the set of equations used by Dgani et al. [1993] led to inconsistencies in the dispersion relations, casting doubt on the theoretical rates to expect. We thus cannot identify the TAI in my simulations, although an instability is present and has some similarities with the TAI.

3.2.2.3 Impact of pressure

Pressure widens the shocked region and has a stabilising effect on both instabilities. I perform a simulation with $\mathcal{M}_1 = \mathcal{M}_2 = 6$ with all other physical and numerical parameters identical to those used in the previous section. Both instabilities are seen to develop but on a longer timescale than when $\mathcal{M}_{1,2} = 30$. Keeping the wind velocity constant, a lower Mach number implies a higher sound speed but the thickness of the shell increases $\propto \mathcal{M}^{-2}$ so that the growth timescale of the NTSI ($\propto L/c_s \propto 1/\mathcal{M}$) is longer. The NTSI is also harder to trigger as it requires a perturbation of amplitude comparable to the size of the shell. The TAI develops more slowly as pressure suppresses the development of small wavelength perturbations in the radial directions [Dgani et al., 1993]. The final non-linear phase with high amplitude perturbations, shown in Fig. 3.17, appears later than in Fig. 3.15. The shell is indeed thicker and presents smaller density contrasts than for high Mach numbers.

3.2.3 A dominant instability?

The simulations show that the saturation amplitude of the instability that has the properties of the TAI is low compared to the perturbations due to the NTSI. In all the simulations I perform, the non-linear evolution is dominated by the large scale, high amplitude perturbations induced

by the NTSI. The TAI-like instability probably plays a role in the early stages as a seed instability for the NTSI, as described in §3.2.2.1 but does not impact the outcome.

The respective impact of the KHI and NTSI is less obvious. Even for a 1% velocity difference between the winds, the KHI theoretically has a larger growth rate than the TAI and NTSI. Fig. 3.18 compares simulations for η =1, 16 and $v_{\infty 1} = v_{\infty 2}$ and $v_{\infty 1} = 2v_{\infty 2}$. The simulations where winds have different velocities are subject to the KHI. The density maps (left column) show there is little difference in the outcome between equal winds and $v_{\infty 1} = 2v_{\infty 2}$. The maps of the r.m.s. of the velocity fluctuations (right column) indicate a similar amplitude in both cases. If anything, the KHI seems to increase slightly the size of the region where strong fluctuations occur. However, as both simulations show a very similar outcome, it means the NTSI dominates the final non-linear phase even when the KHI is initially present. This is consistent with Blondin and Marks [1996] who concluded from their simulations of perturbed slabs that the KHI does not strongly modify the outcome of the NTSI.

The simulations with $\eta = 0.0625$ give the same results. The NTSI was studied theoretically for planar shocks but the simulations show it is also present and dominant when the shock is curved. However, following it requires higher numerical resolution. The simulation is performed with $n_x = 128$ and 5 levels of refinement in a box of size $8a$. For lower resolutions the NTSI is not triggered and the final result is stable. The density maps for equal winds and $v_{\infty 1} = 2v_{\infty 2}$ look similar. The highest velocity perturbations are at the same location but the r.m.s values are higher when an initial velocity difference is present. I conclude that having a velocity difference in a thin shell increases the amplitude of the perturbations but does not affect much the morphology of the unstable flow, which is mostly set by the NTSI.

This section shows that hydrodynamical instabilities have a major impact on the structure of the colliding wind binary. Although the overall aspect of the interaction region can still be recognised in a time-averaged sense, the wind interface can become highly turbulent, generating strong time and location-dependent fluctuations in the flow quantities. In adiabatic simulations, only the KHI can develop when winds have different speeds. This instability mostly affects the contact discontinuity between the winds, although the location of the stagnation point remains unaffected.

In isothermal simulations, an instability reminiscent of the TAI develops initially away from the binary axis. A second instability develops on the axis, which growth rate and properties match those of the NTSI. The NTSI dominates the non-linear evolution of isothermal colliding winds, leading to highly turbulent structures and large amplitude fluctuations in the location of the interface, including the stagnation point on the binary axis. These results confirm the conclusions of Blondin and Koerwer [1998] who stressed the dominance of the NTSI and the stabilising effect of pressure in their simulations of bow shocks. They also saw 'wiggles' developing early on in the shock with the same properties as those we attribute to the TAI-like instability. The trigger for the NTSI is not discussed but it is likely provided by the wiggles. However, they did not attribute these to the TAI and instead argued that the TAI acts only once the shell is perturbed by the NTSI.

3.3 Numerical requirements for a reliable simulation

Comparisons between my numerical simulations and analytic solutions validate the numerical setup I have used. They also highlight proper simulations of colliding wind binaries are computationally demanding, especially when one wind strongly dominates the other one. I have determined some criteria that should be satisfied in order to have a reliable simulation.

- The size of the masks can be an issue for winds with $\eta \ll 1$ where the shocks form very close to the second star. In this case, only an increase in resolution and a decrease in the

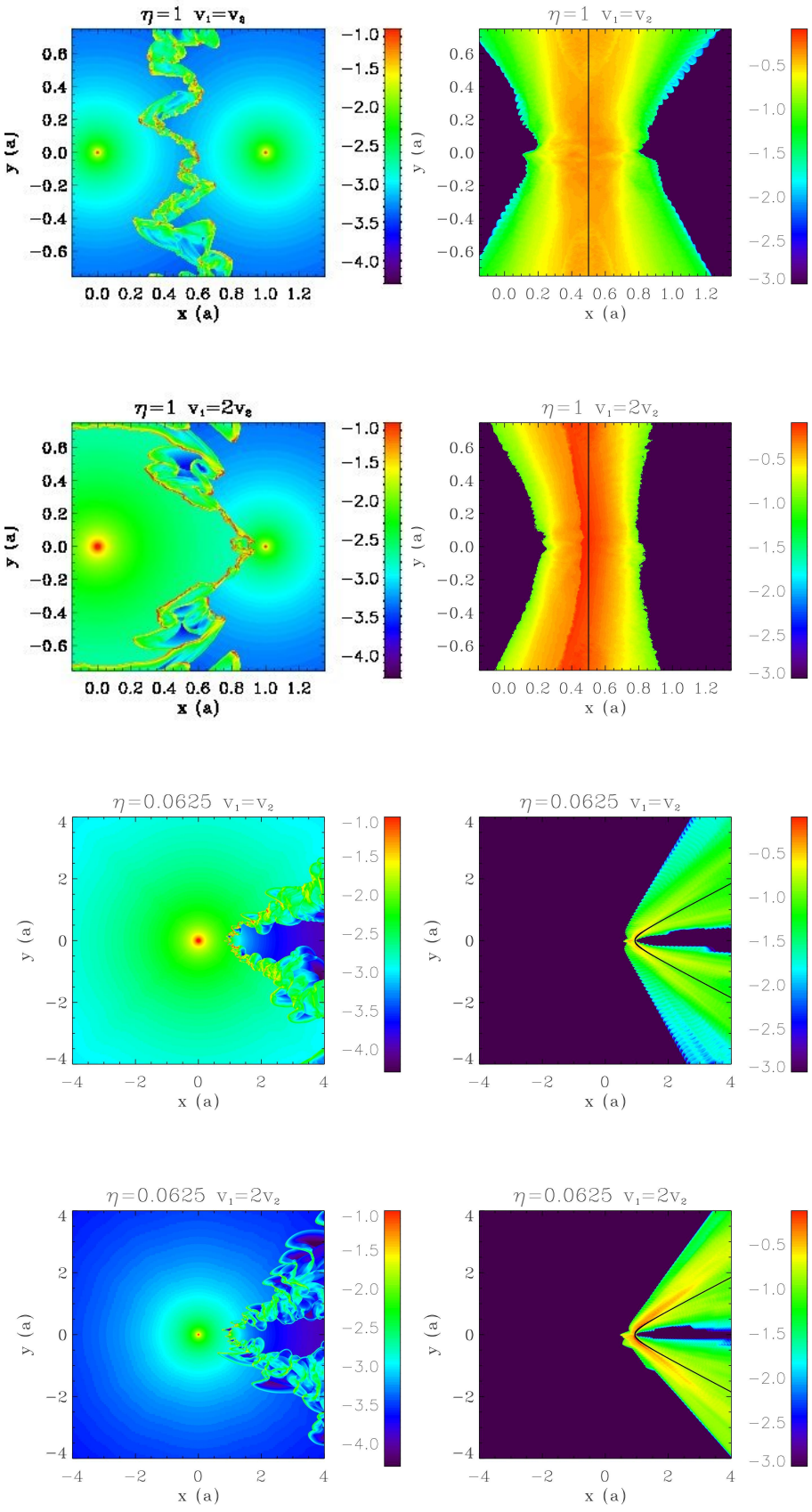

Figure 3.18: Density maps (right column) and maps of the r.m.s. (left column) for $\eta = 1$ (top panels) and $\eta = 16$ (bottom panels) with $v_{\infty 1} = v_{\infty 2}$ and $v_{\infty 1} = 2v_{\infty 2}$. The r.m.s. is a time average of the velocity fluctuations (on a logarithmic scale). The black lines give the position of the contact discontinuity determined by Eq. 3.7.

size of the masks allows for proper shock formation. This aspect is sometimes overlooked [Schneiter et al., 2007]. Fig. 3.6 clearly shows that this may become an issue for large scale simulations with $\eta \leq 0.01$. in this case the first shock forms at less than $0.01\,a$ from the second star. AMR is a well adapted tool for such simulations.

- The most stringent constraints on the resolution are set by the necessity to resolve the shocked zone in isothermal simulations for the NTSI to develop. The size of the shocked zone decreases with η and *e.g.* for $\eta = 0.03125$, in a $8\,a$ simulation box, I find that a simulation with $n_x = 128$ needs 7 levels of refinement to allow the development of the NTSI. At lower resolution, the TAI develops far from the binary but the perturbations are advected away before they can seed the NTSI. I find that the shell needs to be resolved by at least 4 computational cells on the binary axis in order to trigger the NTSI. The values given on Fig. 3.6 should be taken as upper limits for the size of the shell, as they have been determined for adiabatic shocks that have a compression rate of 4 instead of $\mathcal{M}^2$ for isothermal winds. I have found that in some simulations, the KHI can seed the NTSI and allow for the development of the instability but this effect seems to decrease with resolution. Large scale simulations of the NTSI have a very high computational cost.

- To model instabilities, one should use a numerical scheme with little numerical diffusion. A Riemann solver with little diffusivity is necessary. The absence of the Kelvin-Helmholtz instability in some simulations is probably related to the use of a highly diffusive solver (see §3.1.2 but also van Marle et al. [2011a]).

3.4 What did we learn in this chapter? What should be taken into account in improved models?

- Comparisons with analytic solutions show a good agreement and validate our numerical setup. The solution from Stevens et al. [1992] gives a better agreement at low values of η, the solution by Canto et al. [1996] gives a better agreement for high values of η.

- However at low η, the numerical simulations show strong departures from the analytic solutions : the opening angle is narrower than expected and the reconfinement shock cannot be modelled.

- Pressure widens the shocked region, in the limit of high Mach numbers, the exact value has little impact.

- The structure of 2D and 3D simulations can be connected using the mapping $\sqrt{\eta}_{2D} \rightarrow \eta_{3D}$.

- In the adiabatic limit the Kelvin-Helmholtz instability affects the contact discontinuity even when there is a 10% velocity difference between the winds. For important velocity differences, the positions of the shocks are affected.

- In the isothermal case, an instability reminiscent of the Transverse Acceleration Instability develops with a limited amplitude but is likely to trigger the Non-linear Thin Shell instability that strongly distorts the shocked region and dominates the structure, even when the KHI is present.

- Simulations at low η are computationally demanding, especially in the isothermal case.

- Modelling the instabilities requires high resolution and a Riemann solver with little numerical diffusivity.

My simulations are focused on the isothermal (radiatively efficient) and adiabatic limit, one should keep in mind that the behaviour of real colliding wind binaries is somewhere in between those extrema. More realistic simulations including a cooling function show the shocks become thinner and unstable as cooling increases (Stevens et al. 1992, Pittard 2009). Cooling is mainly due to line emission and free-free emission. Inverse Compton scattering and particle acceleration can also play a role (see § 1.3.2.3). Cooling can be estimated by the ratio between the cooling time scale and the advection time scale χ [Stevens et al., 1992] (§1.3.2.3).

$$\chi \approx \left(\frac{v_\infty}{1000\ \mathrm{km\,s^{-1}}}\right)^4 \left(\frac{a}{10^{12}\,\mathrm{cm}}\right) \left(\frac{10^{-7}\,\mathrm{M_\odot\,yr^{-1}}}{\dot{M}}\right), \tag{3.10}$$

with $\chi \gtrsim 1$ for an adiabatic wind and $\chi \lesssim 1$ for a radiatively efficient wind. This only provides a rough estimate; using numerical simulation, Pittard [2009] determines cooling becomes non-negligible as soon as $\chi \lesssim 3$. In the next chapter (§ 4.3), I provide more details on the manner to determine whether a system presents strong coooling or not.

The ratio χ_1/χ_2 of the wind is thus $\propto (v_{\infty 1}/v_{\infty 2})^5 \eta$. Because v appears with a large power, a significant difference in wind velocities essentially implies that the slowest wind will be close to isothermal. In this case, thin shell instabilities develop but their outcome may be different because of the stabilising effect of thermal pressure from the neighbouring adiabatic shock [Stevens et al., 1992, Walder and Folini, 1998, van Marle et al., 2011a]. The saturation amplitude of the NTSI depends strongly on the radiative losses and including a realistic cooling function in the energy equation of the fluid is essential for a detailed comparison with observations (Strickland and Blondin 1995, Walder and Folini 1996). The thickness of the shocked region will necessarily be larger than the idealised isothermal case.

In my simulations, both winds have reached their terminal velocity when they collide. This does not take into account different mechanisms that may accelerate and decelerate the wind at different distances from the stars. The first one is radiative acceleration of the winds that occurs on a few stellar radii (see §1.3.1.4). When $\eta \ll 1$ the shocks are close to the second star and the second wind is not fully accelerated yet and the collision probably occurs with an even lower value for η. Stevens and Pollock [1994] explain the acceleration can also be limited by the radiation field from the companion star, by radiative inhibition. Complementary, when getting very close to the second star, its strong radiation field can suddenly brake the wind from the primary star [Gayley et al., 1997] and moderate the wind-wind collision causing radiative braking. A proper estimate of the velocities of the winds and thus of the position of the stagnation point requires to determine the effects of both stellar fields through line scattering in a set of spectral lines, following the CAK formalism.

The curvature of the shock region due to orbital motion can be neglected close to the binary. Still, orbital motion also induces a skew angle between the line-of-centres of the binary and the symmetry axis of the shocked structure [Parkin and Pittard, 2008] that we have neglected in this chapter. In the next chapter I will detail the impact of orbital motion on the colliding wind region. I will focus on adiabatic winds as our final goal is to model γ-ray binaries where the cooling timescale is long enough so that the collision region can be considered as adiabatic.

Compressed magnetic fields in the shock region, if present, can also modify the growth rates and saturation amplitudes of the instabilities. For instance, the KHI is stabilised when the flow is parallel to the magnetic field and the velocity difference is smaller than the Alvén speed [Gerwin, 1968]. Similarly, Heitsch et al. [2007] find that an ordered magnetic field has a stabilising effect on the NTSI in a thin slab.

The work presented in this chapter has been published in Lamberts et al. [2011a] that is included at the end of this chapter.

3.5 Resumé en français

Ce chapitre présente des simulations à deux et trois dimensions de la zone d'interaction des vents proche du système binaire (<10 fois la séparation du système binaire). Dans ce cas on peut s'affranchir de l'impact du mouvement orbital. Dans un premier temps j'ai effectué des simulations avec une importante diffusivité numérique qui empêche le développement d'instabilités. Cela m'a permis de comparer les résultats des simulations avec des solutions analytiques pour la position de la discontinuité de contact (Stevens et al. [1992], [Canto et al., 1996]). Il y a un bon accord entre les deux, que ce soit dans la limite adiabatique ou isotherme. Cependant, lorsque l'un des deux vents domine fortement l'autre, l'angle asymptotique prédit par la théorie est supérieur au résultat de la simulation. Dans ce cas il y a un choc de reconfinement qui ne peut pas être prédit analytiquement. J'ai montré que la pression peut elargir la zone choquée.

Les solutions analytiques ne permettent pas de prendre en compte le dévelopement d'instabilités. La discontinuité de contact entre les vents est sujette à l'instabilité de Kelvin-Helmholtz qui apparait même pour une différence de vitesse entre les vents de 10%. A moins d'avoir un très grand rapport de vitesses ($v_{\infty 1}/v_{\infty 2} = 20$ par ex.), elle n'impacte que la zone choquée. La collision de vents isothermes résulte en une zone d'interaction beaucoup plus mince et très instable. Elle est soumise à une instabilité de faible amplitude [Dgani et al., 1993] qui se développe en dehors de l'axe des deux étoiles. Cette instabilité permet probablement d'en déclencher une autre, de nature non-linéaire [Vishniac, 1994b], au centre de la binaire. Celle-ci crée d'importantes perturbations qui affectent fortement la position des chocs et dominent la structure finale, même en présence de l'instabilité de Kelvin-Helmholtz.

Ces instabilités n'apparaissent que si la résolution numérique est suffisante et la diffusivité faible. Lorsque l'un des vents domine fortement l'autre, la zone choquée est mince et très près de l'étoile au vent le plus faible. Une résolution élevée est nécéssaire pour que les chocs puissent se former correctement. Si les vents sont isothermes la couche choquée est encore plus fine. J'ai découvert qu'elle doit couvrir au moins quatre cellules pour que des instabilités puissent s'y développer. A l'heure actuelle, des simulations à grande échelle de vents isothermes instables semblent encore trop couteuses en temps de calcul.

L'ensemble de cette étude et ses conclusions ont été publiés dans l'article Lamberts et al. [2011a] joint à la fin de ce chapitre.

3.6 Paper: High resolution numerical simulations of unstable colliding stellar winds (MNRAS, 2011)

Mon. Not. R. Astron. Soc. **000**, 1–?? (2011) Printed 8 September 2011 (MN LATEX style file v2.2)

High resolution numerical simulations of unstable colliding stellar winds

A. Lamberts[1⋆], S. Fromang[2] and G. Dubus[1]
[1] *UJF-Grenoble 1 / CNRS-INSU, Institut de Planétologie et d'Astrophysique de Grenoble (IPAG) UMR 5274, Grenoble, F-38041, France.*
[2] *Laboratoire AIM, CEA/DSM - CNRS - Université Paris 7, Irfu/Service d'Astrophysique, CEA-Saclay, 91191 Gif-sur-Yvette, France*

Accepted 2011 August 18. Received 2011 May 20

ABSTRACT
We investigate the hydrodynamics of the interaction of two supersonic winds in binary systems. The collision of the winds creates two shocks separated by a contact discontinuity. The overall structure depends on the momentum flux ratio η of the winds. We use the code RAMSES with adaptive mesh refinement to study the shock structure up to smaller values of η, higher spatial resolution and greater spatial scales than have been previously achieved. 2D and 3D simulations, neglecting orbital motion, are compared to widely-used analytic results and their applicability is discussed. In the adiabatic limit, velocity shear at the contact discontinuity triggers the Kelvin-Helmholtz instability. We quantify the amplitude of the resulting fluctuations and find that they can be significant even with a modest initial shear. Using an isothermal equation of state leads to the development of thin shell instabilities. The initial evolution and growth rates enables us to formally identify the non-linear thin shell instability (NTSI) close to the binary axis. Some analogue of the transverse acceleration instability is present further away. The NTSI produces large amplitude fluctuations and dominates the long-term behaviour. We point out the computational cost of properly following these instabilities. Our study provides a basic framework to which the results of more complex simulations, including additional physical effects, can be compared.

Key words: hydrodynamics — instabilities — binaries: general — stars: massive — stars: winds, outflows — methods:numerical

1 INTRODUCTION

The stellar winds of massive stars are driven by radiation pressure to highly supersonic terminal velocities $v_\infty \approx 1000 - 3000$ km s^{-1}, with mass loss rates that can reach $\dot{M} \approx 10^{-6}$ M$_\odot$ yr^{-1} in O stars and 10^{-4} M$_\odot$ yr^{-1} in Wolf-Rayet stars (Puls et al. 2008). The interaction of two such stellar winds in a binary system creates a double shock structure where the material is condensed, heated and mixed with important observational consequences (see Pittard et al. 2005 for a review). For instance, these colliding wind binaries (CWB) have much larger X-ray luminosities than seen in isolated massive stars due to the additional emission from the shock-heated material. The increased density in the shock region also has an impact on the absorption of light within the binary. Further away from the system, free-free emission is detected in the radio, possibly supplemented by synchrotron radiation from electrons accelerated at the shock. High-resolution imaging in infrared (Tuthill et al. 1999) and radio (Dougherty et al. 2003) has made it possible to trace the large scale spiral structure created by the winds with the orbital motion of the stars. The interpretation of these observations requires knowledge of the shock structure and geometry.

Assuming a purely hydrodynamical description, the interaction results in the formation of two shocks separated by a contact discontinuity. In the adiabatic limit, the gas behind the shock is heated to temperatures $T \sim \mathcal{M}^2 T_w$ (where T_w is the wind temperature and $\mathcal{M} > 1$ is the Mach number of the wind). The structure is shaped primarily by the momentum flux ratio of the winds (Lebedev & Myasnikov 1990)

$$\eta \equiv \frac{\dot{M}_2 v_{\infty 2}}{\dot{M}_1 v_{\infty 1}}. \quad (1)$$

The subscript 1 stands for the star with the stronger wind, the subscript 2 for the star with the weaker wind. For reasons of symmetry, the contact discontinuity is on the midplane between the stars when $\eta = 1$. Pilyugin & Usov (2007) obtained a complete semi-analytic description of the interaction region for this specific case. When $\eta \neq 1$ the shock structure bends towards one of the stars as the stronger wind gradually overwhelms the weaker wind. This leads to a bow shock shape close to the binary and the contact discontinuity shows an asymptotic opening angle at large scales (neglecting orbital motion, Girard & Willson 1987). The shock structure must then be derived from numerical simulations (Luo et al. 1990). It

⋆ E-mail: Astrid.Lamberts@obs.ujf-grenoble.fr

depends on other parameters (Mach number, velocity ratio of the winds) and, crucially, on the cooling properties of the gas. Cooling becomes efficient when the radiative time scale of the shocked flow becomes shorter than its dynamical time scale (Stevens et al. 1992). In this case, the kinetic energy of the wind (typically $\sim 10^{36}$ erg s^{-1}) is radiated away and the incoming gas is strongly decelerated at the shock ($v = v_\infty/\mathcal{M}^2$ in the isothermal limit compared to $v = v_\infty/4$ in the adiabatic limit). The interaction region becomes thin and the double shock structure indistinguishable from the contact discontinuity. Analytical solutions for the interaction geometry can be derived in the limit of an infinitely thin shock (Girard & Willson 1987; Luo et al. 1990; Dyson et al. 1993; Canto et al. 1996; Gayley 2009, see §3 below).

The analytical solutions provide useful approximations but their validity may be questioned as numerical simulations show that shocks become unstable (see §4). The contact discontinuity separates two media with different tangential velocities, triggering the Kelvin-Helmholtz instability (KHI) in adiabatic or radiatively-inefficient shocks. The impact is more or less pronounced (Stevens et al. 1992; Lemaster et al. 2007; Pittard 2009; Parkin & Pittard 2010; van Marle et al. 2011) and has not been quantified yet. Thin shocks become violently unstable and have garnered more attention. The instability was initially seen in simulations where the gas was assumed to be isothermal, mimicking the effect of efficient cooling (Stevens et al. 1992; Blondin & Koerwer 1998 but see Myasnikov et al. 1998), and has since also been seen in simulations including a more realistic treatment of radiative cooling (Pittard 2009; van Marle et al. 2011). The resulting mixing and variability can have important observational consequences. The origin of the instability remains unclear (Walder & Folini 1998). Two mechanisms have been proposed in the thin shell limit: the non-linear thin shell instability (NTSI, Vishniac 1994) and the transverse acceleration instability (TAI, Dgani et al. 1993, 1996) ; both may be at work in colliding winds (Blondin & Koerwer 1998).

Much progress has been made in including more realistic physics in simulations of CWB (wind acceleration, gravity from the stars, radiative inhibition, cooling functions, heat conduction, orbital motion etc.). These are undoubtedly important effects to consider when comparing with observations but they complicate the comparison with basic analytical expectations which, in turn, makes it more difficult to assess their contributions. Here, we present simulations neglecting all these effects, assuming a polytropic gas $P \propto \rho^\gamma$ with $\gamma = 5/3$ (adiabatic) or $\gamma = 1$ (isothermal). Our purpose is to understand how the shock region compares to expectations and to constrain the conditions giving rise to instabilities particularly in the limit of low η. We performed a systematic set of 2D and 3D numerical simulations using the hydrodynamical code RAMSES (Teyssier 2002) with adaptive mesh refinement, allowing us to reach the high resolutions required for thin shocks and low η while keeping a wide simulation domain to study the asymptotic behaviour (§2). Notable features of the wind interaction region are discussed and compared to the analytical solutions: shock location, width, opening angle and the presence of reconfinement shocks at low η (§3). We present our investigations of the instabilities in the adiabatic and isothermal case in §4. We find that the non linear thin shell instability (NTSI) is the dominant mechanism for isothermal winds. We then replace this work in its larger context, discussing the impact that including additional physics would have on our conclusions and the computational cost required to follow the instabilities (§5).

2 NUMERICAL SIMULATIONS

We use the hydrodynamical code RAMSES (Teyssier 2002) to perform our simulations. This code uses a second order Godunov method to solve the equations of hydrodynamics

$$\frac{\partial \rho}{\partial t} + \nabla \cdot (\rho \mathbf{v}) = 0 \quad (2)$$

$$\frac{\partial (\rho \mathbf{v})}{\partial t} + \nabla \cdot (\rho \mathbf{v}\mathbf{v}) + \nabla P = 0 \quad (3)$$

$$\frac{\partial E}{\partial t} + \nabla \cdot [\mathbf{v}(E + P)] = 0 \quad (4)$$

where ρ is the density, $\mathbf{v}$ the velocity and P the pressure of the gas. The total energy density E is given by

$$E = \frac{1}{2}\rho v^2 + \frac{P}{(\gamma - 1)} \quad (5)$$

γ is the adiabatic index, its value is 5/3 for adiabatic gases and 1 for isothermal gases. For numerical reasons γ is set to 1.01 for isothermal simulations (Truelove et al. 1998). We use the MinMod slope limiter. We compare our simulations with analytic solutions in §3. In order to do this, we prevent the development of instabilities in the shocked region by using the local Lax-Friedrich Riemann solver, which is more diffusive. An exact Riemann solver is used to study the development of instabilities in §4. We perform 2D and 3D simulations on a Cartesian grid with outflow boundary conditions. We use adaptive mesh refinement (AMR) which enables to locally increase the spatial resolution according to the properties of the flow. In 2D the grid is defined by a coarse resolution $n_x = 128$ with up to 6 levels of refinement. In 3D the grid is defined by $n_x = 32$ with up to 5 levels of refinement. The refinement criterion is based on density gradients.

2.1 Model for the winds

Our method to implement the winds is similar to the one developed by Lemaster et al. (2007) and described in the appendix of their paper. The main aspects are recalled here for completeness. Around each star, we create a wind by imposing a given density, pressure and velocity profile in a spherical zone called mask. The masks are reset to their initial values at all time steps to create steady winds. The velocity is purely radial and set to the terminal velocity v_∞ of the wind in the whole mask. Setting the velocity to v_∞ supposes the winds have reached their terminal velocity at the interaction zone. This might not be applicable for very close binaries or if $\eta \ll 1$ because the shocks are then very close to one of the stars. Our 2D setup differs from those usually found in the literature (e.g. Stevens et al. 1992; Brighenti & D'Ercole 1995; Pittard et al. 2006) in that we work in the cylindrical (r, θ) plane instead of the (r, z) plane. A drawback of our 2D method is that the structure of the colliding wind binary is not identical when going from a 2D to 3D simulation with the same wind parameters. However, as described later, we found that the 3D structure is mostly recovered in 2D by using the scaling $\sqrt{\eta_{3\mathrm{D}}} \rightarrow \eta_{2\mathrm{D}}$. An advantage of our 2D approach is that it is straightforward to include binary motion without resorting to full 3D simulations. Such simulations will be described elsewhere (see Lamberts et al. 2011 for preliminary calculations). The density profile is determined by mass conservation through the mask

$$\rho_{3D} = \frac{\dot{M}}{4\pi r^2 v_\infty} \quad \text{(3D)} \qquad \rho_{2D} = \frac{\dot{M}}{2\pi r v_\infty} \quad \text{(2D)} \quad (6)$$

where r is the distance to the centre of the mask. The pressure is determined using $P\rho^{-\gamma} = K$ with K constant in each region. Time is expressed in years and mass loss rates are expressed in $10^{-8} M_\odot$ yr^{-1}. We decide to scale all distances to the binary separation a. This way the results of a simulation can easily be rescaled to systems with a different separation. For each simulation, the input parameters are the mass loss rate, terminal velocity and Mach number $\mathcal{M}$ at $r = a$ of each wind. We then derive the hydrodynamical variables at a. After that the corresponding density, pressure and velocity profile in the mask are computed.

For $\eta \ll 1$ the shocks form very close to the second star. In this case, the mask of the star has to be as small as possible so that the shocks can form properly (Pittard 1998). However a minimum length of 8 computational cells per direction is needed to obtain spherical symmetry of the winds. We thus fix the size of the masks to 8 computational cells in each direction for the highest value of refinement. We performed tests with a single star for different sizes of the mask ranging from $0.03a$ to $1.5a$. The tests were performed for $n_x = 128$ and 4 levels of refinement. The resulting density profiles all agree with the analytic solution with less than 1 % offset. The surrounding medium is filled with a density $\rho_{amb} = 10^{-4}\rho(a)$ and pressure $P_{amb} = 0.1P(a)$. This initial medium is pushed away by the winds. Simulations with different ρ_{amb} and P_{amb} show the same final result, to round-off precision. The size of the computational domain varies between $l_{box} = 2a$ and $l_{box} = 80a$ according to the purpose of the simulation. Except where stated otherwise, we took $\dot{M}_1 = \dot{M}_2 = 10^{-7}\ M_\odot$ yr^{-1}, $\mathcal{M}_1 = \mathcal{M}_2 = 30$, $v_{\infty 2} = 2000$ km s^{-1} and η was varied by changing $v_{\infty 1}$.Hence, our low momentum flux ratios can imply very high velocities for the first wind.

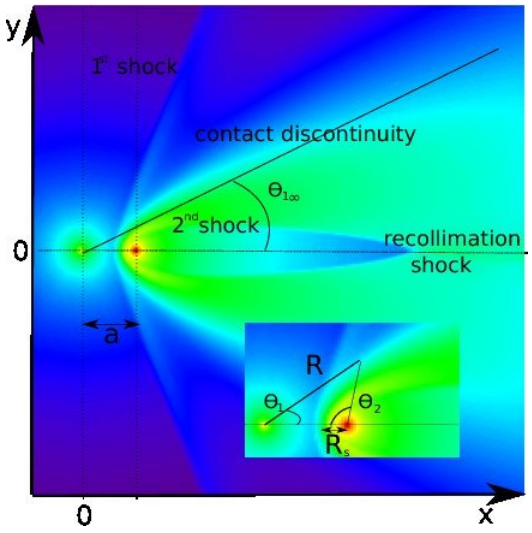

Figure 1. Density map of the interaction zone for $\eta = 1/32 = 0.03125$ (3D simulation). It is a cut perpendicular to the line of centres taken from a 3D simulation. A zoom on the binary system is shown at the bottom right corner. The stars are positioned at the intersections of the dotted lines. The first star has coordinates (0,0), the second one has coordinates (a,0). There are three density jumps (for increasing x). The first shock separates the unshocked wind from the first star from the shocked wind. The contact discontinuity separates the shocked winds from both stars. It intersects the line of centres at the standoff point R_s. The second shock separates the shocked and unshocked parts of the wind from the second star. As the wind from the second star is collimated, there is a reconfinement shock along the line of centres. $R(\theta_1)$ is the distance between the contact discontinuity and the first star, θ_1 is the polar angle. The asymptotic opening angle is given by $\theta_{1\infty}$. l is the distance to R_s along the contact discontinuity.

3 THE SHOCK REGION

In this section we study the dependence on η of the geometry of the interaction zone. We discuss he analytic solutions for the colliding wind geometry, in 2D and 3D, to which we compare our simulations. Simulations are performed with adiabatic and isothermal equations of state. In both cases the numerical diffusion introduced by the solver is sufficient to quench the development of instabilities. Section 4 deals with high resolution simulations of the development of these instabilities.

3.1 Analytical approximations

The overall structure of the colliding wind binary is given in Fig. 1. The density map shows two shocks separating the free winds from the shocked winds. The shocked winds from both stars are separated by a contact discontinuity. The Bernouilli relation is preserved across shocks hence

$$\frac{1}{2}v_{\infty 1}^2 = \frac{\gamma}{\gamma - 1}\frac{P_{1s}}{\rho_{1s}} + \frac{1}{2}v_{1s}^2 \tag{7}$$

across the first shock. The subscript s refers to quantities in the shocked region and we have neglected the thermal pressure in the unshocked wind due to its high Mach number. A similar equation holds for the second shock. The Bernouilli relation is constant in each shocked region but discontinuous at the CD. There, $P_{1s} \equiv P_{2s}$ by definition and $v_{1s} = v_{2s} = 0$ on the line-of-centres so that the two Bernouilli equations combine to give $\rho_{1s}v_{\infty 1}^2 = \rho_{2s}v_{\infty 2}^2$, with ρ_s the value of the density on each side of the contact discontinuity. Assuming that the density is constant in each shocked region on the binary axis (the numerical simulations carried out below show this is a very good approximation) then

$$\rho_1 v_{\infty 1}^2 \approx \rho_2 v_{\infty 2}^2 \tag{8}$$

where ρ_1 (ρ_2) is the value of the density at the first (second) shock. The above relation states the balance of ram pressures (Stevens et al. 1992). Using Eqs. (1) and (6) then yields

$$r_2 \approx \sqrt{\eta} r_1 \quad \text{(3D)} \qquad r_2 \approx \eta r_1 \quad \text{(2D)} \tag{9}$$

where r_1 is the distance between the first star and the first shock and r_2, the distance between the second star and the second shock. If the shock is thin then $r_1 + r_2 \approx a$ and the distance $R_s \approx r_2$ of the CD to the second star is

$$\frac{R_s}{a} \approx \frac{\sqrt{\eta}}{1+\sqrt{\eta}} \quad \text{(3D)} \qquad \frac{R_s}{a} \approx \frac{\eta}{1+\eta} \quad \text{(2D)} \tag{10}$$

Note that, for a given $\eta \leqslant 1$, the contact discontinuity is closer to the second star for a 2D geometry than for a 3D geometry.

The shock positions are not easily derived away from the line-of-centres, where the density is not constant in the shocked winds. Analytic solutions have been derived based on the thin shell hypothesis, which considers both shocks and the contact discontinuity are merged into one single layer. Stevens et al. (1992) (see also Luo et al. 1990, Dyson et al. 1993 and Antokhin et al. 2004) derive the following equation for the shape of the interaction region by assuming that it is located where the ram pressures normal to the shell balance:

$$\frac{dx}{dy} = \frac{x}{y} - \left(\frac{a}{y}\right)\left[1 + \sqrt{\eta}\left(\frac{r_2}{r_1}\right)^2\right]^{-1} \quad (11)$$

The same analysis for the 2D structure (Eq. 6) leads to

$$\frac{dx}{dy} = \frac{x}{y} - \left(\frac{a}{y}\right)\left[1 + \sqrt{\eta}\left(\frac{r_2}{r_1}\right)^{3/2}\right]^{-1} \quad (12)$$

Canto et al. (1996), extending the work of Wilkin (1996), found an analytical solution in the thin shell limit based on momentum conservation (hence, taking into account the centrifugal correction *i.e.* the forces exerted on the gas as it follows a non-linear path along the shock, Baranov et al. 1971; Dyson 1975; Girard & Willson 1987):

$$\theta_2 \cot\theta_2 - 1 = \eta\left(\theta_1 \cot\theta_1 - 1\right) \quad (13)$$

(see Fig. 1 for the definition of θ_1 and θ_2.) The same analysis in 2D leads to

$$\frac{\cos\theta_2 - 1}{\sin\theta_2} = \eta\frac{\cos\theta_1 - 1}{\sin\theta_1} \quad (14)$$

3.2 2D study

We performed a systematic study of the 2D geometry of the interaction zone in the adiabatic case for η ranging from 1 down to $1/128$ with Mach number $\mathcal{M} = 30$ for both winds. Fig. 2 shows how the main features of the colliding wind binary vary with η. The positions of the discontinuities on the binary axis (top left) were computed by determining the local extrema of the slope of the density, excluding the masks. There is very good agreement with the analytic solution for the position of the standoff point (Eq. 10). The relation for the ratio of shock positions (Eq. 9) is also verified (top right). As η decreases both shocks and the contact discontinuity get closer to the star with the weaker wind. Since the thickness of the shell decreases as η decreases, proper modelling of the interaction region for low η requires a higher numerical resolution. For $\eta \lesssim 0.25$, the second wind is totally confined and there is a reconfinement shock on the line of centres behind the second star (see Fig. 1). This shock draws closer to the second star as η decreases (Fig. 2, bottom left). Similar structures were found by Myasnikov & Zhekov (1993) and Bogovalov et al. (2008) (in the latter case for $\eta < 1/800$). The last panel (bottom right) shows the asymptotic opening angle of the contact discontinuity. The solution from Stevens et al. (1992) gives a better agreement for low values of η.

For given Mach numbers, the geometrical structure of the colliding wind binary is set by η. We performed a series of tests for $\eta = 1/8 = 0.125$ and different combinations for $v_{\infty 1}$, $v_{\infty 2}$, $\dot{M}_1$ and $\dot{M}_2$. Although the density and velocity fields were different in all cases, both shocks and the contact discontinuity were located at the same place along the line of centers. Further away from the star we notice that the reconfinement shock position changes up to $\simeq 25\%$ when changing the velocity and mass loss rate of the winds. All other discontinuities are located at the same place. Simulations with $\mathcal{M}_1 = \mathcal{M}_2 = 100$ do not show differences from the case $\mathcal{M}_1 = \mathcal{M}_2 = 30$, as could be expected since thermal pressure is negligible in both cases. However, the structure for given η depends somewhat on the Mach number of the winds if these are not very large. Fig. 3 shows the density maps for 2D simulations with $\eta = 0.25$ but with different values for the wind Mach numbers obtained by changing the wind temperature. If both winds have $\mathcal{M} = 5$ instead of $\mathcal{M} = 30$, the shocked region is wider and a reconfinement shock appears at $\approx 15a$ (beyond the region shown in Fig. 3). The position of the contact discontinuity remains the same. When both winds have different Mach numbers, the whole shocked structure is more bent towards the wind with the higher Mach number : thermal pressure from the low Mach number wind is not negligible in the shock jump conditions (see Eq. 7) and the added term displaces the shock away from the low Mach number wind.

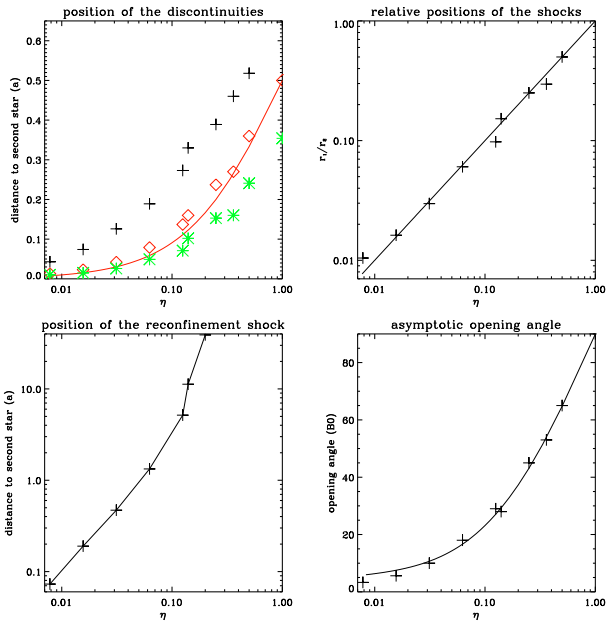

Figure 2. Dependence of the shock geometry with η in 2D. Top left panel: Position of the different density jumps: first shock (black crosses), contact discontinuity (blue diamonds) and second shock (green asterisks). The 2D analytic solution for the contact discontinuity (Eq. 10) is overplotted (blue solid line). Top right panel: ratio of the shock positions measured from the simulations and compared to Eq. 9. Bottom left panel : position of the reconfinement shock. Bottom right panel: asymptotic opening angle (crosses) compared with the asymptotic angle derived from the Canto et al. (1996) (dashed line) and Stevens et al. (1992) (solid line) solutions.

We also investigated the overall structure in the isothermal case, quenching the strong instabilities that are present in this case (see §4.2) by using a highly diffusive solver. In this case pressure support is weaker and the shell is much thinner, as expected. The double shock structure and CD are only visible on the line of centres when using a very high spatial resolution. The position of the thin shock structure on the line of centres is within 10% of the CD position found in adiabatic simulations. The asymptotic angle is difficult to assess as the shock structure is smoother than in the adiabatic case (see e.g. Fig. 4 below) but the bracketing values are consistent with those found in the adiabatic case. We find that the weaker wind can be fully confined as in the adiabatic case. However, this occurs further away from the star than in the adiabatic case shown in Fig. 2 (at $\approx 6.4a$ for $\eta = 1/16$ and $2.2a$ for $\eta = 1/32$).

3.3 3D study

We completed this 2D study with the analysis of a few large scale 3D simulations, computationally more expensive than the previous 2D simulations. Fig. 4 shows the density maps for adiabatic and isothermal 3D simulations with $\eta = 0.5$ and $\eta = 1/32$ ($\mathcal{M}$=30). In the adiabatic case, one can clearly see the two shocks and the

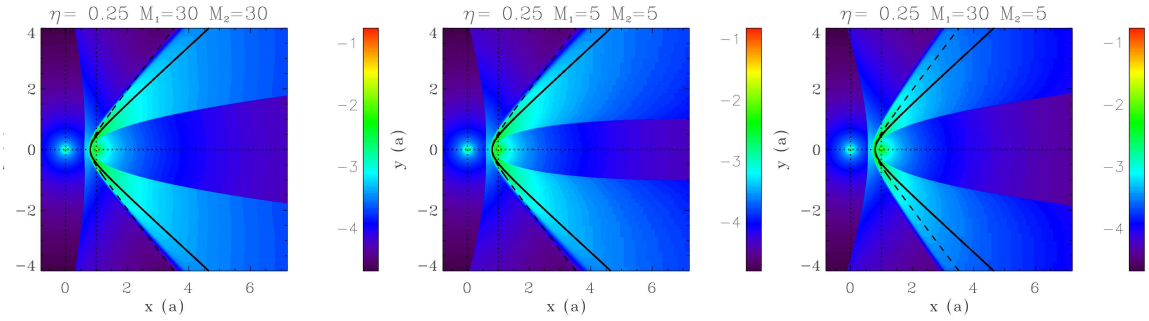

Figure 3. Density maps for 2D simulations with $\eta = 0.25$ and different Mach numbers for the winds ($\mathcal{M}_1$, $\mathcal{M}_2$). The 2D analytic solutions derived from the assumptions of Canto et al. (1996) and Stevens et al. (1992) are represented respectively by the dashed and solid line. The analytic solutions both assume infinite Mach numbers for both winds.

contact discontinuity. For $\eta = 1/32$ the weaker wind is totally confined with maximum extension along the axis up to $5a$ away behind the star. For $\eta = 1/64 \approx 0.016$ (not shown) we find the reconfinement shock occurs at $1.0a$. This is consistent with the 2D results (Fig. 2) if assuming the rough mapping $\sqrt{\eta_{3D}} \rightarrow \eta_{2D}$ suggested by Eq. 10. Indeed, we find no reconfinement shock for 3D simulations with $\eta = 0.08$ (which would correspond to $\eta_{2D} \approx 0.29$ in Fig. 2).Pittard & Dougherty (2006) performed 2D axisymmetric simulations showing a reconfinement shock for
$eta = 0.02$ but not for $\eta = 0.036$. We performed several 3D simulations with $\eta = 1/32 = 0.03125$ or $\eta = 0.02$ and for different values of the Mach number $\mathcal{M}$ (assumed identical in both winds). We found that reconfinement occurs in all cases when $\mathcal{M} = 30$ or 100 but that no reconfinement occurs for $\eta = 0.02$ or $\eta = 1/32$ when $\mathcal{M} = 5$. As in the 2D case, non-negligible thermal pressure has an impact on the structure of the colliding wind binary. Whereas the presence of reconfinement for low η and high Mach numbers around a threshold value 0.02-0.03 appears robust, the precise determination of this threshold value or of the properties of the reconfinement region is sensitive to the exact wind properties (Mach number). Radiative cooling, which is neglected here, can also have an impact on reconfinement (e.g. 2D isothermal simulation showed reconfinement further away from the star than in the adiabatic case, §3.2).

The positions of the discontinuities along the line of centres agree within 2% with the expected values. As with the 2D case, the shock shape is better approximated by the solution of Stevens et al. (1992) at low η. For $\eta = 0.5$ we find $\theta_\infty = 71^\circ$ whereas the asymptotic angle from both Stevens et al. (1992) and Canto et al. (1996) give 78°; for $\eta = 1/32 = 0.03125$ we get 23° compared to theoretical estimates of 27° (Stevens et al. 1992) and 35° (Canto et al. 1996). On the other hand, Figs. 3-4 show that the analytic solution of Canto et al. (1996) is a better approximation to the contact discontinuity shape at high η. For $\eta \geqslant 1/32$, close to the line of centres, the shocked region is thinner in the 3D case than in the 2D. For smaller values of η, the shocked zone is thicker in the 3D case. In all cases the contact discontinuity is further away from the second star in the 3D case than in the 2D case.

We have studied the geometry of the interaction region in 2D and 3D. We conclude that analytic solutions give satisfactory agreement with the results of the simulations. The solution based on ram pressure balance normal to the shock reproduces better the asymptotic opening angle of the flow at low η. We also find that the weaker wind can be entirely confined for low values of η. However, the interaction region is susceptible to instabilities that can modify these conclusions. This is investigated in the next section.

4 INSTABILITIES

4.1 The Kelvin-Helmholtz instability (KHI)

When the exact Riemann solver is used, there is less numerical diffusion and the velocity shear at the contact discontinuity leads to the development of the KHI. The interface of two fluids is unstable to any velocity perturbation along the flow in the absence of surface tension or gravity (Chandrasekhar 1961). The growth rate of the instability in the linear phase is $\tau_{KHI} = \lambda/(2\pi\Delta v)$ where Δv is the difference of velocity between the two layers and λ the wavelength of the perturbation. In practice, numerical simulations are limited by diffusivity and the minimum resolvable structure, inevitably stunting the instability at small λ. At the other end of the scale, the development of instabilities with large wavelengths can be hampered by their advection in the flow. The dynamical timescale can be estimated by $\tau_{dyn} \sim a/c_s$ where c_s is the post-shock sound speed, which is of the order of the wind velocity v_∞ in a strong adiabatic shock. Hence, the scale of the perturbations may be expected to be limited to $\lambda/a < \Delta v/v$. For two identical winds with terminal velocities of 2000 km s^{-1} and $a = 1$ AU, $\tau_{dyn} \simeq 6.8 \times 10^4s= 2.2 \times 10^{-3}$ yr.

We performed a set of simulations with $\eta = 1$, increasing the velocity $v_{\infty 1}$ of the first wind to investigate the impact of the KHI in the adiabatic case. The mass loss rate $\dot{M}_1$ was simultaneously decreased and the Mach number $\mathcal{M}_1$ of the wind was kept equal to 30. The size of the domain is $8a$ and the resolution is $n_x = 128$ with 5 levels of refinement. The simulations were run up to $t = 600\tau_{dyn}$. A steady state is reached well before the end of the simulation, as determined by looking at the time evolution of the total r.m.s. of the density or velocity perturbations over the whole simulation domain. Restricting ourselves to this steady state interval, which we checked to be much longer than the advection time along the contact discontinuity, we then computed the time average of the velocity r.m.s. for each cell of the domain. We used the median value over the same time period as our reference. The purpose was to quantify the saturation amplitude of the perturbations.

The results are shown in Fig. 5. The upper panels gives the density maps for the different cases while the corresponding lower

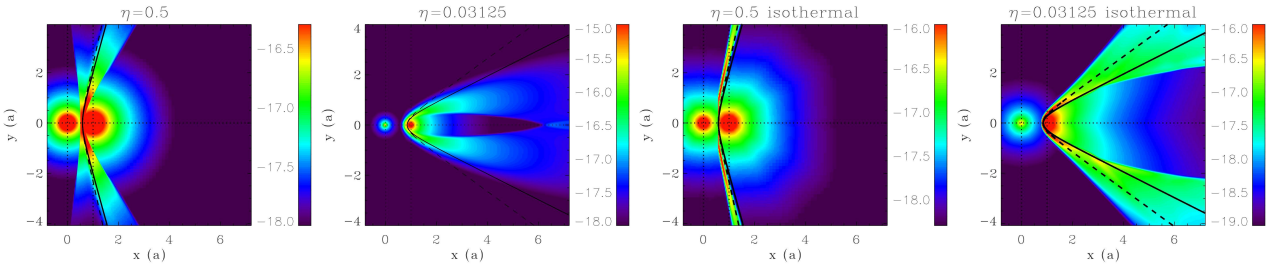

Figure 4. Density maps for 3D simulations with $\eta = 0.5$ and $\eta = 1/32 = 0.03125$ in the adiabatic ($\gamma = 5/3$) and isothermal ($\gamma = 1.01$) limits. The stars are located at the intersections of the dotted lines. The dashed line represents the solution from Canto et al. (1996), the solid line the solution from Stevens et al. (1992). The length scale is the binary separation a.

panels show the time average of the r.m.s of the velocity fluctuations. No instabilities are present when the two winds are exactly identical, as expected since there is no velocity shear. Introducing a 10% difference in the velocity of the winds leads to low amplitude perturbations that are significant only close to the contact discontinuity. A dominant wavelength can be identified, probably because growth for such a weak velocity shear is restricted to a small domain by diffusivity at short wavelengths and advection at long wavelengths. The r.m.s. of the velocity and density perturbations saturates at about 10%. When $v_{\infty 1} = 2v_{\infty 2}$ small scale eddies are visible. They are stretched in the direction of the flow. The position of the shocks is barely affected by the instability. The perturbations affect a larger zone on both sides of the contact discontinuity but their amplitude remains around a few tens of percent r.m.s., somewhat higher for the density than for the velocity perturbations. When $v_{\infty 1} = 20v_{\infty 2}$ (fourth panel) the instability has become non-linear judging by the 100% r.m.s. of the velocity (and density) fluctuations. The location of the contact discontinuity fluctuates significantly yet the region with the strongest r.m.s. is not much wider than for the previous cases. We also investigated in this last case whether keeping the wind temperature constant as $v_{\infty 1}$ is varied, instead of keeping $\mathcal{M}_1$ constant, led to differences. The outcome was similar.

A similar set of simulations was performed with $\eta = 1/16 = 0.0625$ (Fig 6). There is no velocity shear or contact discontinuity when $v_{\infty 1} = v_{\infty 2}$, even in the case $\eta \neq 1$. This can be proven as follows. The Bernouilli constant (Eq. 7) has the same value in both shocked region when $v_{\infty 1} = v_{\infty 2}$, so the densities are identical at the contact discontinuity (where pressures equalise) on the line-of-centres. The gas is polytropic with $P \equiv K\rho^{-\gamma}$ and K constant in each region. Writing that ρ and P are equal on both sides of the contact discontinuity on the line-of-centres requires that K has the same value in both shocked regions. Therefore, $\rho_{1s} = \rho_{2s}$ along the contact discontinuity. Using that the Bernouilli constant is the same in both shocked regions then proves that $v_{1s} = v_{2s}$ at the contact discontinuity. Actually, there is no discontinuity in this case. The simulation with $v_{\infty 1} = v_{\infty 2}$ confirms that there is no velocity shear and that the KHI does not develop. When $v_{\infty 1} = 1.1v_{\infty 2}$ only weak perturbations are seen, limited to a small region close to the contact discontinuity. A dominant wavelength can be identified as in the case $\eta = 1$. When $v_{\infty 1} = 2v_{\infty 2}$ the center line of the perturbations approximately matches the shape of the unperturbed contact discontinuity. The first shock is not affected by the instability. The velocity perturbations affect all the region of the shocked second wind and part of the shocked wind of the first star. The density perturbations have a higher r.m.s. than the velocity perturbations, reaching close to 100% close to the contact discontinuity. The velocity perturbation are strong when $v_{\infty 1} = 20v_{\infty 2}$ and are mostly confined to the shocked second wind. High r.m.s. density fluctuations extend to the first wind, distorting slightly the first shock. (The sawtooth appearance of the wings in the $v_{1\infty} = v_{20\infty}$ r.m.s. maps are an artefact of the limited time range over which the average was done.) The backward reconfinement of the wind of the second star is affected by the instability, occurring much closer to the second star than in the case with equal wind velocities.

The KHI modifies the interaction region as soon as the wind velocities are slightly different. The simulations suggest that the relative amplitude of the perturbations becomes significant when $v_1 \gtrsim 2v_2$, although we cannot rule out that limited numerical resolution does not impact the growth of the instability for smaller velocity shears. The instability does not erase completely the contact discontinuity. However, the turbulent motions tend to smooth out the initial structures in the region of the wind with the smaller velocity.

4.2 Isothermal equation of state: thin shell instabilities

When thermal support in the shocked zone is too weak, the shell becomes thin and unstable. This occurs for instance when the adiabatic index is decreased (Mac Low & Norman 1993). More realistic numerical simulations including radiative cooling functions also show the shocks become thinner and unstable as cooling increases (Stevens et al. 1992; Pittard 2009, but see Myasnikov et al. 1998). The instability is usually referred to as 'thin shell instability' although several physical mechanisms may be at work, including the KHI. The non-linear thin shell instability (NTSI, Vishniac 1994) is found in hydrodynamical simulations when the thin shell is moved away from its rest positions by perturbations with an amplitude at least greater than the shell width (Blondin & Marks 1996). The instability is due to an imbalance in the momentum flux within the shell as shocked fluid moves towards opposing kinks. The transverse acceleration instability (TAI, Dgani et al. 1993, 1996) occurs when at least one of the colliding flows is divergent and assumes an infinitely thin shell. Both linearly unstable breathing and bending modes are found. The breathing mode is due to the acceleration of the flow along the shell whereas the bending mode arises from the mismatch in ram pressure of the wind impacting each side of the thin shell when it is displaced from its equilibrium value.

We studied the growth of thin shell instabilities in colliding wind binaries using 2D simulations with an isothermal equation of state. Initial investigations showed that the thin shock structure

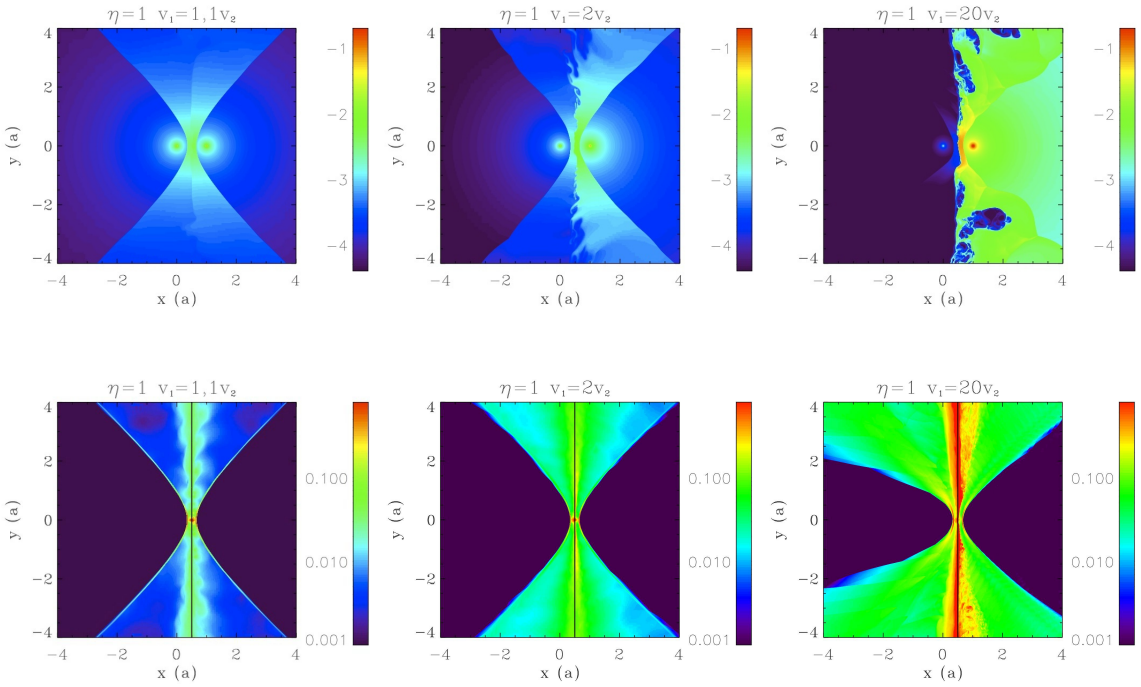

Figure 5. Development of Kelvin-Helmholtz instability in the adiabatic case for $\eta = 1$. Upper panel: density maps from left to right : $v_{\infty 1} = 1.1 v_{\infty 2}, \rho_1 = 0.91\rho_2$; $v_{\infty 1} = 2v_{\infty 2}, \rho_1 = 0.5\rho_2$; $v_{\infty 1} = 20v_{\infty 2}, \rho_1 = 0.05\rho_2$. Lower panel : r.m.s. of the velocity perturbations on a logarithmic scale. The fastest wind originates from the star on the left hand side.

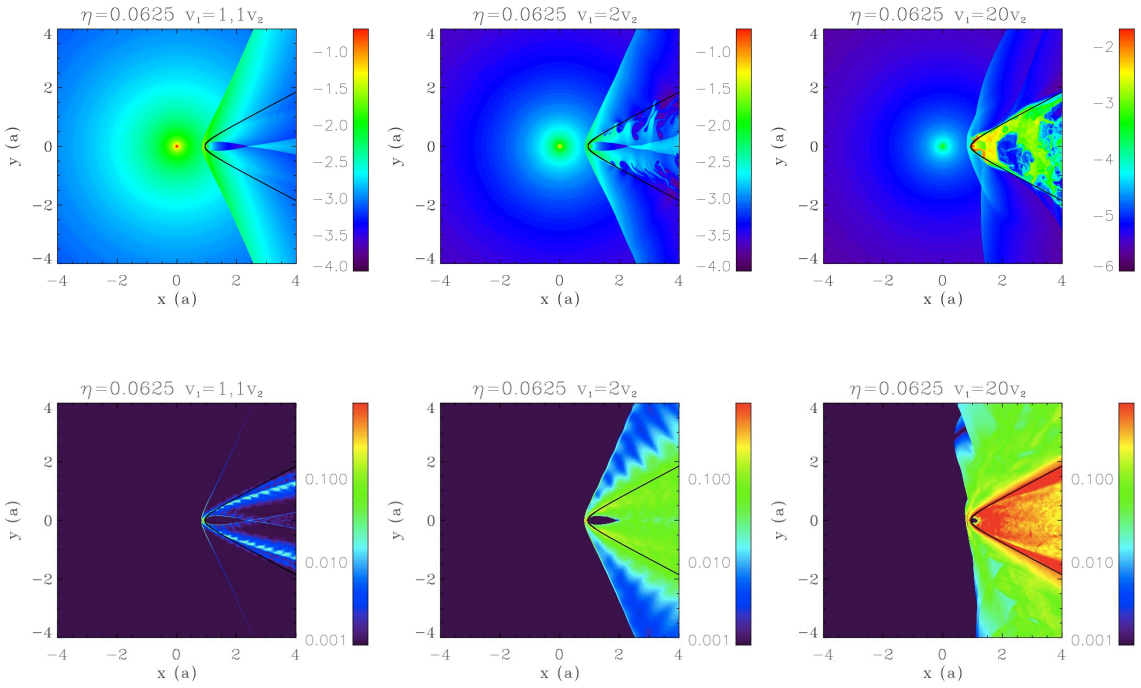

Figure 6. Same as Fig. 5 but for $\eta = 1/16 = 0.0625$.

(§3.2) becomes unstable only if there are a sufficient number of cells available ($\gtrsim 4$) to resolve the shock structure. The minimum number of cells required is even larger if a highly diffusive solver is used. Low resolution simulations without mesh refinement (256×256 cells) do not resolve the shock structure and stay stable. We decided to use those steady state solutions as the initial input for simulations at higher resolution, so as to be able to study in as much as possible the initial linear growth phase of the instabilities. The winds are chosen to have identical velocities in order to exclude any seeding by the KHI (§4.1).

The evolution of a colliding wind binary with $\eta = 1$, identical velocities and an isothermal equation of state is shown in Fig. 7. The size of the domain is $3a$. The left panels show the case with one level of mesh refinement, the right panels show the case with four levels. At low resolution (left panels), perturbations become visible away from the line-of-centres early in the simulation ($t = 9.5 \times 10^4$ s). These perturbations grow slowly as they are advected, thickening the layer. At $t = 1.5 \times 10^5$ s another instability develops close to the binary with a growth rate faster than the advection rate and a distinct morphology. In this case matter piles up in the convex parts of the shell, which move steadily away from the initial shock position without the oscillatory behaviour seen in the wings. At the end of the simulation ($t = 3.1 \times 10^5$ s) the colliding wind region is dominated by these large scale perturbations. At higher resolution (right panels), the initial instability appears earlier and is also present closer to the binary axis. At $t = 9.5 \times 10^4$ s there already is a superposition of modes and one cannot define a unique wavelength any more. At $t = 1.8 \times 10^5$ s oscillations are present even on the binary axis and the structure is not symmetric any more. The final density maps shows a thicker shell with small scale structures. The oscillations are smaller than for the low resolution simulation at this time. The evolution at subsequent times shows comparable amplitudes in the oscillations at high and low resolution.

Similar behaviour was described by Blondin & Koerwer (1998) in their simulations of stellar wind bow shocks. We tentatively associate the small amplitude instability that develops first, away from the binary axis, with the TAI. This is a linear instability that can be seeded by the initial numerical noise. The large amplitude instability that develops later on the binary axis is likely to be the NTSI. We examine below the supporting evidence.

4.2.1 *Evidence for the Non-linear Thin Shell Instability (NTSI)*

The NTSI shows the highest growth rate for perturbations of order of the shell width L. The theoretical estimate is $\tau_{th} = L/c_s = 2.0 \times 10^4$ s (Vishniac 1994) for the parameters appropriate to our simulations, smaller than the advection timescale ($\tau_{dyn} \simeq 6.8 \times 10^4$, increasing near the binary axis as the flow velocity in the shocked region goes to zero on axis). Hence, the fastest growing mode of the NTSI should be seen, independently of the numerical resolution, as long as the shell is resolved. We compared this estimate with the time evolution of the velocity perturbations in four simulations with 1, 2, 3 and 4 levels of refinement, using an exact Riemann solver. For each simulation, we computed the r.m.s. of the velocity for a line of cells along the binary axis, where the NTSI is presumed to dominate. We normalised the data to the value at the same arbitrary reference time taken close to the beginning of each simulation. The r.m.s. were smoothed to suppress small wavenumber perturbations that appear at high resolutions. The logarithm of the r.m.s is shown in Fig. 8. The shell readjusts to the higher numerical resolution up to $t \simeq 9.5 \times 10^4$ s. Close inspection of the density maps reveals the presence of density fluctuations on the scale of the shock width during this transition. This numerical relaxation triggers the NTSI close to the binary axis (left panels of Fig. 7). In the simulations with highest numerical resolution (right panels of Fig. 7) the NTSI develops in regions that are already perturbed by the growth of the first instability (most likely the TAI, see §4.2.2). These fast growing perturbations may contribute to trigger the NTSI. The NTSI moves the shock away from its rest position as the bending modes are amplified and mass collects at the extrema

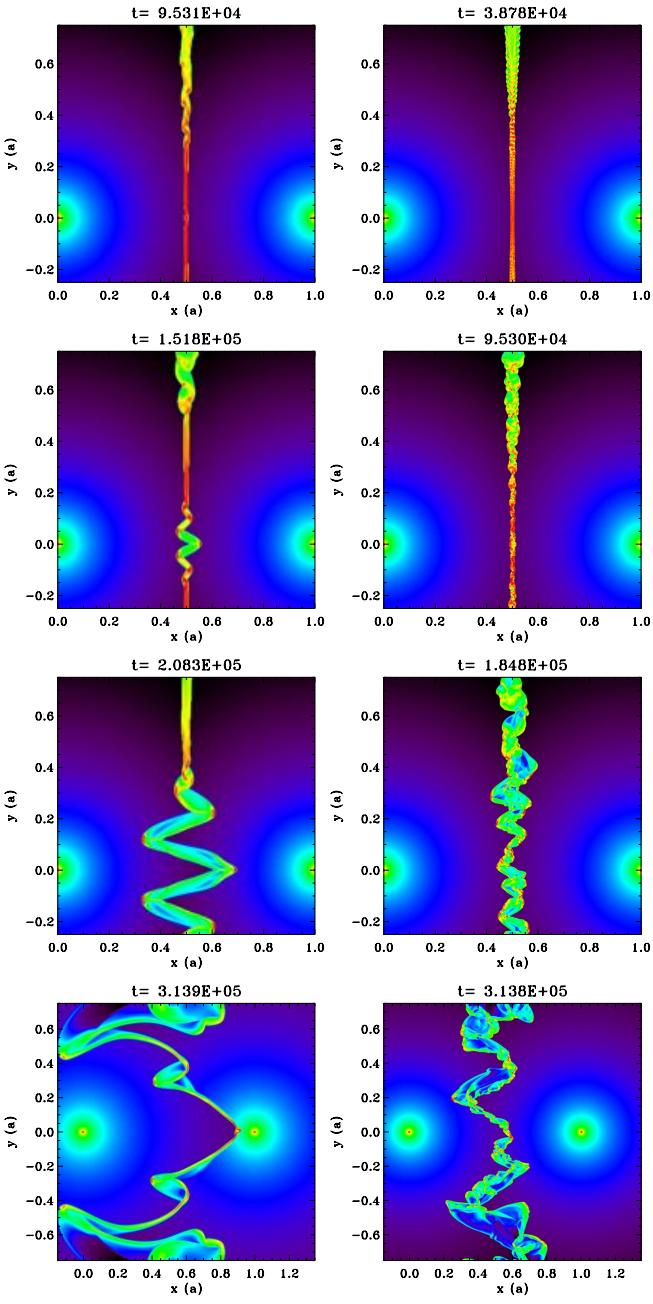

Figure 7. Density maps showing the evolution of a 2D colliding wing binary when $\eta = 1$ and $\gamma = 1.01$. Time is given in seconds. $t = 0$ corresponds to the restart at high resolution of an initial low resolution simulation (256 cells, no mesh refinement). On the left panel there is one level of refinement (maximum resolution equivalent to 512 cells), on the right panel there are four levels (maximum resolution equivalent to 4096 cells).

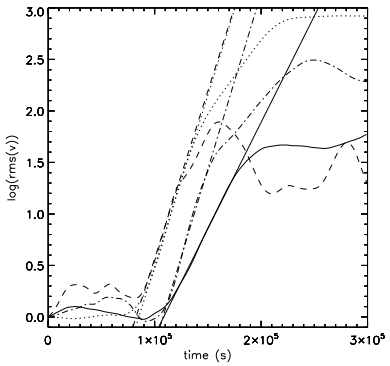

Figure 8. Logarithm of the root mean square of the velocity on the line of centres as a function of time. The curves represent maximal resolutions of 512 (dotted), 1024 (dot-dashed), 2048 (dashed) and 4096 (solid) cells per dimension. The thin straight lines show the fits to the linear phase for each resolution.

(Vishniac 1994). The exponential growth timescale estimated from fitting the r.m.s values are $\tau \approx 3.1 \times 10^4$, $2.9{\times}10^4$, $4.5{\times}10^4$ and $4.7{\times}10^4$ s for increasing resolutions (mesh refinement). There is an increase of 50% of the measured growth timescale whereas the cell size (and therefore the available wavelength range potentially accessible) increases by a factor 16. This is in reasonable agreement with the theoretical value and the expected behaviour with changing resolution, confirming that the NTSI is triggered in our simulations. Fig. 8 also shows that the saturation amplitude is somewhat smaller as the resolution is increased (compare also the bottom left and right panels of Fig. 7) and that it converges to a resolution-independent value.

4.2.2 Evidence for the Transverse Acceleration Instability (TAI)

The numerical simulations show that the initial perturbations are preferentially located off the binary axis, have an oscillatory behaviour with a small wavelength and grow faster when the spatial resolution is increased (Fig. 7). The rapid development of these perturbations is consistent with a linear instability. These properties are reminiscent of the TAI. The TAI studied by Dgani et al. (1993, 1996) is an overstability with an oscillation frequency of the velocity perturbations $\propto 1/\lambda$. The growth timescale is $\propto \sqrt{\lambda}$ and indeed smaller wavelength perturbations grow faster at higher resolution. Vishniac (1994) noted that the growth is limited by pressure effects and that the TAI grows faster than the NTSI when

$$\frac{l}{R_s} > \frac{2\pi}{\mathcal{M}^2}\frac{R_s}{\lambda} \tag{15}$$

Here, l is the minimum distance along the contact discontinuity ($l = 0$ on the binary axis) beyond which the TAI can develop for a given wavelength λ. The relevant wavelengths are smaller than R_s and larger than the shell width $L \sim R_s/\mathcal{M}^2$, with the smaller scales growing faster. The instability develops preferentially along the wings (Blondin & Koerwer 1998). The presence of the TAI closer to the binary axis at the highest resolution may explain why the growth rate of the NTSI (see Fig. 8) does not perfectly match the theoretical value.

Despite the similarities, we could not formally identify the TAI. One difficulty is that we were not able to quantify the growth rates as several modes interact quickly and make the linear phase very short. Another is that we found that our initial velocity profile along the shock is inconsistent with the equilibrium solution proposed by Dgani et al. (1993). This was corrected by Myasnikov et al. (1998) but they concluded that the set of equations used by Dgani et al. (1993) led to inconsistencies in the dispersion relations, casting doubt on the theoretical rates to expect. We suggest that it is not possible to neglect, as was done, the derivatives $\partial/\partial\theta$ in the equations (θ corresponds to the polar angle to the binary axis with the origin at the stagnation point), since there is a significant change in the azimuthal speed of the incoming flow as it is decelerated and redirected along the shock. Although our results still support the presence in the simulations of some form of the TAI, the simulations also show that the saturation amplitude of this instability is low compared to the NTSI. In all the simulations we performed, the non-linear evolution was dominated by the large scale, high amplitude perturbations induced by the NTSI. At best, the TAI may play a role in the early stages as a seed instability for the NTSI, as described in §4.2.1.

4.2.3 Evolution with an initial velocity shear and at low η

In real systems the velocities of the winds are never exactly equal and the contact discontinuity is subject to the KHI. Even for a 1% velocity difference between the winds, this instability theoretically has a larger growth rate than the TAI and NTSI. Fig. 9 compares simulations for $\eta = 1$ with equal winds or $v_{1\infty} = 2v_{2\infty}$, subject to the KHI. We also include here a map of the r.m.s. of the velocity fluctuations observed over a long averaging period. There is little difference in the outcome between equal winds and $v_{1\infty} = 2v_{2\infty}$, either in the appearance of the turbulent region (top row) or in the r.m.s. of the perturbations (second row). If anything, the KHI seems to increase slightly the region where strong fluctuations occur. The NTSI dominates the final non-linear phase even when the KHI is initially present. The r.m.s. values close to one are the expected outcome of the NTSI (Vishniac 1994).

We found the same results for simulations with $\eta = 1/16 = 0.0625$. The corresponding density maps and velocity perturbations are given in the bottom two rows of Fig. 9. The NTSI was studied theoretically for planar shocks but the $\eta = 0.0625$ simulations show it is also present and dominant when the shock is curved, although following it requires high numerical resolutions. The simulations were performed with $n_x = 128$ and 5 levels of refinement in a box of size $8a$. For lower resolutions the NTSI is not triggered and the final result is stable (the same is observed for $\eta = 1$). The density maps for equal winds and $v_{1\infty} = 2v_{2\infty}$ look similar. The highest velocity perturbations are at the same location but the r.m.s values are higher when an initial shear is present. We conclude that having a velocity shear in a thin shell increases the amplitude of the perturbations but does not affect much the morphology of the unstable flow, which is mostly set by the NTSI. This is consistent with Blondin & Marks (1996) who concluded from their simulations of perturbed slabs that the KHI does not strongly modify the outcome of the NTSI.

4.2.4 Effect of increasing pressure in the stellar winds

Pressure has a stabilising effect on both instabilities. We performed a simulation with $\mathcal{M}_1$=$\mathcal{M}_2$=6 with all other physical and numerical parameters identical to those of the $\eta = 1$, $v_{1\infty} = v_{2\infty}$ simulations. Both instabilities are seen to develop but more slowly. Keeping the wind velocity constant, a lower Mach number implies a

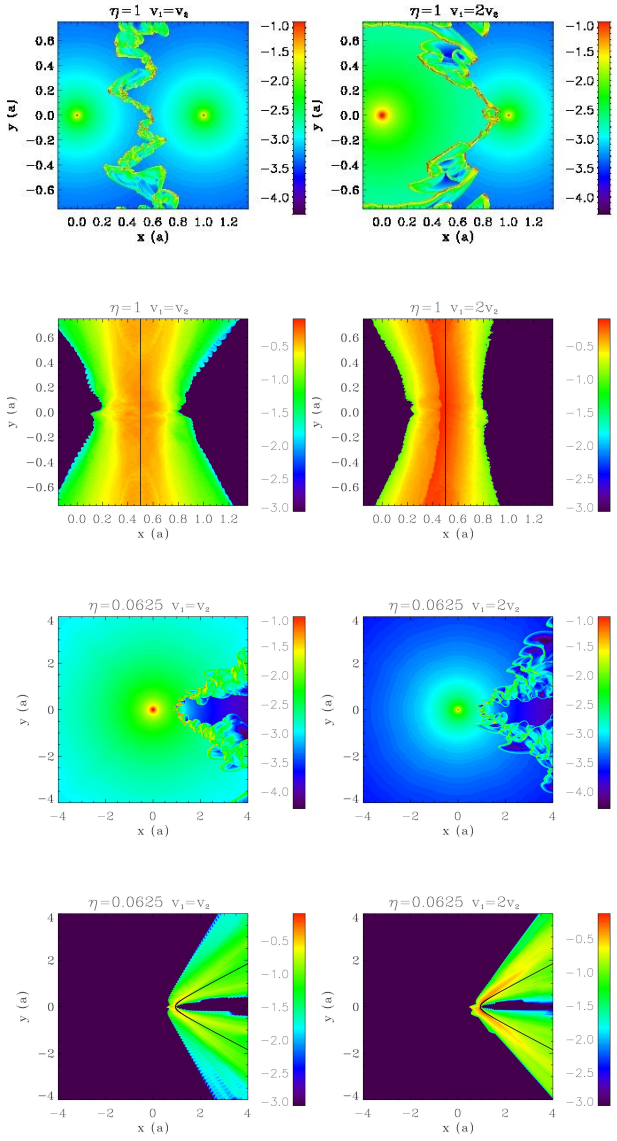

Figure 9. Top row: density maps for $\eta = 1$ with $v_{1\infty} = v_{2\infty}$ (left panel, from the same model shown in Fig. 7) and $v_{1\infty} = 2v_{2\infty}$ (right panel). Second row: corresponding time-averaged r.m.s. of the velocity fluctuations (on a log scale). Bottom two rows: same for $\eta = 1/16 = 0.0625$.

higher sound speed but the thickness of the shell increases faster so that the growth timescale of the NTSI ($\propto L/c_s \propto 1/\mathcal{M}$) is longer. The NTSI is also harder to trigger as it requires a perturbation of amplitude comparable to the size of the shell. The TAI develops more slowly as pressure suppresses the development of small wavelengths perturbations in the radial directions (Dgani et al. 1993). The final non-linear phase with high amplitude perturbations, shown in Fig. 10, appears later than in Fig. 7. The shell is indeed thicker and presents smaller density contrasts than for high Mach numbers. Comparing Fig. 9 with Fig. 10, the amplitude of the variations in shock location or the r.m.s of the fluctuations do not appear to change much but the oscillations in shock location seem to have a longer wavelength.

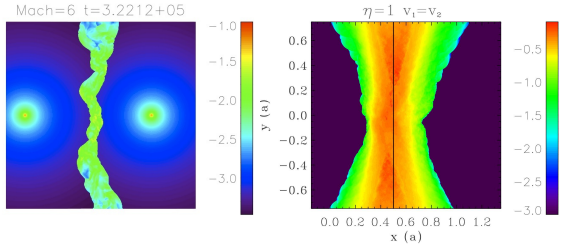

Figure 10. Left: density map of 2D colliding wing binary when $\eta = 1$, $\gamma = 1.01$ and $\mathcal{M} = 6$ for the highest resolution. Time is given in seconds. Right: time-averaged map of the r.m.s of the velocity fluctuations.

4.3 A comparison of unstable adiabatic and isothermal cases

Finally, we compare the non-linear outcome of simulations with unstable colliding wind regions in the isothermal and adiabatic cases. Figs. 5-6 and Fig. 9 show cases with $\eta = 1$ or $\eta = 1/16$ and $v_{1\infty} = 2v_{2\infty}$ for both the adiabatic and isothermal cases. The r.m.s. amplitude is larger for isothermal winds than for adiabatic winds when the same wind parameters are used. The unstable region extends beyond the wings of the contact discontinuity in the case of isothermal winds, unlike the adiabatic case where most of the fluctuations seem to take place within the shocked region of the weaker wind. The NTSI creates more small scale structures and higher density contrasts are possible when the winds are isothermal. The weaker wind still propagates freely over a significant fraction of the domain despite the strong perturbations at the interface in the isothermal case. In contrast, the adiabatic simulations show that the free flowing weaker wind is confined to a very small region (§4.1). The wind is still expected to be confined at some distance from the star in the isothermal case (see §3.2) but this happens further away than in the adiabatic case even when the thin shell instabilities develop.

5 DISCUSSION

5.1 Morphology of the interaction region

We have carried out 2D and 3D hydrodynamical simulations of colliding winds to study the morphology of the interaction region and the instabilities that can affect it when orbital motion can be neglected. We first examined the relevance of widely-used analytical estimates. The position of the standoff point is very well predicted by the standard ram pressure balance on the line-of-centres. Away from the binary axis, when η is close to 1, the opening angle of the contact discontinuity is well approximated by the analytical solution proposed by Canto et al. (1996), which assumes conservation of mass and momentum in a thin shell. The semi-analytical solution of Stevens et al. (1992), which assumes balance of the ram pressures normal to the surface, is a better approximation when $\eta \ll 1$. This clarifies the range of validity for these approximations that have found widespread practical use in the literature.

Numerical simulations also show that the weaker wind can be fully confined for low η, with the presence of a backward termination (reconfinement) shock, for both isothermal and adiabatic winds. The region where the weaker wind propagates freely is reduced when the Mach number of the wind is small, when the KHI develops or when the wind is isothermal. This may have some observational consequences. One possibility is that the lines from the

confined wind show unusual profiles or intensities because the wind terminates very close to the star. Another possibility is stronger, variable absorption instead of smooth absorption when the line-of-sight crosses the region where a freely-expanding wind is expected.

More realistic simulations would include wind acceleration and radiative inhibition or braking (Stevens & Pollock 1994; Owocki & Gayley 1995; Pittard 2009; Parkin & Gosset 2011). The wind velocity at the stagnation point is then different from its asymptotic value, increasingly so when ram pressure balance occurs close to one of the stars. The principal consequence is to change the location of the stagnation point (Antokhin et al. 2004). The basic geometry of the interaction region does not change although the asymptotic values e.g. of the contact discontinuity are probably best described by some effective η. In some extreme cases a stable balance may not be achieved and the wind-wind collision region collapses onto the star with the weaker wind (Stevens et al. 1992; Pittard 1998). Another possible consequence is that a velocity shear may appear even if the coasting velocities of the winds are assumed to be equal, generating the KHI where it would not be expected.

Orbital motion must be included when studying the large-scale structure of colliding winds. The interaction region wraps around the binary at distances of order $v_\infty P_{\rm orb}$, where v_∞ is the velocity of the stronger wind (Walder et al. 1999). On smaller scales (intra-binary), a non-zero orbital velocity skews the interaction region by an angle $\tan\alpha \sim v_{\rm orb}/v_\infty$ at the apex (Parkin & Pittard 2008). The opening angles of the shocks are slightly modified on the leading and trailing edges but the morphology of the interaction region does not dramatically change on scales $\ll v_\infty P_{\rm orb}$ (Lemaster et al. 2007). Exploratory simulations show that the reconfinement shock is still present when orbital motion is included in a low η model. According to our results (§3.3), no such shock is expected to form in the adiabatic simulation of van Marle et al. (2011) since it has $\eta = 1/7.5 \approx 0.14$. Reconfinement shocks can occur at some phases and not at others in binaries with highly eccentric orbits, as different cooling or wind velocities are probed when the separation changes (e.g. the periastron passage of the η Carinae, see Parkin et al. 2011). The morphology also depends on the history of the shocked gas and can exhibit strong hysteresis effects in eccentric systems (Pittard 2009).

5.2 Impact of instabilities

Hydrodynamical instabilities have a major impact on the structure of the colliding wind binary. Although the overall aspect of the interaction region can still be recognised in a time-averaged sense, the wind interface can become highly turbulent, generating strong time and location-dependent fluctuations in the flow quantities. Velocity shear at the contact discontinuity in the shock region leads to the development of the KHI. An accurate Riemann solver is required to follow this instability. Eddies are already present at the interface even with a 10% velocity difference. The amplitude of the perturbations can be significant with r.m.s. values in the tens of percent for the case of adiabatic colliding winds with $v_{1\infty} = 2v_{2\infty}$. The mixing is limited to the region of the weaker wind, with the strongest perturbations located close to the initial contact discontinuity. The KHI has no impact on the location of the stagnation point. Equal winds are not expected to trigger the instability but introducing orbital motion was found to generate a small velocity shear even for this case (Lemaster et al. 2007). Curiously, van Marle et al. (2011) find the opposite *i.e.* no KHI for nearly adiabatic winds with orbital motion, $v_{1\infty} = 1.3v_{2\infty}$ and $\eta = 0.14$. We would expect to see significant mixing in the inner binary system, where the interaction region is only slightly skewed, unless it is dampened by numerical diffusion.

In isothermal simulations, an instability reminiscent of the TAI develops initially away from the binary axis. A second instability develops on the axis whose growth rate and properties identify as the NTSI. The NTSI dominates the non-linear evolution of isothermal colliding winds, leading to highly turbulent structures and large amplitude fluctuations in the location of the interface, including the stagnation point on the binary axis. Our results confirm the conclusions of Blondin & Koerwer (1998) who stressed the dominance of the NTSI and the stabilising effect of pressure in their simulations of bow shocks. They also saw 'wiggles' developing early on in the shock with the same properties as those we attribute to the TAI-like instability. The trigger for the NTSI is not discussed but it is likely provided by the wiggles. However, they did not attribute these to the TAI and instead argued that the TAI acts only once the shell is perturbed by the NTSI.

The presence of instabilities in real systems is probably unavoidable. The KHI may lead to moderate mixing of the material in adiabatic situations. The strongest mixing is obtained for high velocity shears which, in astrophysical systems, is likely to mean that at least one of the winds is radiatively efficient and not adiabatic. The radiative efficiency of the wind is classically parametrized by the ratio χ of the cooling and advection timescales, which can be evaluated as (Stevens et al. 1992)

$$\chi \approx \left(\frac{v}{1000\ {\rm km\,s^{-1}}}\right)^4 \left(\frac{a}{10^{12}\ {\rm cm}}\right) \left(\frac{10^{-7}\ {\rm M_\odot\ yr^{-1}}}{\dot{M}}\right) \qquad (16)$$

with $\chi \gtrsim 3$ for an adiabatic wind and $\chi \lesssim 3$ for a radiatively efficient wind. The ratio χ_1/χ_2 is therefore $\propto (v_1/v_2)^5\eta$. Because v appears with a large power, a significant difference in wind velocities essentially implies that the slowest wind will be close to isothermal. In this case, thin shell instabilities develop but their outcome may be different because of the stabilising effect of thermal pressure from the neighbouring adiabatic shock (Stevens et al. 1992; Walder & Folini 1998; Pittard 2009; Parkin & Pittard 2010; van Marle et al. 2011). For thin, highly radiative shocks, the NTSI can probably be triggered by wind variability or changes in shock width as χ varies along the orbit, if it is not already triggered by the TAI or KHI. The saturation amplitude depends strongly on the radiative losses and including a realistic cooling function in the energy equation of the fluid is essential for a detailed comparison with observations (Strickland & Blondin 1995; Walder & Folini 1996). The shock will necessarily be larger than the idealised isothermal case so the saturation amplitudes of the fluctuations can be expected to be in between the adiabatic and isothermal cases. Other instabilities may also be at work in radiative shells (Chevalier & Imamura 1982; Walder & Folini 1996). Compressed magnetic fields in the shock region, if present, can also modify the growth rates and saturation amplitudes. For instance, the KHI is stabilised when the flow is parallel to the magnetic field and the velocity shear is smaller than the Alvén speed (Gerwin 1968). Heitsch et al. (2007) find that an ordered magnetic field has a stabilising effect on the NTSI in a thin slab.

In conclusion, the impact of the instabilities studied here is conveniently summarised by saying that some amount of variability and mixing is expected in all cases but that the strongest variability and mixing are expected to be associated with the most radiative (hence luminous) colliding winds.

5.3 Computational requirements

Following these instabilities is computationally demanding, especially for low momentum flux ratios η, and imposes a minimum spatial resolution together with an accurate Riemann solver. There are three numerical constraints on the spatial resolution. First, there must be enough cells within the stellar masks to properly generate the winds. For a coasting wind the mask can be larger than the actual size of the star. This cannot be the case if the stagnation point is close to one of the stars low η) and/or if wind acceleration, braking or inhibition is taken into account. The second condition is that the resolution must be sufficient to resolve the location of the stagnation point on the binary axis. This is increasingly demanding as η decreases, but the increase in computational cost is steeper when working in the 2D setup (see §3.1). The last conditions relates directly to the instabilities. For $\eta = 1/32 = 0.03125$, in a $8a$ simulation box, we found that a simulation with $n_x = 128$ needs 7 levels of refinement in order to avoid numerical damping of the instabilities. At lower resolutions we see the initial development of the TAI far from the binary but it is quickly advected out of the simulation box without being maintained. The NTSI is not triggered and the final result is stable. We find that the shell needs to be resolved by at least 4 computational cells on the binary axis in order to develop the NTSI. Resolving the shell *i.e.* shock structure is the stringiest constraint on the numerical resolution. The thickness of the shell for the 2D adiabatic simulations given in Fig. 2 (upper left panel) can be used to estimate the numerical resolution required to achieve this for a given η. It drastically decreases for low values of η (slightly less so in 3D, which show thicker structures when $\eta \leqslant 1/32 = 0.03125$, see §3.3). The shell width is thinner in the isothermal case so the values derived from Fig. 2 are strict lower limits for the required resolution.

Large scale simulation of a system with low η and isothermal winds require high resolutions for the instabilities to develop. The NTSI develops at slightly lower resolutions when the KHI is present and acts as the initial seed perturbation. For instance, with $\eta = 1/32$, isothermal winds and $v_{1\infty} = 2v_{\infty}$ the NTSI develops with 6 levels of refinement instead of 7 in the case of equal winds. However, it seems that the effect decreases with lower values of η. The shell always needs to be resolved, if only minimally, because the NTSI involves an imbalance of momentum *within* the thin shock layer. The Kelvin-Helmholtz instability in adiabatic winds is easier to model. It develops even for low resolution simulations when the velocity difference between both winds is large enough. For $\eta = 1/32$, adiabatic winds and $v_{1\infty} = 2v_{\infty}$ the instability develops for 4 levels of refinement. The study of the large scale 3D evolution of unstable colliding winds remains a tremendous computational challenge.

6 CONCLUSION

We have studied the morphology and the instability of colliding wind regions using numerical simulations. Compared to previous works, our study extends to much lower values of the wind momentum ratio, larger simulation domain and higher spatial resolution thanks to adaptive mesh refinement. We investigate the applicability of semi-analytical estimates for the contact discontinuity, finding that the solution of Stevens et al. (1992) is the best approximation to the asymptotic opening angle for small η. We find that the weaker wind can be entirely confined to a small region instead of expanding freely up to infinity over some solid angle when low η colliding winds are considered in both the isothermal and adiabatic limits. Instabilities in the colliding wind region are important because of the mixing and variability they induce. Resolving the shock structure is required to follow the development of instabilities, which imposes increasingly stringent minimal numerical requirements for smaller η. Simulations that do not meet these requirements artificially dampen the instabilities that may be present. We follow the evolution of the KHI triggered by the velocity shear at the contact discontinuity between two winds and show that the eddies yield large fluctuations even for moderate initial shears. We formally identify the NTSI in our isothermal simulations and find that it dominates the long-term behaviour. Another instability, similar to the TAI, is present at the beginning of the simulations. Thin shell instabilities yield large fluctuations of the flow quantities over a wide region. Our study clarifies several issues in colliding wind binary models and provides a basic framework to which the results of more complex simulations, including additional physical effects, can be compared.

ACKNOWLEDGMENTS

We thank Geoffroy Lesur for discussions and remarks that helped improve this study. AL and GD are supported by the European Community via contract ERC-StG-200911. Calculations have been performed at CEA on the DAPHPC cluster and using HPC resources from GENCI- [CINES] (Grant 2010046891).

REFERENCES

Antokhin I. I., Owocki S. P., Brown J. C., 2004, ApJ, 611, 434
Baranov V. B., Krasnobaev K. V., Kulikovskii A. G., 1971, Soviet Physics Doklady, 15, 791
Blondin J. M., Koerwer J. F., 1998, New Astronomy, 3, 571
Blondin J. M., Marks B. S., 1996, New Astronomy, 1, 235
Bogovalov S. V., Khangulyan D. V., Koldoba A. V., Ustyugova G. V., Aharonian F. A., 2008, MNRAS, 387, 63
Brighenti F., D'Ercole A., 1995, MNRAS, 277, 53
Canto J., Raga A. C., Wilkin F. P., 1996, ApJ, 469, 729
Chandrasekhar S., 1961, Hydrodynamic and hydromagnetic stability
Chevalier R. A., Imamura J. N., 1982, ApJ, 261, 543
Dgani R., van Buren D., Noriega-Crespo A., 1996, ApJ, 461, 927
Dgani R., Walder R., Nussbaumer H., 1993, A&A, 267, 155
Dougherty S. M., Pittard J. M., Kasian L., Coker R. F., Williams P. M., Lloyd H. M., 2003, A&A, 409, 217
Dyson J. E., 1975, Ap&SS, 35, 299
Dyson J. E., Hartquist T. W., Biro S., 1993, MNRAS, 261, 430
Gayley K. G., 2009, ApJ, 703, 89
Gerwin R. A., 1968, Reviews of Modern Physics, 40, 652
Girard T., Willson L. A., 1987, A&A, 183, 247
Heitsch F., Slyz A. D., Devriendt J. E. G., Hartmann L. W., Burkert A., 2007, ApJ, 665, 445
Lamberts A., Fromang S., Dubus G., 2011, in C. Neiner, G. Wade, G. Meynet, & G. Peters ed., IAU Symposium Vol. 272 of IAU Symposium, Hydrodynamical simulations of Pinwheel nebula WR 104. pp 402–403
Lebedev M. G., Myasnikov A. V., 1990, Fluid Dynamics, 25, 629
Lemaster M. N., Stone J. M., Gardiner T. A., 2007, ApJ, 662, 582
Luo D., McCray R., Mac Low M., 1990, ApJ, 362, 267
Mac Low M., Norman M. L., 1993, ApJ, 407, 207

Myasnikov A. V., Zhekov S. A., 1993, MNRAS, 260, 221
Myasnikov A. V., Zhekov S. A., Belov N. A., 1998, MNRAS, 298, 1021
Owocki S. P., Gayley K. G., 1995, ApJ, 454, L145+
Parkin E. R., Gosset E., 2011, ArXiv e-prints
Parkin E. R., Pittard J. M., 2008, MNRAS, 388, 1047
Parkin E. R., Pittard J. M., 2010, MNRAS, 406, 2373
Parkin E. R., Pittard J. M., Corcoran M. F., Hamaguchi K., 2011, ApJ, 726, 105
Pilyugin N. N., Usov V. V., 2007, ApJ, 655, 1002
Pittard J. M., 1998, MNRAS, 300, 479
Pittard J. M., 2009, MNRAS, 396, 1743
Pittard J. M., Dougherty S. M., 2006, MNRAS, 372, 801
Pittard J. M., Dougherty S. M., Coker R. F., Corcoran M. F., 2005, in L. O. Sjouwerman & K. K. Dyer ed., X-Ray and Radio Connections X-ray and Radio Emission from Colliding Stellar Winds
Pittard J. M., Dougherty S. M., Coker R. F., O'Connor E., Bolingbroke N. J., 2006, A&A, 446, 1001
Puls J., Vink J. S., Najarro F., 2008, A&A Rev., 16, 209
Stevens I. R., Blondin J. M., Pollock A. M. T., 1992, ApJ, 386, 265
Stevens I. R., Pollock A. M. T., 1994, MNRAS, 269, 226
Strickland R., Blondin J. M., 1995, ApJ, 449, 727
Teyssier R., 2002, A&A, 385, 337
Truelove J. K., Klein R. I., McKee C. F., Holliman II J. H., Howell L. H., Greenough J. A., Woods D. T., 1998, ApJ, 495, 821
Tuthill P. G., Monnier J. D., Danchi W. C., 1999, Nature, 398, 487
van Marle A. J., Keppens R., Meliani Z., 2011, A&A, 527, A3+
Vishniac E. T., 1994, ApJ, 428, 186
Walder R., Folini D., 1996, A&A, 315, 265
Walder R., Folini D., 1998, Ap&SS, 260, 215
Walder R., Folini D., Motamen S. M., 1999, in K. A. van der Hucht, G. Koenigsberger, & P. R. J. Eenens ed., Wolf-Rayet Phenomena in Massive Stars and Starburst Galaxies Vol. 193 of IAU Symposium, Colliding winds in Wolf-Rayet binaries: further developments within a complicated story. pp 298–+
Wilkin F. P., 1996, ApJ, 459, L31+

Chapter 4

Large scale simulations including orbital motion

Contents

4.1 Geometry of the shocked arms 112
4.1.1 Estimating the skew angle 112
4.1.2 Does the KHI develop when the winds are identical? 113
4.1.3 Differentiation of the spiral arms 114
4.2 The large scale spiral structure 114
4.2.1 Determining the step of the spiral 118
4.2.2 To spiral or not to spiral? 118
4.2.3 Observational consequences 121
4.3 Application to WR 104 123
4.3.1 Parameters of the system 123
4.3.2 Structure of the colliding wind region 124
4.3.3 Conditions for dust formation 126
4.4 What did we learn? What are possible extensions? 127
4.5 Résumé en français 128
4.6 Paper : Impact of orbital motion on the structure and stability of adiabatic shocks in colliding wind binaries (A&A, 2012) 129

In this chapter I present simulations of the large scale environment of the binary. At this scale, orbital motion cannot be neglected anymore as it bends the shocked structure and eventually turns it into a spiral. A remarkable example of spiral structures are Pinwheel nebulae such as WR 104 brought to light by infrared dust emission in the colliding wind region (see Fig. 1.7).

Fig. 4.1 shows the geometry of both shocked arms. I define the leading arm as the arm preceding the second star (clockwise motion), the trailing arm is the other arm. When there is no dominant wind ($\eta = 1$), this definition is degenerate. Each arm is composed of one shock from each wind and a contact discontinuity. Simulations indicate both arms may develop differently (§4.1), one expanding, the other one being compressed. According to Parkin et al. [2011] this is due to radiation pressure of the stars that acts differently according to the distance to the stars and the density in the winds.van Marle et al. [2011a] do not include radiative effects in their simulations and find a similar effect. They argue it comes from the loss of ram pressure balance when the stronger wind has a velocity comparable to the orbital velocity that makes the trailing arm fall behind.

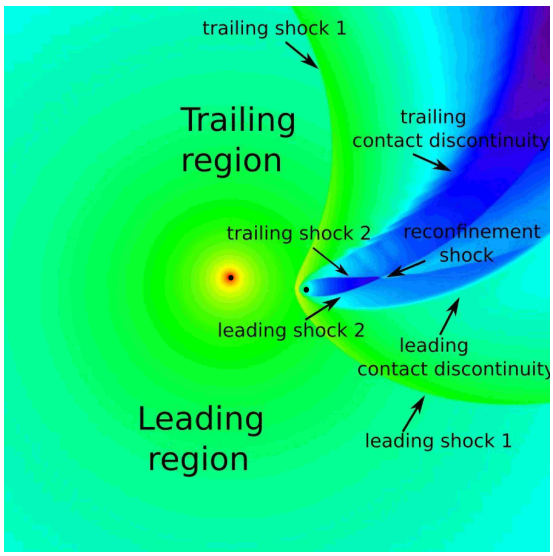

Figure 4.1: Density map of a colliding wind binary including orbital motion. The stars are shown by the black circles. In this case both shocks from the wind of the second star intersect, totally confining the second wind.

The spiral is assumed to be an Archimedean spiral, or arithmetic spiral. Such spirals have a constant step S and their shape $r(\theta)$ is determined by $r = S\theta$. Ths step S is determined by $P_{orb} \times v$ where P_{orb} is the orbital period and v a typical velocity in the system. Is it the velocity of the dominant wind ? or of the slower wind ? (see *e.g.* Tuthill et al. [2008] and Parkin and Pittard [2008] for both hypotheses). To answer this question, I have performed a systematic study of spiral structures in colliding wind binaries (§4.2). Its answer has implications for the determination of distances in pinwheel nebulae derived from the combined measurement of v by spectroscopic observations and S by infrared interferometry.

The infrared emission in WR 104 is very well matched by an Archimedean spiral although its brightest point is shifted by 13 milli-arcseconds from its centre, possibly because dust formation is inhibited closer in [Tuthill et al., 2008]. The high temperatures and low densities in WR winds are difficult to reconcile with dust formation. Dust production appears closely-related to binarity and the presence of dense colliding wind structures: in eccentric systems, such as WR 48 or WR 112, it is limited to orbital phases close to periastron while it is continuous in systems with circular orbits. The large scale spiral structure in WR +O binaries has been described by

Walder and Folini [2002], Walder and Folini [2003], who expect dust formation only at the very centre of the binary. WR 104 is a long orbital period binary system and the collision between the winds of the WR and its early-type companion is expected to be close to adiabatic. I carry out 2D and 3D hydrodynamical simulations to determine whether a hydrodynamical model with adiabatic winds reproduces the observed large-scale structure of WR 104. I study mixing and identify regions where dust production may be possible (§4.3) and I discuss the impact of different cooling and heating mechanisms.

The only instability we expect in adiabatic winds is the Kelvin-Helmholtz instability (KHI). The impact of orbital motion on the development of the KHI is not well established. Lemaster et al. [2007] found that eddies develop even when the winds are completely identical, because orbital motion introduces a velocity difference. Pittard [2009] found no eddies in a simulation with a similar setup.van Marle et al. [2011a] did not find eddies either, although their simulation has an initial non zero velocity difference $\beta = v_1/v_2 = 3/4$, and argued that orbital motion stabilises the KHI. I studied the evolution of colliding wind binaries with increasing velocity differences (§4.1) and studied the impact of the KHI on the structure of both spiral arms. The KHI leads to mixing between the winds. My simulations show that in some configurations, the large scale spiral structure is destroyed. I explain that the presence or absence of the structure is related to the KHI in the winds and provide predictions on the large scale structure of different types of colliding wind binaries. In Pinwheel nebulae, mixing is thought to facilitate dust formation as it enriches the WR wind with hydrogen from the companion star. In γ-ray binaries, mixing between the tenuous pulsar wind and the dense wind from the companion could strongly reduce particle acceleration which would have observational consequences.

The questions this chapter would like to answer are:

- What explains the formation of distinct spiral arms?
- How does orbital motion impact the development of the KHI in colliding wind binaries?
- What determines the step of the spiral?
- What is the internal structure of the colliding wind region in WR 104?
- Can an adiabatic model put constraints on dust formation in WR 104?

4.1 Geometry of the shocked arms

For each simulation, the input parameters are the mass M, mass loss rate $\dot{M}$, wind velocity v, and wind Mach number $\mathcal{M}$ of both stars. The wind Mach numbers are set to 30. The values of the mass loss rates and wind velocities in the simulations in this chapter are given in the Appendix of Lamberts et al. [2012], included at the end of this chapter. Both stars have a mass of $15\,M_\odot$ and the binary separation a is 1AU, the orbits are circular. The corresponding orbital period $P_{\rm orb}$ is 0.18 yr, or 67 days, which gives an orbital velocity of the stars of $v_{orb} = 81\,{\rm km\,s^{-1}}$.

I perform simulations where the size of the computational domain is $l_{box} = 40a$, with a the binary separation. I set $n_x = 64$ for the resolution of the coarse (unrefined) grid and use 7 levels of refinement. This gives an equivalent resolution that is at least two times better than in former studies [Lemaster et al., 2007, Pittard, 2009, van Marle et al., 2011a]. I use the exact Riemann solver. As I want to quantify mixing, I include two passive scalars that measure the concentration of each wind.The mixing is determined by the product of the passive scalars $s_1 \times s_2$.

4.1.1 Estimating the skew angle

Even very close to the binary, rotation affects the flow, by creating an offset between the symmetry axis of the shocked region and the line of centres. This is because the star moves along its orbit while the wind propagates before it reaches the shock. Parkin and Pittard [2008] introduce the skew angle

$$\tan \mu = \frac{v_{orb}}{v}, \tag{4.1}$$

where the velocity v to use is probably the velocity of the stronger wind [Parkin and Pittard, 2008]. This angle remains small unless the velocities of the winds are strongly reduced or orbital motion becomes important. I measure μ in my simulations by finding the best fit by eye of the analytic position of the contact discontinuity derived by Canto et al. [1996]. An example is given on Fig. 4.2. I measure $\mu \simeq 22°$ in the simulation $\{\eta = 0.0625, \beta = 0.05\}$ while the theory predicts $\mu = 21°$. The simulation of WR 104 (see §4.3) gives $\mu \simeq 9°$ while the theory predicts $\mu = 8°$. μ is too small in the other simulations to allow correct measurements.

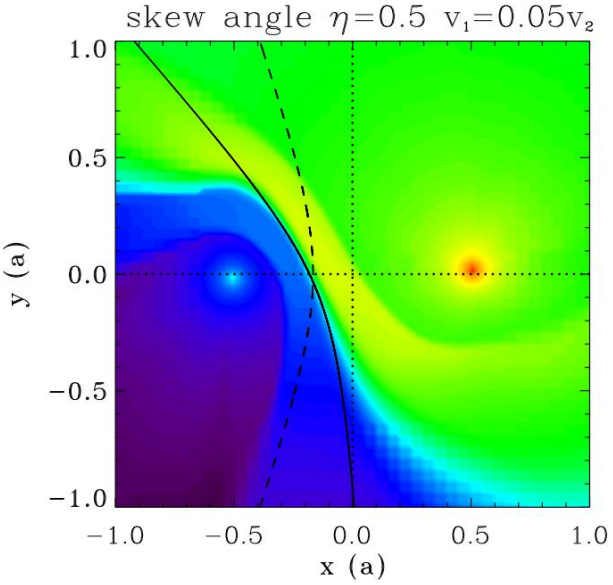

Figure 4.2: Determination of the skew angle μ for $\{\eta = 0.5, \beta = 0.05\}$ using a density map. The dashed line showes the theoretical position of the contact discontinuity for $\mu = 0$ (no orbital motion). The solid line fits the contact discontinuity in the simulation. The length scale is set by the binary separation a.

4.1.2 Does the KHI develop when the winds are identical?

At larger scales rotation bends the shocked structure. Fig. 4.3 shows the density, velocity, and mixing map for a simulation with identical winds $\{\eta = 1, \beta = 1\}$. The free (unshocked) winds correspond to the low density parts at the top and bottom. The denser parts are the shocked winds. The radial inhomogeneities visible in the unshocked wind region of the velocity map are numerical artefacts. They correspond to minute anisotropies in the stellar wind due to the finite size of the masks. The left column shows a simulation with the exact Riemann solver, the right column a simulation with the Lax-Friedrichs solver. When using the exact solver, the velocity map shows that a $\simeq 20\%$ velocity difference develops in each arm at a distance $\simeq 20\,a$ from the binary. Orbital motion makes the shocked material leading the contact discontinuity (red region on the velocity map) accelerate in the lower density free wind region while the shocked wind trailing the contact discontinuity (in green) moves into the denser, shocked material of the

other wind. The resulting velocity difference is sufficient to trigger the KHI even though the original wind speeds are equal. The instability is clearly present in the mixing map, confirming the results of Lemaster et al. [2007] showing that orbital motion triggers the KHI even when the winds are identical. My simulations contradict the results from van Marle et al. [2011a] who find no KHI. Their simulations are performed with a Lax-Friedrichs Riemann solver that is more diffusive. On the right column we can see the global shape of the interaction region is similar than with the exact solver but there is no development of the KHI because of the important numerical diffusivity.

4.1.3 Differentiation of the spiral arms

When both winds have different speeds, the differentiation between both shocked arms is more striking. Fig. 4.4-4.5 show the density and mixing for simulations with $\{\eta = 1, \beta = 2, 20\}$ and $\{\eta = 0.0625, \beta = 0.05, 0.5, 2, 20\}$. These maps show the impact of rotation on arm geometry and the development of the instabilities.

The leading and trailing arms become markedly different when the velocity difference increases, even when $\eta = 1$. The shocked zone preceded by the unshocked wind with the higher velocity and lower density is larger than the zone preceded by the lower velocity and higher density wind. The latter shocked zone is compressed by the high velocity wind into a high density region. Conversely, for $\beta > 1$ the compressed arm is the trailing arm while for $\beta < 1$ the compressed arm is the leading arm (see Fig. 4.5). According to Parkin et al. [2011] radiation pressure can have a similar effect, either enhancing or reducing the initial difference. For $\beta = 20$, compression results in a rim of puffed up matter where the density increases by two orders of magnitude with respect to the simulation with $\beta = 1$. The differentiation of both arms is independent of the instabilities in the winds but plays a role in their development.

The KHI starts similarly in both arms close to the binary major axis as the velocity difference and density jump across the contact discontinuity are the same in both arms. The symmetry between both arms is broken as the flow moves outwards. The compression of the shocked zone in the narrower arm results in a thin mixed zone with small scale structures, whereas the eddies are stretched out in the wider arm. Mixing covers a larger area in the wider zone. This is not just a geometrical effect. In the Appendix A of Lamberts et al. [2012] is shown that when media have different densities mixing by the KHI occurs preferentially in the least dense medium. This can be seen on Fig. 4.4-4.5 *e.g* for $\{\eta = 1, \beta = 20\}$ and suggests that the mixing is due to the KHI. Both velocity and density profiles thus play a role in the development of the KHI in colliding wind binaries. They both impact the large scale outcome of the spiral structure as will be shown in the following section.

As in all simulations, one has to check whether the observed feature results from a physical effect or a numerical artefact. In this case, one may wonder whether the mixing is physical and not numerical. If mixing results from numerical diffusion, the physical size of the mixed zone increases with decreasing resolution. If mixing follows from instabilities, the physical size of the mixed zone is constant with resolution. I measure the width of both mixed zone across the contact discontinuity at $y = 6$ for $\{\eta = 0.0625, \beta = 2\}$ in a set of simulations with different resolutions. In all cases $n_x = 64$ and I successively add levels of refinement. The limit of the zone is determined by $s_1 \times s_2 = 0.05$. Fig. 4.6. shows the evolution of the size of the mixed zone for the different maximal resolutions. In the wider arm, the width is almost constant for the three highest resolutions, the mixing is resolved. The width of the mixed region in the the narrower arm decreases with increasing resolution. For the highest tested resolutions, the decrease is slower, suggesting convergence is almost reached.

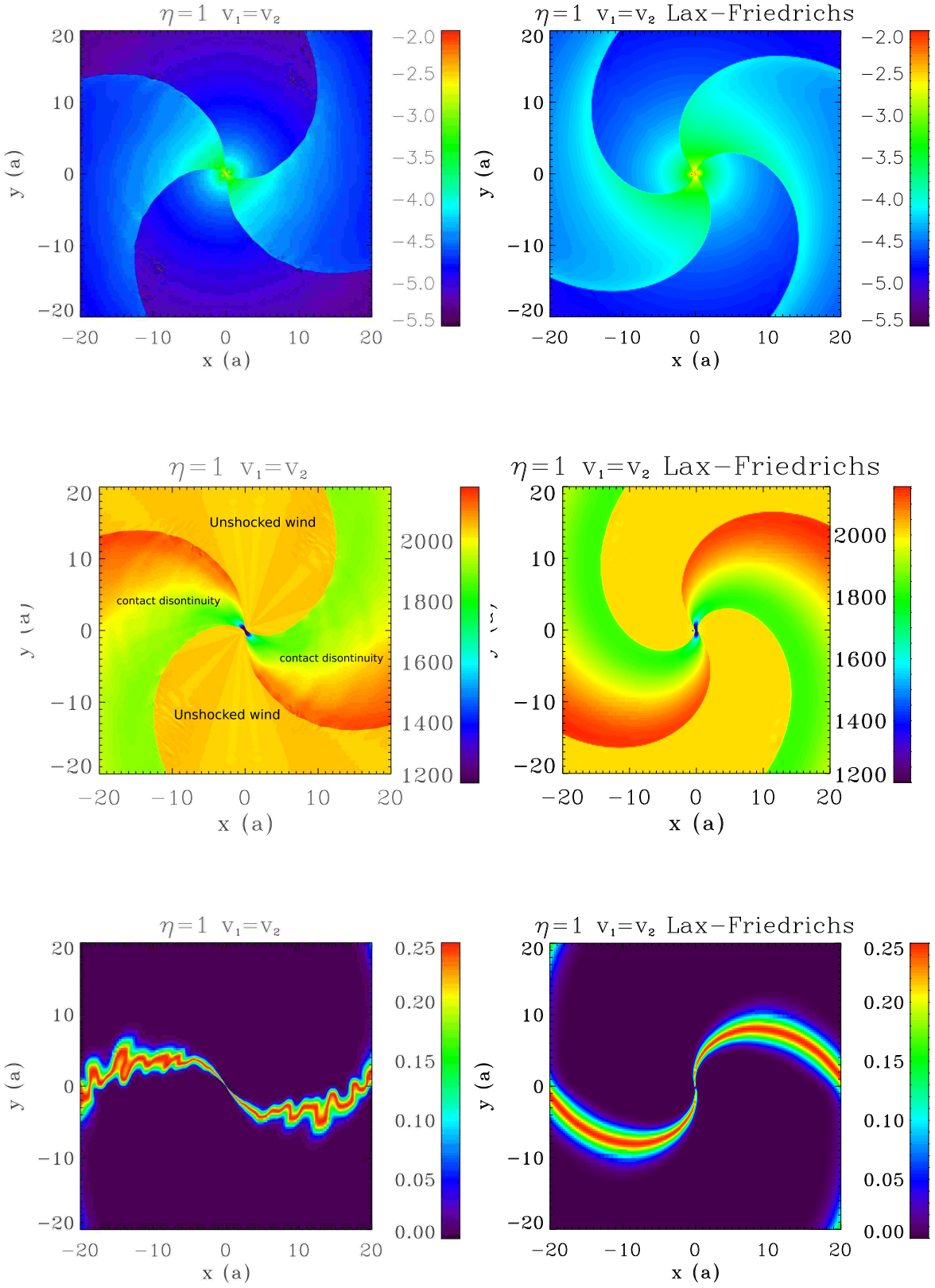

Figure 4.3: Medium scale simulation, from top to bottom :density, velocity, and mixing for a simulation with identical winds $\{\eta = 1, \beta = 1\}$. The density is given in $\mathrm{g\,cm^{-2}}$, the velocity is in $\mathrm{km\,s^{-1}}$, the mixing of the winds is a dimensionless variable. The length scale is the binary separation a. The left column shows a simulation with the exact Riemann solver, the right column shows a simulation using the Lax-Friedrichs solver (opposite direction of motion).

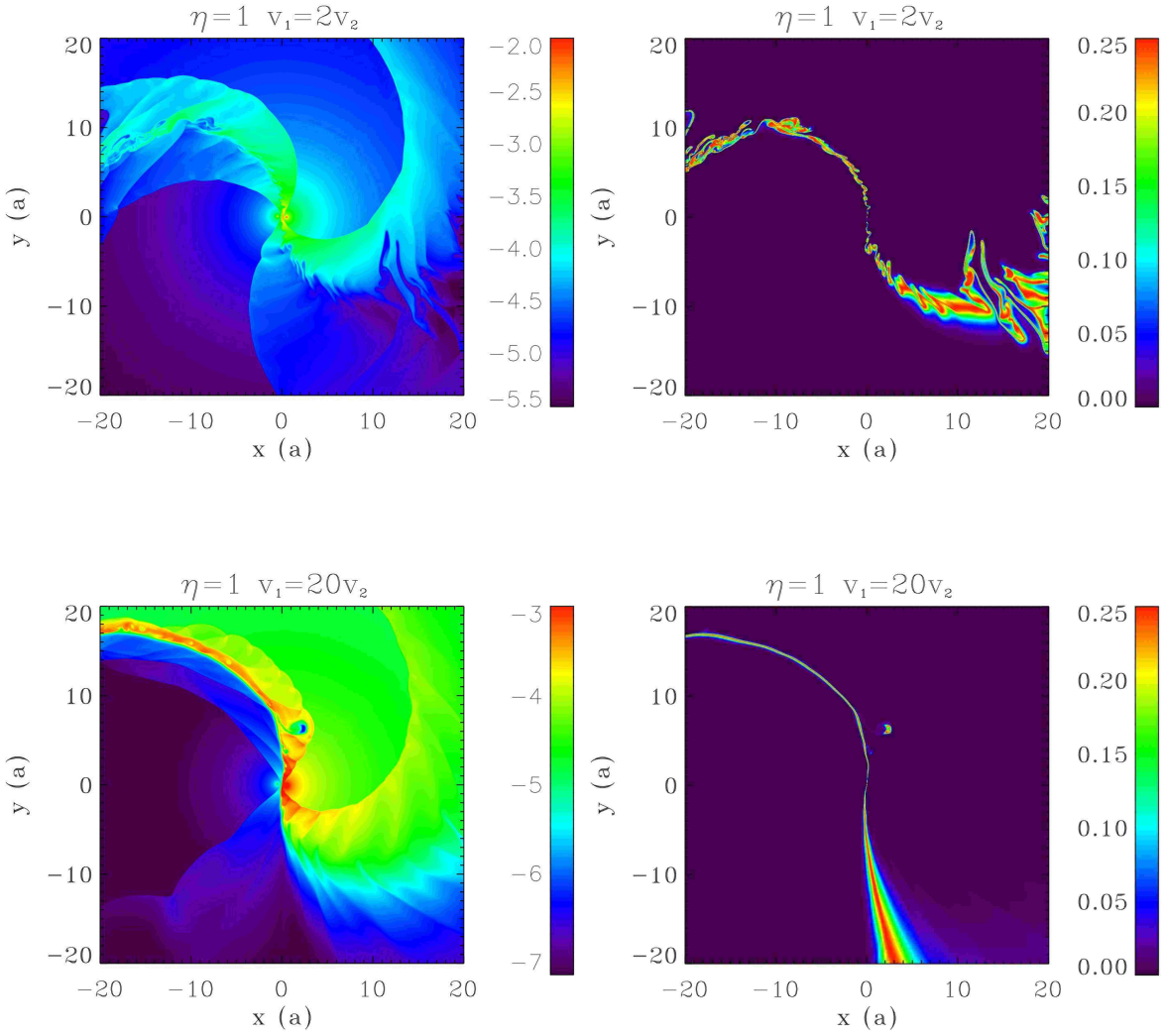

Figure 4.4: Medium scale simulation : density (left column) and mixing (right column) maps for simulations with $\eta = 1$ and $\{\beta = 2,\ 20\}$. The length scale is the binary separation a.

4.2 The large scale spiral structure

To measure the step of the spiral I perform larger scale simulations with $l_{box} = 400\,a$. The coarse grid still has $n_x = 64$ but I use up to 9 levels of refinement. The highest resolution is required at the center of the binary to allow proper shock formation. It is restricted to a small area around the stars. These simulations are computationally demanding, because they require a high resolution and because they have to model at least one complete orbit. Each simulation usually takes between 5 000 and 10 000 hours CPU time, spread over 32 to 128 processors.

Density and mixing maps are shown for $\eta = 1$ in Fig. 4.7 and for $\eta = 0.0625$ in Fig. 4.8, with β increasing from left to right in both figures. The different behaviour of mixing in both arms discussed in §4.1.3 persists on the larger scales, eventually causing both contact discontinuities to merge into one single spiral in simulations with $\eta = 0.0625$ (Fig. 4.8). This merger may result from numerical artefacts due to the use of a Cartesian grid to describe an inherently spherical phenomenon. Comparing the two first plots for $\eta = 1$, we see that a smaller wind velocity

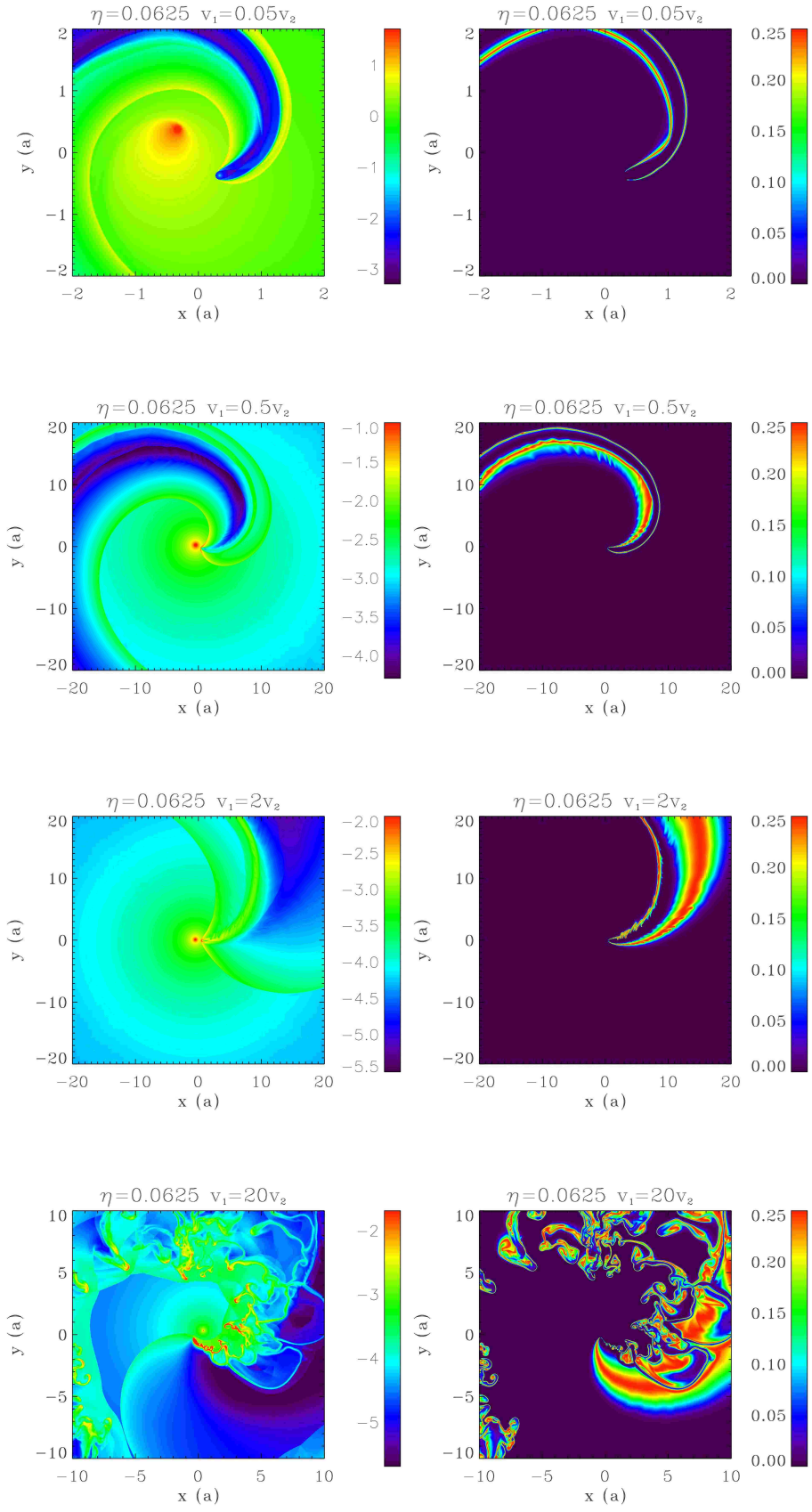

Figure 4.5: Medium scale simulation: density (left column) and mixing (right column) maps for simulations with $\{\eta = 0.0625, \beta = 0.05, 0.5, 2, 20\}$ (from top to bottom). The length scale is the binary separation a. For $\beta = 0.05$, the size of the box is reduced to avoid unnecessary computational costs.

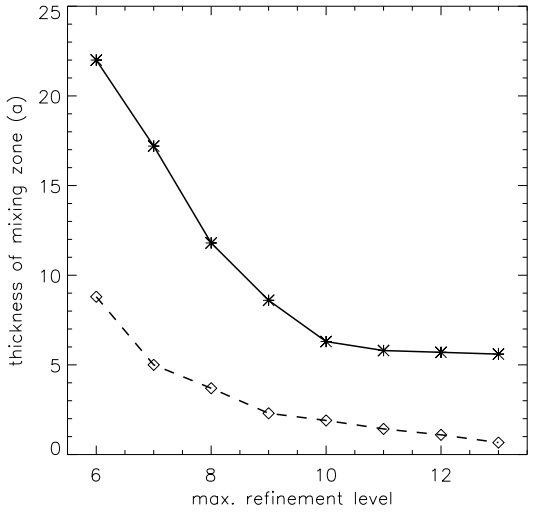

Figure 4.6: Width of the mixed zone in the narrow arm (dashed line) and wide arm (solid line) for increasing levels of refinement. The symbols indicate the measured values.

induces a smaller spiral step. I will quantify this behaviour in §4.2.1. The plots show that in some cases, the spiral structure is not maintained beyond $\simeq 20\,$a. I will explain this surprising result in §4.2.2.

4.2.1 Determining the step of the spiral

I determine the step of the spirals using the mixing map, as mixing follows closely the contact discontinuities. The spiral is not always clearly apparent in the density maps (*e.g.* $\{\eta = 0.0625, \beta = 1\}$ in Fig. 4.8), especially when a complex flow is established by the presence of a reconfinement shock behind the weaker star. I measure the step of the spiral (S) by overplotting an Archimedean spiral to the mixing maps and finding the best fit of the spiral arms, by eye. Measurements for both spiral arms lead to the same result. I confirm them by measuring the mean size of the steps on the same maps. As in Pittard [2009], I find that when a stable spiral structure is formed, an Archimedean spiral with a step size S provides a good fit to the results of our simulations, except very close to the binary. However, the deviation is small and limited to a region $\simeq 10\,a$.

The fitted S for various values of η and β is compared to the theoretical estimate S_1 in Fig. 4.9. S_1 assumes the velocity of the stronger wind controls the structure so that $S_1 = P_{\rm orb} v_1$ (*e.g.* Tuthill et al. [2008]). When the winds have equal speeeds, there is no ambiguity in the velocity that sets the step size and I verify that, in this case, $S = S_1$ for all η. This also rules out any significant numerical issue with the way the spiral develops. There are significant deviations from S_1 in all the other cases, except when $\eta \ll 1$ *i.e.* when the first wind largely dominates momentum balance. For more balanced ratios, the spiral step is smaller than expected when the weaker wind is slower than the stronger wind, and vice-versa when the weaker wind is the fastest. Using the slowest wind speed instead of v_1 (*e.g.* Parkin and Pittard [2008]), or the weaker wind, does not work better. I did not find any straightforward analytical model using η and β that could explain the values given in Fig. 4.9.

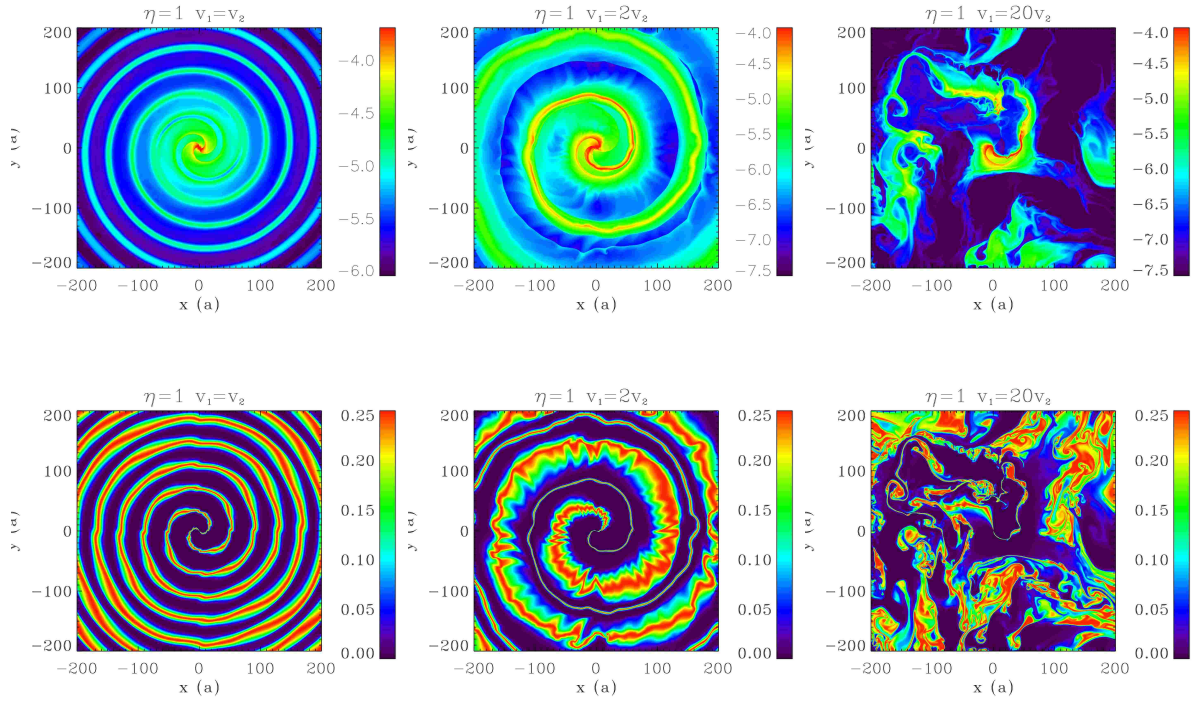

Figure 4.7: Large scale simulation : density (top row) and mixing (bottom row) for simulations with $\{\eta = 1, \beta = 1, 2, 20\}$ (from left to right) in the large boxes. The length scale is the binary separation a. The mixing of the winds is a dimensionless variable.

Table 4.1: Presence (S) or absence (X) of a spiral structure in simulations for various wind momentum (η) and velocity (β) ratio.

$\eta\backslash\beta$	.01	.05	0.1	0.5	1	2	4	8	20	200
1		X		S	S	S	S	X	X	X
0.5	S	X	X	S	S	S		X	X	X
0.0625		S	X	S	S	S	S/X	X	X	

4.2.2 To spiral or not to spiral?

The complete disruption of the spiral structure for large velocity ratios (Figs. 4.7-4.8) is unexpected. There does not seem to be a satisfactory "dynamical" explanation involving for example the orientation of the momentum with respect to orbital motion. I find that the structure is stabilised when using a Lax-Friedrichs Riemann solver and a smaller resolution, in which case the KHI is artificially suppressed (see Chapter 3). This indicates the breakdown is due to the KHI. The amplitude of the KHI appears to destroy the spiral when strong velocity gradients are present, resulting in widespread turbulence and important mixing throughout the domain. Curiously, for $\eta = 0.625$, the structure is unstable when $v_1 = 20v_2$ while it is stable for the opposite velocity gradient $v_1 = 0.05v_2$. The strong density gradient ($\dot{M}_1/\dot{M}_2 = 320$) seems to play a role in the stability.

I perform additional simulations to confirm this hypothesis. Table 1 summarises the presence or absence of spiral structures in all the simulations I ran.

In Appendix A of Lamberts et al. [2012] we explain that the growth rate of the KHI, nor-

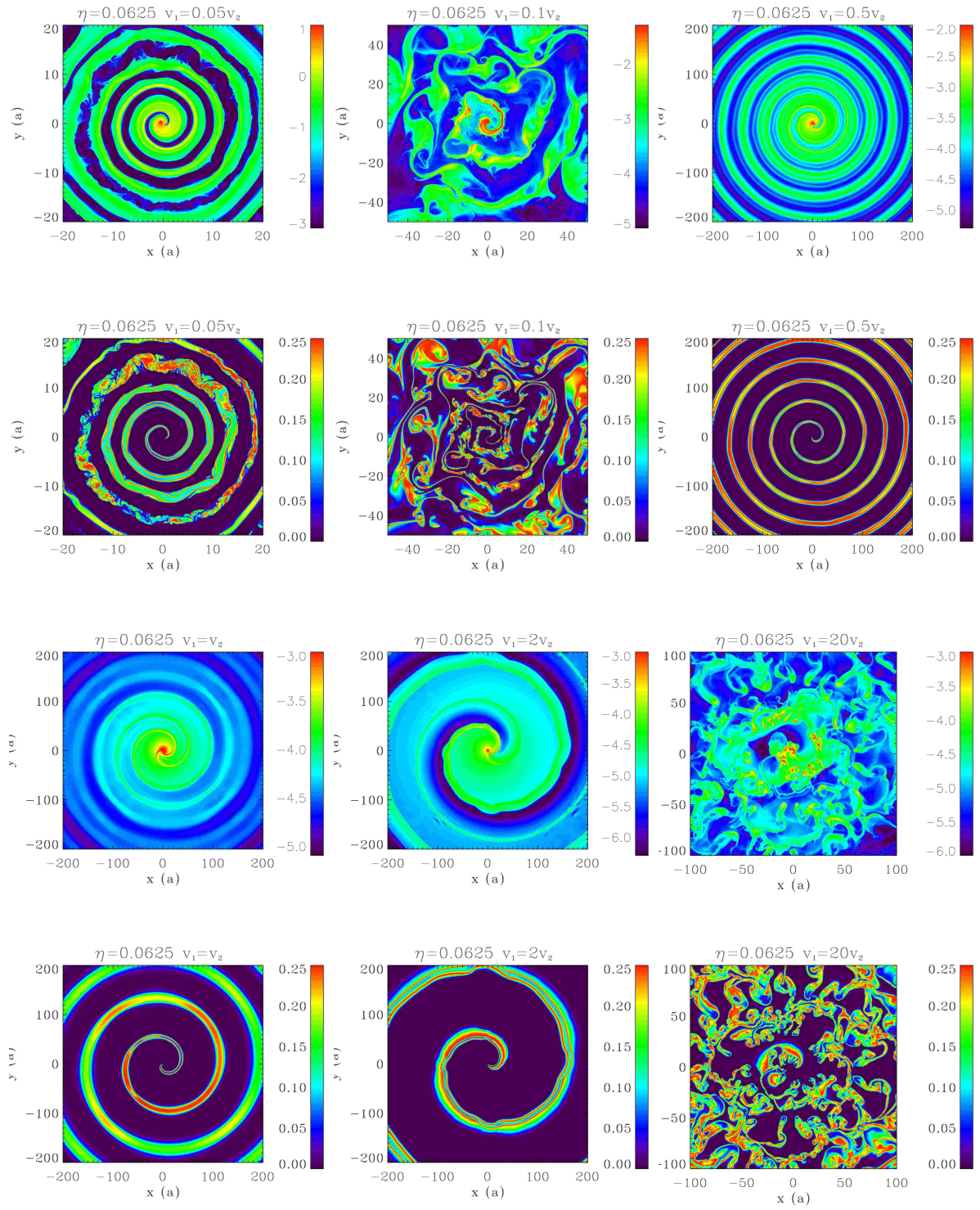

Figure 4.8: Large scale simulation : same as Fig. 4.7 for $\{\eta = 0.0625, \beta = 0.05,\ 0.1,\ 0.5,\ 1,\ 2,\ 20\}$. When going from left to right and top to bottom, β increases, which corresponds to increasing values of the x axis in Fig. 4.10.

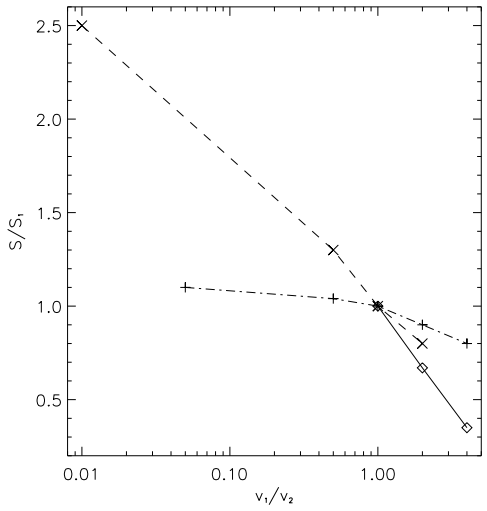

Figure 4.9: Step of the spiral S/S_1 as a function of β for η =1 (diamonds), 0.5 (diagonal crosses), and 0.0625 (crosses). The symbols are respectively joined by a solid, dashed, and dash-dotted line for easier identification.

malised by the rate at which the eddies are advected, is given by

$$\frac{\tau_{\rm adv}}{\tau_{\rm KHI}} = \frac{|\beta-1|\sqrt{1-\alpha^2}}{-\alpha(\beta-1)+(\beta+1)} = \frac{\eta^{1/2}\beta|\beta-1|}{1+\eta\beta^3}, \tag{4.2}$$

where $\alpha = (\rho_1-\rho_2)/(\rho_1+\rho_2)$ measures the density difference between the wind. This normalised growth rate is shown on Fig. 4.10 for $\eta = 1$, 0.5, and 0.0625. Although it gives no indication on the saturation in the non-linear regime, it suggests the spiral is destabilised most easily when the eddies grow quickly before propagating further away. For $\eta = 1$ the curve is symmetric. The KHI does not develop when there is no velocity difference, peaks at $\beta_{\rm max} \simeq 2$ and drops for higher values of β, because the density gradient dampens the growth rate. The symmetry with respect to $\beta = 1$ is broken when the winds have different momentum fluxes : the normalised growth rate is weaker for $\beta < 1$ and stronger for $\beta > 1$. The lower the value of η, the stronger this asymmetry. Hence, stable structures are expected for winds with comparable speeds, and when one of the winds is much faster than the other one. In addition, when $\eta \neq 1$, structures with $\beta < 1$ should be more stable than with $\beta > 1$.

The results of the simulations are in qualitative agreement with these expectations. When $\eta = 1$, there is a spiral for $\beta = 1$, 2, 4 but not for $\beta = 8$, 20 (Tab. 1), which is consistent with the faster growth of the KHI when β increases from 1. However, the transition from stable to unstable spirals occurs further away than expected from Fig. 4.10 ($\beta_{\rm max} \simeq 2$). Also, I am not able to recover a stable final structure for very high β, up to $\beta = 200$ (Fig. 4.10). Tests at higher β are computationally too expensive. For $\eta = 0.5$, I find that the spiral is maintained for values close to $\beta = 1$ but is quickly destroyed for higher/lower values of β. In this case, a stable spiral is recovered when $\beta \leq 0.01$, consistent with the lower growth rate, while the spiral remains destroyed for the symmetric value of $\beta = 20$ (higher growth rate). I observe a similar behaviour for $\eta = 0.0625$. Stabilisation is possible for a higher $\beta = 0.05$, which is consistent with the lower growth rate of the instability for $\beta < 1$ as η decreases.

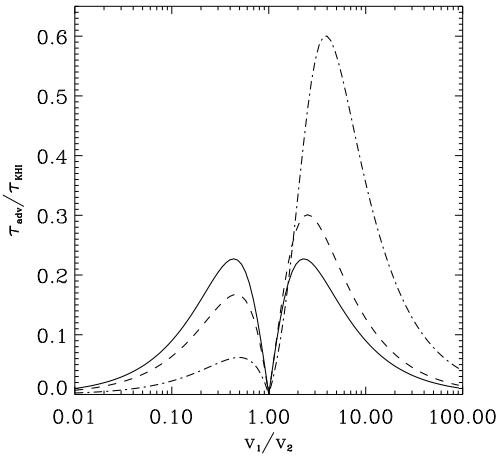

Figure 4.10: Theoretical 2D growth rate of the KHI in colliding wind binaries as a function of the velocity ratio $\beta = v_1/v_2$ of the winds. The solid, dashed and dash-dotted lines correspond to $\eta = 1$, 0.5, 0.0625 respectively.

4.2.3 Observational consequences

The differentiation between the leading and the trailing arm could account for some spectral line features that are not explained by models where both arms have equal emission (absorption)[Stevens and Howarth, 1999]. Varricatt et al. [2004] modelled the variations in emission line profiles of WR 140 by a rotating cone with dense edges, allowing them to constrain the opening angle of the colliding wind region. They found a wider opening angle than expected using the analytic formula for the opening angle of the contact discontinuity [Canto et al., 1996] with the standard value of η for this system. My simulations show that matter accumulates at the shock rather than at the contact discontinuity. The observed opening angle thus corresponds to the opening angle of the shocks, which is wider than the opening angle of the contact discontinuity. This also increases the fraction of the WR wind involved in the collision compared to estimates using the contact discontinuity.

My simulations indicate that a spiral structure is expected when both winds have roughly the same speed or when the slower wind is much denser than the faster one. This is consistent with the observations of pinwheel nebulae in several WR + O star binaries [Tuthill et al., 2006, Monnier et al., 2007, Millour et al., 2009], since their winds do have comparable velocities. I expect the formation of large scale structures for O+O type binaries, as both winds have equivalent speeds. Unfortunately, the density in the colliding wind region is too low to be able to observe it.

The spiral is destabilised when the stronger wind has a velocity between 10-50% of the weaker wind (Tab. 1). η Carinae may be a case where any large scale structure generated near apastron (when the system is closer to being adiabatic) is destroyed because of the destabilising velocity ratio $\beta \simeq 1/6$, although this would have to be assessed against the effects of the high orbital eccentricity. Parkin et al. [2011] show that thin shell instabilities develop at periastron but the consequences on the spiral structure are unknown.

The spiral is stabilised again when the velocity ratio $\beta \ll 1$. Such a situation may occur in gamma-ray binaries where the stellar wind interacts with the tenuous, relativistic pulsar wind. Bosch-Ramon and Barkov [2011] have argued that the KHI would destroy any large-scale structure. If the above results hold in the relativistic regime, I expect the formation of a stable spiral if the stellar wind dominates because $\beta \ll 1$ in this situation. When the pulsar wind dominates, $\beta \simeq 100$. Using Fig. 4.10 one cannot conclude with certainty whether this would

give a stable structure or not. The regular changes in radio morphology with orbital phase are compatible with non-thermal synchrotron emission from a stable collimated pulsar wind structure [Dhawan et al., 2006, Ribó et al., 2008, Moldón et al., 2011b]. The luminosity and frequency of the radiation are probably too low to be able to detect the spiral structure on larger scales.

On the other hand, binaries composed of a pulsar and a low-mass companion (so-called black widows, [Roberts, 2011]) are unlikely to present large scale structures. The weak stellar wind is overwhelmed by the relativistic wind of the recycled millisecond pulsar.

4.3 Application to WR 104

4.3.1 Parameters of the system

WR 104 is composed of an early type star and Wolf-Rayet star with a carbon-rich atmosphere (WC star). The characteristics of the companion to the WR star are not well constrained [van der Hucht, 2001] and I will refer to the companion star as the "OB" star. The OB wind has a estimated terminal velocity of $\simeq 2000\,\mathrm{km\,s^{-1}}$ [Harries et al., 2004b] and an estimated mass loss of $6 \times 10^{-8}\ M_\odot\,\mathrm{yr}^{-1}$ (using the mass-loss luminosity relation by Howarth and Prinja [1989]). The WR wind has a velocity of $1200\,\mathrm{km\,s^{-1}}$ [Howarth and Schmutz, 1992] and a estimated mass loss rate ranging from 0.8×10^{-5} to $3 \times 10^{-5}\,M_\odot\,\mathrm{yr}^{-1}$ [Crowther, 1997].

The orbital period (241.5 ± 0.5 days), eccentricity ($e < 0.06$), inclination ($i < 16°$), and angular outflow velocity of the spiral ($0.28\,\mathrm{mas\,day^{-1}}$) were found by fitting an Archimedean spiral to the IR maps [Tuthill et al., 2008]. The orbital separation a is about 2.1-2.8 AU for a total mass of 20-50 $\mathrm{M}_\odot$. I set $e = 0$ and $a = 2.34\,\mathrm{AU}$. Given the uncertainties on mass loss rate and velocities η varies between $0.0125 = 1/80$ and $0.0033 = 1/300$. Assuming a constant velocity for the OB wind and a radius for the OB star $R_{OB} = 10\ \mathrm{R}_\odot$ [Harries et al., 2004b], the second shock forms at $2.7 R_{\mathrm{OB}} < r < 5.1 R_{\mathrm{OB}}$ depending on η.

At such a distance, the OB wind has not necessarily reached its terminal velocity, which decreases the effective momentum flux ratio of the collision. On the other hand, radiative braking of the WR wind by the OB photon field may increase the effective η, although its effect should be limited [Tuthill et al., 2008]. As the importance of these effects is unclear, and as the effects might have compensating influences, I chose not to take them into account. I set the wind of the OB star to its terminal velocity and chose $\eta = 0.0033$, as it is the most commonly used value.

Radiative cooling can significantly change the shock structure. The ratio χ of the cooling timescale t_{cool} over the dynamical timescale t_{esc} provides an estimate of its importance [Stevens et al., 1992] (see §1.3.2.3).

$$\chi = \frac{t_{cool}}{t_{esc}} = \frac{k_B T_s}{4 n_w \Lambda(T_s)} \frac{c_s}{a}, \tag{4.3}$$

where $\Lambda \approx 2 \times 10^{-23}\ \mathrm{erg\,cm^3\ s^{-1}}$ is the emission rate for solar abundances, n_w the number density of the unshocked wind, $k_B T_s = (3/16)\mu m_p v_w^2$ the shock temperature and c_s the associated sound speed. Taking into account the uncertainty on the value of η, I find $1.5 < \chi_{\mathrm{OB}} < 5$ for the OB star and $0.4 < \chi_{\mathrm{WR}} < 1.4$ for the WR star. The system is at the transition between the two regimes. However, in Eq. 5.16 the escape timescale is assumed to be $\simeq a/c_s$ but, taking into account the value of η, it could be as short as $2.7 - 5.1 R_{\mathrm{OB}}/c_s$ if one takes the distance from the OB star, roughly equal to the curvature radius [Stevens et al., 1992]. This considerably increases the value of χ. In the following I will thus neglect cooling and assume adiabatic winds. I will discuss the consequences of this hypothesis in §4.3.3.

The low value of η is challenging when simulating WR 104. The mask of the star needs to be as small as possible so that the shocks can form properly. A minimum length of 8 computational cells per direction is needed to obtain spherical symmetry of the winds. Numerical resolution

on scales much smaller than a stellar radius (0.05 AU) is thus required close to the binary. Further away, I need to maintain a high resolution in order to properly study the instabilities, while following a spiral step requires a box size ≥ 200 AU . I thus carry out two complementary simulations: a 3D simulation covering scales up to $12a$ and a 2D simulation to model a whole step of the spiral structure.

I use the large scale 2D simulation to determine the step of the spiral and the impact of mixing. Using the mapping $\sqrt{\eta_{3D}} \rightarrow \eta_{2D}$ described in Chapter 3, I find $\eta_{2DWR104} \simeq 0.057$. I take the close value, $\eta_{2D} = 0.0625$ to help comparisons with the results in §4.1-4.2. It is important to have the right velocity difference for the study of the Kelvin-Helmholtz instability. I thus adapted $\dot{M}_{WR}$ in order to have $\eta_{2D} = 0.0625$ for the 2D simulation. I use a $200a \approx 500$ AU simulation box with $n_x = 128$ and 12 levels of refinement. This gives an equivalent resolution equal to $2^{19} \simeq 5 \times 10^5$ cells. I use nested grids to slowly decrease the maximum allowed resolution away from the binary.

I use the smaller scale 3D simulations for quantitative results on the density and temperature in the winds. The 3D simulation follows 1/8th of an orbit of WR 104 in a $12a \approx 30$ AU simulation box, large enough to see the impact of orbital motion. The orbital plane is the midplane of the box and the centre of mass of the binary is placed in a corner of the box to maximise the use of the simulated volume. I use adaptive mesh refinement with a maximal equivalent resolution of 4096^3. I start the simulation with a lower maximal resolution and restart it twice with increasing maximal resolution. I limit the high resolution to a narrow zone of $3a$ close to the binary where the instabilities develop. It corresponds to the same equivalent resolution as in the 2D model. I model only $\simeq 20$ layers at this high resolution in the z direction and I gradually reduce the resolution when going away from the orbital plane. I use the HLLC Riemann solver in this simulation as the exact solver is computationally too expensive.

4.3.2 Structure of the colliding wind region

Fig. 4.11 shows the density, mixing, velocity and temperature in the binary orbital plane of the 3D simulation (left column). The right column has the corresponding 2D maps on the same scale. The comparison confirms the mapping $\sqrt{\eta_{3D}} \rightarrow \eta_{2D}$ captures adequately the 3D structure in the 2D simulation. The positions of the shocks and contact discontinuity along the line of centres are similar in both 2D and 3D simulation and match the analytic solutions (see Chapter 3). The 3D opening angle defined by the contact discontinuities, well traced in the mixing map, is $15 \pm 1°$. This angle is consistent with the analytical estimates that have been used to model WR 104 [Harries et al., 2004b, Tuthill et al., 2008]. Because of the low η, there is a reconfinement shock behind the OB wind at a distance $\simeq 0.7\,5a$ in the 3D simulation ($1.5\,a$ in the 2D simulation). All of the OB wind is involved in the collision and no fraction escapes freely to infinity.

Material piles up in both arms of the spiral. Tuthill et al. [2008] suggest different strengths of the shock can change the conditions for dust formation in each arm. In the 3D simulation, the Mach number of the trailing arm at $r \simeq 12a$ is 13% higher than in the leading arm. The small temperature difference is unlikely to affect dust formation. A more significant effect is that compression keeps a hotter temperature in the leading arm than in the trailing arm. Material in the mixing zone of the trailing arm experiences a temperature an order-of-magnitude cooler than in the mixing zone of the leading arm, dust formation may be favoured in this arm. The velocity map shows that the velocity is mostly radial and that matter is accelerated on a distance of a few times the binary separation.

Fig. 4.12 shows the 2D simulation on the largest scale ($200\,a$ or about 470 AU). A stable spiral structure forms as expected for $\beta = 0.6$ and $\eta = 0.0625$. The collimated OB wind generates a low density spiral bounded on each side by walls of material where the density is about 100 times larger. The initially different mixing in both arms blurs at a distance of about $50\,a$. It

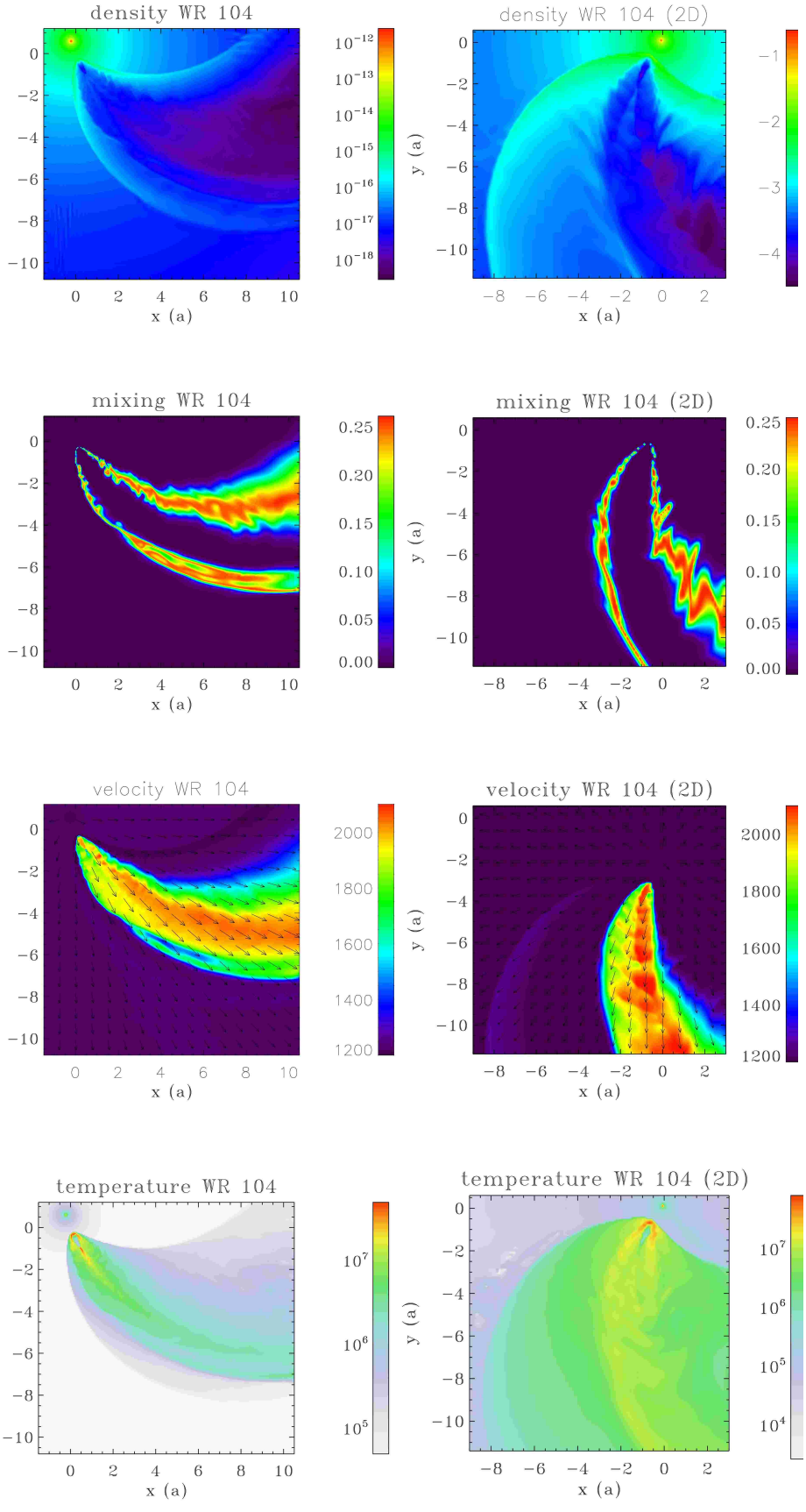

Figure 4.11: Density ($\mathrm{g\,cm^{-3}}$), mixing, velocity ($\mathrm{km\,s^{-1}}$), and temperature (K) in the orbital plane of the 3D simulation of WR 104 (left column). Corresponding 2D maps on the same scale (right column). The length scale is the binary separation a.

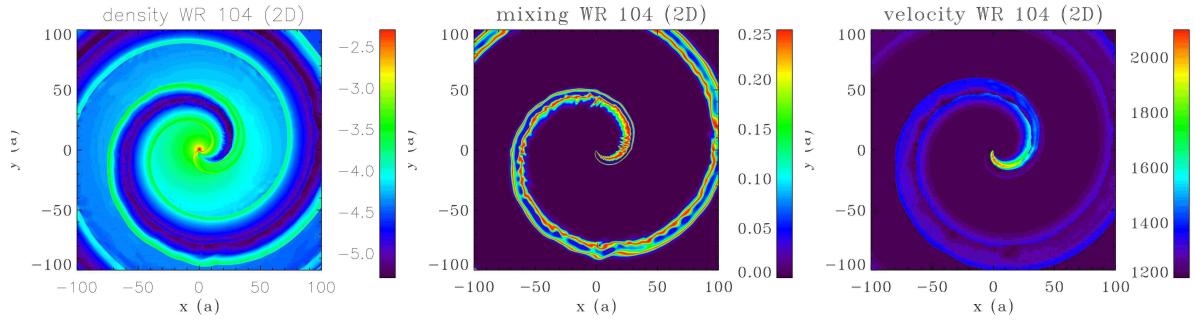

Figure 4.12: Density ($\mathrm{g\,cm^{-2}}$), mixing and velocity ($\mathrm{km\,s^{-1}}$) in 2D simulations of WR 104. The length scale is the binary separation.

slightly overlaps with the density enhancement of the arm. The single-armed spiral observed in infrared seems to be matched by the mixing region rather than the double spiral in the density map. A double-armed spiral structure, separated by a very under-dense region of angular size $\simeq 27$ mas (at 2.6 kpc, the estimated distance of the system), would have been resolved if the IR emission correlated with density, meaning the dust-to-gas ratio is constant. Simulations of the dust distribution around bow shocks suggest that this is not the case for large dust grains [van Marle et al., 2011b]. The width of the low density zone may be overestimated in this 2D simulation since it is likely to be related to the opening angle of the shocks, which Fig. 4.11 shows to be wider in 2D than in 3D. Whether one observes this tube as one or two pieces depends on the optical depth of the material. If it is optically thin, one likely observes two spirals. However, if the material is opaque, one observes only one spiral.

The step of the spiral is $1.05 S_{\mathrm{WR}}$ where $S_{\mathrm{WR}} = v_{\mathrm{WR}} P_{\mathrm{orb}} = 170\,\mathrm{AU} = 77\,a$. Tuthill et al. [2008] assumed S_{WR} to determine a distance of 2.6 kpc from the observed step size. The 5% correction to this distance due to the intrinsically larger spiral step is smaller than the uncertainty on the measured WR wind velocity and observed angular step size.

4.3.3 Conditions for dust formation

4.3.3.1 Results from the simulation

One criterion for dust formation is a high enough density. Cherchneff and Tielens [1995] indicate different paths towards the formation of amorphous carbon for number densities n ranging from 10^6 to $10^{13}\,\mathrm{cm^{-3}}$ and give a detailed study for $n = 10^{10}\,\mathrm{cm^{-3}}$. This gives $\rho = 1.4 \times 10^{-14}\,\mathrm{g\,cm^{-3}}$ assuming a mean molecular weight $\mu = 1.4$, typical for an ionized WC wind [Stevens et al., 1992]. Such a density is only present in the 3D simulation at the edge of the spiral, up to a distance $\simeq 2a$ from the WR star. In the 2D simulation, along the walls, the density drops as $\rho \propto r^{-1}$. Using this as guidance, I expect $\rho \propto r^{-2}$ in 3D on large scales. The minimum value $n = 10^6$ $\mathrm{cm^{-3}}$ considered by Cherchneff and Tielens [1995] is reached at $r \simeq 25\,a$ at the inner wall of the spiral. This is equivalent to a third of a turn along the spiral. The density is too low for dust formation beyond this distance so that any dust present far away has been advected out.

Using a similar method, I also expect the temperature to drop beyond the dust condensation limit at roughly half a turn of the spiral by extrapolating the temperatures close to the binary. The highest possible temperature for dust condensation is $\simeq 6000$ K in WR atmospheres [Cherchneff et al., 2000]. The distance I derived from my simulation can be taken as an upper limit to the dust condensation distance as this is calculated in the adiabatic approximation that constitutes a worst case scenario. It is consistent with the infrared observations of a quarter-orbit

shift between the maximum infrared emission and the binary centre.

Mixing between both winds brings hydrogen and is likely to facilitate the formation of dust. The amount of mixing increases with the distance to the binary. Integrated in spheres of increasing radii, the ratio of mixed material to the total amount of material in the spiral within r increases from $\lesssim 0.1\%$ at $r = a$ to $\simeq 5\%$ at $r = 10a$. These values are constant during the last stages of the simulation (lasting $\simeq 0.1 P_{\rm orb}$), indicating the development of the instabilities has reached a steady state. As can be seen on Fig. 4.11 and as explained in §4.1.3, mixing occurs mostly in the lower density regions of the colliding wind zone. It might be enhanced by the presence of clumps in the winds [Moffat et al., 1988].

4.3.3.2 Discussion

In my simulations I have assumed adiabatic winds since $\chi \gtrsim 1$ for both stars. However, the shocked structure and temperature profile can be strongly affected by additional cooling and heating processes, which may significantly affect dust formation.

Inverse Compton (IC) cooling is important for temperatures above 5×10^6K. The luminosity from both stars and electron temperatures in the winds are roughly equal. The corresponding cooling rate for the OB star is $\simeq 6.3 \times 10^{-23}\,\mathrm{erg\,cm^3\,s^{-1}}$ and $2.4 \times 10^{-25}\,\mathrm{erg\,cm^3}\,s^{-1}$ for the WR star. For a given temperature and stellar luminosity, it scales as the inverse of the mass loss rate. Inverse Compton cooling of electrons on the OB stellar photons can thus be expected to contribute significantly to cooling and help drive the WR wind into the radiative regime.

Acceleration of non-thermal particles also allows for cooling in the system [Pittard, 2010]. Its exact impact can only be determined by proper modelling of particle distributions and the corresponding energy losses.

Heat could be redistributed by thermal conduction. It creates a pre-heated zone around the shocks and widens the region with the highest temperature [Myasnikov and Zhekov, 1998] but the impact at larger distances seems limited. However, it may be important at the contact discontinuity if one of the winds is radiative and the other adiabatic. Similarly, large clumps could survive when passing through the shock and bring cooler material in the shocked region [Walder and Folini, 2003].

Additional heating comes from photoionisation by both stellar fields. As the geometry of the region is complex and there are two sources of photons, determining the size of the ionised region requires radiative transfer calculations.

The densities in the colliding wind region are on the low side compared to what dust formation models require. Adiabatic shocks only enhance the density by a factor 4 so cooling is required to reach higher compression ratios. Close to the binary, the winds are likely to present some cooling due to bremsstrahlung in the WR wind but even more due to IC losses in the OB wind. This results in a thinner and denser shocked layer. Pittard [2009] shows the post-shock density is about 100 times higher in their model cwb1, which has strong cooling, than in their adiabatic model cwb3. Radiative cooling also decreases the temperature, bringing the region where dust condensation is possible, closer to the binary. Thin shell instabilities can develop when cooling is strong, enhancing mixing of the winds. Given the impact of the KHI in adiabatic colliding winds, thin shell instabilities can also be expected to significantly influence the large scale structure. Pittard [2009] has shown that the differentiation of the arms remains when thin shell instabilities are present but the large scale outcome has not been studied yet.

Strong cooling is not necessarily present in all WR binaries. Williams et al. [2012] present evidence from long-term IR observations of WR 48 for dust production throughout the orbit. The stellar winds in this system have similar characteristics than in WR 104 but the (tentative) orbital period is much longer, 32 years. Williams et al. [2012] estimate the system to be adiabatic with an average $\chi \simeq 11$. The value will be even higher at apastron in the eccentric orbit ($e = 0.6$),

yet dust formation is present. Unfortunately the properties of the winds are unknown and one cannot determine whether IC cooling could be important in this system. High densities will be much more difficult to reach than in WR 104, requiring dust formation at hitherto lower densities than have been considered possible.

4.4 What did we learn? What are possible extensions?

- Because of orbital motion, the KHI arises even when the winds have identical terminal velocities.
- Orbital motion causes differentiation between the shocked arms. The arm propagating into the higher density wind is slowed down and compressed while the one propagating in a lower density region expands.
- The KHI develops more strongly in the wider arm and mixing occurs preferentially in the lower density zones in the shocked regions.
- At large scale, the spiral structure may be destroyed due to the KHI. Strong density gradients have a stabilising effect.
- The step of the spiral is mainly determined by the stronger wind but there is a correction due to the presence of the weaker wind.
- The large scale structure of WR 104 can be determined by an adiabatic model. The spiral structure follows an Archimedean spiral with an important density enhancement at both walls and some mixing in the inner regions.
- The density and temperature profiles in the shocked region are not compatible with the expected conditions for dust formation. Some cooling in the winds seems to be necessary to decrease the temperature and increase the density. Inverse Compton cooling in the OB wind and free-free emission in the WR wind are probably the most efficient mechanisms.

When cooling is important the shocked region is subject to the Non-linear Thin Shell Instability (see §3.2.2). Simulations focussing on the regions close to the binary ($< 10\,a$) indicate the instabilities have an important impact on the geometry of the shocked arms [Pittard, 2009, Parkin et al., 2011, van Marle et al., 2011a]. Whether the spiral structure can subsist has never been looked at. Unfortunately, such simulations require a very high resolution and simulating a complete spiral step of a colliding wind binary which displays strong cooling is still out of reach.

Using a dynamical model, Parkin and Pittard [2008] show that the spiral becomes increasingly asymmetric when the eccentricity of the system increases. In highly eccentric systems, the orbital velocity has important variations throughout the orbit. Therefore, the step of the spiral varies and different turns from the spiral can interact as is shown in simulations from η Carinae [Parkin et al., 2011]. Simulations at larger scale could explain whether this is an additional mechanism that can destroy the spiral structure. Such systems probably alternate between a radiative state at periastron and an adiabatic state at apastron.

The work presented in this chapter is explained in detail Lamberts et al. [2012] accepted for publication in *Astronomy and Astrophysics* and that can be found at the end of this chapter.

4.5 Résumé en français

Ce chapitre présente des simulations de collisions de vents à une échelle bien plus grande que dans le chapitre 3 (jusqu'à 200 fois la séparation du système). Dans ce cas l'impact du mouvement

orbital est fondamental pour la structure du système. Près de la binaire, il introduit un angle d'aberration entre l'axe de la binaire et le plan de symmétrie de la zone choquée. Plus loin, on s'attend à ce que la courbure de la zone choquée forme une spirale Archimédienne. Je me suis focalisée sur les systèmes adiabatiques car la résolution nécessaire pour la simulation d'un système isotherme est prohibitive. La seule instabilité attendue est donc l'instabilité de Kelvin-Helmholtz (KHI). J'étudie le mélange entre les vents qu'elle induit en introduisant un scalaire passif dans les vents. L'étude du mélange est important car il pourrait faciliter la formation de poussières dans les systèmes WR+O en apportant de l'hydrogène au vent de la WR pauvre en hydrogène. Dans les binaires γ il pourrait diminuer l'accélération des particules et supprimer ainsi l'émission radio observée à grande echelle.

J'ai tout d'abord confirmé que le mouvement orbital crée une différence de vitesses entre les deux vents, ce qui permet le développement de KHI même lorsque les deux vents ont une vitesse terminale identique. Ceci n'était pas clairement établi [Lemaster et al., 2007, van Marle et al., 2011a]. Lorsqu'on augmente la différence de vitesse entre les vents, les deux zones choquées se différencient de plus en plus. Celle qui se propage dans le vent le plus dense est ralentie et comprimée alors que celle qui s'étend dans le vent le plus rapide s'élargit. Mes simulations indiquent que le KHI se développe plus facilement dans le bras le plus large car le contraste de densité y est plus faible. De plus, le mélange qui en résulte a lieu principalement dans les régions peu denses.

La différenciation des bras se retrouve dans la structure spirale à plus grande échelle. Le pas de la spirale est déterminé par $v \times P$ où P est la période orbitale du système et v la vitesse du vent mais la valeur à choisir pour la vitesse du vent n'est pas évidente. En mesurant les pas des spirales dans un ensemble de simulations avec différents rapports de flux de quantité de mouvement et de vitesse, j'ai déterminé qu'il n'existe pas de règle simple pour déterminer le pas de la spirale. Il est principalement déterminé par la vitesse du vent dominant, mais le vent le plus faible peut apporter une correction non-négligeable. De façon très surprenante, certaines simulations ne présentent pas de structure spirale mais un état final très turbulent. J'explique que cela est dû à l'instabilité de Kelvin Helmholtz qui peut détruire la structure si la différence vitesse est importante. Néanmoins, un fort gradient de densité permet de stabiliser la structure. Mon étude permet de prédire la présence ou non de spirales dans les différents types de binaires à collision de vents. En supposant que les résultats de ce chapitre se transposent aux vents relativistes, on s'attend à une spirale à grande échelle dans les binaires γ si le vent de l'étoile domine la structure.

Les binaires composées d'une étoile de type Wolf-Rayet (WR) et une étoile de type O ou B forment des spirales qui peuvent être observées en infrarouge, grâce à la présence de poussière [Tuthill et al., 2008]. L'origine de cette poussière est mal comprise car elle nécessite une densité plus forte et une température plus faible que celles trouvées dans les vents stellaires. La zone de collision dans les systèmes binaires semble présenter des conditions plus favorables. J'ai étudié l'une de ces binaires, WR 104, dans laquelle le vent de l'étoile WR domine fortement la structure. Une très haute résolution est donc requise au centre, ce qui limite l'étendue de la simulation. J'ai réalisé une simulation 3D à petite échelle et une simulation complémentaire à 2D à beaucoup plus grande échelle. Elles confirment la structure en spirale Archimédienne et montrent que les zones de plus forte densité sont concentrées sur ses bords. Du mélange se produit au centre de la spirale. Cependant, le modèle de vents adiabatiques ne permet pas de créer des zones où la formation de poussière serait possible, en terme de température et de densité. Cela suggère que du refroidissement radiatif a lieu au sein de ce système. Il serait dû au rayonnement de freinage dans le vent dense de la WR et au refroidissement inverse Compton dans le vent du compagnon.

L'ensemble des résultats présentés dans ce chapitre a été présenté dans l'article Lamberts et al. [2012] accepté pour publication dans *Astronomy and Astrophysics*qui est joint à la fin de

ce chapitre.

4.6 Paper : Impact of orbital motion on the structure and stability of adiabatic shocks in colliding wind binaries (A&A, 2012)

Astronomy & Astrophysics manuscript no. KHrot
July 3, 2012

Impact of orbital motion on the structure and stability of adiabatic shocks in colliding wind binaries

A. Lamberts[1], G. Dubus[1], G. Lesur[1], and S. Fromang[2]

[1] UJF-Grenoble 1 / CNRS-INSU, Institut de Planétologie et d'Astrophysique de Grenoble (IPAG) UMR 5274, Grenoble, F-38041, France
[2] Laboratoire AIM, CEA/DSM - CNRS - Université Paris 7, Irfu/Service d'Astrophysique, CEA-Saclay, 91191 Gif-sur-Yvette, France

July 3, 2012

ABSTRACT

Context. The collision of winds from massive stars in binaries results in the formation of a double-shock structure with observed signatures from radio to X-rays.
Aims. We study the structure and stability of the colliding wind region as it turns into a spiral owing to the orbital motion. We focus on adiabatic winds, where mixing between the two winds is expected to be restricted to the Kelvin-Helmholtz instability. Mixing of the Wolf-Rayet wind with hydrogen-rich material is important for dust formation in pinwheel nebulae such as WR 104, where the spiral structure has been resolved in infrared.
Methods. We use the hydrodynamical code RAMSES to solve the equations of hydrodynamics on an adaptive grid. A wide range of binary systems with different wind velocities and mass-loss rates are studied with two-dimensional simulations. A specific three-dimensional simulation is performed to model WR 104.
Results. Orbital motion leads to the formation of two distinct spiral arms where the Kelvin-Helmholtz instability develops differently. We find that the spiral structure is destroyed when there is a large velocity gradient between the winds, unless the collimated wind is much faster. We argue that the Kelvin-Helmholtz instability plays a major role in determining whether the structure is maitained. We discuss the consequences for various colliding-wind binaries. When their spiral structure is stable, there is no straightforward relationship between the spatial step of the spiral, the wind velocities, and the orbital period. Our 3D simulation of WR 104 indicates that the colder, well-mixed trailing arm has more favourable conditions for dust formation than the leading arm. The single-arm infrared spiral follows more closely the mixing map than the density map, suggesting that the dust-to-gas ratio may vary between the leading and trailing density spirals. However, the density is much lower than what dust formation models require. Including radiative cooling would lead to higher densities, and also to thin shell instabilities whose impact on the large-scale structure remains unknown.

Key words. hydrodynamics - instabilities - binaries :general - stars: individual : WR 104 - stars: winds, outflows

1. Introduction

During the main-sequence and Wolf-Rayet (WR) phase, massive stars possess highly supersonic winds due to radiation pressure on atomic lines. Wind mass-loss rates range from $\dot{M} \simeq 10^{-8} M_\odot$ yr^{-1} for O or B type stars to $\dot{M} \simeq 10^{-4} M_\odot$ yr^{-1} for Wolf-Rayet stars (Puls et al. 2008). Many massive stars lie in binary systems, although the binary fraction differs from one stellar cluster to another: Kobulnicky & Fryer (2007) give a binary fraction of 70 % for the OB2 cluster, while Ritchie et al. (2009) give a binary fraction of at least 30 % in the Westerlund I cluster. In binary systems, the interaction of the two supersonic stellar winds creates two strong shocks separated by a contact discontinuity. First of all, the geometry of the colliding wind region depends on the momentum-flux ratio of the winds (Lebedev & Myasnikov 1990)

$$\eta \equiv \frac{\dot{M}_2 v_2}{\dot{M}_1 v_1}, \tag{1}$$

where v is the wind velocity. The subscript 1 usually stands for the stronger wind, and the subscript 2 for the weaker one so that $\eta \leq 1$. There are several important observational signatures of the colliding wind region. The shock-heated gas generates observable thermal X-ray emission (e.g. Cherepashchuk 1976; Luo et al. 1990; Usov 1992; Stevens et al. 1992). The presence of intra-binary structures causes variations in the emission line profiles with orbital phase (e.g. Shore & Brown 1988; Wiggs & Gies 1993). The high densities reached in the colliding wind region are thought to enable the formation of dust, explaining the large infrared emission from binary systems with WR stars (Williams et al. 1987; Usov 1991), and the formation of spiral structures extending to distances of up to 300 times the binary separation ("pinwheel nebulae", Tuthill et al. 1999). In some systems, the diffusive shock acceleration of particles leads to non-thermal radio emission (Dougherty & Williams 2000, see De Becker 2007 for a review). The radio emission has been resolved by long-baseline interferometry and shown to have a morphology changing with orbital phase (e.g. Dougherty et al. 2005). A new exotic class of colliding wind binaries is gamma-ray binaries, where the non-thermal emission is thought to arise from the interaction of a pulsar relativistic wind with the wind of its massive stellar companion (Dubus 2006). Interpreting all these observational data requires increasingly detailed knowledge of the physics of colliding winds, hence numerical simulations, notably of the large-scale regions that can be resolved in radio or infrared.

Send offprint requests to: A. Lamberts: astrid.lamberts@obs.ujf-grenoble.fr

On large scales, orbital motion is expected to turn the shock structure into a spiral, although we show that this is not always true. Orbital motion breaks the symmetry with respect to the binary axis and no analytic solution predicts the detailed structure of the colliding wind region. Material in the spiral is generally assumed to behave ballistically, so that the step of the spiral is the wind velocity v times the orbital period $P_{\rm orb}$. The wind velocity to use is unclear. Tuthill et al. (2008) took the speed of the dominant wind v_1 (dominant in the sense that $\dot{M}_1 v_1 \geq \dot{M}_2 v_2$), whereas Parkin & Pittard (2008) assumed that it is the slower wind that determines the step of the spiral but focus their study on binaries with equal wind velocities. Simple dynamical models of the shocked layer have been developed for use with radiative transfer codes, assuming that the double shock structure is infinitely thin (thin shell hypothesis) and that the material is ballistic (Harries et al. 2004; Parkin & Pittard 2008). The spiral structure is then reproduced at small computational cost but this neglects the impact of the pressure, which creates a distinction between both arms of the spiral (Lemaster et al. 2007; Pittard 2009; van Marle et al. 2011), the influence of the reconfinement of the weaker wind for small η (Lamberts et al. 2011), and the large-scale evolution of instabilities in the colliding wind region (see below). Walder & Folini (2003) provide the first large-scale three-dimensional simulation showing a few spiral steps. The resolution in the simulation is too low to model instabilities. Okazaki et al. (2008) and Parkin et al. (2011) both present a three-dimensional simulation of η Carinae showing instabilities at the wind interface, using respectively a SPH method and a grid-based method. Up to now, neither a two-dimensional nor three-dimensional hydrodynamical simulation has modelled a complete step of the spiral at high resolution. We achieve this by using the hydrodynamical code RAMSES (Teyssier 2002) with adaptive mesh refinement (AMR). Adaptive mesh refinement allows large scale simulations to be performed while keeping a high enough resolution close to the binary in order to form the shocks properly (§2).

Small-scale simulations without orbital motion (see Stevens et al. 1992 and references in Lamberts et al. 2011, hereafter paper I) have shown that several instabilities are at work in colliding wind binaries. Thin shell instabilities occur when cooling is important so that the shocked zone narrows to a thin layer, which is easily perturbed (Vishniac 1994). They provoke strong distortions of the whole colliding region (Pittard 2009; van Marle et al. 2011). However, these instabilities are unlikely to be dominant in wide binary systems where cooling is inefficient, the shocks adiabatic, and the colliding wind region wider (Stevens et al. 1992). In this case, the velocity difference between both winds triggers the Kelvin-Helmholtz instability (KHI) at the contact discontinuity (paper I). The inlusion of orbital motion has led to contradictory results. Lemaster et al. (2007) found that eddies develop even when the winds are completely identical, because orbital motion introduces a velocity difference. Pittard (2009) found no eddies in a simulation with a similar setup. van Marle et al. (2011) also found no eddies, although their simulation has an initial non-period binary system where the collision between the winds of the WR and its early-type companion is expected to be close to adiabatic (see §5). The infrared emission is very well-matched by an Archimedean spiral, although its brightest point is shifted by 13 milli-arcseconds from its centre, possibly because dust formation is inhibited at smaller radii (Tuthill et al. 2008, hereafter T2008). The WR wind is hostile to dust formation owing to its high temperature, low density, and absence of hydrogen (Cherchneff et al. 2000). The wind collision region is more favourable, providing high densities, shielding from the ultraviolet radiation of the WR star, and the possibility of mixing with hydrogen from the companion star (Marchenko & Moffat 2007). We carried out 2D and 3D hydrodynamical simulations using the parameters of WR 104 to investigate these questions (§5). We then relate all our results to observations (§6).

2. Numerical simulations

2.1. Equations

We use the hydrodynamical code RAMSES for our simulations (Teyssier 2002). This code uses a second-order Godunov method to solve the equations of hydrodynamics

$$\frac{\partial \rho}{\partial t} + \nabla \cdot (\rho \mathbf{v}) = 0 \tag{2}$$

$$\frac{\partial (\rho \mathbf{v})}{\partial t} + \nabla (\rho \mathbf{v}\mathbf{v}) + \nabla P = 0 \tag{3}$$

$$\frac{\partial E}{\partial t} + \nabla \cdot [\mathbf{v}(E + P)] = 0, \tag{4}$$

where ρ is the density, $\mathbf{v}$ the velocity, and P the pressure of the gas. The total energy density E is given by

$$E = \frac{1}{2}\rho v^2 + \frac{P}{(\gamma - 1)}, \tag{5}$$

where γ is the adiabatic index, which set to 5/3 to model adiabatic flows.

2.2. Numerical parameters

We use the MinMod slope limiter together with the exact Riemann solver (§3-4) or the HLLC (§5) Riemann solver to avoid numerical quenching of instabilities. We perform 2D and 3D simulations on a cartesian grid with outflow boundary conditions. We use AMR, which enables to locally increase the spatial resolution according to the properties of the flow. We base the refinement criterion on velocity gradients. Fig. 1 shows the AMR mesh of the central part of the simulation of WR 104 and the corresponding density map. Refinement occurs very close to the stars and at the discontinuities. In section §3 we perform small-scale simulations where the size of the computational domain is $l_{box} = 40a$, with a the binary separation. We have $n_x = 64$ for the resolution of the coarse (unrefined) grid and use seven levels of refinement. This gives an equivalent resolution that is at least two times higher than in former studies (Lemaster et al. 2007; Pittard 2009; van Marle et al. 2011). In section §4, we perform larger-scale simulations where $l_{box} = 400a$ and the coarse grid also has $n_x = 64$ although we use up to nine levels of refinement. In some cases, we adapt the size of our grid to larger or smaller values to model a complete step of the spiral.

2.3. Generation of the winds

To simulate the winds, we keep the same method as used in paper I, which was largely inspired by Lemaster et al. (2007). Around each star, we create a wind by imposing a given density, pressure, and velocity profile in a spherical zone called a mask. The masks are reset to their initial values at each time step to create steady winds. We add two passive scalars s_1 and s_2 to distinguish both winds and to quantify mixing. We initialise the passive scalars in the masks; their evolution is determined by

$$\frac{\partial \rho s_i}{\partial t} + \nabla \cdot (\rho s_i \mathbf{v}) = 0 \qquad i = 1, 2. \tag{6}$$

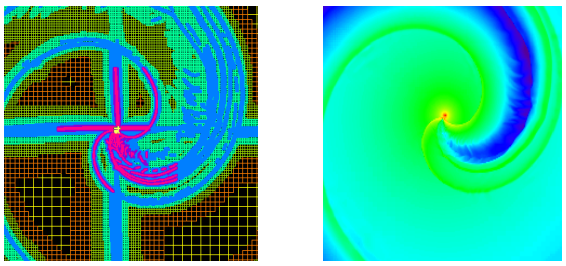

Fig. 1. 2D simulation of WR104. Left panel : AMR map, the coarse level is $l_{min} = 7$ (yellow grid in outer regions), the highest resolution is $l_{max} = 16$ (pale yellow at the very center of the grid). Right panel: The density map shows refinement happens at the shocks.

In the free wind of the first star, $s_1 = 1$ and $s_2 = 0$, whereas in the second wind it is the other way round. In the shocked zone, both scalars have an intermediate value which accounts for the mixing of the winds. The rotation of the stars is clockwise in the figures, their positions are updated using a leapfrog method. For each simulation, the input parameters are the mass M, mass-loss rate $\dot{M}$, wind velocity v (which we assume to be constant), and Mach number $\mathcal{M}$ at $r = a$ for each star. The exact value of the Mach number does not matter for the colliding wind region, as long as it is high enough for pressure terms to be neglected (paper I), which is the case for massive-star winds. Here, the Mach numbers of both winds are set to 30. In all our simulations, the star with the highest momentum flux is considered as the first star. We refer to its wind as the stronger wind. The values of the parameters of the winds in the simulations are given in the table in Appendix B. Both stars have a mass of 15 $M_\odot$ and the binary separation a is 1 AU. The corresponding orbital period $P_{\rm orb}$ is 0.18 yr (67 days). The orbital velocity of the stars is $v_{orb} = 81$ km s^{-1}. The winds are isotropic in the workframe of the simulation. As the orbital velocity is negligible with respect to the speed of the winds, each wind can also be considered isotropic in the frame corotating with the corresponding star. We neglect stellar rotation and the wind acceleration. We only study circular orbits.

2.4. 2D and 3D simulations

We perform our 2D simulations in the orbital plane of the binary. We thus model the cylindrical (r, θ) plane instead of the (r, z) plane as classically done (e.g. Stevens et al. 1992; Brighenti & D'Ercole 1995; Pittard et al. 2006). This implies that the density evolves $\propto r^{-1}$ instead of $\propto r^{-2}$ in a spherical geometry. For a given η, the structure of the colliding wind binary is thus different in 2D and 3D. However, as discussed in paper I, the mapping $\sqrt{\eta_{3D}} \rightarrow \eta_{2D}$ captures most of the 3D structure in the 2D simulations. This point is re-discussed in §5, where we compare the results of a 2D simulation of WR 104 with a full 3D simulation including orbital motion. A major advantage of our 2D setup is the possibility of implementing orbital motion for a modest computational cost, enabling the study of the flow structure up to scales currently inaccessible to full 3D calculations.

3. Impact of orbital motion on the shock arms

We carried out simulations of adiabatic colliding winds identical to those carried out in paper I, except that they now include orbital motion to study its impact on the shock structure and development of the KHI. The simulations explore $\eta = 1$ and $\eta = 0.0625$ for different velocity ratios $\beta \equiv v_1/v_2 = 1, 2, 20$, and all in a box of size $8a$. Briefly, the results without orbital motion were that (1) no instability is seen when β=1; (2) for $\beta \geqslant 2$, the instabilities affect the position of the contact discontinuity, while for $\beta = 20$ the KHI also affects the shock positions; (3) for $\eta = 0.0625$ the instabilities remain confined to the weaker wind. We present first the results of the simulations for β=1, where the KHI instability may be triggered (or not) by orbital shear (§3.1). We then discuss the simulations with $\beta \neq 1$. In these cases, the dominant wind is slower and much denser than the weaker wind. For $\eta = 1$, there is no difference between simulations where $\beta = B$ and $\beta = 1/B$.

A view of the overall colliding-wind structure is given in Fig. 2. We define the leading arm as the arm preceding the second star, with respect to orbital motion (clockwise motion). The trailing arm is the second part of the spiral. We note that there is no dominant wind when $\eta = 1$ so that the definition of leading/trailing is degenerate in this case. (The definition also has no link with the definition commonly used in galactic dynamics.) In each arm, there is a shock in the wind from the first star and a shock in the wind from the second star, separated by a contact discontinuity. In 2D simulations, when $\eta < 0.25$ the second wind is confined by the intersection of the shocks. In a 3D simulation, this occurs for $\eta \simeq 0.06$ (paper I).

Close to the binary, the relative motion of the stars creates an "aberration" (Parkin & Pittard 2008) of the shocked zone.Parkin & Pittard (2008) introduce the skew angle μ, which measures the offset between the line of centres of the stars and the symmetry axis of the shocked region. It is given by

$$\tan \mu = \frac{v_{orb}}{v}, \tag{7}$$

where v is taken as the speed of the slowest wind. This angle remains small unless the velocities of the winds are strongly reduced or orbital motion becomes important We measured μ in our simulations by finding the best fit of the analytic position of the contact discontinuity derived by Canto et al. (1996). An example is given on Fig. 3. We measured $\mu \simeq 22°$ in the simulation $\{\eta = 0.0625, \beta = 0.05\}$, while the theory predicts $\mu = 21°$. The simulation of WR 104 (see §5) gives $\mu \simeq 9°$, while the theory predicts $\mu = 8°$. We found thatμ is too small in our other simulations to allow correct measurements.

3.1. Simulations with $\beta = 1$

Fig. 4 shows the density, velocity, and mixing map for a simulation with identical winds $\{\eta = 1, \beta = 1\}$. We define the mixing to be the product of the passive scalars $s_1 \times s_2$. The free (unshocked) winds correspond to the low density parts at the top and bottom. The denser parts are the shocked winds. The radial inhomogeneities visible in the unshocked wind region of the velocity map is a numerical artefact: it corresponds to minute anisotropies in the stellar wind due to the finite size of the masks. As shown in Appendix A, the orbital period is much longer than the local shear timescale. The Coriolis force does not impact the development of the KHI. However, the velocity map shows that a $\simeq$ 20% velocity difference develops in each arm at a distance $\simeq 20a$ from the binary. Orbital motion makes the shocked material leading the contact discontinuity (red region on the velocity map) accelerate in the lower-density free-wind region. Conversely, the shocked wind trailing the contact discontinuity (in green) moves into the denser, shocked material of the other wind. The resulting velocity difference is sufficient to trigger the KHI, even though the original wind speeds

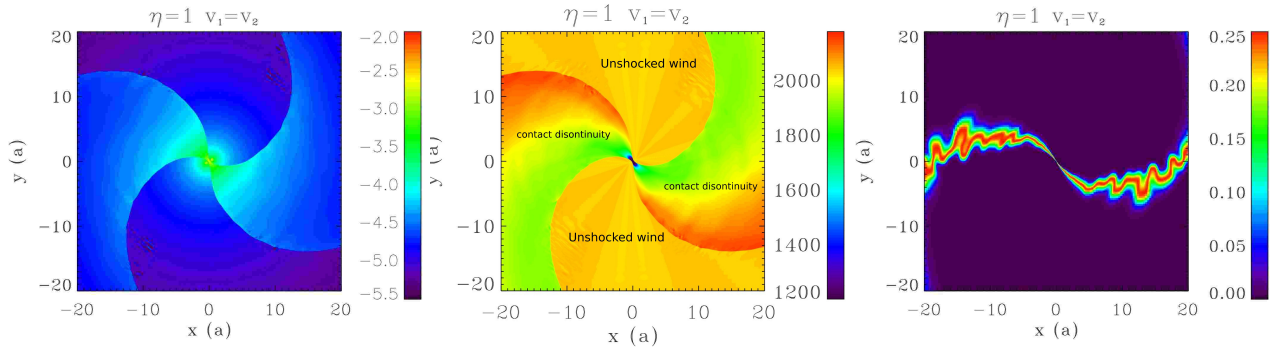

Fig. 4. Small-scale simulation: density, velocity, and mixing for a simulation with identical winds ($\eta = 1, \beta = 1$). The density is given in g cm^{-2}, the velocity is in km s^{-1} and the mixing of the winds is a dimensionless variable. The length scale is the binary separation a.

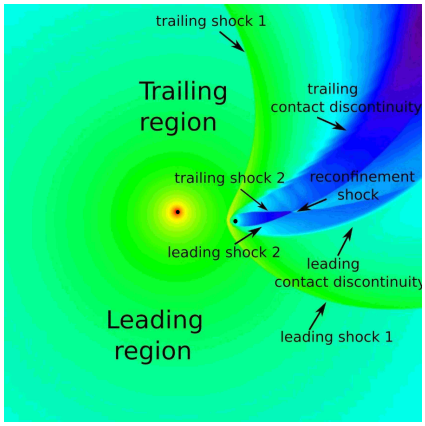

Fig. 2. Density map of a colliding wind binary including orbital motion ($\{\eta$=0.065,β=0.5$\}$). The stars are shown by the black circles. The spiral structure has a leading and trailing arm. Each arm is composed of one shock from each wind and a contact discontinuity. In this case, both shocks from the wind of the second star intersect, totally confining the second wind.

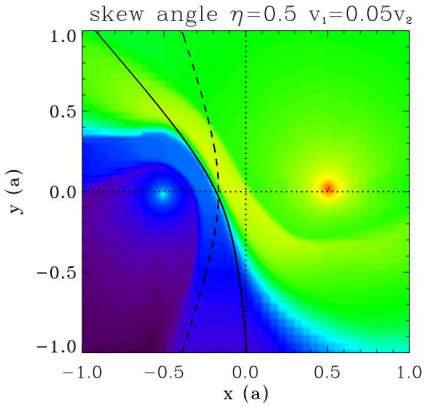

Fig. 3. Determination of the skew angle μ for $\{\eta = 0.5, \beta = 0.05\}$ using a density map. The dashed line shows the theoretical position of the contact discontinuity for $\mu = 0$ (no orbital motion). The solid line fits the contact discontinuity in the simulation. The length scale is set by the binary separation a.

are equal. The instability is clearly present in the mixing map. We therefore confirm the results of Lemaster et al. (2007) that orbital motion triggers the KHI, even when the winds are identical. We also observe, as they do, an artificial enhancement of the instabilities when the shocks align with the grid. Our simulations contradict the results of van Marle et al. (2011), who find no KHI. Their simulations are performed with a Lax-Friedrichs Riemann solver. We ran a test simulation with the Lax-Friedrichs Riemann solver and observed no development of the KHI either, owing to the high numerical diffusivity.

Fig. 5 shows the density, velocity, and mixing for $\{\eta = 0.0625, \beta = 1\}$. Because of the low value of η, there is a reconfinement shock (paper I) behind the second star. The various discontinuities are indicated in the velocity map, which should be compared with the simpler geometry shown previously in Fig. 2. Our simulations without orbital motion showed no KHI because the initial velocities are identical. Here, as in the $\eta = 1$ case, orbital motion leads to velocity shear and mixing at the contact discontinuity. The KHI is confined to narrow regions close to the discontinuity because the velocity difference is small. We had found the same behaviour in the models explored in paper I. We also see that complex velocity structures arise in the colliding wind region even in this *a priori* simple case where both winds have the same velocity, highlighting the possible difficulties in interpreting spectral line features arising from this region without any guidance from numerical simulations.

3.2. Simulations with $\beta \neq 1$

Fig. 6 shows the density and mixing for simulations with $\{\eta = 1, \beta = 2, 20\}$ and $\{\eta = 0.0625, \beta = 0.05, 0.5, 2, 20\}$. These maps show the impact of rotation on the arm geometry and the development of the instabilities.

The leading and trailing arms become markedly different when the velocity difference increases, even when η=1. The shocked zone preceded by the unshocked wind with the high velocity and low density is larger than the zone preceded by the lower-velocity, higher-density wind. The latter shocked zone is compressed by the high velocity wind into a high density region (van Marle et al. 2011). We verified that, as expected if this explanation is correct, for $\beta > 1$ the compressed arm is the trailing arm, while for $\beta < 1$ the compressed arm is the leading arm (see Fig. 6). For $\beta = 20$, compression results in a rim of puffed-up matter where the density increases by two orders of magnitude with respect to the simulation with $\beta = 1$. The differentiation of both arms is independent of the instabilities in the winds but plays a role in their development.

The KHI starts similarly in both arms close to the binary major axis as the velocity difference and density jump across the

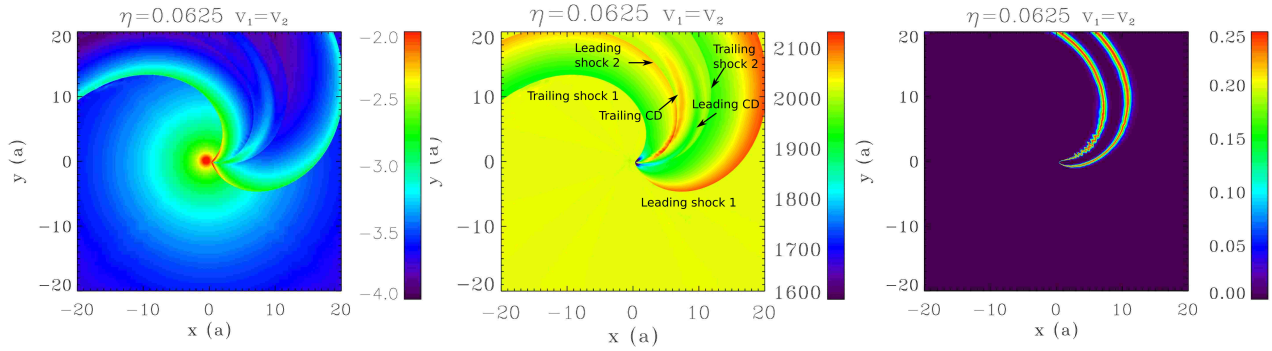

Fig. 5. Small-scale simulation: same as Fig. 4 for $\{\eta = 0.0625, \beta = 1\}$

.

contact discontinuity are the same in both arms. The symmetry between both arms is broken as the flow moves outwards. The compression of the shocked zone in the narrower arm results in a thin mixed zone with small-scale structures, whereas the eddies are stretched out in the wider arm. Mixing covers a larger area in the wider zone. This is not just a geometrical effect. We show in Appendix A that when media have different densities ($\alpha \neq 0$, see Eq. A.10) mixing by the KHI occurs preferentially in the least dense medium. This can be observed on Fig . 6, *e.g* for $\eta = 0.0625, \beta = 2$) and indicates that the mixing we observe is results from the KHI. Both velocity and density profiles thus play a role in the development of the KHI in colliding wind binaries. They both impact the large-scale outcome of the spiral structure as we demonstrate in §4.

We checked that the mixing is physical and not numerical. If mixing results from numerical diffusion, the physical size of the mixed zone increases with decreasing resolution. If mixing follows from instabilities, the physical size of the mixed zone is constant with resolution. We measured the width of both mixed zone across the contact discontinuity at $y = 6$ for $\{\eta = 0.0625, \beta = 2\}$ in a set of simulations with different resolutions. In all cases, n_x=64 and we successively added levels of refinement. The limit of the zone was determined to be $s_1 \times s_2 = 0.05$. The successive widths of the mixed layer are for the wider arm : 22 a, 17a, 12a, 8.6a, 6.3a, 5.8a, 5.7a, and 5.6a. For the narrower arm we measure 8.8a, 5.0a,3.7a, 2.3a, 1.9a, 1.4a , 1.1a and 0.67a. In the wider arm, the width is almost constant for the three highest resolutions, which enables mixing to be resolved. In the narrower arm, the difference between simulations decreases with resolution, but the width is not constant. The narrower arm is only marginally resolved.

4. Formation of a spiral structure

We now consider the large-scale evolution of the previous simulations (§3) in a box of size $l_{box} = 400a$. Density and mixing maps are shown for $\eta = 1$ in Fig. 7 and for $\eta = 0.0625$ in Fig. 8, with β increasing from top to bottom in both figures. The spatial scale is the same in all plots except for the top two panels of Fig. 8, where we reduced the size of the domain to avoid unnecessary computational costs. The different behaviour of mixing in both arms discussed in §3 persists on the larger scales, eventually causing both contact discontinuities to merge into one single spiral in simulations with $\eta = 0.0625$ (Fig. 8). We cannot exclude that this merger results from numerical artefacts owing to the use of a cartesian grid to describe an inherently spherical phenomenon. Merging should still occur naturally from inhomogeneities in the winds. Figures 7-8 also show that the colliding wind region does not always turn into a stable spiral and that, for a given η the appearance depends strongly on the velocity ratio β. We discuss below the step size that we measure when a steady spiral forms before addressing the issue of the stability of the pattern.

4.1. The step of the spiral

We found that, when a stable spiral structure is formed, an Archimedean spiral with a step size S provides a good fit to the results of our simulations. We measured S by overplotting an Archimedian spiral to the mixing maps and finding the best fit of the spiral arms, by eye. We checked our result by measuring the mean size of the steps in the same maps. As in Pittard (2009), we found that the fit with an Archimedean spiral is imperfect at the apex. However, the deviation is small and limited to a region $\simeq 10a$. Mixing closely follows the contact discontinuities in the arms so we used the mixing maps to trace the spiral. The spiral is not always clearly apparent in the density maps (*e.g.* $\{\eta = 0.0625, \beta = 1\}$ in Fig. 8), especially when a complex flow is established by the presence of a reconfinement shock behind the weaker star (Fig. 1). The fitted S for various values of η and β is compared to the theoretical estimate S_1 in Fig. 9, S_1 is based on the assumption that the velocity of the stronger wind controls the structure scale so that $S_1 = P_{\rm orb} v_1$ (e.g. T2008). When $v_1 = v_2$, there is no ambiguity in the velocity that sets the step size, and we verify that, in this case, $S = S_1$ for all η. This also rules out any significant numerical issue with the way in which the spiral develops. There are significant deviations from S_1 in all the other cases, except when $\eta \ll 1$ *i.e.* when the first wind largely dominates the momentum balance. For more balanced ratios η, the spiral step is smaller than expected when the weaker wind is slower than the stronger wind, and vice-versa when the weaker wind is the fastest. The use of the slowest wind speed instead of v_1 (e.g. Parkin & Pittard 2008) does not provide a better agreement with our simulations. The results do not provide a straightforward analytical correction using η and β that could be used to interpret observations of pinwheel nebulae without requiring hydrodynamical simulations.

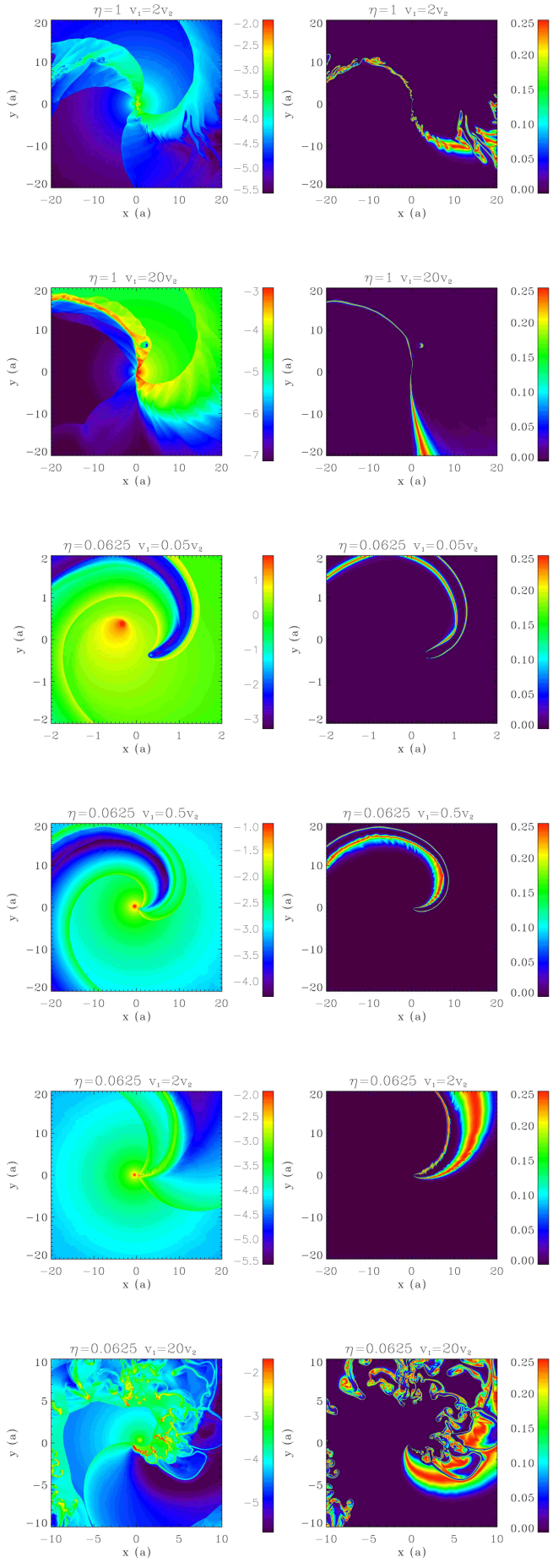

Fig. 6. Small scale simulation: density (left column) and mixing (right column) for simulations with $\{\eta = 1, \beta = 2, 20\}$ (two upper rows) and $\{\eta = 0.0625, \beta = 0.05, 0.5, 2, 20\}$ (lower rows). The length scale is the binary separation a.

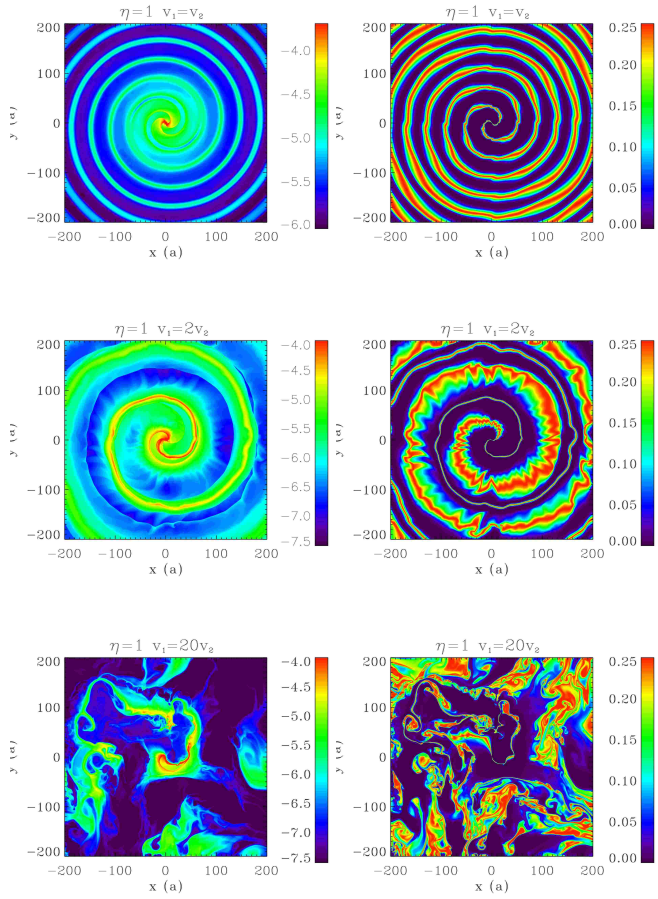

Fig. 7. Large-scale simulation : density (left column) and mixing (right column) for simulations with $\{\eta = 1, \beta = 1, 2, 20\}$ (from top to bottom) in the large boxes. The length scale is the binary separation a. The mixing of the winds is a dimensionless variable.

4.2. Stability of the spiral structure

The complete disruption of the spiral structure for large velocity ratios (Figs. 7-8) was unexpected. The breakdown can be traced to the KHI: we found that the structure was stabilised when we tested a setup with a Lax-Friedrichs Riemann solver and a smaller resolution, in which case the KHI is artificially suppressed (paper I). The amplitude of the KHI appears to destroy the spiral when strong velocity gradients are present, resulting in widespread turbulence and important mixing throughout the domain. Curiously, for $\eta = 0.625$, the structure is unstable when $v_1 = 20v_2$, while it is stable for the opposite velocity gradient $v_1 = 0.05v_2$: the strong density gradient ($\dot{M}_1/\dot{M}_2 = 320$) is also likely to play a role in the stability. We indeed measure $\alpha \simeq 0.95$ in the mixed region at $r \simeq 50a$, which implies there has been a strong reduction in the KHI growth rate.

Table 1 summarises the presence or absence of spiral structures, for all the simulations we performed. We compared these results with the KHI growth rate, normalised by the rate at which eddies propagate (see Appendix A for details). Although the growth rate gives no indication of the saturation in the non-linear regime, we suspect that the spiral is destabilized most easily when the eddies grow quickly before propagating further away.

Figure 10 shows the normalised growth rate (see Eq. A.12) as a function of β for $\eta = 1, 0.5$, and 0.0625. For $\eta = 1$, the curve is symmetric. The KHI does not develop when there is

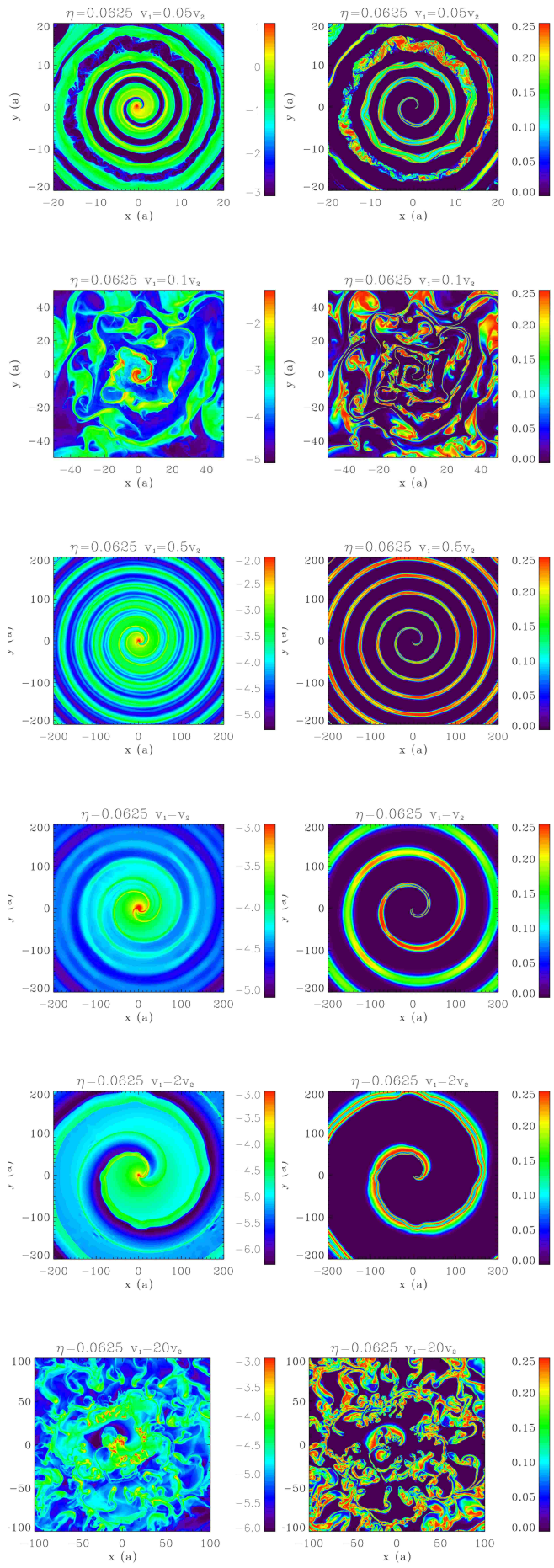

Fig. 8. Large-scale simulation : same as Fig. 7 for $\{\eta = 0.0625, \beta = 0.05, 0.5, 0.1, 1, 2, 20\}$.

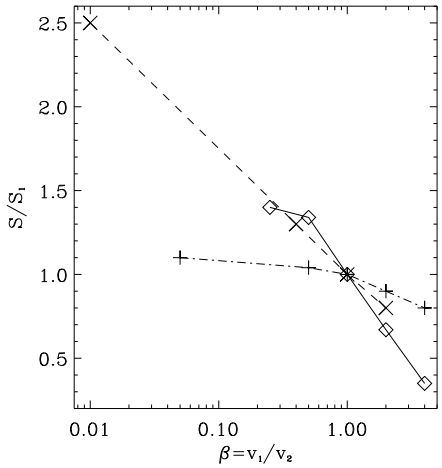

Fig. 9. Step of the spiral S/S_1 as a function of β for η =1 (diamonds), 0.5 (diagonal crosses), and 0.0625 (crosses). The symbols are respectively joined by a solid, dashed, and dash-dotted line for easier identification.

Table 1. Presence (S) or absence (X) of a spiral structure in simulations for various wind-momentum (η) and velocity (β) ratio.

$\eta\backslash\beta$	.01	.05	.1	.5	1	2	4	8	20	200
1		X		S	S	S	S	X	X	X
0.5	S	X	X	S	S	S		X	X	X
0.0625		S	X	S	S	S	S/X	X	X	

no velocity difference, peaks at $\beta_{\max} \simeq 2$, and drops for higher values of β because the density gradient dampens the growth rate. The symmetry with respect to $\beta = 1$ is broken when $\eta < 1$: the normalised growth rate is weaker for $\beta < 1$ and stronger for $\beta > 1$. The lower the value of η, the stronger this asymmetry. Hence, stable structures are expected near $\beta = 1$, for $\beta \gg 1$, and for $\beta \ll 1$. In addition, when $\eta \neq 1$, structures with $\beta < 1$ should be more stable than with $\beta > 1$.

The results of the simulations are in qualitative agreement with these expectations. When $\eta = 1$, there is a spiral for $\beta = 1, 2, 4$ but not for $\beta = 8, 20$ (Tab. 1), which is consistent with the faster growth of the KHI when β increases from 1. However, the transition from stable to unstable spirals occurs further away than expected from Fig 10 ($\beta_{\max} \simeq 2$). In addiation, we were unable to recover a stable final structure for very high β (or, equivalently in the case $\eta = 1$, very low β), up to $\beta = 200$ (Fig. 10). Tests at higher β are computationally too expensive (and may not have much astrophysical relevance). For $\eta = 0.5$, we found that the spiral is maintained for values close to $\beta = 1$ but is quickly destroyed for higher/lower values of β. In this case, a stable spiral is recovered when $\beta \leq 0.01$, which is consistent with the lower growth rate, while the spiral remains destroyed for the symmetric value of $\beta = 20$ (higher growth rate). We observe a similar behaviour for $\eta = 0.0625$. Stabilisation is possible for a higher $\beta = 0.05$, which is consistent with the lower growth rate of the instability for $\beta < 1$ as η decreases. We conclude that the presence of a spiral depends on η and β in a way that is consistent with having stable structures for near-equal velocity winds ($v_1 \simeq v_2$) or when the weaker wind is much faster ($\dot{M}_1 v_1 \geq \dot{M}_2 v_2$ and $v_2 \gg v_1$).

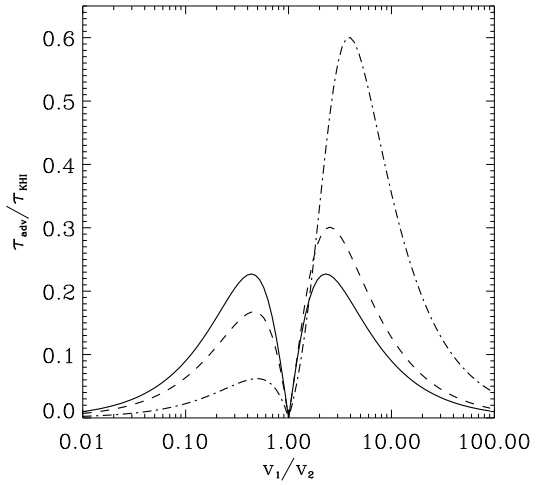

Fig. 10. Theoretical 2D growth rate of the KHI in colliding wind binaries as a function of the velocity ratio $\beta = v_1/v_2$ of the winds. The solid, dashed, and dash-dotted lines correspond to $\eta = 1, 0.5, 0.0625$ respectively.

5. The pinwheel nebula WR 104

WR 104 is a binary composed of an early-type star and a WR star. The system shows an excess of infrared (IR) emission related to dust production. The IR emission has been resolved into a spiral structure with several steps imaged (T2008). The high temperatures and low densities in WR winds are difficult to reconcile with dust formation, which requires a temperature of around 1000 K and a number density of between 10^6 cm^{-3} and 10^{13} cm^{-3} (Cherchneff & Tielens 1995). An additional constraint for dust formation arises from the absence of hydrogen in the WR wind, leading to uncommon chemical processes (Cherchneff et al. 2000). Dust production appears to be closely-related to binarity and the presence of dense colliding-wind structures: in eccentric systems, such as WR 48 or WR 112, dust production is limited to orbital phases close to periastron, while it is continuous in systems with circular orbits. Systems viewed pole-on show an extended spiral structure in IR. WR 104 is the prototype system of these pinwheel nebulae. Pioneering work on the large-scale spiral structure of WR +O binaries led Walder & Folini (2002, 2003) to expect dust formation only at the very centre of the binary. Our aim is to determine whether a hydrodynamical model with adiabatic winds reproduces the observed large-scale structure of WR 104, study mixing, and identify regions where dust production may be possible. Detailed modelling of dust formation and growth in colliding wind binaries is beyond the scope of this study.

5.1. Simulation parameters

Table 2 has the wind parameters of the binary system WR 104. The characteristics of the companion to the WR star are poorly constrained (van der Hucht 2001) and, like T2008, we refer to the companion star as the "OB" star. An orbital period (241.5±0.5 days), eccentricity $e < 0.06$, inclination ($i < 16°$), and angular outflow-velocity of the spiral 0.28 mas day^{-1} in WR 104 were found by fitting an Archimedean spiral to the IR maps (T2008). The orbital separation a is about 2.1-2.8 for a total mass of 20-50 M$_\odot$. We took $e = 0$ and $a = 2.34$. Given the uncertainties in both the mass-loss rate and velocities, η varies between $0.0125 = 1/80$ and $0.0033 = 1/300$. Assuming a constant velocity for the OB wind and $R_{\rm OB} = 10$ R$_\odot$ (Harries et al. 2004), the second shock forms at $2.7R_{\rm OB} < r < 5.1R_{\rm OB}$, depending on η.

Table 2. System parameters for WR 104

	WR	OB
v (km s^{-1})	1200 (a)	2000 (b)
$\dot{M}$ ($M_\odot$ yr^{-1})	$0.8 \times 10^{-5} - 3 \times 10^{-5}$ (c)	6×10^{-8} (d)

(a) Howarth & Schmutz 1992, (b) estimate according to spectral type (Harries et al. 2004), (c) Crowther 1997, (d) using the mass-loss luminosity relation by Howarth & Prinja 1989.

The shock position can be influenced by additional physical processes. The OB wind is accelerated within distances of $\simeq 2-3$ stellar radii and has not necessarily reached its final velocity at the shock, which modifies the effective momentum-flux ratio of the collision. The shock position moves to $2.2R_{\rm OB} < r < 4.7R_{\rm OB}$, if acceleration is taken into account by using the velocity law $v = v_\infty(1 - R_{\rm OB}/r)$. Radiative braking of the WR wind by the OB radiation field (Gayley et al. 1997) can also play a role in WR 104 (T2008). A slower WR wind moves the shock away from the OB star (up to 12 $R_{\rm OB}$ if radiative braking is able to stop the WR wind completely, which is only marginally possible in WR 104, see T2008). The magnitude of both effects, their compensating influence, and the uncertainties in the wind parameters did not justify including these processes. We adopted constant velocity winds and $\eta = 0.0033$ to ease comparison with T2008.

Radiative cooling can significantly change the shock structure. The ratio χ of the cooling timescale t_{cool} to the dynamical timescale t_{esc} provides an estimate of its importance (Stevens et al. 1992)

$$\chi = \frac{t_{cool}}{t_{esc}} = \frac{k_B T_s}{4 n_w \Lambda(T_s)} \frac{c_s}{a}, \tag{8}$$

where $\Lambda \approx 2 \times 10^{-23}$ erg cm^3 s^{-1} is the emission rate for solar abundances, n_w the number density of the unshocked wind, $k_B T_s = (3/16)\mu m_p v_w^2$ the shock temperature, and c_s the associated sound speed. The system is adiabatic if $\chi > 1$ and isothermal if $\chi \ll 1$. According to the value of η, we found that $1.5 < \chi_{\rm OB} < 5$ for the OB star and $0.4 < \chi_{\rm WR} < 1.4$. for the WR star. The system is at the transition between the two regimes. The emission rate is of the same order of magnitude for the chemical composition of a WO star (St-Louis et al. 2005). Although chemical abundances are different in oxygen-rich in oxygen-rich WO stars and carbon rich WC stars, their cooling curves are similar, especially in the bremsstrahlung regime (beyond $10^{6.5}$K), as the winds are mostly composed of helium. Inverse Compton (IC) cooling is important for temperatures $\geq 10^{6.5}$K. The luminosities of both stars and electron temperatures in the winds are roughly equal. The corresponding cooling rate for the OB star is $\simeq 6.3 \times 10^{-23}$ erg cm ^{3} s $^{-1}$ and 2.4×10^{-25} erg cm ^{3} s^{-1} for the WR star, as it scales as $\dot{M}^{-1}$. Inverse Compton cooling of electrons on the OB stellar photons can thus be expected to contribute significantly to cooling and help drive the WR wind into the radiative regime. The acceleration of non-thermal particles also allows for cooling in the system (Pittard 2010). The exact impact can only be determined by proper modelling of particle distributions and the corresponding energy losses, which is beyond the scope of this paper. In Eq. 8, the escape timescale is assumed to be $\simeq a/c_s$ but could be as short $2.7 - 5.1R_{\rm OB}/c_s$ (increasing χ by a factor of 10-20) if one takes the distance from

the OB star (∼ shock curvature radius, Stevens et al. 1992). In the following, we neglect cooling in the energy equation and assume adiabatic winds.

The low value of η is challenging for numerical simulations (see discussion in paper I). The mask of the star needs to be as small as possible so that the shocks can form properly. A minimum length of eight computational cells per direction is needed to obtain the spherical symmetry of the winds. Numerical resolution on scales much smaller than a stellar radius (0.05) is thus required close to the binary. Further away, we need to maintain a high resolution in order to properly study the instabilities, while following a spiral step requires a box size ≥ 200 . We carried out two complementary simulations: a 3D simulation covering scales up to $12a$ and a 2D simulation to model a whole step of the spiral structure.

We used the large-scale 2D simulation to determine the step of the spiral and the impact of mixing. As explained in §2.4, we used the mapping $\sqrt{\eta_{3D}} \rightarrow \eta_{2D}$ to obtain comparable 2D and 3D results. We took $\eta_{2D} = 0.0625$ to help comparisons with the results in §3-4, which is close enough to $\eta_{2DWR104} \simeq 0.057$ derived from a straight application of the mapping. It is important to have the right velocity difference for the Kelvin-Helmholtz instability. We thus adapted $\dot{M}_{WR}$ in order to have $\eta_{2D} = 0.0625$ for the 2D simulation. We used a $200a \approx 500$ simulation box with $n_x = 128$ and 12 levels of refinement. This gives an equivalent resolution equal to $2^{19} \simeq 5 \times 10^5$ cells. We used nested grids to slowly decrease the maximum allowed resolution away from the binary.

We used the smaller-scale 3D simulations to obtain quantitative results on the density and temperature in the winds. The 3D simulation follows one-eight of an orbit of WR 104 in a $12a \approx 30$ simulation box, which is large enough to see the impact of orbital motion. The orbital plane is the mid-plane of the box and the centre of mass of the binary is placed in a corner of the box to maximise the use of the simulated volume. We used AMR with a maximal equivalent resolution of 4096^3. We limited the high resolution to a narrow zone of $3a$ close to the binary where the instabilities develop. This corresponds to the same equivalent resolution as in our 2D model. We modelled only ≃ 20 layers at this high resolution in the z direction and we gradually reduced the resolution when going away from the orbital plane.

5.2. Global structure

Figure 11 shows the density, velocity, mixing, and temperature in the binary orbital plane of the 3D simulation (top row). The bottom row displays the corresponding 2D map on the same scale. The comparison confirms that the mapping in η captures adequately the 3D structure in the 2D simulation. The positions of the shocks and contact discontinuity along the line of centres are similar in both the 2D and 3D simulations and match the analytic solutions (paper I). The opening angle defined by the contact discontinuities, which are well traced in the mixing map, is $15 \pm 1°$. This angle is consistent with the analytical estimates that have been used (Harries et al. 2004, T2008). However, the opening angle defined by the location of the shocks is wider in 2D than in 3D, which may have some influence on the density structure on larger scales (see §5.3). Because of the low η, there is a reconfinement shock behind the OB wind at a distance ≃ $0.75a$ in the 3D simulation ($1.5a$ in the 2D simulation). All of the OB wind is involved in the collision and no fraction escapes freely to infinity.

Material piles up in both arms of the spiral. T2008 suggest that different strengths of the shock can change the conditions for dust formation in each arm. In the 3D simulation, the Mach number of the trailing arm at $r \simeq 12a$ is 13% higher than in the leading arm, in agreement with the results of Lemaster et al. (2007). The small temperature difference is unlikely to affect dust formation. A more significant effect is that compression leads to a hotter temperature in the leading arm than in the trailing arm. Material in the mixing zone of the trailing arm experiences a temperature an order-of-magnitude cooler than in the mixing zone of the leading arm. Dust formation may be favoured in this arm, seeding the spiral structure when the contact discontinuities merge farther out (see below).

The amount of mixing increases with the distance to the binary. Integrating in spheres of increasing radii, the ratio of mixed material to the total amount of material in the spiral within r increases from $\lesssim 0.1\%$ at $r = a$ to ≃ 5% at $r = 10a$. These values are constant during the last stages of the simulation (lasting ≃ $0.1P_{\rm orb}$), indicating the development of the instabilities has reached a steady state. As can be seen on Fig. 11 and expected from theory (Appendix A), mixing occurs mostly in the lower density regions of the colliding wind zone. The velocity map shows that the velocity is mostly radial and that matter is accelerated on a distance of a few times the binary separation. After substraction of the radial component, we have found the velocity of the flow along the spiral in the 3D simulation reaches a maximal value of ≃ 800 km s^{-1}. This corresponds to the low density region in the centre of the spiral. In the outer regions of the spiral, the velocity along the spiral reaches ≃ 500 km s^{-1}.

Figure 12 shows the 2D simulation on the largest scale ($200a$ or about 470). A stable spiral structure forms as expected for $\beta = 0.6$ and $\eta = 0.0625$ (Tab. 1). The collimated OB wind generates a low density spiral bounded on each side by walls of material where the density is ∼100 times higher. The initially different mixing in both arms blurs at a distance of ≃ $50a$. The mixing zones more or less merge and follow the leading arm, overlapping slightly with the density enhancement of the arm. The step of the spiral is $1.05S_{\rm WR}$ where $S_{\rm WR} = v_{\rm WR} \times P_{\rm orb} = 170 = 77a$. T2008 assumed $S_{\rm WR}$ to determine a distance of 2.6 kpc from the observed step size. The 5% correction to this distance required owing to the intrinsically larger spiral step is smaller than the uncertainties in the measured WR velocity and observed angular step size.

The single-armed spiral observed in the IR is more reminiscent of the mixing region than the double spiral in the density map. A double-armed spiral structure, separated by a very underdense region of angular size ≃ 27 mas (at 2.6 kpc), would have been resolved if the IR emission correlated with density (*i.e.* for a constant gas-to-dust ratio). However, we caution that the width of the low density zone may be overestimated in this 2D simulation since it is likely to be related to the opening angle of the shocks, which Fig. 11 shows to be wider in 2D than in 3D. Whether one observes this tube as one or two pieces depends on the optical depth of the material. If it is optically thin, one likely observes two spirals. However, if the material is opaque, one observes only one spiral. The inclusion of dust radiative transfer would be required for a closer comparison of the observations with the hydrodynamical simulation.

5.3. Conditions for dust formation

One criterion for dust formation is a high enough density. Cherchneff & Tielens (1995) indicate different paths towards the formation of amorphous carbon for number densities n rang-

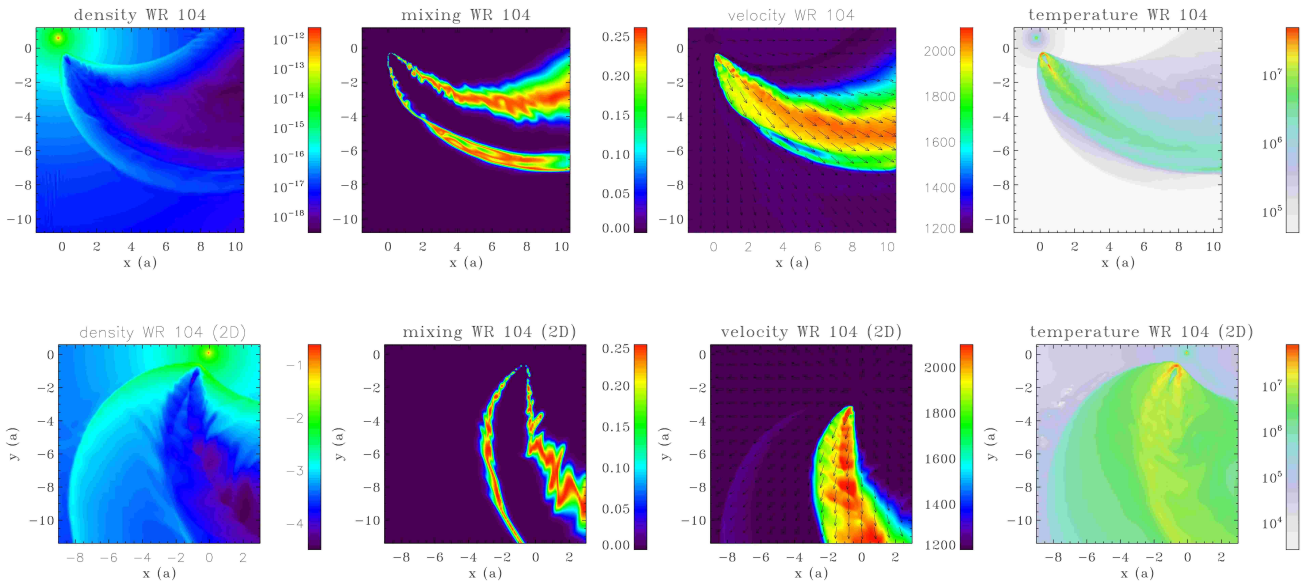

Fig. 11. Density (g cm^{-3}), mixing, velocity (km s^{-1}), and temperature (K) in the orbital plane of the 3D simulation of WR 104 (top row). Corresponding 2D maps on the same scale (bottom row). The length scale is the binary separation a.

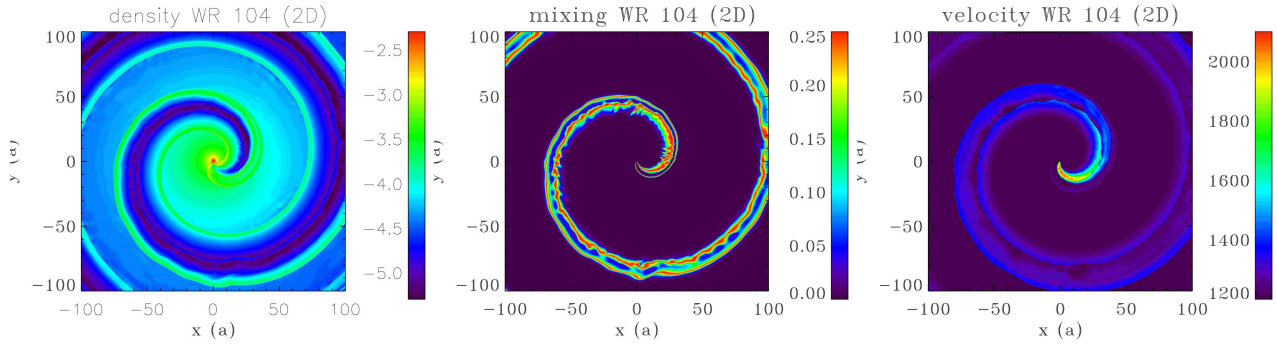

Fig. 12. Density (g cm^{-2}), mixing and velocity (km s^{-1}) in 2D simulations of WR 104. The length scale is the binary separation.

ing from 10^6 to 10^{13} cm^{-3} and present a detailed study for $n = 10^{10}$cm^{-3}. This gives $\rho = 1.4 \times 10^{-14}$ g cm^{-3} assuming a mean molecular weight $\mu = 1.4$, which is typical of a ionized WC wind (Stevens et al. 1992). Such a density is only present in our 3D simulation at the edge of the spiral, up to a distance $\simeq 2a$ from the WR star. In the 2D simulation, along the walls we find that the density drops as $\rho \propto r^{-1}$. Using this as guidance, we expect $\rho \propto r^{-2}$ in 3D on large scales. The minimum value n=10^6 cm^{-3} considered by Cherchneff & Tielens (1995) is reached at $r \simeq 25\ a$ at the inner wall of the spiral. This is equivalent to one-third of a turn along the spiral. The density is too low for dust formation beyond this distance so that any dust present far away has been advected out.

We also expect the temperature to drop beyond 6000K at roughly half a turn of the spiral by extrapolating the temperatures close to the binary. This is the limit for dust condensation (Cherchneff et al. 2000). It is consistent with the IR observations of a quarter-orbit shift between the maximum IR emission and the binary centre. Both the radiative cooling and photoionization heating of the wind would have to be included to permit an accurate determination of the temperature and the impact of shielding from the stellar radiation fields.

6. Discussion

6.1. Asymmetries due to orbital motion

Orbital motion breaks the symmetry around the binary axis and introduces significant differences from the stationary case with adiabatic winds. It causes a velocity difference that triggers the KHI even when both winds are strictly identical. It results in differentiation of the two arms flanking the weaker star. The arm moving into the densest unshocked wind is compressed, dampening the KHI, while the other arm expands and sees Kelvin-Helmholtz eddies of larger size. The density difference between the inner cavity and the bracketing walls can reach two orders of magnitude. According to Parkin et al. (2011), radiation pressure can have a similar effect, either enhancing or reducing the initial difference. Varricatt et al. (2004) modelled the variations in the emission-line profiles of WR 140 by using a rotating cone with dense edges, allowing them to constrain the opening angle of the colliding wind region. They found a wider opening angle

than expected using the analytic formula for the opening angle of the contact discontinuity (Canto et al. 1996) with the standard value of η for this system. Our simulations also show that matter accumulates at the shock rather than the contact discontinuity. The observed opening angle thus corresponds to the opening angle of the shocks, which is wider than the opening angle of the contact discontinuity. This also increases the fraction of the WR wind involved in the collision compared to estimates using the contact discontinuity. Some of the spectral line features that are not explained by models where both arms have equal emission (absorption) could be due to differences between the leading and trailing arm (Stevens & Howarth 1999). The skew angle that we measured in the simulations matches the theoretical value given by Eq. 7. However, as we found that the step of the spiral is mostly determined by the speed of the stronger wind (and not the speed of the slower wind), we wonder whether this could also be the case for the skew angle. This is implicitly assumed by Kenny & Taylor (2007). Our simulations do not allow us to answer this question.

6.2. To spiral or not to spiral

The simulations presented here are the first including at least one step of the spiral. We have shown that a structure is maintained on these scales when the two winds have nearly equal velocities ($\beta \simeq 1$). This is consistent with the observations of pinwheel nebulae in several WR + O star binaries (Tuthill et al. 2006; Monnier et al. 2007; Millour et al. 2009), since their winds do have comparable velocities. The spiral is destabilised when the stronger wind has a velocity between 10-50% of the weaker wind (Tab. 1). For example, the episodic ejection of large amounts of (initially) slow-moving material could have temporarily destabilised any spiral structure in the luminous blue variable (LBV) / WR binary HD 5980 (Nazé et al. 2007; Georgiev et al. 2011). Eta Carina may be a case where any large-scale structure generated near apastron (when the system is closer to being adiabatic) is destroyed because of the destabilising velocity ratio $\beta \simeq 1/6$ — although this would have to be examinated in order to assess the effects of the high orbital eccentricity (Parkin et al. 2011). We expect our results to hold for eccentric orbits if the system stays adiabatic. If the system moves from adiabatic to radiative along its orbit then thin-shell instabilities develop with unknown consequences for the large-scale structure.

The spiral is stabilised again when the velocity ratio $\beta \ll 1$. This situation may occur in gamma-ray binaries composed of a young non-accreting pulsar and an early-type star (Dubus 2006). In this case, the stellar wind interacts with the tenuous, relativistic pulsar wind. Bosch-Ramon & Barkov (2011) argued that the KHI would destroy any large-scale structure. Assuming our results hold in the relativistic regime, we find that a stable spiral can form on large scales if the stellar wind dominates, because $\beta \ll 1$ in this situation. The structure is unstable if the pulsar wind dominates, pointing to the intriguing possibility that the interaction may switch from one regime to another in gamma-ray binaries with Be companions such as PSR B1259-63. The highly eccentric orbit takes the pulsar close to the equatorial disc where the slow-moving stellar outflow dominates momentum balance (Tavani & Arons 1997), leading to a stable colliding-wind region. However, at apastron, the pulsar wind may dominate over the radiatively-driven stellar wind and be unable to form a stable structure. Strong mixing of the two winds leads to rapid Coulomb or bremsstrahlung losses for the high energy particles, which has an impact on the gamma-ray emission (Zdziarski et al. 2010). Extended radio emission was detected around PSR B1259-63 near periastron (Moldón et al. 2011a). Regular changes in the radio morphology with orbital phase have been observed in other gamma-ray binaries that are compatible with non-thermal synchrotron emission from a stable collimated pulsar wind structure on scales $\leq v_w P_{\rm orb}$ (Dhawan et al. 2006; Ribó et al. 2008; Moldón et al. 2011b). The luminosity and frequency of the radiation are probably too low to be able to detect the spiral structure on larger scales.

An example of colliding winds with $\beta \gg 1$ also involves pulsars, this time with a low-mass companion (Roberts 2011). The weak stellar wind is overwhelmed by the relativistic wind of the recycled millisecond pulsar. No stable spiral is expected in this case. Another possible case is eruptive symbiotics such as AG Peg, HM Sge, or V1016 Cyg. These systems are composed of a red giant, with a very slow wind ($\simeq 20$ km s^{-1}) and a hot companion, a white dwarf in nova outburst at the origin of a fast outflow of several 1000 km s^{-1} (Girard & Willson 1987). We expect the spiral structure to be destroyed if the hot companion dominates. The radio maps of HM Sge (which has a possible 90 year orbit) show a more fragmented emission-region than expected from colliding wind models (Kenny & Taylor 2005), possibly because of thin shell instabilities triggered by radiative losses.The radio maps of AG Peg have been interpreted by assuming a stable spiral structure and a reversal in with time (Kenny & Taylor 2007). However, the application to symbiotics is not straightforward. For AG Peg, the comparable orbital and wind speeds may significantly change the dynamics of the interaction (e.g. Folini & Walder (2000)). For HM Sge, there is probably no time to form a spiral because of the long orbital period.

Finally, we note that the KHI also intervenes in the bow shock structure created by the adiabatic interaction of the wind of a fast-moving star with the interstellar medium (e.g. Mira). The controlling parameter is the ratio of wind speed to star velocity. Much like with spirals, fast growth of the KHI may strongly disturb the cometary structure at large distances, as seen in some hydrodynamical simulations (Wareing et al. 2006, 2007).

6.3. Dust formation in pinwheel nebulae

Dust formation in WR 104 and other pinwheel nebulae should be helped by the mixing with hydrogen-rich material from the early-type star that we observe in the 2D and 3D simulations. Williams et al. (2009) argued that stronger dust emission in the trailing arm would explain better the IR high-resolution images of WR 140, and attributed this to density variations. The winds have nearly identical velocities but the WR has a mass-loss rate ten times higher than its O companion. The O wind is therefore in-between two high-density regions. Our simulations do not suggest very different densities. However, larger amplitude mixing is expected in the trailing arm because it propagates in the more tenuous O wind, possibly enhancing dust formation in this arm. The lower temperature in the trailing arm also helps, both effects being enhanced by IC cooling in the OB wind. Hence, a different dust-to-gas ratio between both arms could be an alternative explanation. High density eddies triggered by the KHI in the arms could also be responsible for the observation of IR obscuration events by dust clouds in other WR+O star systems (Veen et al. 1998).

The offset of the peak IR emission in WR 104 is consistent with the distance at which we estimated the temperature to fall below the dust sublimation temperature. This estimate is based on an adiabatic computation and neglects the impact

of photoionisation by the stars and cooling by either radiative losses or particle acceleration. It assumes there is no thermal conduction that creates a pre-heated zone around the shocks and widens the region with the highest temperature (Myasnikov & Zhekov 1998). It also results in a higher density, and thus enhanced cooling in the shocked region (see Fig. 5 Myasnikov & Zhekov (1998)). It may be important at the contact discontinuity if one of the winds is radiative and the other adiabatic. The determination of the limit of the ionised region and the exact temperature within the spiral requires a radiative transfer computation, which is beyond the scope of this paper. The densities in the colliding wind region are on the low side compared to what dust formation models require. Adiabatic shocks only enhance the density by a factor of four so cooling is required. Close to the binary, the winds are likely to display evidence of some cooling due to bremsstrahlung in the WR wind but even more due to IC losses in the OB wind. This results in a thinner and denser shocked layer. Pittard (2009) show the post-shock density is about 100 times higher in their model cwb1, which has strong cooling, than in their adiabatic model cwb3. Radiative cooling also decreases the temperature, bringing the region where dust condensation is possible closer to the binary. Thin-shell instabilities can develop when cooling is strong, enhancing the mixing of the winds. Given the impact of the (weaker) KHI in adiabatic colliding winds, thin shell instabilities can also be expected to significantly influence the large-scale structure. Pittard (2009) showed that the differentiation of the arms remains when thin-shell instabilities are present but the large-scale outcome has not yet been studied. Mixing is probably enhanced by the presence of clumps in the winds (Moffat et al. 1988). Walder & Folini (2003) argued that clumps of sizes comparable to the stellar radii survive in the shocked region and can strongly increase cooling. Smaller clumps are destroyed when passing the shocks and do not affect the temperature distribution in the winds(Pittard 2007).

Strong cooling is not necessarily present in all WR binaries. Williams et al. (2012) present evidence from long-term IR observations of WR 48 for dust production throughout the orbit. The stellar winds in this system have similar characteristics to those of WR 104 but the (tentative) orbital period is much longer at 32 years. Williams et al. (2012) estimate the system to be adiabatic with an average $\chi \simeq 11$. The value will be even higher at apoastron in the eccentric orbit ($e = 0.6$), still dust formation is present. High densities will be much more difficult to reach than in WR 104, requiring dust formation at hitherto lower densities than have been considered possible.

7. Conclusion

We have studied the large-scale impact of orbital motion and the Kelvin-Helmholtz instability on adiabatic shocks in colliding wind binaries. We have used hydrodynamical simulations with AMR to perform the first high-resolution simulations of complete spiral steps. Orbital motion induces differentiation between both arms of the spiral. The arm propagating in the higher density wind gets compressed, while the arm propagating in the lower density wind expands. We explained that this is due to a stronger growth of the KHI in the wider arm and discuss possible observational signatures in spectral lines. We confirmed that the KHI arises even when both winds have identical speeds. We computed the step of the spiral and caution that there can be large differences from the standard estimates. We discovered that the large-scale spiral structure is destroyed when the velocity gradient between the winds is sufficiently steep. Strong density gradients have a stabilizing effect. According to our simulations, we are able to predict whether certain types of binaries display an extended spiral. Systems with stable spirals are those with near-equal velocity winds and those where the weaker wind is much faster. Performing high-resolution simulations of the pinwheel nebula WR 104, we demonstrated that in an adiabatic model, significant mixing of the WR wind occurs with the hydrogen-rich wind of the companion. We found the temperature drops beyond the limit of dust formation at roughly half a step of the spiral. However, we cautioned that this is based on simplified assumptions that neglect the effects of ionisation, and cooling through either radiative processes or the acceleration of non-thermal particles. Nonetheless, the density in those regions falls short of the critical density for dust condensation. Including radiative cooling would lead to higher densities, and also to thin shell instabilities. The impact of these instabilities both on the differentiation of the two arms and the spiral structure is unknown: resolving the thin shock layer in a large-scale simulation remains a very challenging numerical problem.

Acknowledgements. The authors thank the anonymous referee for pointing out the importance of inverse Compton cooling. AL and GD are supported by the European Community via contract ERC-StG-200911. Calculations have been performed at CEA on the DAPHPC cluster and using HPC resources from GENCI- [CINES] (Grant 2011046391)

References

Bosch-Ramon, V. & Barkov, M. V. 2011, A&A, 535, A20
Brighenti, F. & D'Ercole, A. 1995, MNRAS, 277, 53
Canto, J., Raga, A. C., & Wilkin, F. P. 1996, ApJ, 469, 729
Chandrasekhar, S. 1961, Hydrodynamic and hydromagnetic stability, ed. Chandrasekhar, S.
Cherchneff, I., Le Teuff, Y. H., Williams, P. M., & Tielens, A. G. G. M. 2000, A&A, 357, 572
Cherchneff, I. & Tielens, A. G. G. M. 1995, in IAU Symposium, Vol. 163, Wolf-Rayet Stars: Binaries; Colliding Winds; Evolution, ed. K. A. van der Hucht & P. M. Williams, 346
Cherepashchuk, A. M. 1976, Pis ma Astronomicheskii Zhurnal, 2, 356
Crowther, P. A. 1997, MNRAS, 290, L59
De Becker, M. 2007, A&A Rev., 14, 171
Dhawan, V., Mioduszewski, A., & Rupen, M. 2006, in VI Microquasar Workshop: Microquasars and Beyond
Dougherty, S. M., Beasley, A. J., Claussen, M. J., Zauderer, B. A., & Bolingbroke, N. J. 2005, ApJ, 623, 447
Dougherty, S. M. & Williams, P. M. 2000, MNRAS, 319, 1005
Dubus, G. 2006, A&A, 456, 801
Folini, D. & Walder, R. 2000, Ap&SS, 274, 189
Gayley, K. G., Owocki, S. P., & Cranmer, S. R. 1997, ApJ, 475, 786
Georgiev, L., Koenigsberger, G., Hillier, D. J., et al. 2011, AJ, 142, 191
Girard, T. & Willson, L. A. 1987, A&A, 183, 247
Harries, T. J., Monnier, J. D., Symington, N. H., & Kurosawa, R. 2004, MNRAS, 350, 565
Howarth, I. D. & Prinja, R. K. 1989, ApJS, 69, 527
Howarth, I. D. & Schmutz, W. 1992, A&A, 261, 503
Kenny, H. T. & Taylor, A. R. 2005, ApJ, 619, 527
Kenny, H. T. & Taylor, A. R. 2007, ApJ, 662, 1231
Kobulnicky, H. A. & Fryer, C. L. 2007, ApJ, 670, 747
Lamberts, A., Fromang, S., & Dubus, G. 2011, MNRAS, 418, 2618 (paper I)
Landau, L. & Lifshitz, D. 1959, Fluid mechanics, ed. Elsevier (Butterworth-Heinemann)
Lebedev, M. G. & Myasnikov, A. V. 1990, Fluid Dynamics, 25, 629
Lemaster, M. N., Stone, J. M., & Gardiner, T. A. 2007, ApJ, 662, 582
Luo, D., McCray, R., & Mac Low, M. 1990, ApJ, 362, 267
Marchenko, S. V. & Moffat, A. F. J. 2007, in Astronomical Society of the Pacific Conference Series, Vol. 367, Massive Stars in Interactive Binaries, ed. N. St.-Louis & A. F. J. Moffat, 213–+
Mignone, A., Bodo, G., Massaglia, S., et al. 2007, ApJS, 170, 228
Millour, F., Driebe, T., Chesneau, O., et al. 2009, A&A, 506, L49
Moffat, A. F. J., Drissen, L., Lamontagne, R., & Robert, C. 1988, ApJ, 334, 1038
Moldón, J., Johnston, S., Ribó, M., Paredes, J. M., & Deller, A. T. 2011a, ApJ, 732, L10+
Moldón, J., Ribó, M., & Paredes, J. M. 2011b, A&A, 533, L7
Monnier, J. D., Tuthill, P. G., Danchi, W. C., Murphy, N., & Harries, T. J. 2007, ApJ, 655, 1033

Myasnikov, A. V. & Zhekov, S. A. 1998, MNRAS, 300, 686
Nazé, Y., Corcoran, M. F., Koenigsberger, G., & Moffat, A. F. J. 2007, ApJ, 658, L25
Okazaki, A. T., Owocki, S. P., Russell, C. M. P., & Corcoran, M. F. 2008, MNRAS, 388, L39
Parkin, E. R. & Pittard, J. M. 2008, MNRAS, 388, 1047
Parkin, E. R., Pittard, J. M., Corcoran, M. F., & Hamaguchi, K. 2011, ApJ, 726, 105
Pittard, J. M. 2007, ApJ, 660, L141
Pittard, J. M. 2009, MNRAS, 396, 1743
Pittard, J. M. 2010, in Astronomical Society of the Pacific Conference Series, Vol. 422, High Energy Phenomena in Massive Stars, ed. J. Martí, P. L. Luque-Escamilla, & J. A. Combi, 145
Pittard, J. M., Dougherty, S. M., Coker, R. F., O'Connor, E., & Bolingbroke, N. J. 2006, A&A, 446, 1001
Puls, J., Vink, J. S., & Najarro, F. 2008, A&A Rev., 16, 209
Ribó, M., Paredes, J. M., Moldón, J., Martí, J., & Massi, M. 2008, A&A, 481, 17
Ritchie, B. W., Clark, J. S., Negueruela, I., & Crowther, P. A. 2009, A&A, 507, 1585
Roberts, M. S. E. 2011, in American Institute of Physics Conference Series, Vol. 1357, American Institute of Physics Conference Series, ed. M. Burgay, N. D'Amico, P. Esposito, A. Pellizzoni, & A. Possenti , 127–130
Shore, S. N. & Brown, D. N. 1988, ApJ, 334, 1021
St-Louis, N., Moffat, A. F. J., Marchenko, S., & Pittard, J. M. 2005, ApJ, 628, 953
Stevens, I. R., Blondin, J. M., & Pollock, A. M. T. 1992, ApJ, 386, 265
Stevens, I. R. & Howarth, I. D. 1999, MNRAS, 302, 549
Tavani, M. & Arons, J. 1997, ApJ, 477, 439
Teyssier, R. 2002, A&A, 385, 337
Tuthill, P., Monnier, J., Tanner, A., et al. 2006, Science, 313, 935
Tuthill, P. G., Monnier, J. D., & Danchi, W. C. 1999, Nature, 398, 487
Tuthill, P. G., Monnier, J. D., Lawrance, N., et al. 2008, ApJ, 675, 698
Usov, V. V. 1991, MNRAS, 252, 49
Usov, V. V. 1992, ApJ, 389, 635
van der Hucht, K. A. 2001, New Astronomical Review, 45, 135
van Marle, A. J., Keppens, R., & Meliani, Z. 2011, A&A, 527, A3+
Varricatt, W. P., Williams, P. M., & Ashok, N. M. 2004, MNRAS, 351, 1307
Veen, P. M., van Genderen, A. M., van der Hucht, K. A., et al. 1998, A&A, 329, 199
Vishniac, E. T. 1994, ApJ, 428, 186
Walder, R. & Folini, D. 2002, in Astronomical Society of the Pacific Conference Series, Vol. 260, Interacting Winds from Massive Stars, ed. A. F. J. Moffat & N. St-Louis, 595
Walder, R. & Folini, D. 2003, in IAU Symposium, Vol. 212, A Massive Star Odyssey: From Main Sequence to Supernova, ed. K. van der Hucht, A. Herrero, & C. Esteban, 139
Wareing, C. J., Zijlstra, A. A., & O'Brien, T. J. 2007, ApJ, 660, L129
Wareing, C. J., Zijlstra, A. A., Speck, A. K., et al. 2006, MNRAS, 372, L63
Wiggs, M. S. & Gies, D. R. 1993, ApJ, 407, 252
Williams, P. M., Marchenko, S. V., Marston, A. P., et al. 2009, MNRAS, 395, 1749
Williams, P. M., van der Hucht, K. A., & The, P. S. 1987, A&A, 182, 91
Williams, P. M., van der Hucht, K. A., van Wyk, F., et al. 2012, MNRAS, 420, 2526
Zdziarski, A. A., Neronov, A., & Chernyakova, M. 2010, MNRAS, 403, 1873

Appendix A: The Kelvin Helmholtz Instability in stratified flows

A.1. Linear theory (Chandrasekhar 1961)

A flow can be considered as incompressible with respect to the Kelvin-Helmholtz-instability if the Mach number of the velocity discontinuity $\mathcal{M}_{cd} = \Delta v / c_s \lesssim .3$where Δv is the velocity difference at the interface and c_s the sound speed. At the centre of the binary system, the winds are subsonic and the flow is incompressible as the two winds collide head-on. We use the incompressible approximation in the following computations. However, this may not be fully applicable further away from the binary as the winds re-accelerate. That said, the interface remains marginally sonic ($\mathcal{M}_{cd} \leqslant 2.6$ in all our simulations). In this case, the evolution of the KHI is complex to determine as it depends on the binary parameters (η, β) but also on the development of the KHI closer to the binary. We have a system with a mean profile $\mathbf{U} = \pm U \mathbf{e_x}$. Above $y = 0$, the flow has a density ρ^+ and ρ^- for $y < 0$ (see Fig. A.1). We neglect the Coriolis force since the local shear timescale $\tau_S = \Delta x / \Delta U \sim 10^{-6}$ yr is much shorter than the orbital period $\tau_\Omega \sim 10^{-1}$ yr. In this approximation, the linearised equation of motion is:

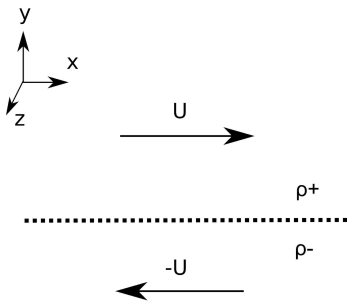

Fig. A.1. Configuration of the stratified flow

$$\rho \frac{\partial \mathbf{v}}{\partial t} + \rho U \frac{\partial \mathbf{v}}{\partial x} + \nabla P = 0, \tag{A.1}$$

$$\nabla \cdot \mathbf{v} = 0. \tag{A.2}$$

In the following, each quantity is Fourier transformed in x and t thanks to homogeneity: $Q = Q \exp[i(\omega t - kx)]$. Rewriting the equation of motions and combining them leads to

$$\partial_y^2 v_y - k^2 v_y = 0, \tag{A.3}$$

which is solved with two decaying solutions

$$v_y^+ = A^+ \exp(-ky) \text{ for } y > 0, \tag{A.4}$$

$$v_y^- = A^- \exp(ky) \text{ for } y < 0, \tag{A.5}$$

A^+ and A^- being two arbitrarily chosen constants that are adjusted by jump conditions at the interface $y = 0$: pressure should be continuous and fluid particles should stick to the interface on both sides. The pressure condition is given by :

$$\rho^+ \frac{\sigma^+}{k} \partial_y v_y^+ = \rho^- \frac{\sigma^-}{k} \partial_y v_y^+, \tag{A.6}$$

where $\sigma^\pm = \omega \pm U$. The second condition is obtained defining a displacement vector $\xi(x)$ that follows the interface. By definition, a fluid particle located at $(x, \xi(x) - \epsilon)$ satisfies

$$v_y = \frac{D\xi}{Dt} = \partial_t \xi + U \partial_x \xi = i\sigma\xi. \tag{A.7}$$

Applying this to both side of interface ($\pm\epsilon$) leads to the jump condition

$$\frac{v_y^+}{\sigma^+} = \frac{v_y^-}{\sigma^-}. \tag{A.8}$$

Combining (A.6) and (A.8) and looking for non trivial solutions gives

$$\omega^2 + 2\alpha\omega k U + (kU)^2 = 0, \tag{A.9}$$

where $\alpha = (\rho^+ - \rho^-)/(\rho^+ + \rho^-)$. An instability arises whenever

$$\Delta = (1 - \alpha^2)(-k^2 U^2) < 0, \tag{A.10}$$

which is always true since $-1 \leq \alpha \leq 1$. The growth rate is $1/\tau_{\rm KHI} = \sqrt{-\Delta} = |kU| \sqrt{1 - \alpha^2}$. Hence, a density contrast $|\alpha|$ close to 1 strongly dampens the growth rate of the KHI.

In colliding wind binaries, the density and the velocity of both winds are related through the momentum-flux ratio η. Using Eq. 1 and mass conservation for both winds then and assuming the interaction occurs far enough from the binary (so that $r_1 \simeq r_2$), the density ratio is roughly

$$\frac{\rho_2}{\rho_1} \simeq \eta\beta^2, \tag{A.11}$$

$$\frac{\tau_{\rm adv}}{\tau_{\rm KHI}} = \frac{|\beta-1|\sqrt{1-\alpha^2}}{-\alpha(\beta-1)+(\beta+1)} = \frac{\eta^{1/2}\beta|\beta-1|}{1+\eta\beta^3}. \tag{A.12}$$

A.2. Nonlinear evolution

A.2.1. two-dimensional Evolution

To investigate the evolution of the KHI in the nonlinear regime, we performed numerical simulations for increasing α. The 2D setup is as follows: box size ($lx = 8, ly = 4$), resolution (1024×256), code PLUTO (Mignone et al. 2007), adiabatic equation of state $P \propto \rho^{5/3}$, background pressure $P = 1$ in the initial state (using units scaled to the box length, density, and velocity shear). Reflective boundary conditions are enforced in y to confine the instability in the simulation box. We always have $\rho^+ > \rho^-$ *i.e.* the densest medium is found where $y > 0$.

In addition to that, we follow the mixing using a passive scalar as explained in §2.3. We performed simulations for $\{\alpha = 0, 0.5, 0.9, 0.99\}$. Kelvin-Helmholtz eddies are clearly present in the density snapshot shown in Fig. A.2 for model $\alpha = 0.5$. To show the diffusion of the passive scalar as a function of time, we plot the evolution of $\overline{s}(y,t) = \int s\,dx$ as a function of y and t in Fig. A.3. These results demonstrate that when $\alpha \neq 0$, the scalar diffusion propagates much less in the denser medium ($y > 0$) and that diffusion looks less efficient when $|\alpha|$ increases, in the sense that the region with intermediate values of the scalar s becomes smaller when α increases.

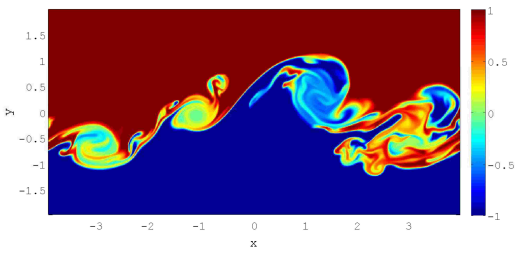

Fig. A.2. Snapshot of the density at t=21 (in dimensionless units) for $\alpha = 0.5$.

A.3. three-dimensional evolution

We performed simulations for $\alpha = 0$ and 0.9 in 3D to compared them to the 2D ones. They are very similar to the 2D configuration, except for the resolution, which was reduced to $500 \times 100 \times 100$ in order to reduce computational costs. We set $l_z = l_x = 4.0$, where $\overline{s}(y,t)$ is shown on Fig. A.4. The direct comparison with the 2D cases indicates that faster diffusion into the more tenuous region still occurs in the 3D simulation. Fig. A.5 shows the mixing at different times in the 2D and 3D simulations, for $\alpha = 0., 0.9$. It confirms that both in the 2D and 3D

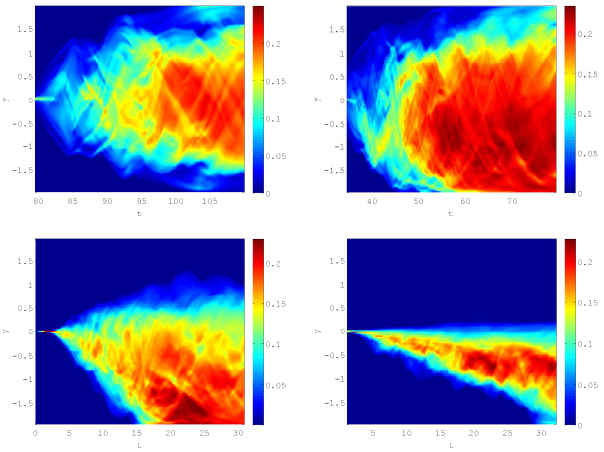

Fig. A.3. Mixing due to the KHI. From left to right, top to bottom: $\alpha = 0, 0.5, 0.9, 0.99$.

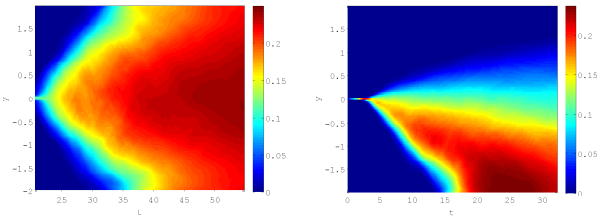

Fig. A.4. Mixing in the 3D simulations with $\alpha = 0$ (left) and $\alpha = 0.9$ (right).

case, the KHI behaves similarly with respect to the velocity gradient.

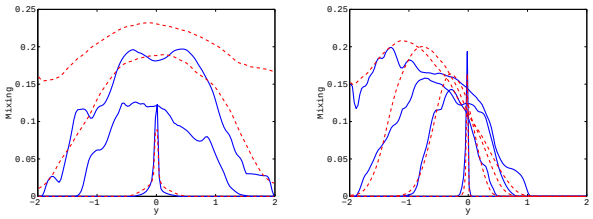

Fig. A.5. Mixing in 2D simulations (blue solid line) and 3D simulations (red dashed line) for $\alpha = 0$ (left panel) and $\alpha = 0.9$ (right panel). The different curves show different timesteps separated by $\Delta t = 5$.

Appendix B: Parameters of the simulations

Table B.1. Parameters of the simulations

$\{\eta,\beta\}$	v_1 (km s^{-1})	v_2 (km s^{-1})	$\dot{M}_1$ ($10^{-7} M_\odot$ yr^{-1})	$\dot{M}_2$ ($10^{-7} M_\odot$ yr^{-1})	spiral?	S/S_1
$\{1, 1\}$	2000	2000	1	1	S	1
$\{1, 2\}$	4000	2000	0.5	1	S	0.67
$\{1, 4\}$	2000	500	0.25	1	S	0.35
$\{1, 8\}$	4000	500	0.25	2	X	
$\{1, 20\}$	40000	2000	0.05	1	X	
$\{1, 200\}$	8000	40	0.05	10	X	
$\{0.5, 0.01\}$	40	4000	100	0.5	S	2.5
$\{0.5, 0.05\}$	200	4000	40	1	X	
$\{0.5, 0.1\}$	400	4000	20	1	X	
$\{0.5, 0.5\}$	1000	2000	4	1	S	1.3
$\{0.5, 1\}$	2000	2000	2	1	S	1
$\{0.5, 2\}$	4000	2000	1	1	S	0.8
$\{0.5, 8\}$	4000	500	1	4	X	
$\{0.5, 20\}$	8000	400	.5	5	X	
$\{0.5, 200\}$	8000	40	.05	5	X	
$\{0.0625, 0.05\}$	100	2000	320	1	S	1.1
$\{0.0625, 0.1\}$	200	2000	160	1	X	
$\{0.0625, 0.5\}$	1000	2000	32	1	S	1.04
$\{0.0625, 1\}$	2000	2000	16	1	S	1
$\{0.0625, 2\}$	4000	2000	8	1	S	0.9
$\{0.0625, 4\}$	4000	1000	4	1	S/X	
$\{0.0625, 8\}$	4000	500	4	2	S	0.8
$\{0.0625, 20\}$	40000	2000	.8	1	S	

Chapter 5

Towards the simulation of γ-ray binairies

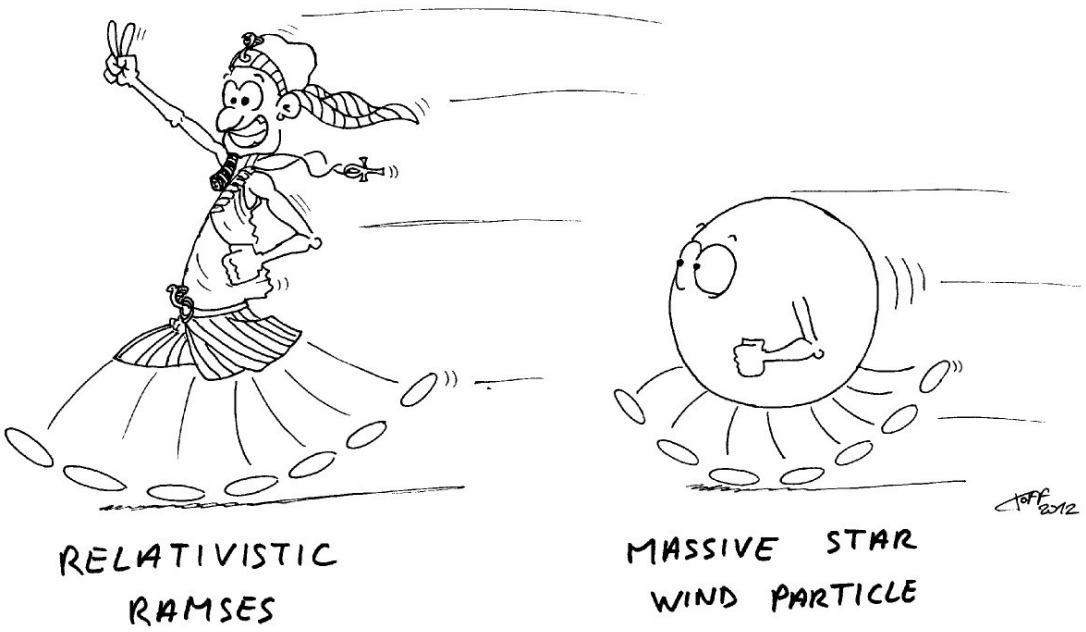

Contents

5.1 Extension of RAMSES to relativistic hydrodynamics 147
5.1.1 Equations of special relativistic hydrodynamics 147
5.1.2 Computation of the primitive variables 149
5.1.3 Relativistic Riemann solvers 151
5.1.4 Reconstruction of the primitive variables for a 2^{nd} order scheme 152
5.1.5 Implementation within the AMR structure 154
5.2 Testing, testing and testing... 155
5.2.1 1D tests : Shock tubes 155
5.2.2 2D tests : inclined shock tubes 156
5.2.3 3D test : relativistic, supersonic jet 158
5.2.4 Applications and future improvements of this new relativistic code 158
5.3 Analytic predictions for the interaction region in γ-ray binaries 161
5.3.1 Position of the contact discontinuity 161
5.3.2 Relativistic jump conditions 162
5.4 Simulations of γ-ray binaries 163
5.4.1 Numerical setup 164
5.4.2 Geometry of the colliding wind region 166
5.4.3 The Kelvin-Helmholtz instability in γ-ray binaries 167
5.5 What do these first results indicate? What could be improved? 169
5.6 Résumé en Français 171

Simultaneously to the study of stellar binaries, I have worked on the development of a relativistic (RHD) version of RAMSES to model the pulsar wind in γ-ray binaries. The first parts of this chapter explain the development of the numerical scheme (§5.1) and the set of tests performed for its validation (§5.2). Then, I present some analytic (§5.3) and numerical results (§5.4) on the collision of pulsar winds and stellar winds. Similarly to Chapter 3 for stellar colliding winds, simulations focus on the geometry of the shocked region and show some differences with the non-relativistic case.

5.1 Extension of RAMSES to relativistic hydrodynamics

Special relativity is necessary to describe the structure of astrophysical flows that have a velocity close to the speed of light. It is used to properly model jets in microquasars or active galactic nuclei but also gamma-ray bursts and pulsar winds.

Wilson [1972] presented the first simulation of relativistic flows, based on a finite difference method, which requires the use of artificial viscosity. The artificial viscosity was treated in a classical manner that led to failures for multidimensional flows even for mildly relativistic cases. Higher Lorentz factors were reached for the first time using Godunov-type methods [Einfeldt, 1988, Miralles, 1991, Marquina et al., 1992]. Since then, many multidimensional codes have been developed with diverse numerical improvements, some including magnetohydrodynamics : Genesis [Aloy and Marti, 1999], ATHENA for relativistic magnetohydrodynamics (RMHD) with static adaptive mesh refinement [Beckwith and Stone, 2011] and r-ENZO [Wang et al., 2008b] with patch-based AMR. MPI-AMRVAC [Keppens et al., 2012] and PLUTO [Mignone et al., 2007, 2012] both allow tree-based AMR and present a similar wealth of implemented numerical schemes for RHD and RMHD. Falle and Komissarov [1996] developed a method based on the evolution of the primitive variables, adapted for a general equation of state. Most of these codes are publicly available. SPH methods have been implemented (see Monaghan [1985] for the first code) but present similar problems to the finite difference method. Another approach is used in TESS [Duffell and MacFadyen, 2011] where the equations are integrated on a moving Voronoi mesh. A complete review of these methods can be found in Martí and Müller [2003].

We started to develop the RHD solver using only uniform computational grids in order to focus on the numerical scheme. Once the code successfully passed all the test on a uniform grid, we transferred everything into the AMR structure.

5.1.1 Equations of special relativistic hydrodynamics

Through all this work the speed of light is $c \equiv 1$. In the frame of the laboratory the 3D-RHD equations for an ideal fluid can be written as a system of conservation equations [Landau and Lifshitz, 1975].

$$\frac{\partial D}{\partial t} + \frac{\partial (D v_j)}{\partial x_j} = 0 \tag{5.1}$$

$$\frac{\partial M_i}{\partial t} + \frac{\partial (M_i v_j + P \delta_{ij})}{\partial x_j} = 0 \tag{5.2}$$

$$\frac{\partial E}{\partial t} + \frac{\partial (E + p) v_j}{\partial x_j} = 0, \tag{5.3}$$

where the vector of conservative variables is given by

$$\mathbf{U} = \begin{pmatrix} D \\ M_i \\ E \end{pmatrix} = \begin{pmatrix} \Gamma \rho \\ \Gamma^2 \rho h v_i \\ \Gamma^2 \rho h - P \end{pmatrix} \tag{5.4}$$

D is the mass density, **M** the momentum density and E the energy density in the frame of the laboratory. The subscripts i, j stand for the dimensions, $\delta_{i,j}$ is the Kronecker symbol. h is the specific enthalpy given by

$$h = h(P, \rho) = 1 + \frac{\gamma}{\gamma - 1}\frac{P}{\rho} = \frac{e + P}{\rho}, \tag{5.5}$$

and ρ is the proper mass density, v_i is the fluid three-velocity, P is the gas pressure. The Lorentz factor is given by

$$\Gamma = \frac{1}{\sqrt{1 - v^2}}. \tag{5.6}$$

Eqs. 5.1-5.3 can be expressed in compact form (such as Eq. 2.5) defining the flux **F** by

$$\mathbf{F} = \begin{pmatrix} \rho\Gamma v_i \\ \rho h \Gamma^2 v_i v_j + P\delta^{ij} \\ \rho h \Gamma^2 v_i \end{pmatrix} \tag{5.7}$$

Equations 5.1-5.3 need a closure equation that is the equation of state. The most commonly used equation of state is the classical equation of state, where the rest mass energy is removed from the total internal energy e.

$$P = (\gamma - 1)(e - \rho), \tag{5.8}$$

where γ is the adiabatic index which is constant and should not be confused with the Lorentz factor Γ. In non-relativistic case $\gamma = 5/3$, in the ultrarelativistic limit $\gamma = 4/3$. e is the sum of the internal energy and the rest-mass energy, in the local frame. The sound speed is then given by

$$c_s^2 = -\frac{\rho}{nh}\frac{\partial h}{\partial \rho} \equiv \left(\frac{\partial P}{\partial e}\right)_s = c_{s,cl}^2 \left(1 + \frac{c_{s,cl}^2}{\gamma - 1}\right)^{-1} \equiv \gamma \frac{P}{\rho h}, \tag{5.9}$$

where $c_{s,cl} = \frac{\partial P}{\partial \rho}$ is the classical definition of the sound speed and n is the polytropic index such as $n = 1 + 1/\gamma$ [Del Zanna and Bucciantini, 2002]. This equation of state is borrowed from classical hydrodynamics and may lead to a superluminal sound speed when the thermal velocity of the particles approaches the speed of light. In simulations of γ-ray binaries, temperature is low enough so that it gives satisfactory results and we restricted ourselves to this equation of state. However, one should keep in mind that more realistic equations of state are possible (see *e.g.*Mignone and McKinney [2007]).

In my simulations, the adiabatic index is set in the beginning of the simulation and is identical in all cells. When simulating a non-relativistic stellar wind colliding with a relativistic pulsar wind, the adiabatic index is adapted either for the stellar wind or the pulsar wind but not for both. A possible approach of improvement is an adaptive equation of state, with a variable adiabatic index, according to the value of $P/\rho c^2$.

A passive scalar s can be added using $S = s\rho\Gamma$ as the conserved variable and $F = \rho s v \Gamma$ to compute its flux.

When developing a numerical method in RHD, most of the difficulties arise from the presence of the Lorentz factor in the conservative variables and an additional pressure term in the expression of momentum. Passing from conserved variables $(D, \mathbf{M}, E)^T$ to primitive variables $(\rho, \mathbf{v}, P)^T$ is trivial for the Euler equations but challenging in RHD (§5.1.2). Similarly, the reconstruction of the variables in the predictor step is more complex (§5.1.4). Following the rule of summation of velocities, the determination of the wavespeeds changes from the Galilean expression (§5.1.3.1). The Riemann solvers also change from the classical expressions (§5.1.3). A few adaptations are necessary to make the new algorithm work with the AMR data structure (§5.1.5).

5.1.2 Computation of the primitive variables

To compute the primitive variables, one has to invert the non-linear system given by equation 5.4. This happens at the beginning of the each timestep to compute the wave speed and the fluxes, but also when creating outputs, determining the timestep or changing the AMR map. This step is at the heart of the program and should be precise, robust, fast, and adaptable to different equations of state. Several methods are described in the literature [Noble et al., 2006], but only a few of them give a satisfying result for all situations with Γ up to 10^6.

Historically, the first methods assumed an ideal equation of state, where one can rewrite the set of equations 5.4 to form one quartic equation on v [Ryu et al., 2006]. Using some intermediate variables, this equation can be solved analytically. There are 4 roots, 2 of them are real but only one is physically satisfactory [Schneider et al., 1993]. When one implements this solution there is a *"catastrophic annihilation in the non-relativistic and ultrarelativistic case"* [Mignone and McKinney, 2007]. One of the intermediate steps is a difference between two very large numbers which result is hidden in the truncation error and leads to unreal solutions. Another option is to numerically solve the equation with a non-linear root finder such as the Newton-Raphson (NR) method. At shocks the velocity may vary a lot from one time step to another and a Newton-Raphson scheme might not find the proper root as in some cases there are two real roots $\in [0, 1]$ [Bernstein and Hughes, 2009]. Although this can be corrected, the method is maladapted to the AMR grid because it requires the storage of the velocity from one timestep to another while the data structure may vary. We decided not to follow this method.

Another option is to rewrite the energy conservation to numerically solve an equation on $W \equiv \Gamma^2 \rho h$

$$f(W) = W - P - E = 0, \tag{5.10}$$

However, Mignone and McKinney [2007] have shown that this may fail

- In the non-relativistic limit which may give inaccurate results for P.
- In the non-relativistic limit $\Gamma - 1 \to 0$ and may lead to catastrophic cancellations.
- In the ultrarelativistic limit the computation of Γ when $v \to 1$ may also lead to catastrophic cancellations.

To avoid this, one can use

$$\begin{cases} E' = E - D \\ W' = W - D \end{cases} \tag{5.11}$$

instead. We thus have to solve

$$f'(W') = W' - P - E' = 0. \tag{5.12}$$

Introducing the classical expression of the enthalpy

$$\chi = e + P - 1, \tag{5.13}$$

one has

$$P = \frac{\gamma - 1}{\gamma} \chi, \tag{5.14}$$

and can express W' as

$$W' = D(h\Gamma - 1) = \frac{Du^2}{1 + \Gamma} + \chi\Gamma^2 \quad \text{with} \quad u^2 = \frac{M^2}{(W + D)^2 - M^2}. \tag{5.15}$$

This equation can be inverted to give χ

$$\frac{W'}{\Gamma^2} - \frac{Du^2}{(1+\Gamma)\Gamma^2} \tag{5.16}$$

Equation 5.12 is solved with a root-finding Newton-Raphson scheme where successive approximations of W' are computed using

$$W'^{k+1} = W'^{k} - \frac{f(W')}{f'(W')}\Big|_{W'=W'^{k}}. \tag{5.17}$$

The NR scheme is initiated using $W'^{(0)} = \bar{W}_+ - D$ where $\bar{W}_+$ is the positive root of

$$f_0(W) = M^2 - W^2 + 2W(2W - 2E), \tag{5.18}$$

which guarantees the positivity of the pressure. Instead of keeping in memory W' at a given timestep in order to initiate the NR scheme at the next step, we have an independent way of initiating the algorithm. This greatly facilitates the use of the NR method with the AMR structure. We have

$$\frac{df'(W')}{dW'} = 1 - \frac{dP}{dW'} = 1 - \left(\frac{\partial P}{\partial \chi}\frac{\partial \chi}{\partial W'} + \frac{\partial P}{\partial \rho}\frac{\partial \rho}{\partial W'}\right). \tag{5.19}$$

In the case of an ideal equation of state, P is given by Eq.5.14

$$\frac{\partial P}{\partial \rho} = 0 \quad \text{and} \quad \frac{\partial P}{\partial \chi} = \frac{\gamma - 1}{\gamma}; \tag{5.20}$$

as $W' \equiv Dh\Gamma - D = D(\Gamma - 1) + \chi\Gamma^2$ one has

$$\frac{d\chi}{dW'} = \frac{1}{\Gamma^2} - \Gamma^2\chi\frac{d|v|^2}{dW'}, \tag{5.21}$$

where

$$\frac{d|v|^2}{dW'} = \frac{d|v|^2}{dW} = \frac{-2M^2}{W^3}. \tag{5.22}$$

Once the NR provides the value of W', one derives u^2 and finds the Lorentz factor

$$\Gamma = (1 + u^2)^{1/2}. \tag{5.23}$$

The density and velocity are then given by

$$\rho = \frac{D}{\Gamma} \tag{5.24}$$

$$v_x = \frac{M_x}{W} \tag{5.25}$$

$$v_y = \frac{M_y}{W} \tag{5.26}$$

$$v_z = \frac{M_z}{W} \tag{5.27}$$

Finally one inverts Eq. 5.15 to derive χ and find the pressure

$$P = \frac{\gamma - 1}{\gamma}\chi. \tag{5.28}$$

Provided the vector of conservative variables is physical, this method converges to a physical primitive state. A physical state means positivity of density and pressure and subluminal velocity. The positivity of the density can be verified by D>0 while the positivity of the pressure is guaranteed when $E^2 > M^2$ and a subluminal velocity is guaranteed by $E^2 > M^2 + D^2$ [Mignone and Bodo, 2005]. Beckwith and Stone [2011] note a few failures when pressure is very low and suggest to use the entropy instead of the energy as conserved variable in those cases.

5.1.3 Relativistic Riemann solvers

When using the HLL Riemann solver, the expression of the Godunov fluxes is identical to the non relativistic expression given by Eq. 2.19. However, the computation of the maximal wavespeeds S_L and S_R is different.

5.1.3.1 Finding the wave speeds

S_L and S_R are the fastest waves propagating in each direction. In Galilean mechanics the wavespeed is the sum of the sound speed and the advection speed of the flow. The relativistic composition of velocities couples the velocity of the flow parallel ($v_\parallel$) and perpendicular ($v_\perp$) to the direction of spatial derivation. All components of the velocity need to be taken into [Del Zanna and Bucciantini, 2002] account, giving

$$S_L = \max(0, -S_{-,R}, -S_{-,L}) \tag{5.29}$$
$$S_R = \max(0, S_{+,R}, S_{+,L}). \tag{5.30}$$

with

$$S_+(v) = \frac{v_\parallel(1-c_s^2) + \sqrt{(1-v^2)(1-v_\parallel^2 - v_\perp c_s^2)}}{1-v^2c_s^2} \tag{5.31}$$
$$S_-(v) = \frac{v_\parallel(1-c_s^2) - \sqrt{(1-v^2)(1-v_\parallel^2 - v_\perp c_s^2)}}{1-v^2c_s^2}. \tag{5.32}$$

5.1.3.2 Relativistic HLLC Riemann solver

The development of a HLLC solver for RHD was done by Mignone and Bodo [2005], whose method we closely follow.

Similarly to the classical HLLC solver (see §2.2.1.1), if one knows the wavespeeds S_L and S_R, the intermediate state can be expressed with respect to $\mathbf{U}_{L,R}$ using the Rankine-Hugoniot jump conditions

$$S_{L,R}(\mathbf{U}^*_{L,R} - \mathbf{U}_{L,R}) = \mathbf{F}^*_{L,R} - \mathbf{F}_{L,R}, \tag{5.33}$$

which gives 10 equations for 21 unknows: $\mathbf{U}^*_L, \mathbf{U}^*_R, \mathbf{F}^*_L, \mathbf{F}^*_R$ (5 components each) and S^*. As pressure and the normal velocity are constant across a contact discontinuity, there are 3 additional equations ($v^*_{x,R} = v^*_{x,L} = S^*$, $P^*_L = P^*_R$). In order to reduce the number of unknowns, one has to assume the fluxes $\mathbf{F}^*_{L,R}$ follow the structure given by Eq. 5.7. After some algebra Eq. 5.33 then yields

$$\begin{cases} D^*_{L,R}(S_{R,L} - S^*_{R,L}) = D_{R,L}(S_{R,L} - v_{x,R,L}) \\ M^*_{x,L,R}(S_{R,L} - S^*_{R,L}) = M_{x,R,L}(S_{R,L} - v_{x,R,L}) + P^*_{R,L} - P_{R,L} \\ M^*_{y,L,R}(S_{R,L} - S^*_{R,L}) = M_{y,R,L}(S_{R,L} - v_{x,R,L}) \\ M^*_{z,L,R}(S_{R,L} - S^*_{R,L}) = M_{z,R,L}(S_{R,L} - v_{x,R,L}) \\ E^*_{L,R}(S_{R,L} - S^*_{R,L}) = E_{R,L}(S_{R,L} - v_{x,R,L}) + P^*_{R,L}S^* - P_{R,L}v_x \end{cases} \tag{5.34}$$

Recombining the last and second line one gets

$$(S_{R,L}P_{R,L} - M_{x,R,L} - S^*P^*_{R,L})v^*_x = M_{x,R,L}(S_{R,L} - v_{x,R,L})P^*_{R,L} - P_{R,L}, \tag{5.35}$$

using $P^*_L \equiv P^*_R$ one gets a quadratic equation for S^*

$$F^{HLL}_E S^{*2} - (E^{HLL} + F^{HLL}_{M_x})S^* - {M_x}^{HLL} = 0, \tag{5.36}$$

where one uses the HLL fluxes and HLL state vector determined by Eq. 2.19 for the energy and momentum components. Only the negative root of the quadratic equation gives a subluminal speed for the contact wave and is physically satisfactory. One then computes the pressure in the intermediate region $P_R^* = P_L^* = P^*$ using Eq. 5.35. The other quantities in the intermediate region are given by Eq. 5.34. The flux across the contact discontinuity $\mathbf{F}^*$ is finally computed using Eq. 5.33. According to the values of the three waves, one then finds the intercell flux $\mathbf{F}$ (see §2.2.1.1)

$$\mathbf{F} = \begin{cases} \mathbf{F}_L & \text{if} \quad S_L \geqslant \chi \\ \mathbf{F}_L^* & \text{if} \quad S_L \leqslant \chi \leqslant S^* \\ \mathbf{F}_R^* & \text{if} \quad S^* \leqslant \chi \leqslant S_R \\ \mathbf{F}_R & \text{if} \quad S_R \leqslant \chi \end{cases}$$

with $\chi = (x - 0.5/t)$

5.1.4 Reconstruction of the primitive variables for a 2^{nd} order scheme

A second order scheme is based on the linear variation of the variables in the cells (see §2.2.1.2 for the HD case). To determine the Riemann fluxes at the interfaces between the cells, one needs to reconstruct the variables at the boundaries between cells. Similarly to the HD scheme, this is performed using a TVD slope limiter, which is not affected by special relativity. One also has to predict the value of the variables half a timestep ahead of the current timestep. Using a first order Euler method the temporal variation of the variables over half a timestep is given by

$$\frac{\partial \mathbf{q}_i}{\partial t}\frac{\Delta t}{2}. \tag{5.37}$$

It is computed using

$$\frac{\partial \mathbf{U}}{\partial t} + \frac{\partial \mathbf{F}}{\partial x} = 0 \tag{5.38}$$

$$\Rightarrow \quad \frac{\partial \mathbf{U}}{\partial \mathbf{q}}\frac{\partial \mathbf{q}}{\partial t} + \frac{\partial \mathbf{F}}{\partial \mathbf{q}}\frac{\partial \mathbf{q}}{\partial x} = 0 \tag{5.39}$$

$$\Rightarrow \quad \mathbf{A}^0\frac{\partial \mathbf{q}}{\partial t} + \mathbf{A}^1\frac{\partial \mathbf{q}}{\partial x} = 0, \tag{5.40}$$

that gives

$$d\mathbf{q} = -\mathbf{A}\frac{\partial \mathbf{q}}{\partial x}dt, \tag{5.41}$$

where $\mathbf{A} = (\mathbf{A}^0)^{-1}\mathbf{A}^1$ is the Jacobian matrix of the system. In classical hydrodynamics, flows are not affected by normal velocity fields. In RHD all spatial directions are coupled through the Lorentz transformation [Pons et al., 2000] : $\mathbf{A}$, $\mathbf{A^0}$ and $\mathbf{A^1}$ are 5×5 matrices even for 1D flows. Following Font et al. [1994] for a 1D flow with transverse velocity we have

$$\mathbf{A^1(q)} = \begin{pmatrix} \Gamma v_x & \rho\Gamma(1+\Gamma^2 v_x^2) & \rho\Gamma^3 v_x v_y & \rho\Gamma^3 v_x v_z & 0 \\ \Gamma^2 v_x^2 & 2\rho h\Gamma^2 v_x(1+\Gamma^2 v_x^2) & 2\rho h\Gamma^4 v_x^2 v_y & 2\rho h\Gamma^4 v_x^2 v_z & \Gamma^2 v_x^2\frac{\gamma}{\gamma-1}+1 \\ \Gamma^2 v_x v_y & \rho\Gamma^2 v_y(1+2\Gamma^2 v_x^2) & \rho h\Gamma^2 v_x(1+2\Gamma^2 v_y^2) & 2\rho h\Gamma^4 v_x v_y v_z & \Gamma^2 v_x v_y\frac{\gamma}{\gamma-1} \\ \Gamma^2 v_x v_z & \rho h\Gamma^2 v_z(1+2\Gamma^2 v_x^2) & 2\rho h\Gamma^4 v_x v_y v_z & \rho h\Gamma^2 v_x(1+2\Gamma^2 v_z^2) & \Gamma^2 v_x v_z\frac{\gamma}{\gamma-1} \\ \Gamma^2 v_x & \rho h\Gamma^2(1+2\Gamma^2 v_x^2) & 2\rho h\Gamma^4 v_x v_y & 2\rho h\Gamma^4 v_x v_z & \Gamma^2 v_x\frac{\gamma}{\gamma+1} \end{pmatrix} \tag{5.42}$$

and

$$\mathbf{A^0(q)} = \begin{pmatrix} \Gamma & \rho\Gamma^3 v_x & \rho\Gamma^3 v_y & \rho\Gamma^3 v_z & 0 \\ \Gamma^2 v_x & \rho h\Gamma^2(1+2\Gamma^2 v_x^2) & 2\rho h\Gamma^4 v_x v_y & 2\rho h\Gamma^4 v_x v_z & \Gamma^2 v_x \frac{\gamma}{\gamma-1} \\ \Gamma^2 v_y & 2\rho h\Gamma^4 v_x v_y & \rho h\Gamma^2(1+2\Gamma^2 v_y^2) & 2\rho h\Gamma^4 v_y v_z & \Gamma^2 v_y \frac{\gamma}{\gamma-1} \\ \Gamma^2 v_z & 2\rho h\Gamma^4\ v_x v_z & 2\rho h\Gamma^4 v_y v_z & \rho h\Gamma^2(1+2\Gamma^2 v_z^2) & \Gamma^2 v_z \frac{\gamma}{\gamma-1} \\ \Gamma^2 & 2\rho h\Gamma^4 v_x & 2\rho h\Gamma^4 v_y & 2\rho h\Gamma^4 v_z & \frac{\gamma}{\gamma-1}\Gamma^2 - 1 \end{pmatrix} \quad (5.43)$$

The complete Jacobian matrix $\mathbf{A}$ has a complex expression and is given in Appendix B. The appendix also provides the corresponding matrices for 2D and 3D flows.

Using this method the three directions of the velocity are reconstructed (in time and space) independently. Although each component is subluminal, nothing guarantees that the norm of the total velocity is subluminal. To avoid this, we tried performing a reconstruction of $\Gamma v_x, \Gamma v_y$ and Γv_z instead of the velocity. In this case, in the Jacobian matrix the coefficients c_{23}, c_{24}, c_{53} and c_{54} are non-zero (see Appendix B). c_{23} and c_{24} respectively correspond to sources of v_x due to gradients in v_y and v_z, c_{53} and c_{53} are sources of pressure due to the same velocity gradients. These source terms are due to the coupling of all directions of the velocity through the Lorentz factor. Strong gradients in the parallel velocity generate some transverse velocity and pressure as can be seen on Fig. 5.1. This occurs at contact discontinuities where pressure and parallel velocity should remain constant. In case of highly relativistic flows this method thus fails.

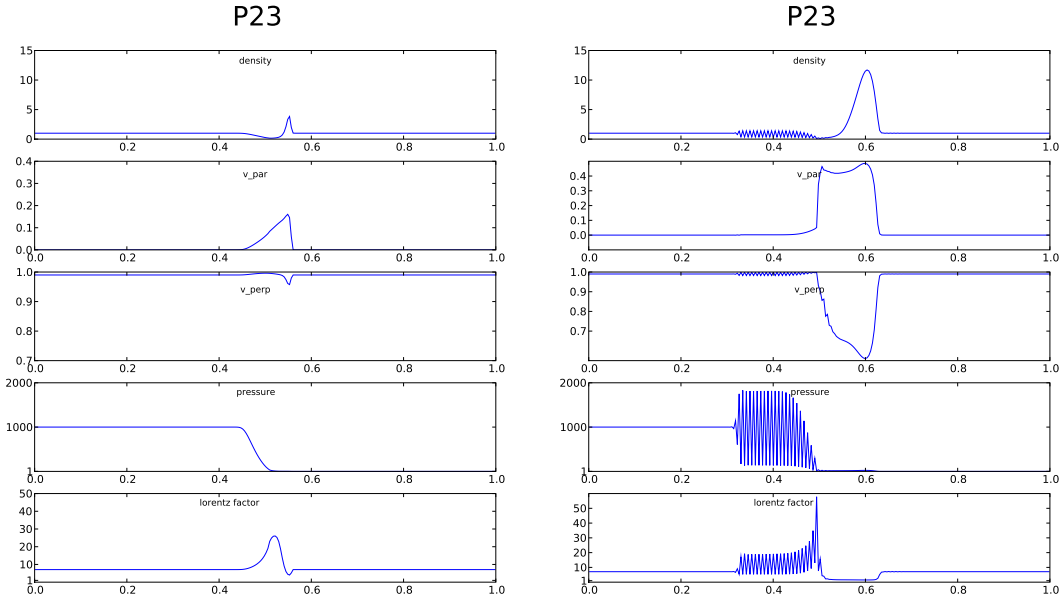

Figure 5.1: Shock tube test problem taken from Ryu et al. [2006]. The left panel shows a simulation where the reconstructed variables are the primitive variables. The right panel shows a simulation where we reconstruct Γv instead of the velocity. This test shows the beginning of the simulation as it crashes later.

We also tried to reconstruct the Lorentz factor separately, in space and time, and use it to derive the norm of the velocity [Wang et al., 2008b]. Fig. 5.2 shows this method, compared with a simulation where the code skips back to first order reconstruction if the reconstructed velocity is superluminal. Reconstructing the Lorentz factor leads to unrealistically high values of it so we decided to give up this method. In the final version of the code, when non-physical states are

obtained we skip back to a first order spatial reconstruction, in all directions, for all variables in the cell. This method works with the *minmod* slope limiter but may fail with other limiters.

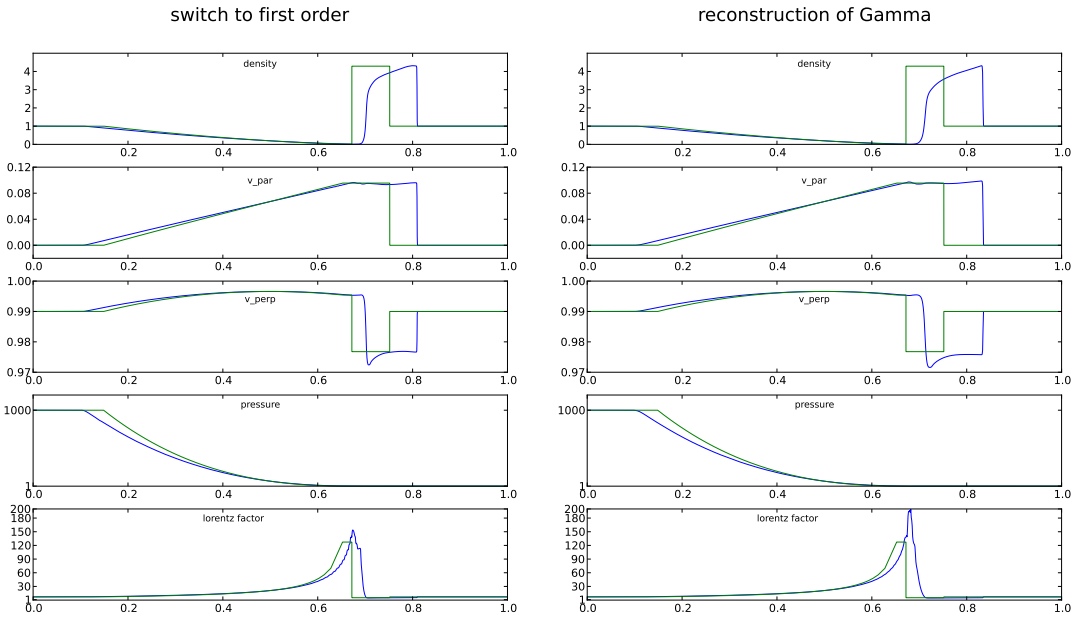

Figure 5.2: Shock tube test problem taken from Ryu et al. [2006]. The left panel shows a simulation where there is a switch to first order when the reconstruction leads to $v > c$. The right panel shows a simulation where we reconstruct the Lorentz factor instead. It shows a spurious increase of the Lorentz factor at the shock. The results from the simulations are shown in blue, the analytic solution [Giacomazzo and Rezzolla, 2006] in green. These tests were performed with 2000 grid cells, which is not enough to reach a satisfactory agreement with the analytic solution. They are very stringent because of the important transverse velocity ($\Gamma > 100$), and only very high resolutions give satisfactory results (see §5.2.1).

We have designed a numerical scheme that solves the equations of relativistic hydrodynamics in 3D dimensions on a uniform grid using the method described above. The next step links this to the Adaptive Mesh Refinement structure.

5.1.5 Implementation within the AMR structure

When using AMR, the code has to be able to derive the variables at a given level according to their value one level above or below. Variables need to be interpolated from level l to level $l+1$ at boundaries between different levels and when creating new refined cells. Conversely, as the hydrodynamical computation is done only for the highest level of refinement, variables are averaged down from level l to $l-1$. Both steps are usually done with the conserved variables D, **M**, E. The interpolation can be done at first order or at second order, using a TVD scheme for the linear reconstruction. Similarly to the reconstruction of the primitive variables to determine the fluxes (§5.1.4), this can lead to non-physical states with a negative density or pressure or a superluminal velocity. We chose to avoid this by switching back to a first order reconstruction when a non-physical reconstructed state occurs.

The averaging step is more complex. Although cells at level l satisfy $E^2 > M^2 + D^2$ individually, nothing guarantees that $E_{oct}^2 > M_{oct}^2 + D_{oct}^2$ where the subscript *oct* means variables are summed over an oct. An oct defines the cells that depend on the same father cell (see §2.2.2). The resulting state can be non-physical. For example, the test shown on Fig. 5.2 fails when using the energy when averaging down. This problem can be bypassed by performing the reconstruction on the specific internal energy ϵ (*i.e.* the temperature) rather than on the total energy using

$$\epsilon = \frac{P}{\rho}\frac{1}{\gamma - 1}, \tag{5.44}$$

where P and ρ are computed with the Newton-Raphson scheme (§5.1.2). After the restriction one switches back to the total energy using

$$E = \Gamma^2 \rho h - P = Dh\Gamma - (\gamma - 1)\frac{D}{\Gamma}\epsilon, \tag{5.45}$$

where

$$h = 1 + \gamma\epsilon \qquad \text{and} \qquad \Gamma = \sqrt{\frac{M^2}{D^2 h^2} + 1}. \tag{5.46}$$

This method is currently implemented in RAMSES and, combined with the *minmod* limiter. It succesfully passes all the commonly used numerical tests. A few of them are detailed in the next section.

5.2 Testing, testing and testing...

An important part (the most important?) of code development consists in designing tests and checking the code does not crash and gives proper results. Failures indicate programming mistakes or weaknesses in the numerical scheme. One starts with easy tests and goes to more and more stringent ones. In our case, stringent tests present either high Lorentz factors, or important pressure gaps, or both. This section presents a few numerical tests, going from easy to decisive. It proves the code works well, and gives the reader an idea of what code development really looks like.

5.2.1 1D tests : Shock tubes

The first tests to do are 1D shock tubes (or Sod tests), which are a large scale version of the Riemann problem. One initially starts with two different media separated by an interface at $x = 0.5$. When the simulation starts the interface is removed and the flow evolves freely and follows a selfsimilar structure. These tests are very common when testing numerical methods because comparisons with analytic solutions are possible (see Martí and Müller [1994] for pioneering work and Rezolla et al. [2003] for a more evolved version including transverse velocities). According to the initial conditions the evolution is numerically more or less difficult to model. I performed a set of tests proposed by Ryu et al. [2006] including transverse velocities.

Unless stated otherwise, I performed the simulations with $C_{CFL} = 0.8$, the *minmod* slope limiter in the MUSCL scheme and for the AMR prolongations, and the HLLC Riemann solver. Refinement is based on density and velocity gradients.

5.2.1.1 Test 1 mildly relativistic case : $\Gamma_{max} = 1.4$

In the first test $\rho_L = 10$, $\rho_R = 1$, $P_L = 13.3$ and $P_R = 10^{-6}$ and there is no initial velocity. Fig. 5.3 gives the density, velocity and pressure at $t_{end} = 0.45$, for first order and second order reconstruction. The AMR levels are indicated on the density map. In the first two maps I used

no AMR. The second order simulation shows a sharper contact discontinuity. The simulation with AMR gives a very good agreement with the analytic solution. Refinement occurs at the rarefaction, the contact discontinuity and the shock.

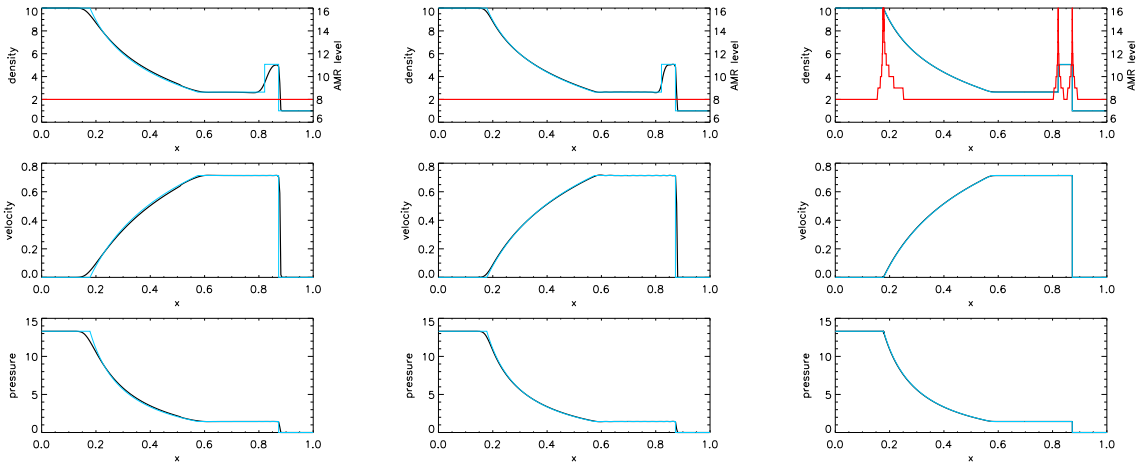

Figure 5.3: Density, AMR levels (red line), velocity and pressure in the frame of the laboratory for the shock test 1, with $\Gamma_{max} = 1.4$. First (left panel) and second order without AMR (middle panel) and second order with AMR (right panel). The analytic solution [Giacomazzo and Rezzolla, 2006] is given in blue. In the first panels $l_{min} = l_{max} = 8$. In the last panel $l_{min} = 8$ and $l_{max} = 16$.

5.2.1.2 Test 2 : highly relativistic case : $\Gamma_{max} = 120$, with transverse velocities

In this test $\rho_L = \rho_R = 1$, $P_L = 10^3$ and $P_R = 10^{-2}$, $v_{x,L} = v_{x,R} = 0$, $v_{y,L} = v_{y,R} = 0.99$ initially. This test is the most stringent Sod test found in the literature due to the high Lorentz factor. Fig. 5.4 gives the density, parallel and transverse velocity and pressure at $t_{end} = 1.8$ for tests with two different resolutions. The AMR levels are superposed to the density maps. Both simulations were run with $l_{max} = 17$, in the left panel $l_{min} = 14$, in the right panel $l_{min} = 5$. When $l_{min} = 14$, the agreement with the analytic solution (in blue) is very good except at the contact discontinuity. Although the simulation with $l_{min} = 5$ has the same maximal resolution, its final result is far from the analytic solution. In this case the number of cells is very low, the refinement criteria do not seem to be adapted. The simulation with $l_{min} = 14$ took 1h35 minutes, on a desktop computer. A possible improvement would be to perform refinement according to the Lorentz factor, which would favour highly relativistic regions for refinement. These tests show that in a simulation, it is sometimes better to increase the minimal resolution than the maximal resolution.

5.2.2 2D tests : inclined shock tubes

Sod tests can also be used to test 2D schemes by inclining the interface between both flows. I performed the two same tests as in the former section but inclining the interface between the two media by $\theta = 21.7°$ with respect to a vertical line. The simulations should give a comparable result to 1D simulations with the same resolution. Otherwise, it means some directions in the grid are strongly favoured with respect to others. A sketch of the simulation domain is shown on Fig. 5.5. In this type of simulation, the initial condition is always shifted by a few cells with respect to the row of cells just above or below. This implies shifted boundary conditions are necessary at the bottom and top of the simulation box. They are not straightforward to

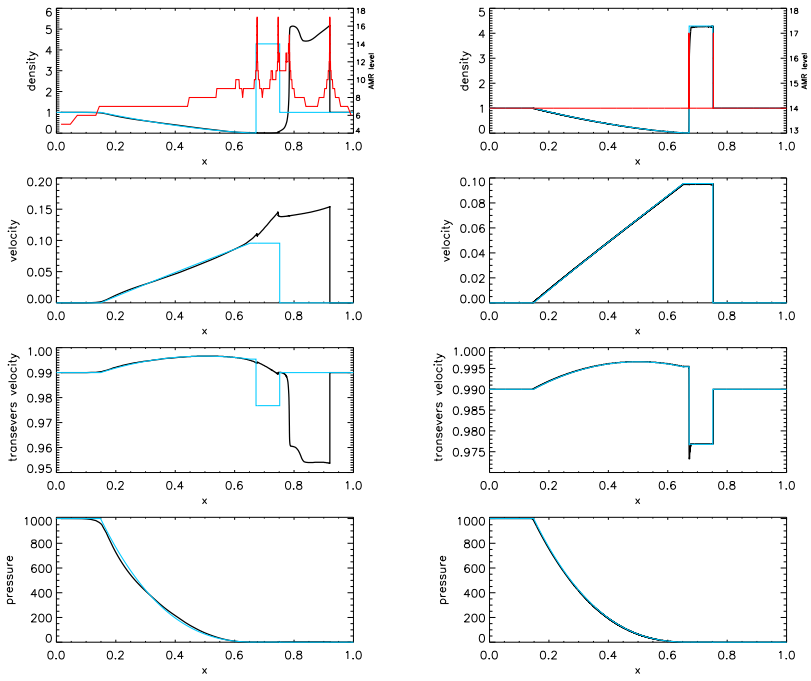

Figure 5.4: Density, AMR levels (red line), velocity and pressure in the frame of the laboratory for the shock test P2 with $\Gamma_{max} = 120$. Left panel : $l_{min} = 5$, $l_{max} = 17$, right panel : $l_{min} = 14$, $l_{max} = 17$.

implement within the AMR structure, so these tests have been performed using a uniform grid, which limits the resolution. In both tests, there are 400 cells in the x direction, and 200 cells in the y direction. The boundary conditions are periodic along the x axis. In RAMSES, at

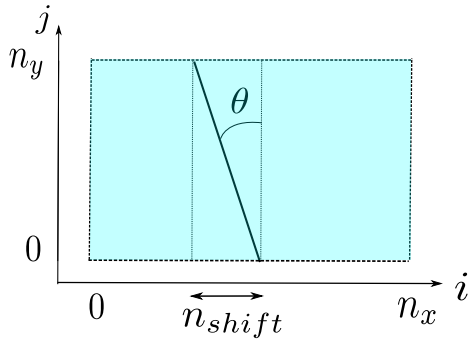

Figure 5.5: Simulation domain (in blue) for inclined shock tubes. The interface is shifted by an angle θ with respect to a vertical line.

each boundary there are three additional cells surrounding the simulation domain. One has to determine the value of the variables in these cells to determine the boundary conditions. At the bottom of the box, when $i - n_{shift} > 0$ then

$$\begin{cases} \mathbf{U}(i,1) = \mathbf{U}(i - n_{shift}, n_y - 2) \\ \mathbf{U}(i,2) = \mathbf{U}(i - n_{shift}, n_y - 1) \\ \mathbf{U}(i,3) = \mathbf{U}(i - n_{shift}, n_y) \end{cases} \tag{5.47}$$

At the top of the box, when $i + n_{shift} > n_x$ then

$$\begin{cases} \mathbf{U}(i, n_y - 2) = & \mathbf{U}(i + n_{shift}, 1) \\ \mathbf{U}(i, n_y - 1) = & \mathbf{U}(i + n_{shift}, 2) \\ \mathbf{U}(i, n_y) = & \mathbf{U}(i + n_{shift}, 3) \end{cases} \tag{5.48}$$

The results for both tests are given in Fig. 5.6. The left panel gives the density contours at the end of the simulation, where one can distinguish the rarefaction propagating to the left and the contact discontinuity and shock propagating to the right. The right panels show the different variables in the direction normal to the shock. The given values were obtained performing a bilinear interpolation of the 2D simulation. I overplotted the analytic solution and the result from a 1D simulation with the same resolution along the interface between the flows ($n_y/cos\theta = 256$ cells).

The first test, with $\Gamma_{max} = 1.4$ shows a good agreement between the 1D and 2D results, although it can be noted that small spurious transverse velocity has been created in the 2D simulation. The second test is more difficult due to the high Lorentz factor $\Gamma_{max} = 120$. The 2D simulation does not show the same result than its equivalent 1D simulation. The 2D result is similar to the result of a 1D simulation with a resolution of 110 grid points (dotted line). This suggests that direct comparison between unidimensionnal and multidimensional simulations is not possible and that, for high Lorentz factors, multidimensional simulations need a higher resolution to be numerically converged. In both the 1D and the 2D simulations, the position of the shock is ahead of its theoretical position. 1D tests have shown this effects weakens at higher resolution. In section §5.2.1 I have shown this test gives a satisfactory result for a minimal level of refinement l_{max}=14. A 2D simulation with equivalent resolution is numerically prohibitive. Although our code converges towards a satisfactory solution for $\Gamma_{max} = 120$, large scale simulations of flows at such high speeds are out of reach.

5.2.3 3D test : relativistic, supersonic jet

Relativistic jets are a common test for RHD codes as they present an astrophysical interest. In this case, no analytic solution exists and validation is done by comparison with former results. I followed the setup by Del Zanna and Bucciantini [2002]

$$\begin{cases} (\rho, v_x, v_y, v_z, P) = (0.1, 0, 0, 0.99, 0.01) & r \leqslant 1, z \leqslant 1 \\ (\rho, v_x, v_y, v_z, P) = (10, 0, 0, 0, 0.01) & \text{outside} \end{cases}$$

The length scale is given by the initial radius of the jet $r_0 = 1$, the size of the box is $20r_0$, with $l_{min} = 6$ and $l_{max} = 9$. This gives an equivalent resolution of 25 cells per radius, while the original test was performed with a resolution of 20 cells per radius. The simulation took 640 CPU hours. The maximum Lorentz factor is 7.1 and the relativistic Mach number 17.9. The resulting density profile is given on Fig. 5.7 with the original simulation given for comparison. The global shape is similar, although the simulation with RAMSES-RHD presents a small extension at head of the jet. This is due to the carbuncle instability [Peery and Imlay, 1988] which arises when cylindrical or spherical phenomena are simulated on a Cartesian grid. The development of the Kelvin-Helmholtz instability is more pronounced in my simulation.

5.2.4 Applications and future improvements of this new relativistic code

The set of tests I have performed indicates this new relativistic hydrodynamical provides satisfactory results for a Lorentz factor above 100. However, such simulations require a very high

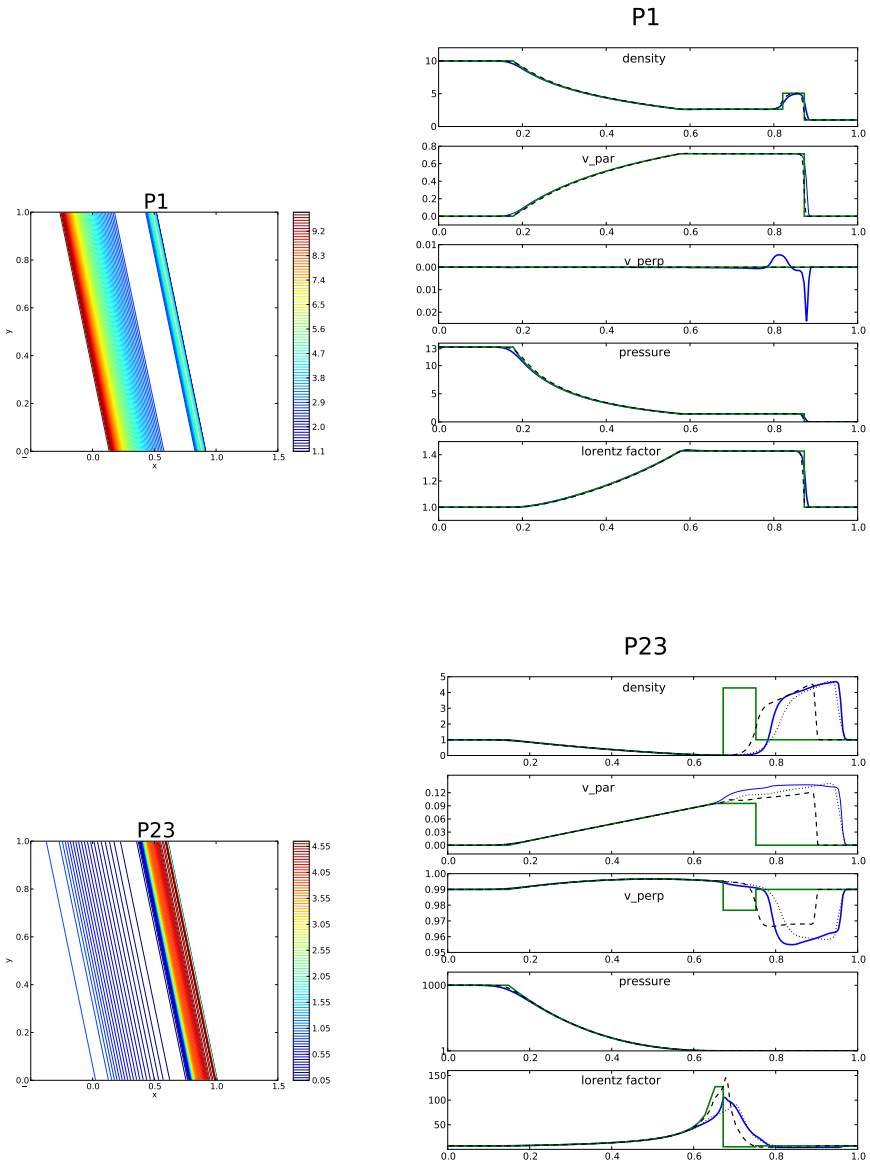

Figure 5.6: Inclined shock tests 1 (upper row) and 2 (bottom row). The left panel gives the contour map at the end of the simulation. The right panel gives density, velocity, pressure and Lorentz factor along the shock normal. The blue lines give the 2D results, the dashed black line the 1D results from a simulation with the same resolution and the green line gives the analytic solution. For the second test, I overplot the 1D solution for a simulation with a resolution of 100 grid points. Note that the resolution is much lower than for the 1D tests in §5.2.1.

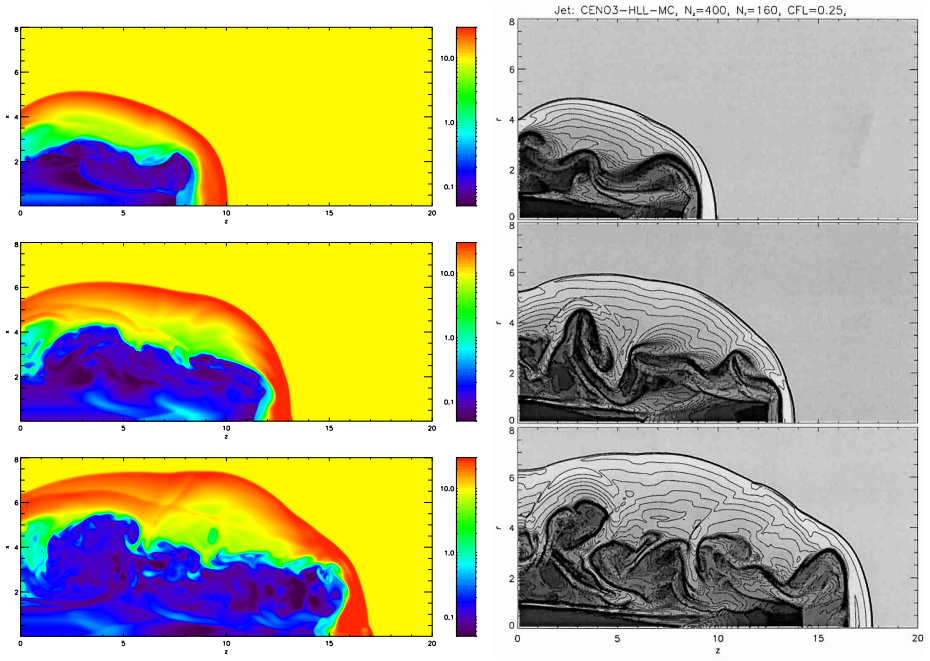

Figure 5.7: Simulation of the propagation of a 3D relativistic jet ($\Gamma_{max} = 7.1$). From top to bottom: density at $t = 20, 30, 40$ in a 3D jet starting form the left boundary of the domain. The left panel shows the simulation with RAMSES-RHD, the right panel the simulation from Del Zanna and Bucciantini [2002].

resolution that strongly limits its applicability to multidimensionnal flows. The 3D jet simulation, with a Lorentz factor of 7.1 gives results in good agreement with former work at a reasonable cost. Intermediate tests we have performed suggest that the code is suited to study flows with Lorentz factors up to roughly ten, and is probably too time consuming beyond. Relativistic simulations found in the literature have similar maximal Lorentz factors : 20 in relativistic jets [Perucho et al., 2004], 10 in pulsar wind nebulae [Bucciantini et al., 2005], and 27 in a simulation of a Gamma-ray burst [Meliani et al., 2007]. Bogovalov et al. [2008] reached a maximal Lorentz factor of 100 in their simulation of γ-ray binary PSR B1259-63 with a totally different numerical method to model the collision region. A Lorentz factor of 2 was used in the simulation of a γ-ray binary by Bosch-Ramon et al. [2012]. All these simulations are 2D simulations.

The current relativistic version of RAMSES could be improved, a few points I would like to work on are :

- Enable adaptive mesh refinement according to the value of the Lorentz factor. This should facilitate simulations with high Lorentz factors.
- Improve the second order scheme to enable more accurate reconstruction of the variables with different slope limiters (see §5.1.4).
- Enable an adaptive value of the adiabatic index to have a simultaneous realistic model for both the non-relativistic part and the relativistic part of a simulation. The adiabatic index could vary according to the value of $P/\rho c^2$. This is a considerable modification as it would impact the Riemann solver. It could be particularly appropriate in γ-ray binaries.
- Add the possibility to use the entropy as conserved variable in low pressure regions. This should avoid numerical failures I have found when simulating low pressure pulsar winds at high Lorentz factors.

The following part of this Chapter is dedicated to some preliminary work on γ-ray binaries. It presents relativistic simulations with our new code.

5.3 Analytic predictions for the interaction region in γ-ray binaries

As in the classic case, one can derive some analytic solutions on the structure of the colliding wind region. In this section I study the position of the contact discontinuity and the shocks in the collision between a relativistic pulsar wind and a stellar wind.

5.3.1 Position of the contact discontinuity

I recall the equations of relativistic hydrodynamics

$$\begin{aligned} \frac{\partial(\rho\Gamma)}{\partial t} + \frac{\partial(\rho\Gamma v_j)}{\partial x_j} &= 0 \\ \frac{\partial(\rho h v_i \Gamma^2)}{\partial t} + \frac{\partial(\rho h \Gamma^2 v_i v_j + P\delta_{ij})}{\partial x_j} &= 0 \\ \frac{\partial(\rho h \Gamma^2 - P)}{\partial t} + \frac{\partial(\rho h \Gamma^2 v_j)}{\partial x_j} &= 0 \end{aligned} \tag{5.49}$$

where the specific enthalpy

$$h = 1 + (\gamma/(\gamma-1))P/\rho. \tag{5.50}$$

The position of the standoff point is determined by equating the momentum flux along the line-of-centres.

$$\rho h \Gamma^2 v^2 + P = \rho_* v_*^2 + P_*, \tag{5.51}$$

where the subscript $*$ represents the variables in the stellar wind, the variables without subscript refer to the pulsar. As in Stevens et al. [1992] I neglect thermal pressure in the winds, which gives

$$\rho\Gamma^2 v^2 = \rho_* v_*^2. \tag{5.52}$$

Using mass conservation in both winds, one can express the momentum flux ratio of the winds

$$\eta_{rel} = \eta\Gamma, \tag{5.53}$$

where $\eta = \dot{M}v/\dot{M}_* v_*$ is the usual definition of the momentum flux ratio of the winds (Eq. 1.31). Using this definition of η we can rederive the position of the contact discontinuity following Antokhin et al. [2004]. We get, in 3D

$$\frac{dx}{dy} = \frac{x}{y} - \left(\frac{a}{y}\right)\left(1 + \sqrt{\Gamma\eta}\left(\frac{r_2}{r_1}\right)^2\right)^{-1}, \tag{5.54}$$

and in 2D

$$\frac{dx}{dy} = \frac{x}{y} - \left(\frac{a}{y}\right)\left[1 + \sqrt{\Gamma\eta}\left(\frac{r_2}{r_1}\right)^{3/2}\right]^{-1}. \tag{5.55}$$

The 2D result corresponds to a cylindrical geometry, as explained in §3.1.3.1. These equations suggest that we can expect a similar structure than in colliding stellar winds, provided we define the momentum flux $\eta_{rel} = \Gamma\eta$. The simulations in §5.4 are meant to verify this assumption.

5.3.2 Relativistic jump conditions

The above equations only indicate the position of the contact discontinuity. To find the positions of the shocks along the line-of-centres, we use the Bernouilli relation in the stellar and pulsar wind [Landau and Lifshitz, 1975]

$$\frac{v_*^2}{2} = \frac{v_{*,s}^2}{2} + \frac{P_{*,s}}{\rho_{*,s}}\frac{\gamma}{\gamma-1} \tag{5.56}$$

$$\Gamma = \left(1 + \frac{P_s}{\rho_s}\frac{\gamma}{\gamma-1}\right)\Gamma_s, \tag{5.57}$$

where the subscript s stands for the shocked winds. I have assumed the shocks have infinite Mach numbers and neglected thermal pressure upstream of the shocks.

At the contact discontinuity between the winds, thermal pressures on both sides equate and the velocity components normal to the discontinuity vanish. At the stagnation point we have

$$v_{*,CD} = v_{CD} = 0 \tag{5.58}$$

$$P_{*,CD} = P_{CD} \tag{5.59}$$

$$\Gamma_{CD} = 1. \tag{5.60}$$

Combining this with Eq. 5.56 we have

$$\frac{v_*^2}{2}\rho_{*,CD} = (\Gamma - 1)\rho_{CD}. \tag{5.61}$$

In both shocked zones, the density can be considered as constant and can be related to the density before the shocks by the Rankine-Hugoniot jump conditions. In the classical case, the compression ratio between the downstream and upstream gas $\rho_s/\rho = 4$ (see §1.3.2.1), but in the relativistic case, the jump conditions are given by [Taub, 1948]

$$\begin{cases} \Gamma\rho v = \Gamma_s\rho_s v_s \\ \Gamma^2\rho h v^2 + P = \Gamma_s^2\rho_s h_s v_s^2 + P_s \\ \Gamma^2\rho h v = \Gamma_s^2\rho_s h_s v_s. \end{cases} \tag{5.62}$$

In the limit of strong shocks one has $P = 0$ and $h = 1$, which gives

$$\begin{cases} \Gamma\rho v = \Gamma_s\rho_s v_s \\ \Gamma^2\rho v^2 = \Gamma_s^2\rho_s h_s v_s^2 + P_s \\ \Gamma^2\rho v = \Gamma_s^2\rho_s h_s v_s. \end{cases} \tag{5.63}$$

Contrary to the classical case, transverse velocities affect the structure of the shocked region through the presence of the Lorentz factor. There is no explicit solution to this set of equations. The second equation gives

$$P_s = \frac{\Gamma^2\rho v^2 - \Gamma_s^2\rho_s v_s^2}{\Gamma_s^2(\frac{\gamma}{\gamma-1})v_s^2 + 1}. \tag{5.64}$$

Inserting this in the last equation of 5.63 gives the density in the downstream flow

$$\rho_s = \rho\left(\frac{\gamma}{\gamma-1}\Gamma^2 v(v_s - v) + \frac{\Gamma^2 v}{\Gamma_s^2 v_s}\right). \tag{5.65}$$

Inserting this in the first equation finally yields the velocity in the downstream flow

$$\gamma\Gamma_s - \frac{1}{\Gamma_s} - \frac{\gamma-1}{\Gamma} - \gamma v \Gamma_s v_s = 0, \tag{5.66}$$

that can be solved using a root-finding algorithm.

In the non-relativistic limit $\Gamma \Rightarrow 1 + v^2/2$ and $\Gamma_s \Rightarrow 1 + v_s^2/2$ and we have

$$\frac{1}{2}\left(\frac{\gamma-1}{\gamma}\right) + \frac{1}{2}\left(\frac{\gamma-1}{\gamma}\right)\frac{v^2}{v_s^2} - \frac{v}{v_s} = 0. \tag{5.67}$$

This quadratic equation has two solutions v/v_s=1 (contact discontinuity) and v/v_s=4 that corresponds to the usual jump condition.

In the ultrarelativistic limit $\Gamma \Rightarrow \infty$ and $v \Rightarrow 1$ and Eq. 5.66 becomes

$$\gamma\Gamma_s - \frac{1}{\Gamma_s} = \gamma\Gamma_s\left(1 - \frac{1}{\Gamma_s^2}\right)^{1/2} \tag{5.68}$$

$$\Rightarrow \quad v_s = \gamma - 1, \tag{5.69}$$

that gives $v_s = 1/3$ when $\gamma = 4/3$. Combining this with Eq. 5.63 gives, in the ultrarelativistic limit

$$\rho_s = \rho\Gamma\sqrt{8}. \tag{5.70}$$

In the above equation, the Lorentz factor is the Lorentz factor of the upstream flow, in the frame of the shock. In the rest frame of the upstream flow (see Fig. 1.12), one has $\Gamma_u = \sqrt{2}\Gamma$ [Blandford and McKee, 1976], which gives

$$\rho_s = 4\rho\Gamma_u. \tag{5.71}$$

Fig. 5.8 represents the solution to the relativistic Rankine-Hugoniot conditions for strong shocks for $\gamma = 5/3$ (non-relativistic limit) and $\gamma = 4/3$ (ultrarelativistic limit). The physical solution progressively switches from the non-relativistic to the ultrarelativistic case. The left panel indicates that for Γ=10, the postshock velocity is close to its asymptotic value. This suggests that a simulation with $\Gamma \simeq 10$ will give satisfactory indications on the structure of the flow in Γ-ray binaries. Fig. 5.8 can be used to relate the downstream density to the upstream density in Eq. 5.61. Using mass conservation, one can then derive the positions of the shocks.

5.4 Simulations of γ-ray binaries

In this section I present some first 2D simulations of the collision of a stellar wind and a pulsar wind. I focus on the small scale structure and neglect orbital motion. The aim is to make comparisons between the results from Chapter 3 and the above analytic solutions. The simulations are also meant to determine whether relativistic effects modify the colliding wind structure or the development of the Kelvin-Helmholtz instability (KHI). The Lorentz factor of unshocked pulsar winds is estimated to be about 10^6 [Gaensler and Slane, 2006]. Former simulations of pulsar winds interacting with the ISM or the wind from a massive companion (see *e.g.* Bucciantini et al. [2005], Bogovalov et al. [2005]) do not clearly identify the differences between the relativistic and classical case. Similarly to what I did in Chapter 3 for non-relativistic winds, the goal of the following section is also to determine the numerical parameters that should be used in simulations of γ-ray binaries.

Simulating γ-ray binaries is computationally demanding because the timestep for hydrodynamical computations is set by the fast pulsar wind while the dynamical timestep is set

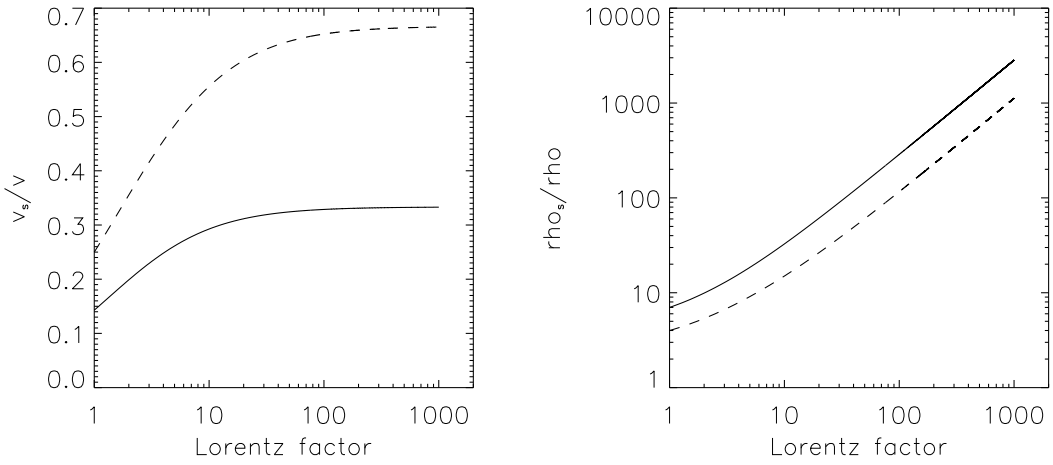

Figure 5.8: Density and velocity jump for strong shocks as a function of the pre-shock Lorentz factor (in the frame of the shock). The solid line represents the solution for $\gamma = 4/3$, the dashed line represents the solution for $\gamma = 5/3$.

by the stellar wind that is roughly 100 times slower. This means that the simulations with $\beta_p = v/c = 0.99$ for the pulsar wind last about hundred times longer than their equivalent with two stellar winds. Performing a 3D large scale simulation of such a system is out of reach in this case. Therefore we want to understand how the colliding wind region evolves when β_p (and the Lorentz factor $\Gamma = (1 - \beta_p^2)^{-1/2}$) increases. We hope that beyond a given value for β_p, the simulation properly models the relativistic effects and that we can determine an asymptotic behaviour. This way we could perform simulations at a reasonable value of β_p and model the most important features of the flow.

5.4.1 Numerical setup

The momentum flux of a pulsar wind is usually not expressed as a function of its density and velocity but by using the rotational losses of the pulsar wind $\dot{E} = \Gamma \dot{M} c^2$. The momentum flux ratio in a γ-ray binary is given by

$$\eta_{rel} = \frac{\dot{E}}{\dot{M}_* v_* c}. \tag{5.72}$$

To draw an easy parallel with the simulations of stellar wind binaries, I use η_{rel} as it is defined by Eq. 5.53. As I want to study the impact of relativistic effects, I do not set the pulsar wind velocity to $\simeq c$ but keep it as a free parameter. Therefore, I set η_{rel} to a given value and derive the pulsar's mass loss rate

$$\dot{M} = \eta_{rel} \frac{\dot{M}_* v_*}{v \Gamma}. \tag{5.73}$$

As for the classical case, the winds are initialised in 'masks'. Following mass conservation, the density in the winds is set by

$$\rho = \frac{\dot{M}}{2\pi r v_\infty \Gamma}, \tag{5.74}$$

where r is the distance to the centre of the mask. The velocity is set to the terminal velocity. As in stellar wind simulations, I set the Mach number $\mathcal{M}$, at a distance $r = a$ to 30. However,

the relativistic Mach number is defined by

$$\mathcal{M}_{rel} = \frac{v\Gamma}{c_s\Gamma_{sound}}, \tag{5.75}$$

where $\Gamma_{sound} = (1 - c_s^2)^{-1/2}$ and the relativistic sound speed is given by Eq. 5.9. In highly supersonic flows, $\mathcal{M}_{rel} = \mathcal{M}\Gamma$, meaning the physical Mach number in the simulation will be higher than 30. I then derive the corresponding pressure in the mask.

To check this setup, I performed a simulation with both wind speeds set to $v_* = v = 3000\,\mathrm{km\,s^{-1}}$ (0.01 c) and compared its result to a simulation with the same parameters but using the hydrodynamical version of RAMSES. The resulting density, velocity and temperature are given on Fig. 5.9 and show there is a very good agreement between the two techniques.

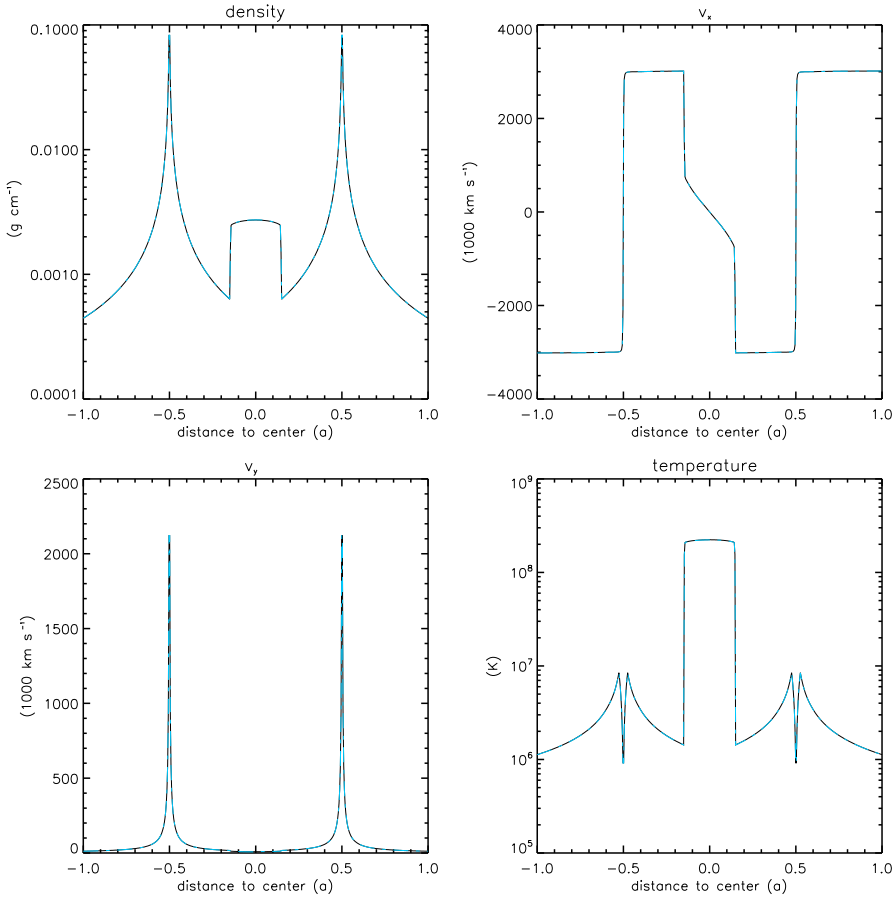

Figure 5.9: Density, v_x, v_y and temperature in two similar simulations. One uses the hydrodynamical version of the code (blue solid lines) while the other one uses the relativistic version (black dashed lines).

To make easy comparisons between the different simulations, I keep the parameters of the star constant, I set $\dot{M}_* = 10^{-7}\,\mathrm{M_\odot\,yr^{-1}}$ and v_*=3000 $\mathrm{km\,s^{-1}}$. I set the adiabatic index to 5/3. At this stage, I use the HLL Riemann solver to prevent the development of the KHI at the contact discontinuity between the winds. The size of the simulation region is $l_{box} = 8\,a$, the coarse grid is set by $l_{min} = 6$. The Sod test problems (§5.2.1-5.2.2) suggested that the higher the Lorentz factor of the flow, the higher the resolution needed to obtain satisfactory simulation.

For each value that I used for the pulsar wind velocity, I have performed test simulations for $\eta_{rel} = 1$ at different resolutions to determine the level of refinement required to reach numerical

convergence. I consider numerical convergence occurs when the positions of the discontinuities do not vary when increasing resolution. The position of the contact discontinuity is given by the maximal density of the passive scalar. The positions of the two shocks are given by the minimal and maximal value of the derivative of the pressure. For the non-relativistic case with β_p=0.01, it occurs for $l_{max} = 10$, for $\beta_p = 0.1$, it occurs for $l_{max} = 11$, for $\beta_p = 0.5$ and 0.9 it occurs for $l_{max} = 12$.

Fig. 5.10 shows the position of both shocks and the contact discontinuity for $\beta_p = 0.5$ for increasing maximal resolutions. I have tested $l_{max} = \{8, 9, 10, 11, 12, 13\}$. One can barely distinguish the red solid line and the black solid line representing the simulations with $l_{max} = 12$ and $l_{max} = 13$. Our 2D shock tube tests (§5.2.2) highlighted the impact of the minimal resolution of a simulation, which has not been determined yet in the case of colliding winds. I have run a simulation with $\beta_p = 0.99$, using a maximal resolution $l_{max} = 13$. Numerical convergence has yet to be checked using a simulation with $l_{max} = 14$.

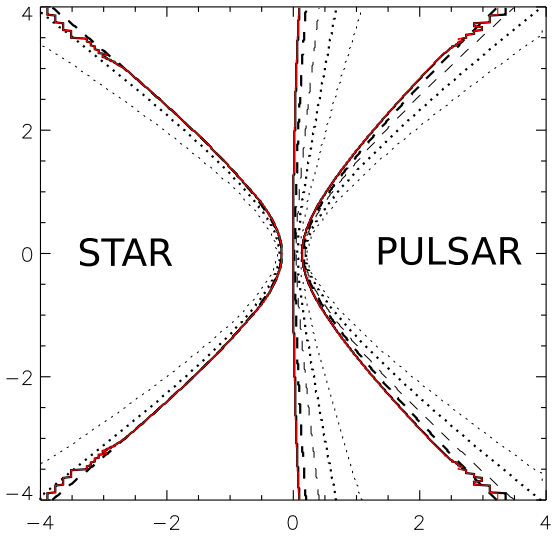

Figure 5.10: Position of both shocks and the contact discontinuity for $\eta_{rel} = 1$, $\beta_p = 0.5$ for increasing resolution $l_{max} = 8$ (thin dotted line), 9 (thick dotted line), 10 (thin dashed line), 11 (thick dashed line), 12 (black solid line) and 13 (red solid line). The last two resolutions give the same result, which indicates numerical convergence is reached. At the edges of the box, there is a numerical artefact due to the AMR grid.

5.4.2 Geometry of the colliding wind region

Fig. 5.11 shows the density map and the Lorentz factor map for a simulation with $\eta_{rel} = 0.1$, 1, 10 and $\beta_p = 0.5$. I set the maximal resolution to $l_{max} = 12$ as tests have shown this gives numerical convergence. I have verified that it is also the case for $\eta_{rel} = 0.1$ and 10. The stellar wind is the dense flow on the left, the pulsar wind is located on the right. The dashed lines shows the analytic solution for the contact discontinuity (Eq. 5.55). The overall structure is similar to what is found for non-relativistic flows (see *e.g* Fig 3.2). As for the non-relativistic simulations, we find that the analytic solution slightly underestimates the asymptotic opening angle. The simulations with $\eta_{rel} = 0.1$, 10 both display a reconfinement shock behind the object with the weaker wind. This is consistent with the 2D results for colliding wind binaries.

The direction of the velocity in the winds is indicated by arrows on the map of the Lorentz

factor. Along the line-of-centres, the winds collide head on, when getting further from the binary the velocity is mostly parallel to the direction of the shocks. This corresponds to the second shock tube test simulation I have performed (§5.2.2) and that required a very high resolution because of the high velocity parallel to the shock ($v = 0.99$). The importance of the velocity parallel to the shock (or, in other words, transverse to the shock normal) is the reason why numerical convergence is more difficult to reach in simulations with increasing Lorentz factors in the pulsar wind.

Although there is a strong similarity with the non-relativistic case, some differences are present. For $\eta_{rel} = 1$, the structure is not totally symmetric with respect to the midplane of the stars. The shocked region from the stellar wind is smaller than the shocked region from the pulsar wind. Similarly, the asymptotic opening angle measured for $\eta_{rel} = 0.1$ equals 22° while I measure an asymptotic opening angle of 32° in the simulation with $\eta_{rel} = 10$. This suggests that the impact of relativistic effects is more subtle than suggested by the definition of the momentum flux ratio.

5.4.2.1 Impact of the Lorentz factor

To quantify the impact of relativistic effects, I perform simulations with $\eta_{rel} = 1$ for increasing values of the pulsar wind velocity $\beta_p = \{0.01, 0.1, 0.5, 0.9\}$. The corresponding Lorentz factors are $\{1.00005, 1.005, 1.15, 2.29\}$. The left panel of Fig. 5.12 shows the positions of both shocks and the contact discontinuity in the different simulations. This plot shows that, on the line-of-centres, the structure is identical in all simulations and is only set by η_{eq}. At the edges of the box, the contact discontinuity is not exactly on the axis of symmetry between the winds. Further away from the binary, it seems that the higher the Lorentz factor, the smaller the shocked region around the star and the larger the shocked region around the pulsar. In these zones, the velocity is mostly transverse to the shock normal. The relativistic Rankine-Hugoniot conditions (Eq. 5.63) show that this impacts the structure of relativistic shocks, as can be observed in 1D Sod tests (see §5.2.1) and Ryu et al. [2006]). This relativistic effect could explain the different positions of the shocks for different values of the Lorentz factor.

Our work on colliding stellar winds showed a similar effect occurs when one of the winds has a low Mach number and the position of the discontinuities changes due to pressure in the winds. Another explanation to the variation of the positions of the shocks is that pressure terms cannot be totally neglected in the pulsar wind. The right panel of Fig. 5.12 shows the results from simulations with $\eta_{rel} = 1$, $\beta_p = 0.5$ and increasing Mach numbers for the pulsar wind $\mathcal{M}_p = 10, 20, 30, 50$. When the Mach number equals 10, the contact discontinuity is bent towards the star, due to higher pressure. In the other cases, the whole structure is more bent towards the pulsar. These simulations indicate that even a low pressure in the pulsar wind has some influence on the structure of the collision region. Still, the impact is small and our simulations can properly model pulsar winds, where thermal pressure can be considered as equal to zero.

5.4.3 The Kelvin-Helmholtz instability in γ-ray binaries

The stellar wind has a velocity of $3000\,\mathrm{km\,s^{-1}}$ while the pulsar wind is almost two orders of magnitude faster. Similarly to what happens for classical flows, at the contact discontinuity between the winds, the Kelvin-Helmholtz instability modifies the structure of the flow [Blandford and Pringle, 1976, Turland and Scheuer, 1976]. Bodo et al. [2004] find analytic solutions to the dispersion relation and show that, in the frame of the laboratory, the stability criteria are the same as in the classical case, provided one uses the relativistic definition of the Mach number (Eq. 5.75). In the incompressible limit, we thus expect the interface between the winds to be unstable. To verify the impact of the KHI on γ-ray binaries, I performed two test simulations with

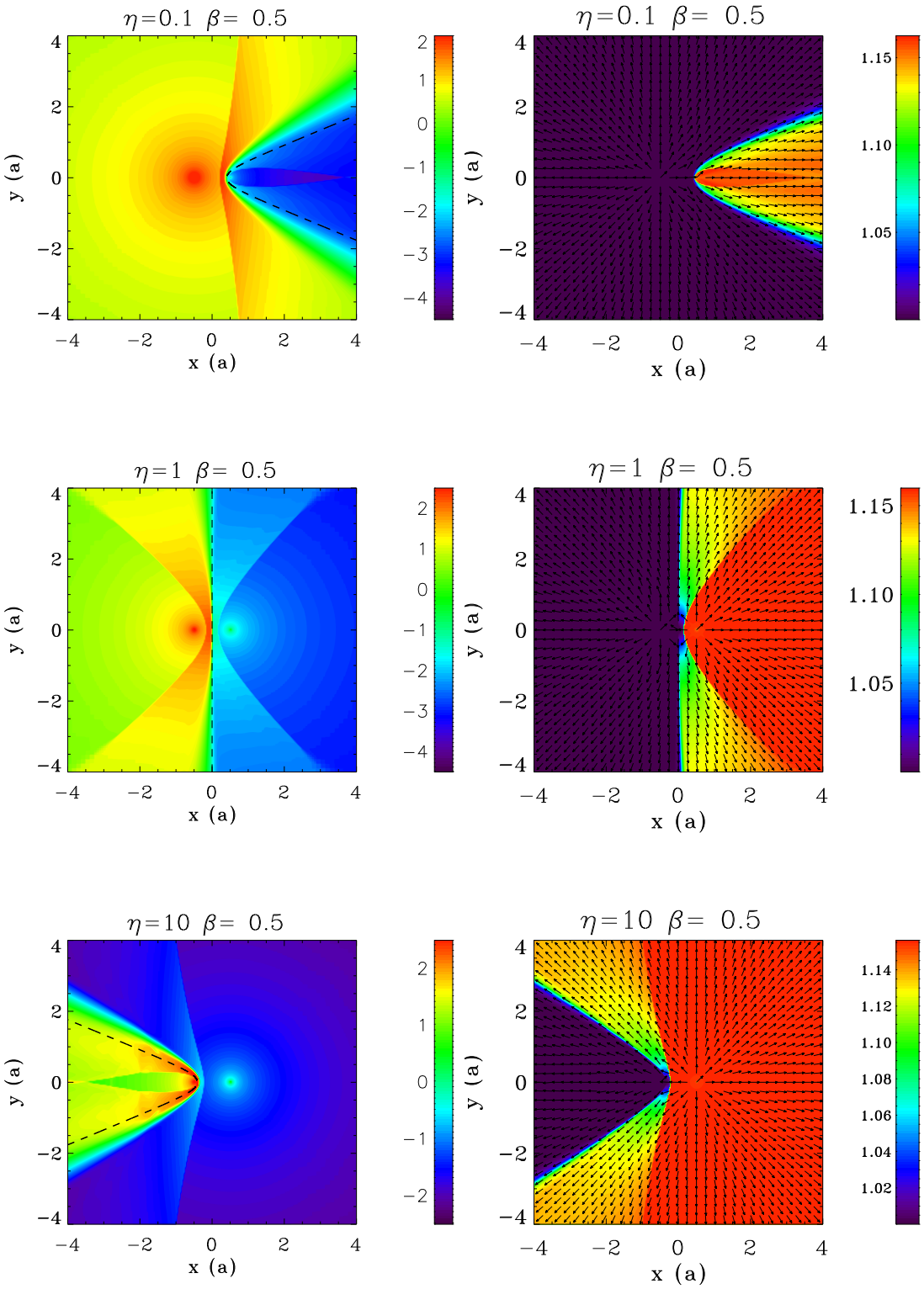

Figure 5.11: Density maps (left panel) and maps of the Lorentz factor (right panel) for simulations with a stellar wind and a pulsar wind with $\eta_{rel} = 0.1$, 1, 10 (from top to bottom) and $\beta_p = 0.5$. The star is located on the left, the pulsar on the right. The density is given in $\mathrm{g\,cm^{-2}}$ and the velocity in $\mathrm{km\,s^{-1}}$. The arrows indicate the direction of the velocity, their size is normalised by the local norm of the velocity vector. The contact discontinuity is smeared out as the simulations use the HLL Riemann solver.

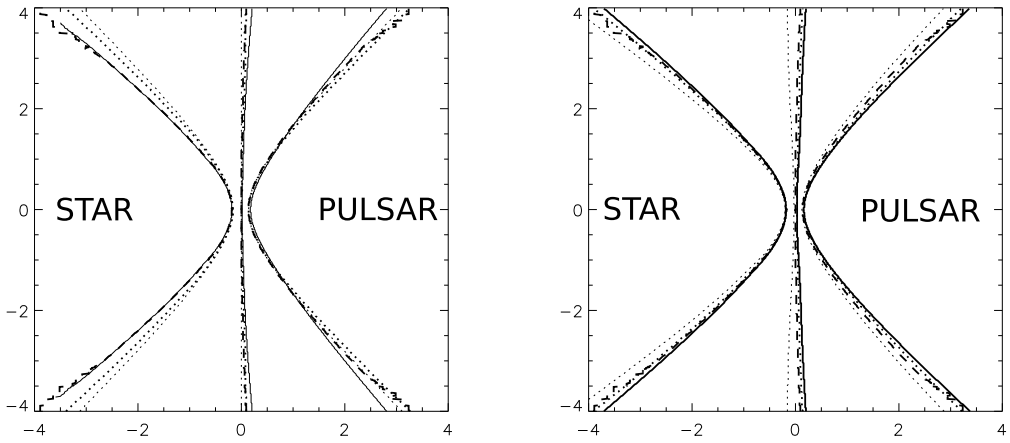

Figure 5.12: Left panel : position of both shocks and the contact discontinuity in a simulation with $\eta_{rel} = 1$, in simulations with different values for the Lorentz factor of the pulsar wind. We have β_p= 0.01 (thin dotted line), 0.1 (thick dotted lined), 0.5 (thick dashed line) and 0.9 (solid line). Right panel : position of both shocks and the contact discontinuity in a simulation with $\eta_{rel} = 1$, and β_p= 0.5 with the Mach number of the pulsar wind = 10 (dotted line), 20 (thin dashed line), 30 (thick dashed line) and 50 (solid line).

$\eta = 1$, using $\beta_p = 0.2$, 0.5. The case $\beta_p = 0.2$ displays the same velocity difference ($v_1/v_2 = 20$) as the colliding wind binary shown on Fig. 3.12. There is no clear difference between the two cases : the most affected region is the one with the slower wind. The velocity difference is high enough to trigger important instabilities that affect the positions of the shocks.

5.5 What do these first results indicate? What could be improved?

The analytic calculations predict that the position of the contact discontinuity between the pulsar wind and the stellar wind is determined in the same way as in the classical case, assuming one defines the momentum flux ratio by $\eta_{rel} = \eta\Gamma$. The determination of the shock positions is more complex as there is no explicit solution to the relativistic Rankine-Hugoniot jump conditions. The Rankine-Hugoniot conditions indicate that, contrary to the classical case, transverse velocities affect the shock structure. The simulations with different momentum flux ratios show a similar structure to the collision region in stellar wind binaries, which is promising for future simulations. However, they indicate that when the Lorentz factor of the pulsar wind increases, the size of the shocked region from the stellar wind decreases. This may be a relativistic effect that results from the velocity tranverse to the shock normal. It could also be due to additional pressure terms in the momentum flux of the pulsar wind. As pressure is close to zero in real pulsar winds, this effect is a numerical limitation to a realistic model.

As in colliding stellar wind binaries, the Kelvin-Helmholtz instability develops at the interface between the two winds. Because of the high velocity difference, it creates important disturbances in the shocked region and modifies the shock positions. The simulations I have performed need to be complemented by simulations at different momentum flux ratios to have a more global view on what we could expect in γ-ray binaries. We would like to model its impact at larger scale and find whether the spiral structure may subsist. The non-linear evolution of the KHI in relativistic flows has been mostly studied in simulations of relativistic jets [Perucho et al., 2004, Komissarov,

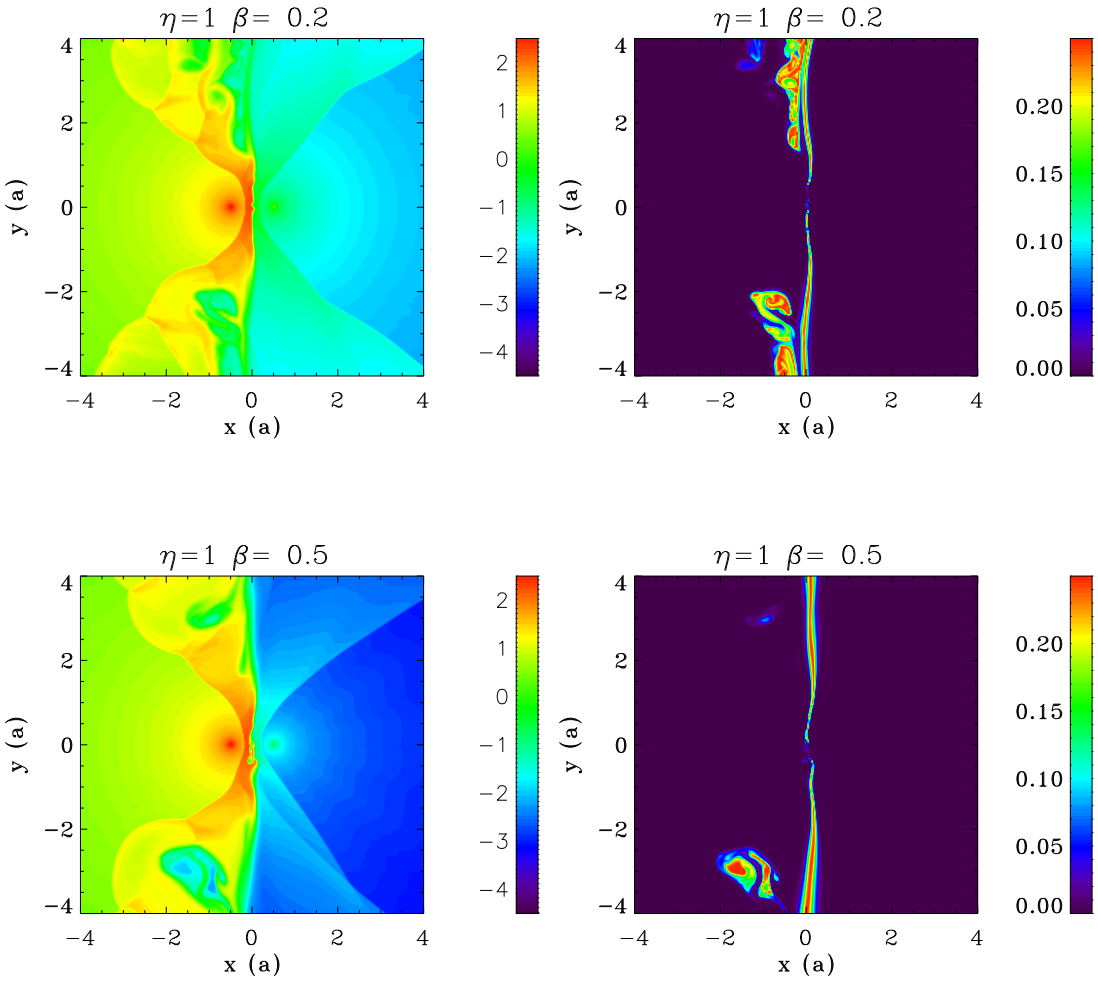

Figure 5.13: Density (left panel) and mixing (right panel) maps for simulations with $\eta_{rel} = 1$ and $\beta_p = 0.2$ (upper row) and $\beta_p = 0.5$ (lower row).

1999] where the stability of the structure is determined both by the Lorentz factor of the jet but also the enthalpy ratio between the jet and ambient medium. The behaviour in γ-ray binaries is unknown, although Bosch-Ramon and Barkov [2011] argue the large scale structure is destroyed.

The above simulations are only very preliminary and are designed to understand the impact of special relativity on the shock structure and its stability and prepare a large scale simulation of a γ-ray binary. Only relativistic simulations can provide the value of the Lorentz factor in the shocked region. Its value is important to determine the impact of Doppler boosting.

Pulsar winds are expected to be weakly magnetised, with a ratio of magnetic to thermal pressure much lower than unity. In this case, the downstream magnetisation is equal to its upstream value and the shock can be considered as a hydrodynamical shock. Using a spherical analytic model, Kennel and Coroniti [1984] show that further out, the magnetisation rises. Magnetic pressure dominates thermal pressure for a distance of 5 to 10 times the distance between the pulsar and its termination shock. If this model applies to γ-ray binaries, magnetic effects may strongly brake the flow at a distance comparable to a few times the binary separation. A relativistic simulation including magnetic fields would be able to model this and provide a more accurate value of the Lorentz factor when getting further from the binary. It would also improve

the modeling of the extended synchrotron radio emission.

5.6 Résumé en Français

Ce chapitre présente l'extension du code RAMSES aux écoulements relativistes et son application aux simulations d'interaction entre un vent stellaire et un vent de pulsar. La modification de RAMSES a constitué une partie importante de ma thèse. L'essentiel des difficultés réside dans le couplage des équations de l'hydrodynamique relativiste par le facteur de Lorentz. L'équation d'état possède aussi un terme supplémentaire dû à l'énergie de masse. Les équations sont donc plus complexes à résoudre. De plus, la vitesse de l'écoulement doit rester strictement inférieure à celle de la lumière, ce qui apporte une contrainte supplémentaire. Des difficultés numériques peuvent apparaître dans les limites non-relativistes ou ultra-relativistes.

Dans RAMSES, certaines étapes s'effectuent non pas avec les variables conservées mais avec les variables dites primitives que sont la densité, la vitesse et la pression. En hydrodynamique classique, on peut basculer d'un jeu de variables à l'autre de façon très simple. En hydrodynamique relativiste la relation est implicite. Un élément crucial du dévelopement numérique a donc consisté à passer d'un jeu de variables à l'autre de façon précise, robuste et efficace. Nous avons aussi modifié le calcul du pas de temps pour tenir compte de la sommation relativiste des vitesses et écrit de nouveaux solveurs de Riemann. Dans un deuxième temps nous avons amélioré la précision du code en écrivant un schéma au deuxième ordre, en temps et espace. Dans une dernière étape nous avons inclu toutes ces modifications dans la structure AMR et adapté le passage d'un niveau de résolution à un autre.

La validation du code relativiste a nécessité de nombreux tests, allant de tests unidimensionnels 'simples' à des tests multidimensionnels plus délicats car comportant des zones de pression et densité très faible et/ou des vitesses très élevées. Actuellement RAMSES résout les équations de l'hydrodynamique relativiste en trois dimensions, avec une précision du deuxième ordre et l'utilisation possible de l'AMR.

J'ai utilisé ce code pour modéliser des binaires γ. Le but des simulations est de quantifier d'éventuels effets relativistes. L'initialisation des vents est similaire au cas classique. En suivant la même méthode que pour les binaires stellaires, on peut déterminer la position de la discontinuité de contact entre les deux vents en definissant le rapport des flux de quantité de mouvement par $\eta_{rel} = \eta\Gamma$ où Γ est le facteur de Lorentz du vent de pulsar. En suivant cette définition, la géométrie de la zone d'interaction est similaire à celle obtenue dans le cas classique. On observe cependant des légères différences. Même lorsque $\eta_{rel} = 1$, la structure n'est pas parfaitement symétrique, le vent choqué de l'étoile ayant une étendue de plus en plus réduite quand le facteur de Lorentz du pulsar augmente. Cette différence pourrait être liée à l'effet de la vitesse transverse sur la structure des chocs ou des termes de pression négligés dans les calculs analytiques. Lorsque la diffusivité numérique est faible, l'instabilité de Kelvin-Helmholtz se développe à l'interface entre les deux vents, de façon comparable aux binaires stellaires.

L'ensemble de ces simulations vise à préparer une simulation la plus réaliste et à la plus grande échelle possible d'une binaire γ. L'ensemble de ces simulations est très coûteux en temps de calcul car son pas de temps est fixé par la vitesse du vent de pulsar alors que son échelle de temps dynamique est déterminée par la vitesse du vent stellaire, et du mouvement orbital. De plus, les simulations que j'ai réalisées indiquent que la résolution nécessaire à la convergence numérique augmente avec le facteur de Lorentz du pulsar. Une simulation à grande échelle d'une binaire γ permettra de déterminer si la structure spirale à grande échelle peut-être maintenue. Elle indiquera également le facteur de Lorentz dans l'écoulement choqué. Sa valeur est importante pour prédire une eventuelle abbération relativiste dans l'émission de la binaire. Pour pouvoir le déterminer avec précision loin de la binaire, il faudrait aussi tenir compte du champ magnétique dans le vent de pulsar.

Chapter 6

Conclusion and Perspectives

Contents

6.1 Conclusions 175
6.2 Looking forwards 176
6.3 Conclusions et perspectives en français 177
6.3.1 Conclusions 177
6.3.2 Perspectives 178

6.1 Conclusions

During this thesis, I have studied colliding wind binaries using mainly numerical simulations with the hydrodynamical code RAMSES. I have considered two types of binaries that share a common hydrodynamical structure: binaries composed of massive stars and γ-ray binaries, composed of a massive star and a young pulsar. The motivation of my research was to model γ-ray binaries at the different scales. Therefore, I followed two complementary paths. On one hand, I modelled colliding stellar winds focussing on the structure and stability of the shocked region. On the other hand, I developed a relativistic version of RAMSES to obtain a more realistic model for pulsar winds. I combined these two aspects to perform preliminary simulations of the collision of a pulsar wind and a stellar wind. In the following paragraphs I will briefly summarise the main results of this research.

Simulations of the region close to the binary (less than 10 times the binary separation) have shown that, when orbital motion can be neglected, analytic solutions provide good estimates for the position of the contact discontinuity. Still, when one of the winds strongly dominates the other one, the asymptotic opening angle is narrower than expected. There are no analytic solutions that predict the shock positions for a given momentum flux ratio of the winds or indicate the presence of a reconfinement shock behind the star with the weaker wind. Simulations are needed to determine the exact structure of the colliding wind region. They indicate the colliding wind region is not necessarily smooth but can be subject to various instabilities. I have shown that, in the adiabatic limit, the Kelvin-Helmholtz instability can considerably affect the structure of the shocked region. In the isothermal limit, the shocked region is much narrower and highly unstable. The resulting structure is dominated by the Non-linear Thin Shell Instability.

When getting further from the binary, orbital motion cannot be neglected anymore. It bends the shocked structure and creates a velocity difference between the winds that triggers the Kelvin-Helmholtz instability, even for identical winds. When the winds are different, the arm propagating into the highest density wind slows down and gets compressed while the other one expands into the lower density wind. The Kelvin-Helmholtz instability develops more strongly in the wider arm.

When zooming even further out, the shocked region is expected to turn into an Archimedean spiral. However, when the velocity gradient between the winds is too strong, the Kelvin-Helmholtz instability can destroy the spiral structure and create a highly mixed turbulent flow. Important density gradients may have a stabilising effect. Analytic calculations give an indication on whether a given binary is expected to form a spiral structure or not. When a spiral structure is possible, simulations have shown that its step is mainly set by the velocity of the stronger wind but that the weaker wind has a non-negligible impact. Adiabatic simulations of the dust producing Pinwheel nebula WR 104 reproduce the observed spiral structure but are not able to create regions where dust formation is expected to be possible. Some cooling due to inverse Compton interactions in the wind of the early type star or free-free emission in the Wolf-Rayet wind is probably at work in this system.

The 2D and 3D simulations have highlighted the importance of a careful choice of the numerical parameters. Diffusive Riemann solvers quench the development of instabilities. When one wind strongly dominates the other one, high resolution is necessary at the very centre of the binary to allow proper shock formation. It has to be maintained in the whole shocked region to allow proper development of the instabilities. I have found that the Non-linear Thin Shell Instability can only be triggered when the shocked region is composed of at least 4 computational cells. The possibility of Adaptive Mesh Refinement in RAMSES is of capital importance in such simulations. Yet, large scale simulations of the Non-linear Thin Shell Instabilities are still out of reach.

Complementary to these studies, we have adapted RAMSES to model relativistic flows, such

as pulsar winds. This new version of RAMSES solves the equations of relativistic hydrodynamics. They are more complicated than the Euler equations because of the Lorentz transformation between the frame of the fluid and the frame of the laboratory. An additional numerical constraint arises from the necessity to keep the velocity subluminal. We have implemented a three-dimensional second order scheme in RAMSES with Adaptive Mesh Refinement. This new code passes the standard set of numerical tests.

This new relativistic code has been used for 2D simulations of the interaction between a stellar wind and a pulsar wind. The simulations model adiabatic winds, close to the binary, where orbital motion can be neglected. Analytic calculations show that when using an adapted definition of the momentum fluxes of the winds, an identical structure to colliding stellar winds is expected. Indeed, the simulations I performed show a structure very similar to a collision between stellar winds. However, they indicate that pressure has an increasing importance when the Lorentz factor in the winds increases. As in colliding stellar winds, the Kelvin-Helmholtz instability arises at the interface between the winds.

6.2 Looking forwards

This work has revealed the importance of the Kelvin-Helmholtz instability in adiabatic colliding winds. In some configurations, it is responsible for the destruction of the large scale spiral structure. When cooling is present, and in the extreme case of isothermal winds, the Non-linear Thin Shell Instability strongly affects the flow. The large scale structure of interacting cooling winds has not been investigated yet. Could the NTSI destroy the spiral in such cases? Could this happen even for weak cooling, as is expected in WR 104? The answer to this question will give indications on the stability of widely studied binaries such as η Carinae. Due to the very high numerical resolution needed to model both the shocked shell between the stars and the large scale structure, such a simulation is a numerical challenge, even when using Adaptive Mesh Refinement.

This research has focused on two limiting behaviours: isothermal or adiabatic winds, while cooling should be treated realistically. Properly modeling it will provide explanations on the dust formation in WR104. In this particular case, inverse Compton cooling by the photons of the early-type star induces the most significant cooling at high temperature. The impact of inverse Compton on thermal electrons has never been studied in colliding wind binaries and is likely to be important for binaries composed of early type stars. To study it, one should either perform 3D simulations or use a code that allows 2D spherical grids. Our current 2D setup assumes a cylindrical geometry that is not well suited to model cooling as variables evolve differently than in a spherical geometry (see §2.3.4).

The simulations of γ-ray binaries are only at their first stages. Our final goal is to obtain a simulation of a γ-ray binary at the largest scale possible. Questions we want to answer are (among many others) : Is there a large scale spiral structure? Can mixing be important enough to strongly cool the accelerated particles and reduce non-thermal emission ? What is the Lorentz factor in the shocked structure, does it lead to an observable Doppler boost? A relativistic simulation of a γ-ray binary can provide estimates of the high-energy emission due to inverse Compton scattering close to the binary. It can also estimate the synchrotron emission arising further out assuming one knows the intensity of the magnetic field. If one wants to go beyond usual assumptions such as equipartition, a relativistic magnetohydrodynamic simulation is needed. To do this, we can choose to modify RAMSES or use another code.

Binaries such as PSR B1259-63 are composed of a Be star that has a slow, dense equatorial outflow on top of the stellar wind. During the periastron passages, the pulsar interacts with this disk, probably forming a colliding wind region. Simulations including the equatorial wind will be able to determine its exact structure and maybe explain the observed radio outbursts. To

prepare these simulations, I have already created a 3D setup that models both the equatorial and isotropic wind of the Be star and models a pulsar on an inclined, eccentric orbit.

I have performed the extension to special relativity of a widely used numerical code. This code could be employed to model a wide variety of relativistic astrophysical flows. The interaction of pulsar winds and supernova remnants or the interstellar medium are a natural extension to the simulations presented in this work. RAMSES could also be used to model relativistic jets in microquasars or active galactic nuclei and gamma-ray bursts.

6.3 Conclusions et perspectives en français

6.3.1 Conclusions

Au cours de cette thèse, j'ai étudié les collisions de vents dans les systèmes binaires principalement au moyen de simulations numériques avec le code hydrodynamique RAMSES. J'ai étudié deux types de binaires qui présentent une structure hydrodynamique commune : celles composées de deux étoiles massives et les binaires γ, composées d'une étoile massive et d'un un pulsar jeune. L'objectif de ma recherche était de modéliser des binaries γ à différentes échelles spatiales. Pour cela, j'ai suivi deux voies complémentaires. D'une part, j'ai modélisé des collision de vents stellaires en me concentrant sur la structure et la stabilité de la région choquée. D'autre part, j'ai développé une version relativiste de RAMSES pour obtenir un modèle plus réaliste pour les vents de pulsars. J'ai combiné ces deux aspects pour effectuer des simulations préliminaires de la collision d'un vent de pulsar et un vent stellaire. Dans les paragraphes qui suivent, je vais résumer brièvement les principaux résultats de ces recherches.

Les simulations de la région à proximité de la binaire (moins de 10 fois la séparation orbitale du système) ont montré que, lorsque le mouvement orbital peut être négligé, les solutions analytiques fournissent de bonnes estimations de la position de la discontinuité de contact. Pourtant, lorsque l'un des vents domine fortement l'autre, l'angle d'ouverture asymptotique est plus étroit que prévu. Il n'existe pas de solution analytique qui permet de trouver la positions des chocs en fonction du flux de quantité de mouvement des vents, ni de prédire la présence d'un choc de reconfinement derrière l'étoile avec le vent le plus faible. Les simulations numériques sont nécessaires pour déterminer la structure exacte de la zone d'interaction des vents. Elles indiquent que la région de collision de vents n'est pas nécessairement régulière, mais peut être soumise à des instabilités diverses. J'ai montré que, dans la limite adiabatique, l'instabilité de Kelvin-Helmholtz peut considérablement affecter la structure de la région choquée. Dans la limite isotherme, la région choquée est beaucoup plus étroite et très instable. La structure qui en résulte est dominée par l'instabilité non-linéaire de couche mince (NTSI).

Lorsqu'on s'éloigne de la binaire, le mouvement orbital ne peut plus être négligé. Il courbe la structure choquée et crée une différence de vitesse entre les vents, qui déclenche l'instabilité de Kelvin-Helmholtz, même lorsque les vents sont identiques. Lorsque les vents sont différents, le bras se propageant dans le vent le plus dense ralentit et est compimé tandis que celui qui se propage dans le vent de plus faible densité s'étend. L'instabilité de Kelvin-Helmholtz se développe plus fortement dans le bras le plus large. Lorsqu'on s'éloigne encore de la binaire, on s'attend à ce que la région choquée présente une structure en spirale d'Archimède. Cependant, lorsque le gradient de vitesse entre les vents est trop important, l'instabilité de Kelvin-Helmholtz peut détruire la structure spirale et créer un écoulement très turbulent. De forts gradients de densité peuvent avoir un effet stabilisateur. Des estimations théoriques permettent d'estimer si l'on s'attend à ce qu'une binaire donnée produise une structure spirale ou non. Quand une structure en spirale est possible, les simulations montrent que son pas est essentiellement déterminé par la vitesse du vent plus fort auquel le vent le plus faible peut apporter une correction non-négligeable. J'ai effectué des simulations adiabatiques du système WR 104 qui montre une structure spirale

riche en poussières. Les simulations permettent de reproduire la structure spirale observée, mais ne sont pas en mesure de créer des régions où la formation de poussière est supposée être possible. Il est probable que des processus de refroidissement doivent être pris en compte. Le vent de l'étoile O-B se refroidit par la diffusion Compton inverse alors que le rayonnement de freinage domine dans le vent de l'étoile Wolf-Rayet.

Les simulations 2D et 3D ont mis en évidence l'importance d'un choix judicieux des paramètres numériques. Les solveurs de Riemann trop diffusifs empêchent le développement d'instabilités. Lorsque l'un des vents domine fortement l'autre, une haute résolution est nécessaire au centre de la binaire pour permettre la formation de façon satisfaisante. Elle doit être maintenue dans toute la région choquée pour permettre le développement correct des instabilités. J'ai trouvé que l'instabilité non-linéaire de couche mince ne peut être déclenchée que lorsque la région choqués est composée d'au moins 4 cellules. La possibilité de raffinement adaptatif de maille (AMR) dans RAMSES est d'une importance capitale dans de telles simulations. Pourtant, les simulations à grande échelle de l'instabilité non linéaires de couche mince ont encore un coût numérique prohibitif.

En complément de ces études, nous avons adapté RAMSES pour modéliser des écoulements relativistes, tels que les vents de pulsars. Cette nouvelle version de RAMSES résout les équations de l'hydrodynamique relativiste. Elles sont plus compliquées que les équations d'Euler en raison de la transformation de Lorentz entre le réferentiel du fluide et celui du laboratoire. Une contrainte supplémentaire numérique découle de la nécessité de maintenir la vitesse inférieure à la vitesse de la lumière. Nous avons mis en place dans RAMSES un schéma numérique du second ordre, à trois dimensions avec la possibilité du raffinement adaptatif de maille. Il réussit l'ensemble standard de tests numériques.

Ce nouveau code relativiste a été utilisé pour des simulations à deux dimensions de l'interaction entre un vent stellaire et un vent de pulsar. Les simulations adiabatiques se focalisent sur l'environnement proche de la binaire, où le mouvement orbital peut être négligée. Les calculs analytiques montrent que lorsqu'on utilise une définition adaptée des flux de quantité de mouvement des vents, une structure identique à celle des vents stellaires est attendue. Une première série de simulations montre effectivement une grande similitude entre les deux types de simulations. Cependant, elles indiquent que la pression a une importance croissante lorsque le facteur de Lorentz du vent de pulsar augmente. Comme dans les collisions de vents stellaires, l'instabilité de Kelvin-Helmholtz se développe à l'interface entre les vents.

6.3.2 Perspectives

Ce travail a révélé l'importance de l'instabilité de Kelvin-Helmholtz dans les collisions de vents adiabatiques. Dans certaines configurations, elle est responsable de la destruction de la structure spirale à grande échelle. Lorsque qu'on tient compte de processus de refroidissement, et dans le cas extrême des vents isothermes, l'instabilité non-linéaire de couche mince affecte fortement l'écoulement. L'impact du refroidissement sur la structure à grande échelle d'une zone de collision de vents n'a pas encore été étudiée. L'instabilité non-linéaire de couche mince pourrait-elle détruire la spirale dans de tels cas? Cela pourrait il se produire, même lorsque le refroidissement est faible, comme cela semble être le cas dans WR 104? La réponse à cette question donnera des indications sur la stabilité de binaires souvent étudiées telles que η Carinae. En raison de la très haute résolution numérique nécessaire pour modéliser, à la fois l'instabilité non-linéaire de couhe mince et la structure à grande échelle, une telle simulation est un défi numérique, même en utilisant du raffinement adaptatif de maille.

Cette recherche s'est concentrée sur deux comportements limites: les vents isotherme et les vents adiabatiques alors qu'il est possible de tenir compte du refroidissement de façon plus réaliste. Cela permettrait améliorer la simulation de WR 104 et fournir des explications sur

la formation de poussières. Dans ce cas particulier, c'est la diffusion Compton inverse sur les photons de l'étoile O-B qui induit le refroidissement dominant à haute température. L'impact du refroidissement Compton inverse sur électrons thermiques n'a jamais été étudié dans les collision de vents et est susceptible d'être important pour les binaires composées d' étoiles de type O ou B. Pour l'étudier, il faudrait effectuer des simulations à trois dimensions ou bien utiliser un code à deux dimensions qui permet la modélisation de domaines sphériques qui modélise correctement l'évolution de la densité et de la température. Notre configuration actuelle à deux dimensions suppose une géométrie cylindrique qui n'est pas bien adaptée à l'étude du refroidissement car les variables y évoluent différemment que dans une géométrie sphérique.

Les simulations binaires γ n'en sont qu'à leurs premiers stades. Notre objectif final est d'obtenir une simulation d'une binaire γ à la plus grande échelle possible. Les questions auxquelles nous voulons répondre sont (parmi d'autres): Y at-il une structure spirale à grande échelle ? Le mélange dû aux instabilités est-il suffisamment important pour refroidir les particule accelérées et diminuer l'émission non-thermique? Quel est le facteur de Lorentz dans la structure choquée, peut-il engendrer des abérrations relativistes observables? A l'aide d'une simulation hydrodynamique relativiste d'une binaire γ, on pourra estimer l'émission à haute énergie due au refroidissement Compton près de la binaire. La modélisation de l'émission synchrotron plus loin de la binaire nécessite de connaître l'intensité du champ magnétique. Si l'on veut aller au-delà des hypothèses habituelles telles que l'équipartition, une simulation magnétohydrodynamique relativiste est nécessaire. Pour ce faire, nous pouvons choisir de modifier RAMSES ou bien utiliser un autre code.

Les binaires comme PSR B1259 -63 sont composées d'une étoile Be qui possède un vent équatorial dense et lent, en plus de son vent stellaire. Au cours des passages au périastre, le pulsar interagit avec ce disque, et forme sans doute une nouvelle zone de collision de vents. Des simulations, tenant compte de la présence du vent équatorial seront en mesure de déterminer sa structure exacte et peut-être expliquer les pics d'émission radio observés. Pour préparer ces simulations, j'ai déjà créé une configuration tridimensionnelle du vent de l'étoile Be qui modélise à la fois le vent équatorial et le vent isotrope. Elle permet de modéliser le pulsar sur une orbite excentrique et inclinée.

Nous avons effectué l'extension à l'hydrodynamique relativiste de RAMSES, un code largement utilisé en astrophysique. Le code que nous avons développé peut trouver son application dans la modélisation de nombreux écoulements relativistes en astrophysique. L'interaction des vents de pulsars avec les restes de supernovae ou le milieu interstellaire sont une extension naturelle des simulations présentées dans cette thèse. RAMSES pourrait également être utilisé pour modéliser des sursauts gamma ou des jets relativistes dans les microquasars ou les noyaux actifs de galaxies.

Appendices

Chapter A

2D analytic solution of the structure of colliding wind binaries

I determine the solution of the two winds interaction problem from Canto et al. [1996] in the 2D limit. The method is the same, only the geometry changes, and is shown on fig. A.1 In

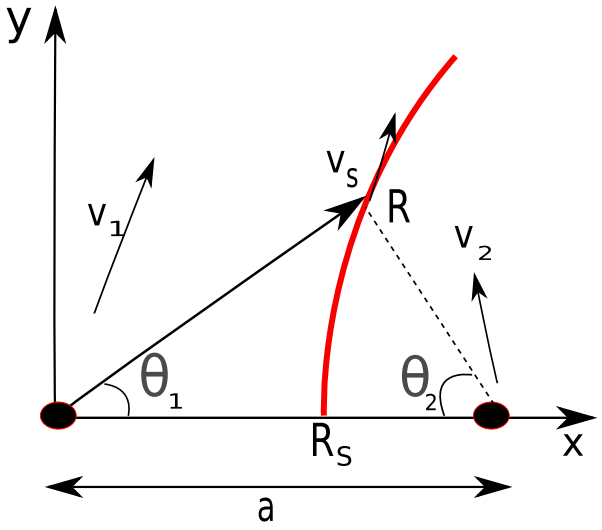

Figure A.1: Diagram of the two-wind interaction problem. The stars are the big dots, the interaction front R(θ_2) is shown with the thick red line.

order to compute the position of the interaction front $R(\theta_2)$, one needs to compute the mass and momentum (linear and angular) rates through the front. Each star has a total mass loss rate $\dot{M}$, a wind velocity v and a wind density ρ. I use subscript 1 for the star at $x = 0$, and subscript 2 for the star at $x = a$. The subscript s is used for the variables in the shocked region. For consistency with the rest of this thesis, I consider the star with the stronger wind as the first star. In Canto et al. [1996] the subscript 0 stands for the star with the stronger wind and the subscript 1 stands for the star with the weaker wind.

For 2D spherical winds, the mass loss rates through the opening angles θ_1 and θ_2 are

$$\dot{M}_1(\theta_1) = \frac{\dot{M}_1 \theta_1}{2\pi} \tag{A.1}$$

$$\dot{M}_2(\theta_2) = \frac{\dot{M}_2\theta_2}{2\pi}. \tag{A.2}$$

The momentum rates along the x and y direction through the angles θ_1 and θ_2 are given by

$$\begin{aligned} \Pi_{1x}(\theta_1) &= \int_0^{\theta_1} v_1 \cos\theta_1 d\dot{M}_1 \\ &= \frac{\dot{M}_1 v_1}{2\pi} \sin\theta_1 \qquad \text{and} \end{aligned} \tag{A.3}$$

$$\begin{aligned} \Pi_{2x}(\theta_2) &= -\int_0^{\theta_2} v_2 \cos\theta_2 d\dot{M}_2 \\ &= -\frac{\dot{M}_2 v_2}{2\pi} \sin\theta_2, \end{aligned} \tag{A.4}$$

and

$$\begin{aligned} \Pi_{1y}(\theta_1) &= \int_0^{\theta_1} v_1 \sin\theta_1 d\dot{M}_1 \\ &= \frac{\dot{M}_1 v_1}{2\pi}(1-\cos\theta_1) \qquad \text{and} \end{aligned} \tag{A.5}$$

$$\begin{aligned} \Pi_{2y}(\theta_2) &= \int_0^{\theta_2} v_2 \sin\theta_2 d\dot{M}_2 \\ &= \frac{\dot{M}_2 v_2}{2\pi}(1-\cos\theta_2). \end{aligned} \tag{A.6}$$

Finally the angular momentum is given by

$$J_1(\theta_1) = 0 \qquad \text{and} \tag{A.7}$$

$$\begin{aligned} J_2(\theta_2) &= a\Pi_{2x} \\ J_2(\theta_2) &= \frac{\dot{M}_2^0 v_2}{2\pi} a(1-\cos\theta_2). \end{aligned} \tag{A.8}$$

Eq. (6) in Canto et al. [1996] gives

$$R_S = \frac{J_1 + J_2}{(\Pi_{1y} + \Pi_{2y})\cos\theta_2 - (\Pi_{1x} - \Pi_{2x})\sin\theta_2}. \tag{A.9}$$

Replacing with Eq. A.3-A.8 gives

$$R_S = \frac{a\dot{M}_2 v_2(1-\cos\theta_2)}{(\dot{M}_1 v_1(1-\cos\theta_1) + \dot{M}_2 v_2(1-\cos\theta_2))\cos\theta_2 - (\dot{M}_1 v_1 \sin\theta_1 - \dot{M}_2 v_2 \sin\theta_2)\sin\theta_2}.$$

Eq. (23) of Canto et al. [1996] gives the geometric relation

$$R_S = a\frac{\sin\theta_1}{\sin(\theta_1+\theta_2)}, \tag{A.10}$$

so we get

$$\frac{\sin\theta_1}{\sin(\theta_1+\theta_2)} = \frac{\dot{M}_2 v_2(1-\cos\theta_2)}{(\dot{M}_1 v_1(1-\cos\theta_1) + \dot{M}_2 v_2(1-\cos\theta_2))\cos\theta_2 - (\dot{M}_1 v_1 \sin\theta_1 - \dot{M}_2 v_2 \sin\theta_2)\sin\theta_2}. \tag{A.11}$$

Dividing by $\dot{M}_2 v_2$ and writing $\eta = \dot{M}_2 v_2 / \dot{M}_1 v_1$ one gets

$$\frac{\sin\theta_1}{\sin(\theta_1+\theta_2)} = \frac{1-\cos\theta_2}{(1/\eta(1-\cos\theta_1)+(1-\cos\theta_2))\cos\theta_2 - (1/\eta\sin\theta_1 - \sin\theta_2)\sin\theta_2}. \tag{A.12}$$

Which gives

$$(\cos\theta_2\sin\theta_1 - \cos^2\theta_2\sin\theta_1 - \sin^2\theta_2\sin\theta_1) = \tag{A.13}$$

$$\eta(-\sin\theta_1\cos\theta_2(1-\cos\theta_2) - \sin\theta_2\sin^2\theta_1 + (1-\cos\theta_2)\sin(\theta_1+\theta_2)). \tag{A.14}$$

Using $\sin(a+b) = \sin a\cos b + \sin b\cos a$ one gets

$$(\cos\theta_2\sin\theta_1 - \sin\theta_1) = \eta(-\sin\theta_2\sin^2\theta_1 + \sin\theta_2\cos\theta_1 - \cos^2\theta_1\sin\theta_2). \tag{A.15}$$

Dividing by $\sin\theta_2\sin\theta_1$ gives the implicit equation of the position of the shell

$$\frac{\cos\theta_2 - 1}{\sin\theta_2} = \eta\frac{\cos\theta_1 - 1}{\sin\theta_1} \tag{A.16}$$

One can deduce the velocity of the flow in the shell $\vec{v_s} = v_{sx}\hat{x} + v_{sy}\hat{y}$ using Eq. (5a) from Canto et al. [1996]

$$\dot{M}(v_{sx}\hat{x} + v_{sy}\hat{y}) = (\Pi_{1x} + \Pi_{2x})\hat{x} + (\Pi_{1y} + \Pi_{2y})\hat{y}, \tag{A.17}$$

where $\dot{M}$ is the sum of the mass loss rates of both winds. We thus get

$$\begin{aligned} v_s &= \frac{1}{\dot{M}}[(\Pi_{1x}+\Pi_{2x})^2 + (\Pi_{1y}+\Pi_{2y})^2]^{1/2} \\ &= \frac{[(\sin\theta_1 - \eta\sin\theta_2)^2 + ((1-\cos\theta_1) + \eta(1-\cos\theta_2))^2]^{1/2}}{1/(v_1\theta_1) + \eta/(v_2\theta_2)}. \end{aligned} \tag{A.18}$$

Thus we have

$$\frac{v_s}{v_2} = [((1-\cos\theta_1) + \eta(1-\cos\theta_2))^2 + (\sin\theta_1 - \eta\sin\theta_2)^2]^{1/2}\frac{\theta_2\alpha + \theta_1\eta}{\theta_1\theta_2}, \tag{A.19}$$

where $\alpha = v_2/v_1$

Similarly, one can determine the linear density along the shell

$$\mu = \frac{\dot{M}}{v_s\theta_2}. \tag{A.20}$$

Using Eq. A.19 we have

$$\begin{aligned} \mu &= \frac{\dot{M}^2}{[(\Pi_{1x}+\Pi_{2x})^2 + (\Pi_{1y}+\Pi_{2y})^2]\theta_2} \\ &= \frac{\dot{M}_1 v_1 (v_1\theta_1 + v_2\theta_2)^2}{\theta_2[((1-\cos\theta_1) + \eta(1-\cos\theta_2))^2 + (\sin\theta_1 - \eta\sin\theta_2)^2]^{1/2}} \\ &= \frac{\dot{M}_1}{v_1}\frac{1}{\theta_2((1-\cos\theta_1) + \eta(1-\cos\theta_2))^2 + (\sin\theta_1 - \eta\sin\theta_2)^2]^{1/2}}. \end{aligned} \tag{A.21}$$

Chapter B

Jacobian matrices for 3D relativistic hydrodynamics

This Appendix provides the Jacobian matrices for the reconstruction of the primitive variables in the 3D-RHD case (§5.1.4). One has

$$\partial \mathbf{q} = -(\mathbf{A}^0)^{-1}\mathbf{A}^1\frac{\partial \mathbf{q}}{\partial x}dt - (\mathbf{A}^0)^{-1}\mathbf{A}^2\frac{\partial \mathbf{q}}{\partial y}dt - (\mathbf{A}^0)^{-1}\mathbf{A}^3\frac{\partial \mathbf{q}}{\partial z}dt. \tag{B.1}$$

Following Font et al. [1994] for a 1D flow with transverse velocity and the general definition of the enthalpy

$$\frac{\partial h}{\partial x} = \frac{\partial h}{\partial \rho}\frac{\partial \rho}{\partial x} + \frac{\partial h}{\partial P}\frac{\partial P}{\partial x} \tag{B.2}$$

$$\frac{\partial h}{\partial x} = \chi\frac{\partial \rho}{\partial x} + \kappa\frac{\partial P}{\partial x}. \tag{B.3}$$

$$\tag{B.4}$$

I find $\mathbf{A^0} = \partial \mathbf{U}/\partial \mathbf{q}$ that is given by

$$\mathbf{A^0}(\mathbf{q}) = \begin{pmatrix} \Gamma & \rho\Gamma^3 v_x & \rho\Gamma^3 v_y & \rho\Gamma^3 v_z & 0 \\ \Gamma^2 v_x(h+\rho\chi) & \rho h\Gamma^2(1+2\Gamma^2 v_x^2) & 2\rho h\Gamma^4 v_x v_y & 2\rho h\Gamma^4 v_x v_z & \Gamma^2 v_x \rho\kappa \\ \Gamma^2 v_y(h+\rho\chi) & 2\rho h\Gamma^4 v_x v_y & \rho h\Gamma^2(1+2\Gamma^2 v_y^2) & 2\rho h\Gamma^4 v_y v_z & \Gamma^2 v_y \rho\kappa \\ \Gamma^2 v_z(h+\rho\chi) & 2\rho h\Gamma^4\ v_x v_z & 2\rho h\Gamma^4 v_y v_z & \rho h\Gamma^2(1+2\Gamma^2 v_z^2) & \Gamma^2 v_z \rho\kappa \\ \Gamma^2(h+\rho\chi) & 2\rho h\Gamma^4 v_x & 2\rho h\Gamma^4 v_y & 2\rho h\Gamma^4 v_z & \rho\kappa\Gamma^2 - 1 \end{pmatrix} \tag{B.5}$$

and $\mathbf{A}^1$ is given by

$$\mathbf{A^1}(\mathbf{q}) = \begin{pmatrix} \Gamma v_x & \rho\Gamma(1+\Gamma^2 v_x^2) & \rho\Gamma^3 v_x v_y & \rho\Gamma^3 v_x v_z & 0 \\ \Gamma^2 v_x^2(h+\rho\chi) & 2\rho h\Gamma^2 v_x(1+\Gamma^2 v_x^2) & 2\rho h\Gamma^4 v_x^2 v_y & 2\rho h\Gamma^4 v_x^2 v_z & \Gamma^2 v_x^2\rho\kappa + 1 \\ \Gamma^2 v_x v_y(h+\rho\chi) & \rho h\Gamma^2 v_y(1+2\Gamma^2 v_x^2) & \rho h\Gamma^2 v_x(1+2\Gamma^2 v_y^2) & 2\rho h\Gamma^4 v_x v_y v_z & \rho\kappa\Gamma^2 v_x v_y \\ \Gamma^2 v_x v_z(h+\rho\chi) & \rho h\Gamma^2 v_z(1+2\Gamma^2 v_x^2) & 2\rho h\Gamma^4 v_x v_y v_z & \rho h\Gamma^2 v_x(1+2\Gamma^2 v_z^2) & \rho\kappa\Gamma^2 v_x v_z \\ \Gamma^2 v_x(h+\rho\chi) & \rho h\Gamma^2(1+2\Gamma^2 v_x^2) & 2\rho h\Gamma^4 v_x v_y & 2\rho h\Gamma^4 v_x v_z & \rho\kappa\Gamma^2 v_x \end{pmatrix} \tag{B.6}$$

$\mathbf{A}^2$ is given by

$$\mathbf{A^2(q)} = \begin{pmatrix} \Gamma v_y & \rho\Gamma^3 v_x v_y & \rho\Gamma(1+\Gamma^2 v_y^2) & \rho\Gamma^3 v_y v_z & 0 \\ \Gamma^2 v_x v_y(h+\rho\chi) & \rho h\Gamma^2 v_y(1+\Gamma^2 v_x^2) & \rho h\Gamma^2 v_x(1+2\Gamma^2 v_y^2) & 2\rho h\Gamma^4 v_x v_y v_z & \rho\kappa\Gamma^2 v_x v_y \\ \Gamma^2 v_y^2(h+\rho\chi) & 2\rho h\Gamma^4 v_x v_y^2 & 2\rho h\Gamma^2 v_y(1+2\Gamma^2 v_y^2) & 2\rho h\Gamma^4 v_y^2 v_z & \Gamma^2 v_y^2\rho\kappa+1 \\ \Gamma^2 v_y v_z(h+\rho\chi) & 2\rho h\Gamma^2 v_x v_y v_z & \rho h\Gamma^2 v_z(1+2\Gamma^2 v_y^2) & \rho h\Gamma^2 v_y(1+2\Gamma^2 v_z^2) & \rho\kappa\Gamma^2 v_y v_z \\ \Gamma^2 v_y(h+\rho\chi) & 2\rho h\Gamma^4 v_x v_y & \rho h\Gamma^2(1+2\Gamma^2 v_y^2) & 2\rho h\Gamma^4 v_y v_z & \rho\kappa\Gamma^2 v_y \end{pmatrix} \tag{B.7}$$

$\mathbf{A}^3$ is given by

$$\mathbf{A^3(q)} = \begin{pmatrix} \Gamma v_z & \rho\Gamma^3 v_x v_z & \rho\Gamma^3 v_y v_z & \rho\Gamma(1+\Gamma^2 v_z^2) & 0 \\ \Gamma^2 v_x v_z(h+\rho\chi) & \rho h\Gamma^2 v_z(1+2\Gamma^2 v_x^2) & 2\rho h\Gamma^4 v_x v_y v_z & \rho h\Gamma^2 v_x(1+2\Gamma^2 v_z^2) & \rho\kappa\Gamma^2 v_x v_z \\ \Gamma^2 v_y v_z(h+\rho\chi) & 2\rho h\Gamma^4 v_x v_y v_z & \rho h\Gamma^2 v_z(1+2\Gamma^2 v_y^2) & \rho h\Gamma^4 v_z(1+2\Gamma^2 v_y^2) & \rho\kappa\Gamma^2 v_y v_z \\ \Gamma^2 v_z^2(h+\rho\chi) & 2\rho h\Gamma^2 v_x v_z^2 & 2\rho h\Gamma^2 v_y v_z & 2\rho h\Gamma^2 v_z(1+2\Gamma^2 v_z^2) & \Gamma^2 v_z^2\rho\kappa+1 \\ \Gamma^2 v_z(h+\rho\chi) & 2\rho h\Gamma^4 v_x v_z & 2\rho h\Gamma^4 v_y v_z & \rho h\Gamma^2(1+2\Gamma^2 v_z^2) & \rho\kappa\Gamma^2 v_z \end{pmatrix} \tag{B.8}$$

The complete Jacobian matrix $\mathbf{A_1}$ is given by

$$\begin{aligned}
Nc_{11} &= v_x N && \text{(B.9)}\\
Nc_{12} &= \rho h\Gamma^2(\rho\kappa - 1) && \text{(B.10)}\\
Nc_{13} &= 0 && \text{(B.11)}\\
Nc_{14} &= 0 && \text{(B.12)}\\
Nc_{15} &= v_x(-\rho\kappa\Gamma^2 + \rho\kappa v^2\Gamma^2 + 1) && \text{(B.13)}\\
Nc_{21} &= 0 && \text{(B.14)}\\
Nc_{22} &= v_x\Gamma^2(\rho h\kappa - h + \rho\chi) && \text{(B.15)}\\
Nc_{23} &= 0 && \text{(B.16)}\\
Nc_{24} &= 0 && \text{(B.17)}\\
Nc_{25} &= \frac{1}{\rho h\Gamma^2}(\rho h\Gamma^2\kappa - \rho h\kappa\Gamma^2 v_x^2 - h - h\Gamma^2(v_y^2+v_z^2) + \rho\chi\Gamma^2(v_y^2+v_z^2)) && \text{(B.18)}\\
Nc_{31} &= 0 && \text{(B.19)}\\
Nc_{32} &= v_y\rho\chi && \text{(B.20)}\\
Nc_{33} &= v_x N && \text{(B.21)}\\
Nc_{34} &= 0 && \text{(B.22)}\\
Nc_{35} &= -\frac{v_x v_y(-h+\rho\chi+\rho h\kappa)}{\rho h} && \text{(B.23)}\\
Nc_{41} &= 0 && \text{(B.24)}\\
Nc_{42} &= v_z\rho\chi && \text{(B.25)}\\
Nc_{43} &= 0 && \text{(B.26)}\\
Nc_{44} &= v_x N && \text{(B.27)}\\
Nc_{45} &= -\frac{v_x v_z(-h+\rho\chi+\rho h\kappa)}{\rho h} && \text{(B.28)}\\
Nc_{51} &= 0 && \text{(B.29)}\\
Nc_{52} &= -\rho^2 h\Gamma^2\chi && \text{(B.30)}\\
Nc_{53} &= 0 && \text{(B.31)}\\
Nc_{54} &= 0 && \text{(B.32)}\\
Nc_{55} &= v_x N && \text{(B.33)}
\end{aligned}$$

with $N = (-h + h\rho\kappa + \rho\chi v^2)\Gamma^2$

The matrix $\mathbf{A}_2$ along the y direction is given by

$$
\begin{aligned}
Nc_{11} &= v_y N && \text{(B.34)}\\
Nc_{12} &= 0 && \text{(B.35)}\\
Nc_{13} &= 0 && \text{(B.36)}\\
Nc_{14} &= 0 && \text{(B.37)}\\
Nc_{15} &= v_y(-\rho\kappa\Gamma^2 + \rho\kappa\Gamma^2 v^2 + 1) && \text{(B.38)}\\
Nc_{21} &= 0 && \text{(B.39)}\\
Nc_{22} &= v_y N && \text{(B.40)}\\
Nc_{23} &= v_x\rho\chi && \text{(B.41)}\\
Nc_{24} &= 0 && \text{(B.42)}\\
Nc_{25} &= -(v_x v_y(-h + \rho\chi + h\rho\kappa)) && \text{(B.43)}\\
Nc_{31} &= 0 && \text{(B.44)}\\
Nc_{32} &= 0 && \text{(B.45)}\\
Nc_{33} &= v_y N && \text{(B.46)}\\
Nc_{34} &= 0 && \text{(B.47)}\\
Nc_{35} &= \frac{1}{\rho h\Gamma^2}(\rho h\Gamma^2\kappa - \rho h\kappa\Gamma^2 v_y^2 - h - h\Gamma^2(v_x^2 + v_z^2) + \rho\chi\Gamma^2(v_x^2 + v_z^2)) && \text{(B.48)}\\
Nc_{41} &= 0 && \text{(B.49)}\\
Nc_{42} &= 0 && \text{(B.50)}\\
Nc_{43} &= v_z\rho\chi && \text{(B.51)}\\
Nc_{44} &= v_y N && \text{(B.52)}\\
Nc_{45} &= \frac{-(v_x v_z(-h + \rho\chi + \rho h\kappa)}{\rho h} && \text{(B.53)}\\
Nc_{51} &= 0 && \text{(B.54)}\\
Nc_{52} &= 0 && \text{(B.55)}\\
Nc_{53} &= -\rho^2 h\Gamma^2\chi && \text{(B.56)}\\
Nc_{54} &= 0 && \text{(B.57)}\\
Nc_{55} &= v_y N && \text{(B.58)}
\end{aligned}
$$

and along z one has A_3 given by

$$
\begin{aligned}
Nc_{11} &= v_z N && \text{(B.59)}\\
Nc_{12} &= 0 && \text{(B.60)}\\
Nc_{13} &= 0 && \text{(B.61)}\\
Nc_{14} &= h\rho\Gamma^2(\rho\kappa - 1) && \text{(B.62)}\\
Nc_{15} &= v_z(-\rho\Gamma^2\kappa + \rho v^2\Gamma^2\kappa + 1) && \text{(B.63)}\\
Nc_{21} &= 0 && \text{(B.64)}\\
Nc_{22} &= v_z N && \text{(B.65)}\\
Nc_{23} &= 0 && \text{(B.66)}\\
Nc_{24} &= v_z\rho\chi && \text{(B.67)}\\
Nc_{25} &= \frac{-(v_x v_z(-h + \rho\chi + \rho h\kappa)}{\rho h} && \text{(B.68)}
\end{aligned}
$$

$$Nc_{31} = 0 \tag{B.69}$$
$$Nc_{32} = 0 \tag{B.70}$$
$$Nc_{33} = v_z N \tag{B.71}$$
$$Nc_{34} = v_y \rho \chi \tag{B.72}$$
$$Nc_{35} = \frac{-(v_y v_z(-h + \rho\chi + \rho h\kappa)}{\rho h} \tag{B.73}$$
$$Nc_{41} = 0 \tag{B.74}$$
$$Nc_{42} = 0 \tag{B.75}$$
$$Nc_{43} = 0 \tag{B.76}$$
$$Nc_{44} = v_z N \tag{B.77}$$
$$Nc_{45} = \frac{1}{\rho h \Gamma^2}(\rho h \Gamma^2 \kappa - \rho h \kappa \Gamma^2 v_z^2 - h - h\Gamma^2(v_x^2 + v_y^2) + \rho\chi\Gamma^2(v_x^2 + v_y^2)) \tag{B.78}$$
$$Nc_{51} = 0 \tag{B.79}$$
$$Nc_{52} = 0 \tag{B.80}$$
$$Nc_{53} = 0 \tag{B.81}$$
$$Nc_{54} = -\rho^2 h \Gamma^2 \chi \tag{B.82}$$
$$Nc_{55} = v_z N \tag{B.83}$$

Bibliography

D. C. Abbott. The theory of radiatively driven stellar winds. II - The line acceleration. ApJ, 259:282–301, August 1982a. doi: 10.1086/160166.

D. C. Abbott. The return of mass and energy to the interstellar medium by winds from early-type stars. ApJ, 263:723–735, December 1982b. doi: 10.1086/160544.

D. C. Abbott, J. H. Beiging, E. Churchwell, and A. V. Torres. Radio emission from galactic Wolf-Rayet stars and the structure of Wolf-Rayet winds. ApJ, 303:239–261, April 1986. doi: 10.1086/164070.

A. A. Abdo and Fermi collaboration. Fermi LAT Observations of LS I +61 303: First Detection of an Orbital Modulation in GeV Gamma Rays. ApJ, 701:L123–L128, August 2009. doi: 10.1088/0004-637X/701/2/L123.

A. A. Abdo and Fermi collaboration. Fermi Large Area Telescope Observation of a Gamma-ray Source at the Position of Eta Carinae. ApJ, 723:649–657, November 2010. doi: 10.1088/0004-637X/723/1/649.

A. A. Abdo and Fermi collaboration. Discovery of High-energy Gamma-ray Emission from the Binary System PSR B1259-63/LS 2883 around Periastron with Fermi. ApJ, 736:L11, July 2011. doi: 10.1088/2041-8205/736/1/L11.

A.A. Abdo and Fermi Collaboration. Fermi-LAT observations of LS 5039. ApJ, 706:L56–L61, November 2009. doi: 10.1088/0004-637X/706/1/L56.

F. Aharonian and HEGRA Collaboration. An unidentified TeV source in the vicinity of Cygnus OB2. A&A, 393:L37–L40, October 2002. doi: 10.1051/0004-6361:20021171.

F. Aharonian and HESS collaboration. 3.9 day orbital modulation in the TeV γ-ray flux and spectrum from the X-ray binary LS 5039. A&A, 460:743–749, December 2006. doi: 10.1051/0004-6361:20065940.

F. Aharonian and HESS collaboration. Very high energy γ-ray observations of the binary PSR B1259-63/SS2883 around the 2007 Periastron. A&A, 507:389–396, November 2009. doi: 10.1051/0004-6361/200912339.

J. Albert and MAGIC collaboration. Variable Very-High-Energy Gamma-Ray Emission from the Microquasar LS I +61 303. *Science*, 312:1771–1773, June 2006. doi: 10.1126/science.1128177.

O. V. Aleksandrova and K. V. Bychkov. Dust Formation in Binaries with OB and WR Components in a Two-Phase Stellar-Wind Model. *Astronomy Reports*, 45:281–286, April 2001. doi: 10.1134/1.1361319.

D. A. Allen, J. P. Swings, and P. M. Harvey. Infrared photometry of northern Wolf-Rayet stars. A&A, 20:333–336, 1972.

J.M Aloy, M.A.and Ibanez and E. Marti, J.M.and Müller. GENESIS: a high resolution code for multidimensionnal relativistic hydrodynamics. ApJS, 122:151, 1999.

I. I. Antokhin, S. P. Owocki, and J. C. Brown. A Steady, Radiative-Shock Method for Computing X-Ray Emission from Colliding Stellar Winds in Close, Massive-Star Binaries. ApJ, 611:434–451, August 2004. doi: 10.1086/422093.

J. Arons and M. Tavani. High-energy emission from the eclipsing millisecond pulsar PSR 1957+20. ApJ, 403:249–255, January 1993. doi: 10.1086/172198.

L. H. Auer and G. Koenigsberger. Line profiles variations from atmospheric eclipses: Constraints on the wind structure in Wolf-Rayet stars. ApJ, 436:859–870, December 1994. doi: 10.1086/174963.

S. A. Balbus and J. F. Hawley. A powerful local shear instability in weakly magnetized disks. I - Linear analysis. II - Nonlinear evolution. ApJ, 376:214–233, July 1991. doi: 10.1086/170270.

V. B. Baranov, K. V. Krasnobaev, and A. G. Kulikovskii. A Model of the Interaction of the Solar Wind with the Interstellar Medium. *Soviet Physics Doklady*, 15:791, March 1971.

C. S. Beals. On the nature of Wolf-Rayet emission. MNRAS, 90:202–212, December 1929.

K. Beckwith and J. M. Stone. A Second-order Godunov Method for Multi-dimensional Relativistic Magnetohydrodynamics. ApJS, 193:6, March 2011. doi: 10.1088/0067-0049/193/1/6.

A. R. Bell. The acceleration of cosmic rays in shock fronts. I. MNRAS, 182:147–156, January 1978.

P. Benaglia, C. E. Cappa, and B. S. Koribalski. Mass loss rate determination of southern OB stars. A&A, 372:952–962, June 2001. doi: 10.1051/0004-6361:20010617.

M. J. Berger and P. Colella. Local adaptive mesh refinement for shock hydrodynamics. *Journal of Computational Physics*, 1989.

M. J. Berger and J. Oliger. Adaptive mesh refinement for hyperbolic partial differential equations. *Journal of Computational Physics*, 1984.

J.P. Bernstein and P.A. Hughes. Refining a relativistic, hydrodynamic solver: Admitting ultra-relativistic flows. *Journal of Computational Physics*, 228:6212 – 6230, September 2009. doi: DOI: 10.1016/j.jcp.2009.05.012.

X.-J. Bi, T.-L. Chen, Y. Wang, and Q. Yuan. The Diffuse GeV-TeV γ-Ray Emission of the Cygnus Region. ApJ, 695:883–887, April 2009. doi: 10.1088/0004-637X/695/2/883.

J. H. Bieging, D. C. Abbott, and E. B. Churchwell. Mass loss rates for Wolf-Rayet stars from radio continuum observations. ApJ, 263:207–214, December 1982. doi: 10.1086/160495.

J. H. Bieging, D. C. Abbott, and E. B. Churchwell. A survey of radio emission from Galactic OB stars. ApJ, 340:518–536, May 1989. doi: 10.1086/167414.

R. D. Blandford and C. F. McKee. Fluid dynamics of relativistic blast waves. *Physics of Fluids*, 19:1130–1138, August 1976. doi: 10.1063/1.861619.

R. D. Blandford and J. E. Pringle. Kelvin-Helmholtz instability of relativistic beams. MNRAS, 176:443–454, August 1976.

J. M. Blondin and J. F. Koerwer. Instability of isothermal stellar wind bowshocks. *New Astronomy*, 3:571–582, December 1998. doi: 10.1016/S1384-1076(98)00028-1.

J. M. Blondin and B. S. Marks. Evolution of cold shock-bounded slabs. *New Astronomy*, 1: 235–244, November 1996. doi: 10.1016/S1384-1076(96)00019-X.

G. Bodo, A. Mignone, and R. Rosner. Kelvin-Helmholtz instability for relativistic fluids. Phys. Rev. E, 70(3):036304, September 2004. doi: 10.1103/PhysRevE.70.036304.

S. Bogovalov and K. Tsinganos. Shock formation at the magnetic collimation of relativistic jets. MNRAS, 357:918–928, March 2005. doi: 10.1111/j.1365-2966.2005.08671.x.

S. V. Bogovalov, V. M. Chechetkin, A. V. Koldoba, and G. V. Ustyugova. Interaction of pulsar winds with interstellar medium: numerical simulation. MNRAS, 358:705–715, April 2005. doi: 10.1111/j.1365-2966.2004.08592.x.

S. V. Bogovalov, D. V. Khangulyan, A. V. Koldoba, G. V. Ustyugova, and F. A. Aharonian. Modelling interaction of relativistic and non-relativistic winds in binary system PSR B1259-63/SS2883 - I. Hydrodynamical limit. MNRAS, 387:63–72, June 2008. doi: 10.1111/j.1365-2966.2008.13226.x.

S. V. Bogovalov, D. Khangulyan, A. V. Koldoba, G. V. Ustyugova, and F. A. Aharonian. Modelling the interaction between relativistic and non-relativistic winds in the binary system PSR B1259-63/SS2883- II. Impact of the magnetization and anisotropy of the pulsar wind. MNRAS, 419:3426–3432, February 2012. doi: 10.1111/j.1365-2966.2011.19983.x.

V. Bosch-Ramon and M. V. Barkov. Large-scale flow dynamics and radiation in pulsar γ-ray binaries. A&A, 535:A20, November 2011. doi: 10.1051/0004-6361/201117235.

V. Bosch-Ramon, M. V. Barkov, D. Khangulyan, and M. Perucho. Simulations of stellar/pulsar wind interaction along one full orbit. *ArXiv e-prints*, March 2012.

A. Brandenburg and W. Dobler. Hydromagnetic turbulence in computer simulations. *Computer Physics Communications*, 147:471–475, August 2002. doi: 10.1016/S0010-4655(02)00334-X.

F. Brighenti and A. D'Ercole. Evolution of WR ring nebulae generated by a moving central star - II. The influence of the red supergiant bow shock. MNRAS, 277:53–69, November 1995.

N. Bucciantini. Pulsar bow-shock nebulae. II. Hydrodynamical simulation. A&A, 387:1066–1073, June 2002. doi: 10.1051/0004-6361:20020495.

N. Bucciantini, J. M. Blondin, L. Del Zanna, and E. Amato. Spherically symmetric relativistic MHD simulations of pulsar wind nebulae in supernova remnants. A&A, 405:617–626, July 2003. doi: 10.1051/0004-6361:20030624.

N. Bucciantini, E. Amato, and L. Del Zanna. Relativistic MHD simulations of pulsar bow-shock nebulae. A&A, 434:189–199, April 2005. doi: 10.1051/0004-6361:20042205.

J. Canto, A. C. Raga, and F. P. Wilkin. Exact, Algebraic Solutions of the Thin-Shell Two-Wind Interaction Problem. ApJ, 469:729–+, October 1996. doi: 10.1086/177820.

A. C. Carciofi. The circumstellar discs of Be stars. In C. Neiner, G. Wade, G. Meynet, & G. Peters, editor, *IAU Symposium*, volume 272 of *IAU Symposium*, pages 325–336, July 2011. doi: 10.1017/S1743921311010738.

J. I. Castor, D. C. Abbott, and R. I. Klein. Radiation-driven winds in Of stars. ApJ, 195: 157–174, January 1975. doi: 10.1086/153315.

B. Cerutti, G. Dubus, and G. Henri. Spectral signature of a free pulsar wind in the gamma-ray binaries LS 5039 and LSI +61 303. A&A, 488:37–46, September 2008. doi: 10.1051/0004-6361:200809939.

S. Chandrasekhar. On the hypothesis of the radial ejection of high-speed atoms for the Wolf-Rayet stars and the novae. MNRAS, 94:522–538, April 1934.

S. Chandrasekhar. *Hydrodynamic and hydromagnetic stability*. 1961.

S. Chatterjee and J. M. Cordes. Bow Shocks from Neutron Stars: Scaling Laws and Hubble Space Telescope Observations of the Guitar Nebula. ApJ, 575:407–418, August 2002. doi: 10.1086/341139.

W. Chen, R. L. White, and D. Bertsch. Possible detection of π^0-decay γ-ray emission from CYG OB2 by EGRET. A&AS, 120:C423, December 1996.

I. Cherchneff and A. G. G. M. Tielens. Dust formation in hot stellar winds (Invited). In K. A. van der Hucht & P. M. Williams, editor, *Wolf-Rayet Stars: Binaries; Colliding Winds; Evolution*, volume 163 of *IAU Symposium*, page 346, 1995.

I. Cherchneff, Y. H. Le Teuff, P. M. Williams, and A. G. G. M. Tielens. Dust formation in carbon-rich Wolf-Rayet stars. I. Chemistry of small carbon clusters and silicon species. A&A, 357:572–580, May 2000.

A. M. Cherepashchuk. Detectability of Wolf-Rayet binaries from X rays. *Soviet Astronomy Letters*, 2:138, August 1976.

R. A. Chevalier and J. N. Imamura. Linear analysis of an oscillatory instability of radiative shock waves. ApJ, 261:543–549, October 1982. doi: 10.1086/160364.

T. Chlebowski and C. D. Garmany. On winds and X-rays of O-type stars. ApJ, 368:241–251, February 1991. doi: 10.1086/169687.

O. Cohen, V. L. Kashyap, J. J. Drake, I. V. Sokolov, C. Garraffo, and T. I. Gombosi. The Dynamics of Stellar Coronae Harboring Hot Jupiters. I. A Time-dependent Magnetohydrodynamic Simulation of the Interplanetary Environment in the HD 189733 Planetary System. ApJ, 733:67, May 2011a. doi: 10.1088/0004-637X/733/1/67.

O. Cohen, V. L. Kashyap, J. J. Drake, I. V. Sokolov, and T. I. Gombosi. The Dynamics of Stellar Coronae Harboring Hot Jupiters. II. A Space Weather Event on a Hot Jupiter. ApJ, 738:166, September 2011b. doi: 10.1088/0004-637X/738/2/166.

B. Commerçon, P. Hennebelle, E. Audit, G. Chabrier, and R. Teyssier. Protostellar collapse: a comparison between smoothed particle hydrodynamics and adaptative mesh refinement calculations. A&A, 482:371–385, April 2008. doi: 10.1051/0004-6361:20078591.

B. Commerçon, P. Hennebelle, and T. Henning. Collapse of Massive Magnetized Dense Cores Using Radiation Magnetohydrodynamics: Early Fragmentation Inhibition. ApJ, 742:L9, November 2011. doi: 10.1088/2041-8205/742/1/L9.

R. H. D. Corbet, C. C. Cheung, M. Kerr, R. Dubois, D. Donato, G. A. Caliandro, M. J. Coe, P. G. Edwards, M. D. Filipovic, J. L. Payne, and J. Stevens. 1FGL J1018.6-5856: a New Gamma-ray Binary. *The Astronomer's Telegram*, 3221:1, March 2011.

R. Courant, K. Friedrichs, and H. Lewy. Über die partiellen Differenzengleichungen der mathematischen Physik. *Mathematische Annalen*, 100:32–74, 1928. doi: 10.1007/BF01448839.

N. L. J. Cox, F. Kerschbaum, A.-J. van Marle, L. Decin, D. Ladjal, A. Mayer, M. A. T. Groenewegen, S. van Eck, P. Royer, R. Ottensamer, T. Ueta, A. Jorissen, M. Mecina, Z. Meliani, A. Luntzer, J. A. D. L. Blommaert, T. Posch, and B. Vandenbussche. A far-infrared survey of bow shocks and detached shells around AGB stars and red supergiants. A&A, 537:A35, January 2012. doi: 10.1051/0004-6361/201117910.

S. R. Cranmer and S. P. Owocki. Hydrodynamical Simulations of Corotating Interaction Regions and Discrete Absorption Components in Rotating O-Star Winds. ApJ, 462:469, May 1996. doi: 10.1086/177166.

P. A. Crowther. Remarkable spectral variability in WR 104 (WC9): dust condensation in a hostile environment? MNRAS, 290:L59–L63, September 1997.

P. A. Crowther. Physical Properties of Wolf-Rayet Stars. ARA&A, 45:177–219, September 2007. doi: 10.1146/annurev.astro.45.051806.110615.

P. A. Crowther, D. J. Hillier, and L. J. Smith. Fundamental parameters of Wolf-Rayet stars. II. Tailored analyses of Galactic WNL stars. A&A, 293:403–426, January 1995a.

P. A. Crowther, L. J. Smith, D. J. Hillier, and W. Schmutz. Fundamental parameters of Wolf-Rayet stars. III. The evolutionary status of WNL stars. A&A, 293:427–445, January 1995b.

M. De Becker. Non-thermal emission processes in massive binaries. A&A Rev., 14:171–216, November 2007. doi: 10.1007/s00159-007-0005-2.

M. De Becker, G. Rauw, R. Blomme, W. L. Waldron, H. Sana, J. M. Pittard, P. Eenens, I. R. Stevens, M. C. Runacres, S. Van Loo, and A. M. T. Pollock. Quasi-simultaneous XMM-Newton and VLA observation of the non-thermal radio emitter HD 168112 (O5.5III(f^+)). A&A, 420: 1061–1077, June 2004. doi: 10.1051/0004-6361:20041030-1.

L. Del Zanna and N. Bucciantini. An efficient shock-capturing central-type scheme for multidimensional relativistic flows. I. Hydrodynamics. A&A, 390:1177–1186, August 2002. doi: 10.1051/0004-6361:20020776.

R. Dgani. 3D stability analysis of colliding winds in a double star system. A&A, 271:527–+, April 1993.

R. Dgani, R. Walder, and H. Nussbaumer. Stability analysis of colliding winds in a double star system. A&A, 267:155–160, January 1993.

R. Dgani, D. van Buren, and A. Noriega-Crespo. The Transverse Acceleration Instability for Bow Shocks in the Nonlinear Regime. ApJ, 461:372–+, April 1996a. doi: 10.1086/177065.

R. Dgani, D. van Buren, and A. Noriega-Crespo. Stability Analysis of Bow Shocks. ApJ, 461: 927–+, April 1996b. doi: 10.1086/177114.

V. Dhawan, A. Mioduszewski, and M. Rupen. LS I +61 303 is a Be-Pulsar binary, not a Microquasar. In *VI Microquasar Workshop: Microquasars and Beyond*, 2006.

S. M. Dougherty and P. M. Williams. Non-thermal emission in Wolf-Rayet stars: are massive companions required? MNRAS, 319:1005–1010, December 2000. doi: 10.1046/j.1365-8711.2000.03837.x.

S. M. Dougherty, J. M. Pittard, L. Kasian, R. F. Coker, P. M. Williams, and H. M. Lloyd. Radio emission models of colliding-wind binary systems. A&A, 409:217–233, October 2003. doi: 10.1051/0004-6361:20031048.

G. Dubus. Gamma-ray binaries: pulsars in disguise? A&A, 456:801–817, September 2006. doi: 10.1051/0004-6361:20054779.

G. Dubus, B. Cerutti, and G. Henri. The modulation of the gamma-ray emission from the binary LS 5039. A&A, 477:691–700, January 2008. doi: 10.1051/0004-6361:20078261.

P. C. Duffell and A. I. MacFadyen. TESS: A Relativistic Hydrodynamics Code on a Moving Voronoi Mesh. ApJS, 197:15, December 2011. doi: 10.1088/0067-0049/197/2/15.

J. E. Dyson. Stellar winds and globules in H II regions. Ap&SS, 35:299–312, July 1975. doi: 10.1007/BF00636999.

J. E. Dyson, T. W. Hartquist, and S. Biro. Mass-loaded astronomical flows. V - Tails: Intermediate-scale structures in flowing clumpy media. MNRAS, 261:430–434, March 1993.

D. Eichler and V. Usov. Particle acceleration and nonthermal radio emission in binaries of early-type stars. ApJ, 402:271–279, January 1993. doi: 10.1086/172130.

B. Einfeldt. On Godunov-type methods for gas dynamics. *SIAM J. Numer. Anal.*, 25:294–318, 1988.

D. Falceta-Gonçalves and Z. Abraham. MHD numerical simulations of colliding winds in massive binary systems - I. Thermal versus non-thermal radio emission. MNRAS, page 2922, April 2012. doi: 10.1111/j.1365-2966.2012.20978.x.

A. Falcone, S. Bongiorno, M. Stroh, and J. Holder. Increased X-ray activity and likely binary period of HESS J0632+057 Observed by Swift-XRT. *The Astronomer's Telegram*, 3152:1, February 2011.

S. A. E. G. Falle and S. S. Komissarov. An upwind numerical scheme for relativistic hydrodynamics with a general equation of state. MNRAS, 278:586–602, January 1996.

A. Ferrari, E. Trussoni, and L. Zaninetti. Relativistic Kelvin-Helmholtz instabilities in extragalactic radio-sources. A&A, 64:43–52, March 1978.

D. Folini and R. Walder. 3D Hydrodynamical Simulations of Colliding Wind Binaries: Theory Confronts Observations. Ap&SS, 274:189–194, October 2000. doi: 10.1023/A:1026560309386.

D. Folini and R. Walder. Supersonic turbulence in shock-bound interaction zones. I. Symmetric settings. A&A, 459:1–19, November 2006. doi: 10.1051/0004-6361:20053898.

J. A. Font, J. M. Ibanez, A. Marquina, and J. M. Marti. Multidimensional relativistic hydrodynamics: Characteristic fields and modern high-resolution shock-capturing schemes. A&A, 282:304–314, February 1994.

S. Fromang, P. Hennebelle, and R. Teyssier. A high order Godunov scheme with constrained transport and adaptive mesh refinement for astrophysical magnetohydrodynamics. *A&A*, 457: 371–384, October 2006.

A. W. Fullerton, D. L. Massa, and R. K. Prinja. The Discordance of Mass-Loss Estimates for Galactic O-Type Stars. ApJ, 637:1025–1039, February 2006. doi: 10.1086/498560.

B. M. Gaensler and P. O. Slane. The Evolution and Structure of Pulsar Wind Nebulae. ARA&A, 44:17–47, September 2006. doi: 10.1146/annurev.astro.44.051905.092528.

K. G. Gayley. Asymptotic Opening Angles for Colliding-Wind Bow Shocks: The Characteristic-Angle Approximation. ApJ, 703:89–95, September 2009. doi: 10.1088/0004-637X/703/1/89.

K. G. Gayley, S. P. Owocki, and S. R. Cranmer. Sudden Radiative Braking in Colliding Hot-Star Winds. ApJ, 475:786–+, February 1997. doi: 10.1086/303573.

R. A. Gerwin. Stability of the Interface between Two Fluids in Relative Motion. *Reviews of Modern Physics*, 40:652–658, July 1968. doi: 10.1103/RevModPhys.40.652.

B. Giacomazzo and L. Rezzolla. The exact solution of the Riemann problem in relativistic magnetohydrodynamics. *Journal of Fluid Mechanics*, 562:223–259, September 2006. doi: 10.1017/S0022112006001145.

R. C. Gilman. On the Coupling of Grains to the Gas in Circumstellar Envelopes. ApJ, 178: 423–426, December 1972. doi: 10.1086/151800.

R. A. Gingold and J. J. Monaghan. Smoothed particle hydrodynamics - Theory and application to non-spherical stars. MNRAS, 181:375–389, November 1977.

T. Girard and L. A. Willson. Winds in collision. III - Modeling the interaction nebulae of eruptive symbiotics. A&A, 183:247–256, September 1987.

S.K. Godunov. A difference method for numerical calculation of discontinuous solutions of the equations of hydrodynamics. *MAT. SB. (N.S.)*, 1959.

M. Güdel and Y. Nazé. X-ray spectroscopy of stars. A&A Rev., 17:309–408, September 2009. doi: 10.1007/s00159-009-0022-4.

D. Hadasch, D. F. Torres, T. Tanaka, R. H. D. Corbet, A. B. Hill, R. Dubois, G. Dubus, T. Glanzman, S. Corbel, J. Li, Y. P. Chen, S. Zhang, G. A. Caliandro, M. Kerr, J. L. Richards, W. Max-Moerbeck, A. Readhead, and G. Pooley. Long-term Monitoring of the High-energy γ-Ray Emission from LS I +61 303 and LS 5039. ApJ, 749:54, April 2012. doi: 10.1088/0004-637X/749/1/54.

T. J. Harries, J. D. Monnier, N. H. Symington, and R. Kurosawa. Three-dimensional dust radiative-transfer models: the Pinwheel Nebula of WR 104. MNRAS, 350:565–574, May 2004a. doi: 10.1111/j.1365-2966.2004.07668.x.

T. J. Harries, J. D. Monnier, N. H. Symington, and R. Kurosawa. Three-dimensional dust radiative-transfer models: the Pinwheel Nebula of WR 104. MNRAS, 350:565–574, May 2004b. doi: 10.1111/j.1365-2966.2004.07668.x.

P.D. Harten and B. Van Leer. On upstream differencing and godunov-type schemes for hyperbolic conservation laws. *SIAM Review*, 25(1):35–61, January 1983.

S. M. Haser, D. J. Lennon, R.-P. Kudritzki, J. Puls, A. W. A. Pauldrach, L. Bianchi, and J. B. Hutchings. The stellar wind of an O8.5 I(f) star in M 31. A&A, 295:136–146, March 1995.

F. Heitsch, A. D. Slyz, J. E. G. Devriendt, L. W. Hartmann, and A. Burkert. Magnetized Nonlinear Thin-Shell Instability: Numerical Studies in Two Dimensions. ApJ, 665:445–456, August 2007. doi: 10.1086/519513.

D. B. Henley, I. R. Stevens, and J. M. Pittard. Probing the wind-wind collision in γ^2 Velorum with high-resolution Chandra X-ray spectroscopy: evidence for sudden radiative braking and non-equilibrium ionization. MNRAS, 356:1308–1326, February 2005. doi: 10.1111/j.1365-2966.2004.08556.x.

J. J. Hester, K. Mori, D. Burrows, J. S. Gallagher, J. R. Graham, M. Halverson, A. Kader, F. C. Michel, and P. Scowen. Hubble Space Telescope and Chandra Monitoring of the Crab Synchrotron Nebula. ApJ, 577:L49–L52, September 2002. doi: 10.1086/344132.

I. D. Howarth and R. K. Prinja. The stellar winds of 203 Galactic O stars - A quantitative ultraviolet survey. ApJS, 69:527–592, March 1989. doi: 10.1086/191321.

I. D. Howarth and W. Schmutz. Near-infrared spectroscopy of Galactic Wolf-Rayet stars. A&A, 261:503–522, August 1992.

R. Q. Huang and A. Weigert. Shock fronts in wide binary systems. A&A, 112:281–286, August 1982.

S. Johnston, R. N. Manchester, A. G. Lyne, M. Bailes, V. M. Kaspi, G. Qiao, and N. D'Amico. PSR 1259-63 - A binary radio pulsar with a Be star companion. ApJ, 387:L37–L41, March 1992. doi: 10.1086/186300.

J. Kallrath. Dynamics of colliding binary stellar winds - Pressure equilibrium models. MNRAS, 248:653–663, February 1991.

O. Kargaltsev and G. G. Pavlov. X-Ray Emission from PSR J1809-1917 and Its Pulsar Wind Nebula, Possibly Associated with the TeV Gamma-Ray Source HESS J1809-193. ApJ, 670: 655–667, November 2007. doi: 10.1086/521814.

C. F. Kennel and F. V. Coroniti. Confinement of the Crab pulsar's wind by its supernova remnant. ApJ, 283:694–709, August 1984. doi: 10.1086/162356.

H. T. Kenny and A. R. Taylor. Colliding Winds in Symbiotic Binary Systems. I. Analytic and Numerical Solutions. ApJ, 619:527–537, January 2005. doi: 10.1086/426309.

H. T. Kenny and A. R. Taylor. Colliding Winds in Symbiotic Binary Systems. II. Colliding Winds Geometries and Orbital Motion in the Symbiotic Nova AG Pegasi. ApJ, 662:1231–1244, June 2007. doi: 10.1086/517902.

R. Keppens, Z. Meliani, A.J. van Marle, P. Delmont, A. Vlasis, and B. van der Holst. Parallel, grid-adaptive approaches for relativistic hydro and magnetohydrodynamics. *Journal of Computational Physics*, 231(3):718 – 744, 2012. ISSN 0021-9991. doi: 10.1016/j.jcp.2011.01.020.

J. G. Kirk, Y. Lyubarsky, and J. Petri. The Theory of Pulsar Winds and Nebulae. In W. Becker, editor, *Astrophysics and Space Science Library*, volume 357 of *Astrophysics and Space Science Library*, page 421, 2009.

H. A. Kobulnicky and C. L. Fryer. A New Look at the Binary Characteristics of Massive Stars. ApJ, 670:747–765, November 2007. doi: 10.1086/522073.

S. S. Komissarov. Numerical simulations of relativistic magnetized jets. MNRAS, 308:1069–1076, October 1999. doi: 10.1046/j.1365-8711.1999.02783.x.

S. S. Komissarov and Y. E. Lyubarsky. Synchrotron nebulae created by anisotropic magnetized pulsar winds. MNRAS, 349:779–792, April 2004. doi: 10.1111/j.1365-2966.2004.07597.x.

A. V. Kravtsov, A. A. Klypin, and A. M. Khokhlov. Adaptive Refinement Tree: A New High-Resolution N-Body Code for Cosmological Simulations. ApJS, 111:73, July 1997. doi: 10.1086/313015.

R. P. Kudritzki, A. Pauldrach, J. Puls, and D. C. Abbott. Radiation-driven winds of hot stars. VI - Analytical solutions for wind models including the finite cone angle effect. A&A, 219: 205–218, July 1989.

S. R. Kulkarni and J. J. Hester. Discovery of a nebula around PSR1957+20. Nature, 335: 801–803, October 1988. doi: 10.1038/335801a0.

K. Kwak, D. B. Henley, and R. L. Shelton. Simulations of High-velocity Clouds. I. Hydrodynamics and High-velocity High Ions. ApJ, 739:30, September 2011. doi: 10.1088/0004-637X/739/1/30.

A. Lamberts, S. Fromang, and G. Dubus. High-resolution numerical simulations of unstable colliding stellar winds. MNRAS, 418:2618–2629, December 2011a. doi: 10.1111/j.1365-2966.2011.19653.x.

A. Lamberts, S. Fromang, and G. Dubus. High resolution numerical simulations of unstable colliding stellar winds. MNRAS, 418:2618 (paper I), November 2011b. doi: 10.1111/j.1365-2966.2011.19653.x.

A. Lamberts, G. Dubus, G. Lesur, and S. Fromang. Impact of orbital motion on the structure and stability of adiabatic shocks in colliding wind binaries. A&A, 2012.

J.G.L.M. Lamers and J.P Cassinelli. *Introduction to stellar winds*. Cambridge University Press, 1999.

L. D. Landau and E. M. Lifshitz. *Fluid Mechanics*. 1975.

S. H. Langer, G. Chanmugam, and G. Shaviv. Thermal instability in accretion flows onto degenerate stars. ApJ, 245:L23–L26, April 1981. doi: 10.1086/183514.

M. Latini, O. Schilling, and W. Don. High-resolution simulations and modeling of reshocked single-mode richtmyer-meshkov instability: Comparison to experimental data and to amplitude growth model predictions. *Physics of Fluids*, 2007.

M. G. Lebedev and A. V. Myasnikov. Interaction of two supersonic radial gas flows. *Fluid Dynamics*, 25:629–635, August 1990.

L. Lefèvre, S. V. Marchenko, S. Lépine, A. F. J. Moffat, A. Acker, T. J. Harries, K. Annuk, D. A. Bohlender, H. Demers, Y. Grosdidier, G. M. Hill, N. D. Morrison, D. C. Knauth, G. Skalkowski, and S. Viti. Spectroscopic study of the long-period dust-producing WC7pd+O9 binary HD192641. MNRAS, 360:141–152, June 2005. doi: 10.1111/j.1365-2966.2005.09017.x.

C. Leitherer, J. M. Chapman, and B. Koribalski. Radio Continuum Measurements of Southern Early-Type Stars. II. A Distance-limited Sample of Wolf-Rayet Stars. ApJ, 481:898–+, May 1997. doi: 10.1086/304096.

M. N. Lemaster, J. M. Stone, and T. A. Gardiner. Effect of the Coriolis Force on the Hydrodynamics of Colliding-Wind Binaries. ApJ, 662:582–595, June 2007. doi: 10.1086/515431.

R. J. Leveque. Nonlinear Conservation Laws and Finite Volume Methods. In O. Steiner and A. Gautschy, editors, *Saas-Fee Advanced Course 27: Computational Methods for Astrophysical Fluid Flow.*, page 1, 1998.

L. B. Lucy. A numerical approach to the testing of the fission hypothesis. AJ, 82:1013–1024, December 1977. doi: 10.1086/112164.

L. B. Lucy and P. M. Solomon. Mass Loss by Hot Stars. ApJ, 159:879, March 1970. doi: 10.1086/150365.

S. Luehrs. A Colliding-Wind Model for the Wolf-Rayet System HD 152270. PASP, 109:504–513, May 1997. doi: 10.1086/133907.

D. Luo, R. McCray, and M.-M. Mac Low. X-rays from colliding stellar winds. ApJ, 362:267–273, October 1990. doi: 10.1086/169263.

M.-M. Mac Low and M. L. Norman. Nonlinear growth of dynamical overstabilities in blast waves. ApJ, 407:207–218, April 1993. doi: 10.1086/172506.

K. B. MacGregor, L. Hartmann, and J. C. Raymond. Radiative amplification of sound waves in the winds of O and B stars. ApJ, 231:514–523, July 1979. doi: 10.1086/157213.

S. V. Marchenko and A. F. J. Moffat. Dust Formation in Massive WR+O Binaries: Recent Results. In N. St.-Louis & A. F. J. Moffat, editor, *Massive Stars in Interactive Binaries*, volume 367 of *Astronomical Society of the Pacific Conference Series*, pages 213–+, 2007.

S. V. Marchenko, A. F. J. Moffat, and G. Koenigsberger. The Wolf-Rayet binary V444 Cygni under the spectroscopic microscope. 1: Improved characteristics of the components and their interaction seen in He I. ApJ, 422:810–822, February 1994. doi: 10.1086/173773.

A. Marquina, J.M. Marti, J.M. Ibanez, J.A. Miralles, and R Donat. Ultrarelativistic hydrodynamics: High-resolution shock capturing methods. A&A, 258:566–571, 1992.

J. M. Martí and E. Müller. Numerical Hydrodynamics in Special Relativity. *Living Reviews in Relativity*, 6:7–+, December 2003.

J.M. Martí and E. Müller. The analytical solution of the Riemann problem in relativistic hydrodynamics. *Journal of Fluid Mechanics*, 258:317–333, 1994.

N. Mauron and P. J. Huggins. Imaging the circumstellar envelopes of AGB stars. A&A, 452: 257–268, June 2006. doi: 10.1051/0004-6361:20054739.

Z. Meliani, R. Keppens, F. Casse, and D. Giannios. AMRVAC and relativistic hydrodynamic simulations for gamma-ray burst afterglow phases. MNRAS, 376:1189–1200, April 2007. doi: 10.1111/j.1365-2966.2007.11500.x.

A. Mignone. The Dynamics of Radiative Shock Waves: Linear and Nonlinear Evolution. ApJ, 626:373–388, June 2005. doi: 10.1086/429905.

A. Mignone and G. Bodo. An HLLC Riemann solver for relativistic flows - I. Hydrodynamics. MNRAS, 364:126–136, November 2005. doi: 10.1111/j.1365-2966.2005.09546.x.

A. Mignone and G. Bodo. An HLLC Riemann solver for relativistic flows - II. Magnetohydrodynamics. MNRAS, 368:1040–1054, May 2006. doi: 10.1111/j.1365-2966.2006.10162.

A. Mignone and J. C. McKinney. Equation of state in relativistic magnetohydrodynamics: variable versus constant adiabatic index. MNRAS, 378:1118–1130, July 2007. doi: 10.1111/j.1365-2966.2007.11849.x.

A. Mignone, G. Bodo, S. Massaglia, T. Matsakos, O. Tesileanu, C. Zanni, and A. Ferrari. PLUTO: A Numerical Code for Computational Astrophysics. ApJS, 170:228–242, May 2007. doi: 10.1086/513316.

A. Mignone, C. Zanni, P. Tzeferacos, B. van Straalen, P. Colella, and G. Bodo. The PLUTO Code for Adaptive Mesh Computations in Astrophysical Fluid Dynamics. ApJS, 198:7, January 2012. doi: 10.1088/0067-0049/198/1/7.

D. Mihalas and B. W. Mihalas. *Foundations of radiation hydrodynamics*. 1984.

F. Millour, T. Driebe, O. Chesneau, J. H. Groh, K.-H. Hofmann, K. Murakawa, K. Ohnaka, D. Schertl, and G. Weigelt. VLTI/AMBER unveils a possible dusty pinwheel nebula in WR118. A&A, 506:L49–L52, November 2009. doi: 10.1051/0004-6361/200912992.

E. A. Milne. On the possibility of the emission of high-speed atoms from the sun and stars. MNRAS, 86:459–473, May 1926.

Marti. J.M.and Miralles. Numerical relativistic hydrodynamics: Local characteristic approach. *Phys. Rev. D*, 43:3794–3801, 1991.

A. F. J. Moffat, L. Drissen, R. Lamontagne, and C Robert. Spectroscopic evidence for rapid blob ejection in Wolf-Rayet stars. ApJ, 334:1038–1043, November 1988. doi: 10.1086/166895.

J. Moldón, S. Johnston, M. Ribó, J. M. Paredes, and A. T. Deller. Discovery of Extended and Variable Radio Structure from the Gamma-ray Binary System PSR B1259-63/LS 2883. ApJ, 732:L10, May 2011a. doi: 10.1088/2041-8205/732/1/L10.

J. Moldón, M. Ribó, and J. M. Paredes. Revealing the extended radio emission from the gamma-ray binary HESS J0632+057. A&A, 533:L7, September 2011b. doi: 10.1051/0004-6361/201117764.

J.J Monaghan. Particle methods for hydrodynamics. *Comput. Phys. Rep.*, 3:71–124, 1985.

J. D. Monnier, P. G. Tuthill, W. C. Danchi, N. Murphy, and T. J. Harries. The Keck Aperture-masking Experiment: Near-Infrared Sizes of Dusty Wolf-Rayet Stars. ApJ, 655:1033–1045, February 2007. doi: 10.1086/509873.

J. P. Moran, R. J. Davis, R. E. Spencer, M. F. Bode, and A. R. Taylor. MERLIN observations of the Wolf-Rayet star AS431 (WR147) - A double radio source. Nature, 340:449, August 1989. doi: 10.1038/340449a0.

J.P. Morris and J.J. Monaghan. A switch to reduce sph viscosity. *Journal of Computational Physics*, 136(1):41 – 50, 1997. ISSN 0021-9991. doi: 10.1006/jcph.1997.5690.

D. C. Morton. The Far-Ultraviolet Spectra of Six Stars in Orion. ApJ, 147:1017, March 1967. doi: 10.1086/149091.

S. M. Motamen, R. Walder, and D. Folini. Heat conduction and colliding winds in Wolf-Rayet binaries. In K. A. van der Hucht, G. Koenigsberger, and P. R. J. Eenens, editors, *Wolf-Rayet Phenomena in Massive Stars and Starburst Galaxies*, volume 193 of *IAU Symposium*, page 378, 1999.

A. V. Myasnikov and S. A. Zhekov. Dissipative models of colliding stellar winds - I. Effects of thermal conduction in wide binary systems. MNRAS, 300:686–694, November 1998. doi: 10.1046/j.1365-8711.1998.01857.x.

A. V. Myasnikov and S. A. Zhekov. Modelling of X-ray emission from WR + O binary systems. MNRAS, 260:221–240, January 1993.

A. V. Myasnikov, S. A. Zhekov, and N. A. Belov. Radiative steady-state colliding stellar wind models: are they correct? MNRAS, 298:1021–1029, August 1998. doi: 10.1046/j.1365-8711.1998.01666.x.

Y. Nazé, M. F. Corcoran, G. Koenigsberger, and A. F. J. Moffat. First Detection of Phase-dependent Colliding Wind X-Ray Emission outside the Milky Way. ApJ, 658:L25–L28, March 2007. doi: 10.1086/513510.

S. C. Noble, C. F. Gammie, J. C. McKinney, and L. Del Zanna. Primitive Variable Solvers for Conservative General Relativistic Magnetohydrodynamics. ApJ, 641:626–637, April 2006. doi: 10.1086/500349.

A. T. Okazaki, S. P. Owocki, C. M. P. Russell, and M. F. Corcoran. Modelling the RXTE light curve of η Carinae from a 3D SPH simulation of its binary wind collision. MNRAS, 388: L39–L43, July 2008. doi: 10.1111/j.1745-3933.2008.00496.x.

A. T. Okazaki, S. Nagataki, T. Naito, A. Kawachi, K. Hayasaki, S. P. Owocki, and J. Takata. Hydrodynamic Interaction between the Be Star and the Pulsar in the TeV Binary PSR B1259-63/LS 2883. PASJ, 63:893–, August 2011.

R. A. Ong. VERITAS Reports Activity from HESS J0632+057 in Very High Energy Gamma Rays. *The Astronomer's Telegram*, 3791:1, November 2011.

S. P. Owocki and G. B. Rybicki. Instabilities in line-driven stellar winds. I - Dependence on perturbation wavelength. ApJ, 284:337–350, September 1984. doi: 10.1086/162412.

N. Panagia and M. Felli. The spectrum of the free-free radiation from extended envelopes. A&A, 39:1–5, February 1975.

J. M. Paredes. Gamma-ray binaries: microquasars and binary systems with pulsar. *ArXiv e-prints*, January 2011.

E. N. Parker. Dynamics of the Interplanetary Gas and Magnetic Fields. ApJ, 128:664, November 1958. doi: 10.1086/146579.

E. N. Parker. Dynamical Theory of the Solar Wind. Space Sci. Rev., 4:666–708, September 1965. doi: 10.1007/BF00216273.

E. R. Parkin and J. M. Pittard. A 3D dynamical model of the colliding winds in binary systems. MNRAS, 388:1047–1061, August 2008. doi: 10.1111/j.1365-2966.2008.13511.x.

E. R. Parkin and J. M. Pittard. Numerical heat conduction in hydrodynamical models of colliding hypersonic flows. MNRAS, 406:2373–2385, August 2010. doi: 10.1111/j.1365-2966.2010.16888.x.

E. R. Parkin, J. M. Pittard, M. F. Corcoran, and K. Hamaguchi. Spiraling Out of Control: Three-dimensional Hydrodynamical Modeling of the Colliding Winds in η Carinae. ApJ, 726: 105, January 2011. doi: 10.1088/0004-637X/726/2/105.

A. Pauldrach, J. Puls, and R. P. Kudritzki. Radiation-driven winds of hot luminous stars - Improvements of the theory and first results. A&A, 164:86–100, August 1986.

K.M. Peery and S.T. Imlay. Blunt-body flow simulations. *AIAA*, 1988.

U.-L. Pen. A High-Resolution Adaptive Moving Mesh Hydrodynamic Algorithm. ApJS, 115:19, March 1998. doi: 10.1086/313074.

M. Perucho, J. M. Martí, and M. Hanasz. Stability of hydrodynamical relativistic planar jets. II. Long-term nonlinear evolution. A&A, 427:431–444, November 2004. doi: 10.1051/0004-6361:20040350.

N. N. Pilyugin and V. V. Usov. Collision of Two Identical Hypersonic Stellar Winds in Binary Systems. ApJ, 655:1002–1009, February 2007. doi: 10.1086/510116.

J. M. Pittard. Hydrodynamic simulations of the colliding winds in IOTA Orionis. MNRAS, 300: 479–492, October 1998. doi: 10.1046/j.1365-8711.1998.01915.x.

J. M. Pittard. A Clumping-independent Diagnostic of Stellar Mass-Loss Rates: Rapid Clump Destruction in Adiabatic Colliding Winds. ApJ, 660:L141–L144, May 2007. doi: 10.1086/518365.

J. M. Pittard. 3D models of radiatively driven colliding winds in massive O+O star binaries - I. Hydrodynamics. MNRAS, 396:1743–1763, July 2009. doi: 10.1111/j.1365-2966.2009.14857.x.

J. M. Pittard. Models of the Non-Thermal Emission from Early-Type Binaries. In J. Martí, P. L. Luque-Escamilla, & J. A. Combi, editor, *High Energy Phenomena in Massive Stars*, volume 422 of *Astronomical Society of the Pacific Conference Series*, page 145, May 2010.

J. M. Pittard and M. F. Corcoran. In hot pursuit of the hidden companion of eta Carinae: An X-ray determination of the wind parameters. A&A, 383:636–647, February 2002. doi: 10.1051/0004-6361:20020025.

J. M. Pittard and S. M. Dougherty. Radio, X-ray, and γ-ray emission models of the colliding-wind binary WR140. MNRAS, 372:801–826, October 2006. doi: 10.1111/j.1365-2966.2006.10888.x.

J. M. Pittard, S. M. Dougherty, R. F. Coker, and M. F. Corcoran. X-ray and Radio Emission from Colliding Stellar Winds. In L. O. Sjouwerman and K. K. Dyer, editors, *X-Ray and Radio Connections*, April 2005.

J. M. Pittard, S. M. Dougherty, R. F. Coker, E. O'Connor, and N. J. Bolingbroke. Radio emission models of colliding-wind binary systems. Inclusion of IC cooling. A&A, 446:1001–1019, February 2006. doi: 10.1051/0004-6361:20053649.

J. A. Pons, J.M Marti, and E. Muller. The exact solution of the Riemann problem with non-zero tangential velocities in relativistic hydrodynamics. *Journal of Fluid Mechanics*, 422:125–139, 2000.

Daniel J. Price. Smoothed particle hydrodynamics and magnetohydrodynamics. *Journal of Computational Physics*, 231(3):759 – 794, 2012. ISSN 0021-9991. doi: 10.1016/j.jcp.2010.12.011.

O. F. Prilutskii and V. V. Usov. X rays from Wolf-Rayet binaries. Soviet Ast., 20:2, February 1976.

J. Puls, R.-P. Kudritzki, A. Herrero, A. W. A. Pauldrach, S. M. Haser, D. J. Lennon, R. Gabler, S. A. Voels, J. M. Vilchez, S. Wachter, and A. Feldmeier. O-star mass-loss and wind momentum rates in the Galaxy and the Magellanic Clouds Observations and theoretical predictions. A&A, 305:171, January 1996.

J. Puls, J. S. Vink, and F. Najarro. Mass loss from hot massive stars. A&A Rev., 16:209–325, December 2008a. doi: 10.1007/s00159-008-0015-8.

J. Puls, J. S. Vink, and F. Najarro. Mass loss from hot massive stars. A&A Rev., 16:209–325, December 2008b. doi: 10.1007/s00159-008-0015-8.

M. J. Rees and J. E. Gunn. The origin of the magnetic field and relativistic particles in the Crab Nebula. MNRAS, 167:1–12, April 1974.

A. Reimer, M. Pohl, and O. Reimer. Nonthermal High-Energy Emission from Colliding Winds of Massive Stars. ApJ, 644:1118–1144, June 2006. doi: 10.1086/503598.

L. Rezolla, 0. Zanotti, and J. Pons. An improved exact Riemann solver for multidimensional relativistic flows. *Journal of Fluid Mechanics*, 479:199–219, 2003.

M. Ribó, J. M. Paredes, J. Moldón, J. Martí, and M. Massi. The changing milliarcsecond radio morphology of the gamma-ray binary <ASTROBJ>LS 5039</ASTROBJ>. A&A, 481:17–20, April 2008. doi: 10.1051/0004-6361:20078390.

M. S. E. Roberts. New Black Widows and Redbacks in the Galactic Field. In M. Burgay, N. D'Amico, P. Esposito, A. Pellizzoni, & A. Possenti , editor, *American Institute of Physics Conference Series*, volume 1357 of *American Institute of Physics Conference Series*, pages 127–130, August 2011. doi: 10.1063/1.3615095.

G. E. Romero, H. R. Christiansen, and M. Orellana. Hadronic High-Energy Gamma-Ray Emission from the Microquasar LS I +61 303. ApJ, 632:1093–1098, October 2005. doi: 10.1086/444446.

G. B. Rybicki and A. P. Lightman. *Radiative processes in astrophysics*. 1979.

D. Ryu, I. Chattopadhyay, and E. Choi. Equation of State in Numerical Relativistic Hydrodynamics. ApJS, 166:410–420, September 2006. doi: 10.1086/505937.

V. Schneider, U. Katscher, D.H. Rischke, B. Waldhauser, J.A. Maruhn, and C.-D. Munz. New algorithms for ultra-relativistic numerical hydrodynamics. *Journal of Computational Physics*, 105(1):92 – 107, 1993. ISSN 0021-9991. doi: DOI: 10.1006/jcph.1993.1056.

E. M. Schneiter, P. F. Velázquez, A. Esquivel, A. C. Raga, and X. Blanco-Cano. Three-dimensional Hydrodynamical Simulation of the Exoplanet HD 209458b. ApJ, 671:L57–L60, December 2007. doi: 10.1086/524945.

V. V. Sobolev and S. Gaposchkin. Review of Publications- Moving Envelopes of Stars. JRASC, 54:254, October 1960.

V. Springel. E pur si muove: Galilean-invariant cosmological hydrodynamical simulations on a moving mesh. MNRAS, 401:791–851, January 2010. doi: 10.1111/j.1365-2966.2009.15715.x.

V. Springel, N. Yoshida, and S. D. M. White. GADGET: a code for collisionless and gasdynamical cosmological simulations. *New Astronomy*, 6:79–117, April 2001. doi: 10.1016/S1384-1076(01)00042-2.

V. Springel, S. D. M. White, A. Jenkins, C. S. Frenk, N. Yoshida, L. Gao, J. Navarro, R. Thacker, D. Croton, J. Helly, J. A. Peacock, S. Cole, P. Thomas, H. Couchman, A. Evrard, J. Colberg, and F. Pearce. Simulations of the formation, evolution and clustering of galaxies and quasars. Nature, 435:629–636, June 2005. doi: 10.1038/nature03597.

N. St-Louis, A. F. J. Moffat, S. Marchenko, and J. M. Pittard. FUSE Observations of the SMC 16 day Wolf-Rayet Binary Sanduleak 1 (WO4+O4): Atmospheric Eclipses and Colliding Stellar Winds. ApJ, 628:953–972, August 2005. doi: 10.1086/430585.

N. St-Louis, D. Soutière, S. Péloquin, A. de La Chevrotière, V. Hénault-Brunet, and A.-N. Chené. Spectroscopic Monitoring in the Optical Wavelength Region of Nine WC9 Stars. *Bulletin de la Societe Royale des Sciences de Liege*, 80:190–194, January 2011.

I. R. Stevens. Colliding wind bindary systems - Monte Carlo simulations of line-profile variability. ApJ, 404:281–293, February 1993. doi: 10.1086/172278.

I. R. Stevens and I. D. Howarth. Infrared line-profile variability in Wolf–Rayet binary systems. MNRAS, 302:549–560, January 1999. doi: 10.1046/j.1365-8711.1999.02151.x.

I. R. Stevens and A. M. T. Pollock. Stagnation-Point Flow in Colliding Wind Binary Systems. MNRAS, 269:226–+, July 1994.

I. R. Stevens, J. M. Blondin, and A. M. T. Pollock. Colliding winds from early-type stars in binary systems. ApJ, 386:265–287, February 1992. doi: 10.1086/171013.

J. M. Stone and M. L. Norman. ZEUS-2D: A radiation magnetohydrodynamics code for astrophysical flows in two space dimensions. I - The hydrodynamic algorithms and tests. ApJS, 80: 753–790, June 1992. doi: 10.1086/191680.

J. M. Stone, T. A. Gardiner, P. Teuben, J. F. Hawley, and J. B. Simon. Athena: A New Code for Astrophysical MHD. ApJS, 178:137–177, September 2008. doi: 10.1086/588755.

R. Strickland and J. M. Blondin. Numerical Analysis of the Dynamic Stability of Radiative Shocks. ApJ, 449:727–+, August 1995. doi: 10.1086/176093.

A. H. Taub. Relativistic Rankine-Hugoniot Equations. *Phys. Rev.*, 74:328–334, Aug 1948. doi: 10.1103/PhysRev.74.328.

M. Tavani and J. Arons. Theory of High-Energy Emission from the Pulsar/Be Star System PSR 1259-63. I. Radiation Mechanisms and Interaction Geometry. ApJ, 477:439, March 1997. doi: 10.1086/303676.

M. Tavani and L. Brookshaw. Outflow hydrodynamics in the eclipsing millisecond pulsar binaries PSR 1957 + 20 and PSR 1744 - 24A. ApJ, 381:L21–L24, November 1991. doi: 10.1086/186187.

M. Teodoro, A. Damineli, J. I. Arias, F. X. de Araújo, R. H. Barbá, M. F. Corcoran, M. Borges Fernandes, E. Fernández-Lajús, L. Fraga, R. C. Gamen, J. F. González, J. H. Groh, J. L. Marshall, P. J. McGregor, N. Morrell, D. C. Nicholls, E. R. Parkin, C. B. Pereira, M. M. Phillips, G. R. Solivella, J. E. Steiner, M. Stritzinger, I. Thompson, C. A. O. Torres, M. A. P. Torres, and M. I. Zevallos Herencia. He II λ4686 in η Carinae: Collapse of the Wind-Wind Collision Region during Periastron Passage. ApJ, 746:73, February 2012. doi: 10.1088/0004-637X/746/1/73.

R. Teyssier. Cosmological hydrodynamics with adaptive mesh refinement. A new high resolution code called RAMSES. *A&A*, 385:337–364, April 2002. doi: 10.1051/0004-6361:20011817.

E. F. Toro. *Riemann solvers and numerical methods for fluid dynamics*. Springer-Verlag, 2009.

E. F. Toro, M. Spruce, and W. Speares. Restoration of the contact surface in the HLL-Riemann solver. *Shock Waves*, 4:25–34, July 1994. doi: 10.1007/BF01414629.

J. K. Truelove, R. I. Klein, C. F. McKee, J. H. Holliman, II, L. H. Howell, J. A. Greenough, and D. T. Woods. Self-gravitational Hydrodynamics with Three-dimensional Adaptive Mesh Refinement: Methodology and Applications to Molecular Cloud Collapse and Fragmentation. ApJ, 495:821, March 1998. doi: 10.1086/305329.

B. D. Turland and P. A. G. Scheuer. Instabilities of Kelvin-Helmholtz type for relativistic streaming. MNRAS, 176:421–441, August 1976.

P. Tuthill, J. Monnier, A. Tanner, D. Figer, A. Ghez, and W. Danchi. Pinwheels in the Quintuplet Cluster. *Science*, 313:935, August 2006. doi: 10.1126/science.1128731.

P. G. Tuthill, J. D. Monnier, and W. C. Danchi. A dusty pinwheel nebula around the massive star WR104. Nature, 398:487–489, April 1999. doi: 10.1038/19033.

P. G. Tuthill, J. D. Monnier, N. Lawrance, W. C. Danchi, S. P. Owocki, and K. G. Gayley. The Prototype Colliding-Wind Pinwheel WR 104. ApJ, 675:698–710, March 2008. doi: 10.1086/527286.

V. V. Usov. Stellar wind collision and dust formation in long-period, heavily interacting Wolf-Rayet binaries. MNRAS, 252:49–52, September 1991.

V. V. Usov. Stellar wind collision and X-ray generation in massive binaries. ApJ, 389:635–648, April 1992. doi: 10.1086/171236.

K. A. van der Hucht. The VIIth catalogue of galactic Wolf-Rayet stars. *New Astronomical Review*, 45:135–232, February 2001. doi: 10.1016/S1387-6473(00)00112-3.

K. A. van der Hucht, P. M. Williams, T. A. T. Spoelstra, and A. G. de Bruyn. Non-thermal radio observations of Wolf-Rayet stars: a case for long-period binaries. In L. Drissen, C. Leitherer, and A. Nota, editors, *Nonisotropic and Variable Outflows from Stars*, volume 22 of *Astronomical Society of the Pacific Conference Series*, pages 253–268, 1992.

E. van der Swaluw. Interaction of a magnetized pulsar wind with its surroundings. MHD simulations of pulsar wind nebulae. A&A, 404:939–947, June 2003. doi: 10.1051/0004-6361:20030452.

E. van der Swaluw, A. Achterberg, Y. A. Gallant, T. P. Downes, and R. Keppens. Interaction of high-velocity pulsars with supernova remnant shells. A&A, 397:913–920, January 2003. doi: 10.1051/0004-6361:20021488.

B. Van Leer. Towards the ultimate conservative difference scheme: IV A new approach to numerical convection. *Journal of Computational Physics*, 23:276–299, 1977.

B. Van Leer. Towards the ultimate conservative difference scheme. V. A second-order sequel to Godunov's method. *Journal of Computational Physics*, 32:101 – 136, July 1979. doi: DOI: 10.1016/0021-9991(79)90145-1.

S. van Loo, M. C. Runacres, and R. Blomme. Can single O stars produce non-thermal radio emission? A&A, 452:1011–1019, June 2006. doi: 10.1051/0004-6361:20054266.

A. J. van Marle, R. Keppens, and Z. Meliani. Thin shell morphology in the circumstellar medium of massive binaries. A&A, 527:A3, March 2011a. doi: 10.1051/0004-6361/201015517.

A. J. van Marle, Z. Meliani, R. Keppens, and L. Decin. Computing the Dust Distribution in the Bow Shock of a Fast-moving, Evolved Star. ApJ, 734:L26, June 2011b. doi: 10.1088/2041-8205/734/2/L26.

W. P. Varricatt, P. M. Williams, and N. M. Ashok. Near-infrared spectroscopic monitoring of WR 140 during the 2001 periastron passage. MNRAS, 351:1307–1318, July 2004. doi: 10.1111/j.1365-2966.2004.07867.x.

P. M. Veen, A. M. van Genderen, K. A. van der Hucht, A. Li, C. Sterken, and C. Dominik. WR 121 obscured by a dust cloud: the key to understanding occasional "eclipses" of "dusty" Wolf-Rayet WC stars? A&A, 329:199–212, January 1998.

M. Vigelius, A. Melatos, S. Chatterjee, B. M. Gaensler, and P. Ghavamian. Three-dimensional hydrodynamic simulations of asymmetric pulsar wind bow shocks. MNRAS, 374:793–808, January 2007. doi: 10.1111/j.1365-2966.2006.11193.x.

E. T. Vishniac. Nonlinear instabilities in shock-bounded slabs. ApJ, 428:186–208, June 1994a. doi: 10.1086/174231.

E. T. Vishniac. Nonlinear instabilities in shock-bounded slabs. ApJ, 428:186–208, June 1994b. doi: 10.1086/174231.

H. J. Völk, E. G. Berezhko, L. T. Ksenofontov, and G. P. Rowell. The high energy gamma-ray emission expected from Tycho's supernova remnant. A&A, 396:649–656, December 2002. doi: 10.1051/0004-6361:20021407.

R. Walder. Simulations of colliding winds in 3 dimensions. In K. A. van der Hucht & P. M. Williams, editor, *Wolf-Rayet Stars: Binaries; Colliding Winds; Evolution*, volume 163 of *IAU Symposium*, page 420, 1995.

R. Walder and D. Folini. Radiative cooling instability in 1D colliding flows. A&A, 315:265–283, November 1996.

R. Walder and D. Folini. The Formation of Knots and Filaments in Shocks. Ap&SS, 260:215–224, October 1998. doi: 10.1023/A:1001801104306.

R. Walder and D. Folini. Theoretical Considerations on Colliding Clumped Winds. In A. F. J. Moffat and N. St-Louis, editors, *Interacting Winds from Massive Stars*, volume 260 of *Astronomical Society of the Pacific Conference Series*, page 595, 2002.

R. Walder and D. Folini. 3D-hydrodynamics of colliding winds in massive binaries. In K. van der Hucht, A. Herrero, and C. Esteban, editors, *A Massive Star Odyssey: From Main Sequence to Supernova*, volume 212 of *IAU Symposium*, page 139, 2003.

R. Walder, D. Folini, and S. M. Motamen. Colliding winds in Wolf-Rayet binaries: further developments within a complicated story. In K. A. van der Hucht, G. Koenigsberger, and P. R. J. Eenens, editors, *Wolf-Rayet Phenomena in Massive Stars and Starburst Galaxies*, volume 193 of *IAU Symposium*, page 298, 1999.

W. L. Waldron and J. P. Cassinelli. An Extensive Collection of Stellar Wind X-Ray Source Region Emission Line Parameters, Temperatures, Velocities, and Their Radial Distributions as Obtained from Chandra Observations of 17 OB Stars. ApJ, 668:456–480, October 2007. doi: 10.1086/520919.

R. Walter, C. Farnier, and J.-C. Leyder. η Carinae:. a very Large Hadron Collider. In S. Giani, C. Leroy, and P. G. Rancoita, editors, *Cosmic Rays for Particle and Astroparticle Physics*, pages 569–574, June 2011.

P. Wang, T. Abel, and W. Zhang. Relativistic Hydrodynamic Flows Using Spatial and Temporal Adaptive Structured Mesh Refinement. ApJS, 176:467–483, June 2008a. doi: 10.1086/529434.

P. Wang, T. Abel, and W. Zhang. Relativistic Hydrodynamic Flows Using Spatial and Temporal Adaptive Structured Mesh Refinement. ApJS, 176:467–483, June 2008b. doi: 10.1086/529434.

C. J. Wareing, A. A. Zijlstra, A. K. Speck, T. J. O'Brien, T. Ueta, M. Elitzur, R. D. Gehrz, F. Herwig, H. Izumiura, M. Matsuura, M. Meixner, R. E. Stencel, and R. Szczerba. Detached shells as tracers of asymptotic giant branch-interstellar medium bow shocks. MNRAS, 372: L63–L67, October 2006. doi: 10.1111/j.1745-3933.2006.00227.x.

C. J. Wareing, A. A. Zijlstra, and T. J. O'Brien. Vortices in the Wakes of Asymptotic Giant Branch Stars. ApJ, 660:L129–L132, May 2007. doi: 10.1086/518308.

E. J. Weber and L. Davis, Jr. The Angular Momentum of the Solar Wind. ApJ, 148:217–227, April 1967. doi: 10.1086/149138.

H.J. Wendker and W. Baars, J.W.M.and Altenhoff. Detection of radio emission from P Cygni. *Nature*, 245:118, 1973.

R. L. White and R. H. Becker. The discovery of a hot stellar wind. ApJ, 272:L19–L23, September 1983. doi: 10.1086/184109.

R. L. White and R. H. Becker. An Eight-Year Study of the Radio Emission from the Wolf-Rayet Binary HD 193793 = WR 140. ApJ, 451:352, September 1995. doi: 10.1086/176224.

R. L. White and W. Chen. Theory and observations of non-thermal phenomena in hot massive binaries (Invited). In K. A. van der Hucht and P. M. Williams, editors, *Wolf-Rayet Stars: Binaries; Colliding Winds; Evolution*, volume 163 of *IAU Symposium*, page 438, 1995.

F. P. Wilkin. Exact Analytic Solutions for Stellar Wind Bow Shocks. ApJ, 459:L31+, March 1996. doi: 10.1086/309939.

P. M. Williams, K. A. van der Hucht, and P. S. The. Infrared photometry of late-type Wolf-Rayet stars. A&A, 182:91–106, August 1987.

P. M. Williams, S. V. Marchenko, A. P. Marston, A. F. J. Moffat, W. P. Varricatt, S. M. Dougherty, M. R. Kidger, L. Morbidelli, and M. Tapia. Orbitally modulated dust formation by the WC7+O5 colliding-wind binary WR140. MNRAS, 395:1749–1767, May 2009a. doi: 10.1111/j.1365-2966.2009.14664.x.

P. M. Williams, G. Rauw, and K. A. van der Hucht. Dust formation by the colliding wind WC5+O9 binary WR19 at periastron passage. MNRAS, 395:2221–2225, June 2009b. doi: 10.1111/j.1365-2966.2009.14681.x.

P. M. Williams, K. A. van der Hucht, F. van Wyk, F. Marang, P. A. Whitelock, P. Bouchet, and D. Y. A. Setia Gunawan. Recurrent dust formation by WR 48a on a 30-year time-scale. MNRAS, 420:2526–2538, March 2012. doi: 10.1111/j.1365-2966.2011.20218.x.

A. J. Willis, H. Schild, and I. R. Stevens. ROSAT observations of γ Velorum (WC8+O9I). I. The discovery of colliding-wind X-ray emission. A&A, 298:549, June 1995.

J.R. Wilson. Numerical study of fluid flow in Kerr space . ApJ, 173:431–438, 1972.

C.J.E. Wolf and G.A.P. Rayet. . *Comptes-Rendus de l'Académie des Sciences*, 65:291, 1867.

A. E. Wright and M. J. Barlow. The radio and infrared spectrum of early-type stars undergoing mass loss. MNRAS, 170:41–51, January 1975.

A. A. Zdziarski, A. Neronov, and M. Chernyakova. A compact pulsar wind nebula model of the γ-ray-loud binary LS I +61 303. MNRAS, 403:1873–1886, April 2010. doi: 10.1111/j.1365-2966.2010.16263.x.

S. A. Zhekov and A. V. Myasnikov. Colliding Stellar Winds: "Asymmetric" Thermal Conduction. ApJ, 543:L53–L56, November 2000. doi: 10.1086/318168.